Vortex Dynamics, Statistical Mechanics, *and* Planetary Atmospheres

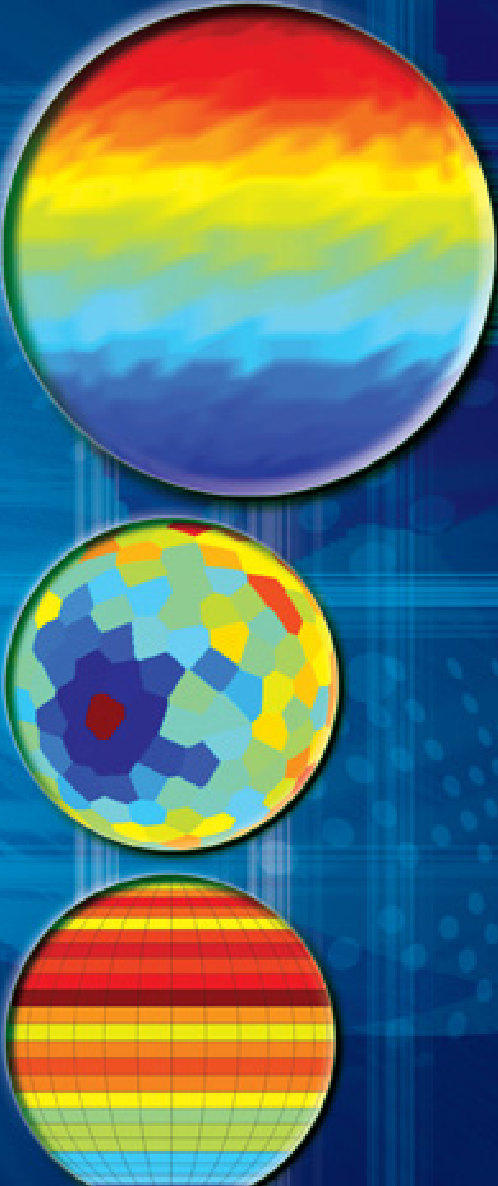

Chjan C Lim
Xueru Ding
Joseph Nebus

World Scientific

Vortex Dynamics, Statistical Mechanics, *and* Planetary Atmospheres

Vortex Dynamics, Statistical Mechanics, *and* Planetary Atmospheres

Chjan C Lim • Xueru Ding • Joseph Nebus
Rensselaer Polytechnic Institute, USA

World Scientific
NEW JERSEY • LONDON • SINGAPORE • BEIJING • SHANGHAI • HONG KONG • TAIPEI • CHENNAI

Published by

World Scientific Publishing Co. Pte. Ltd.
5 Toh Tuck Link, Singapore 596224
USA office: 27 Warren Street, Suite 401-402, Hackensack, NJ 07601
UK office: 57 Shelton Street, Covent Garden, London WC2H 9HE

Library of Congress Cataloging-in-Publication Data
Lim, Chjan C.
Vortex dynamics, statistical mechanics, and planetary atmospheres / Chjan C. Lim, Xueru Ding & Joseph Nebus.
p. cm.
Includes bibliographical references and index.
ISBN-13: 978-981-283-912-1 (hardcover : alk. paper)
ISBN-10: 981-283-912-7 (hardcover : alk. paper)
ISBN-13: 978-981-283-913-8 (pbk. : alk. paper)
ISBN-10: 981-283-913-5 (pbk. : alk. paper)
1. Planets--Atmospheres--Statistical methods. 2. Planets--Atmospheres--Mathematical models. 3. Vortex-motion--Statistical methods. 4. Vortex-motion--Mathematical models. 5. Monte Carlo method. 6. Fluid dynamics. 7. Statistical mechanics. I. Ding, Xueru. II. Nebus, Joseph. III. Title.
QB603.A85L5 2009
551.51'509992--dc22
2009000099

British Library Cataloguing-in-Publication Data
A catalogue record for this book is available from the British Library.

Printed in Singapore.

Preface

This book would not have been written if not for the generosity of the funding agencies, providing sufficient amounts of monies from 2004 - 2008 to buy the computer equipment and most significantly, to support two capable PhD students and two M.Sc graduate students. With one of these recent PhDs, Dr. Xueru Ding, and another PhD student, Dr. Joseph Nebus, we now record the results and products of our work over the last four years, which is informed by several years of earlier works in the subject matter of the book. We would like to acknowledge therefore the program officers, Dr. Chris Arney of the Army Research Office, and Dr. Walt Polansky and Dr. Gary Johnson of the United States Department of Energy.

Many people have contributed to the possibility of this monograph through their works and through helpful discussions but it is only possible to name a few here - the others will have to be content with the knowledge that they and their works are nonetheless appreciated by us. They are Denis Blackmore, Alexey Borizov, Alexandre Chorin, Peter Constantin, Tony Del Genio, Felix Donohue, La Salle PJ, Weinan E, Joe Flaherty, Marty Golubitsky, Tom Hou, Andrew Ingersoll, Joe Keller, Peter Lax, Chuck Leith, David Liao, La Salle PJ, Lin San of Nanyang Technological University, Singapore, Paul Newton, Bob O'Malley, Don Saari, Leslie Sage, Lawrence Sirovich, Eugene Stanley, J.B. Taylor, United Kingdom Fusion Research, Roger Temam, Lu Ting, KK Tung, GertJan van Heijst of Eindhoven, Netherlands, Shouhong Wang, and several anonymous reviewers of journal articles whose critiques and suggestions have been particularly useful.

With Dr. Timothy Andersen, we have several fruitful collaborations in the past and a few exciting on-going projects; with Dr. Junping Shi, we have published a paper on a related topic; with Rajinder Singh Mavi, we have a paper on a topic relevant to chapter 8 in this book and more exciting on-going projects; with Nuwan Silva Induruwege, we have another paper, relevant to this book, to be published; and with Syed M. Assad, we have several papers in this area.

We would also like to acknowledge the support of many in the Department of Mathematical Sciences at Rensselaer Polytechnic Institute, especially, Don Drew, Bill Siegmann, Michele Kronau and Peter Bellamy.

We wish to thank our respective families for their constant support during the preparation of this monograph.

Finally Ms. Chionh at World Scientific Singapore deserves our thanks for persistence over the off and on nature of this book project in the last five years.

The focus of this monograph is a physically sound and rigorous, qualitative theory for the end-states or statistically-stationary asymptotic flow states of the forced-damped rotating shallow water equations, with applications to the super-rotation of slowly-rotating terrestrial planets and major moons and the key large-scale features of the Gas Giants in our solar system. Emphasizing the self-organized emergence of these astrophysical atmospheric structures through first and second order phase transitions, the spin-lattice models under Gibbs canonical constraint on the Lagrangian of the underlying dynamics and various microcanonical constraints on total circulations (sums) and enstrophies (square-norms) of relevant physical quantities, are simulated by Monte-Carlo methods, analyzed by mean-field techniques, and rigorously integrated in closed-form where possible by the non-Gaussian non-mean-field spherical model method. In a 2007 survey of Venusian atmospheric dynamics [87], the retrograde super-rotation of its lower atmosphere, up to 100 km, and also that of Titan, is viewed as a continuing enigma, and all attempts known to the authors of that survey, have so far failed to explain this phenomenon in simple and rigorous physical terms. The Barotropic Vorticity Model which is solved in closed-form by Lim, motivated by the detailed simulation results of Ding and discussed in the first part of this book, offers rigorous predictions on the asymmetry between super-rotation and anti-rotating zonal flows, stating that a slowly-rotating planet can support a super-rotating vertically-averaged barotropic atmosphere at high enough energies, but such coupled atmosphere-planet systems cannot have an anti-rotating barotropic atmosphere unless the planet's spin-rate is fast enough.

Analyzed by rigorous qualitative methods, based on the shallow water equations total mechanical energy, theoretical work independently predict (and further explain the simulation results) the four key Jovian features, namely, (a) anticyclonic predominance, (b) north-south asymmetry of the highest anticyclonic spots, (c) high rim velocity in the circumferential band of Jupiter's Red Spot, and (d) the alternating zones-belts or Limaye bands. In providing this qualitative theory for end-states, by-passing often difficult and costly dynamical simulations of the underlying initial value problems at Jovian parameter sets it is oft asked what is the physical meaning of the statistical models' temperature. We hope to have given here sufficiently detailed discussions of the meaning of this notion in the context of macroscopic flows where subgrid scales could be 1000 km in wavelengths and widely-separated in physical effects from molecular notions of temperature.

Contents

Chapter 1

Planets and Inspiration

1.1 Venus

Only two people are known to have observed the transit of Venus across the sun on the 24th of November, 1639: Jeremiah Horrocks (or Horrox) and his friend William Crabtree, of Toxtenth, a village near Liverpool, England [5]. Johannes Kepler had predicted the 1631 transit, and thought 1639 would be a near miss; Horrocks found Kepler was mistaken. (Horrocks' friend Christopher Townley gave Horrocks's prediction of a transit of Mercury for the 23rd of October, 1651, to Jeremy Shakerley, who moved to Surat, India, to observe it.)

The transit of June 6, 1761, was different: despite the ongoing Seven Years' War making battlegrounds on nearly every continent the major nations of the world launched scientific expeditions which gave many French and British astronomers and surveyors the chance to experience new intensities of frustration, typically at the weather, interrupted with capture and parole by the opposite nation. The scientific result from this which impressed everyone was the roughly modern estimate for the distance between the Earth and the Sun.

But there was another result, one which brings particular inspiration to us, which came from that transit. It was made by the Russian astronomer Mikhail Lomonosov, at the Petersburg Observatory, who saw light refracted around the disc of Venus, indicating there should be an atmosphere. There was a whole new atmosphere and a new meteorology which could be explored, at least provided reliable observations could be made.

But Venus is a difficult planet about which to observe details: 1761 was also the final year in which a putative moon of Venus was observed; observers had seen it, on occasion, since 1645, and even the renowned Giovanni Cassini spotted this moon. Observations of the planet found what appeared to be stable enough formations for many estimates of the planet's day, the majority of them quite close to 24 hours, to be repeatedly made and to sometimes agree with one another. Fine points like the refraction of light around the tiny disc of Venus seen in the precious few moments of the start or end of a transit, an observation which could be made at best twice in a century was slender evidence, were difficult to build a compelling observational history on.

Still, transits are not the only observations that might give evidence for an atmosphere. The German astronomer Johann Hieronymous Schröter observed in 1793 that Venus appears slightly concave at a time in its orbit when it should be exactly half-illuminated. This suggests an atmosphere must be present, and the observation could well be repeated and confirmed. But even there difficulties remain: Schröter also in that time observed evidence suggesting a lunar atmosphere. (Schröter was correct in his analysis of Venus's atmosphere producing the concavity; it would not be until 1996 that this was proven compellingly, however.)

Chester Smith Lyman observed a ring around the whole planet implying light refracted through an atmosphere, but beyond that, any conclusive investigation would have to wait until spectroscopy and photography could be brought in and to make analysis less dependent on too-short moments of good seeing by eyes which could be quite trained and sensitive but which could not be independently checked.

Spectroscopic astronomy could give some suggestions about the content of the upper atmosphere, its top few kilometers, and that showed a lack of oxygen and of water. What was principally learned from the ground was that Venus was very hot, that its rotation was extremely slow. Details would need to wait for planetary probes.

On February 5, 1974, the NASA probe Mariner 10[1] began taking photographs for its flyby of Venus, which began with the photographing of the atmosphere of Venus to seek evidence of cloud tops or other structures. By the 13th of February the probe had taken 4,165 images of the planet, and the atmosphere was finally seen in considerable detail. Among the many fascinating results was the discovery that, in ultraviolet light, one can see the lower atmosphere, up to 100 km, rotates around the planet roughly every four (Earth) days, compared to the relatively sluggish 243 days Venus requires to complete a rotation. Verner E Suomi, one of the founders of

---

[1] Mariner 2 and Mariner 5 had flown by Venus, and the Venera 3 through 8 probes had impacted or orbited Venus before then, but they did not have cameras.

satellite meteorology and inventor of the Spin Scan Radiometer, which allowed the Geostationary Operational Environmental Satellite production of time-lapse motions of cloud images, pointed out cellular structures within the clouds. These cells could reach two hundred to three hundred kilometers across.

With the Pioneer Venus orbiter, operating from December 1978 to June 1980 (with new operations begun in 1991) an abundance of photographic evidence of this super-rotation, and finer information on the structures of this layer, were available. It also discovered a vortex in the north pole. In April 2006 the Venus Express mission photographed over the south pole not only a vortex, but a polar dipole. Polar vortices are known on Earth to form in the stratosphere and the higher layers of the troposphere, typically forming for the winter months. Those on Venus are quadruple the size of Earth's, and the dipole is an exciting new challenge.

Here the atmosphere is thinning, roughly one-tenth the atmospheric pressure of Earth at sea level (and near a thousandth that of Venus's ground level), with the surprisingly cool temperature of about -30 degrees Celsius. At this altitude there is virtually no difference between the day and night temperatures, with the atmosphere's day temperature being only about one degree warmer than the night side.

Sutherland's formula allows us to estimate the dynamic viscosity of an ideal gas as a function of temperature, with the knowledge of some physical constants. With η_0 the viscosity of the gas at a reference temperature T_0, and a constant C unique to each gas, we can estimate the dynamic viscosity η for any temperature T:

$$\eta = \eta_0 \left(\frac{T_0 + C}{T + C} \right) \left(\frac{T}{T_0} \right)^{\frac{3}{2}} \tag{1.1}$$

For sulphur dioxide C is 416 at the reference temperature of 293.65 Kelvin, while the reference viscosity is $\eta_0 = 12.54 \times 10^{-6} Pa{\cdot}s$. This provides an estimate for the dynamics viscosity at that layer to be around $10.2 \times 10^{-6} Pa{\cdot}s$. In comparison the viscosity of normal Earth air is about $18.27 \times 10^{-6} Pa{\cdot}s$. Since we can accept the treatment of the atmosphere of Earth as an inviscid fluid for certain analyses, we can extend this same consideration to the super-rotating layer of the atmosphere of Venus.

And now we have the makings for our physical model: a slender fluid layer, in thermal balance, on a rotating planet. These will be assumptions made which make for straightforward analysis and for numerical simulations. We also have a specific target of the fascinating super-rotation mode which we would like to reproduce.

1.2 Titan

The natural next question is are there other atmospheres known to show super-rotation? This takes us to Titan, largest moon of Saturn, second largest moon in the solar system, discovered in 1655 by the Dutch astronomer Christiaan Huygens. Like Venus, Titan has a thick, heavy and opaque atmosphere on a slowly-rotating planet. Unlike Venus which is a fore-runner of the global-warming that could be earth's fate as a result of greenhouse gases such as water-vapor and carbon dioxide, Titan is nearly a billion km away from the sun, with a surface temperature around 94 kelvin — one of the many reasons why its thick and luxurious atmosphere has persisted for billions of years — and an atmosphere dominated by nitrogen and hydrocarbons such as methane. Although Titan's atmosphere did not undergo a run-away greenhouse phenomenon, its methane gas near the triple-point plays a role similar to water-vapor on earth. It will turn out from the recent Huygen's observations that the upper atmosphere has very high super-rotating winds, not unlike those on Venus. Unfortunately, Titan and Venus are the only data points in our solar system for clearly super-rotating or sub-rotating atmospheres. Nonetheless, with the rapid advancement in telescopy of modern types, the discovery of planets in other solar systems with significant atmospheres, will quickly increase in numbers and it is hoped that some of these new data points will further validate the theories discussed in this book.

Past the fact that it existed, however, there was not much to say definitively about its properties for just short of three hundred years. The moon is too small, too far away, and too close to a large bright object, at least for the observations a human eye and optical telescope can easily make.

Gerard Peter Kuiper, working at the Yerkes observatory for the University of Chicago, discovered in 1944 a curious spectrum in the light from Titan. The absorption bands, at 6190 and 7250 Angstroms, proved to be those of methane at low pressures. Titan was a most curious moon enjoying an atmosphere with at least 10 kPa partial pressure of methane. Kuiper would further learn over the course of a decade that Titan was still unique: there were no other Saturnian moons to have the same abundance of methane.

Was there more to the atmosphere? How thick was the atmosphere? By 1975, limb darkening gave evidence for there being a thick atmosphere, and Laurence Trafton found evidence of absorption which showed that either the methane atmosphere was at least ten times as thick as that which

Kuiper observed or else that there was much more to the atmosphere than just methane. Trafton found tentative evidence of molecular hydrogen, and later evidence of various hydrocarbons would be added to the understanding of what makes up this atmosphere.

Pioneer 11 flew by Saturn and Titan September 1, 1979, showing Titan to be too cold for life as we know it, and leaving unanswered the question of how there could be hydrocarbons long after energy from the Sun would suggest they should have been burned off. Voyager 1, flying by in November 1980, was sent to photograph the haze of Titan's atmosphere (incidentally sending the probe out of the plane of the solar system, ending its planetary science mission) which proved to reach as much as 300 to 350 kilometers above the moon's surface, and to be rich in nitrogen. Voyager 2, which would be sent to the outer planets, was unable to closely photograph Titan.

On July 1, 2004, the probe Cassini entered orbit of Saturn, starting a long and detailed observational campaign for the system. It had its first close flyby of Titan on October 27 that year. Models built in the 1990s by Goddard Institute for Space Sciences researchers suggested that it might be a super-rotating atmosphere — with Titan rotating about once every 16 (Earth) days and having a diameter only slightly larger than Earth's moon this does not require an enormous velocity — and Cassini's sensors showed exactly this sort of speed, with hurricane-force winds in the lower atmosphere.

The Huygens probe dropped into Titan winds of around 120 meters per second at an altitude 120 kilometers above the moon's surface, with wind speeds dropping below the altitude of about 60 kilometers. The highest layers of the atmosphere rotate west-to-east, with a reversal of direction about seven kilometers above the surface, and another reversal at about 700 meters above ground.

1.3 The Great Red Spot

Any discussion of vortices in planetary atmospheres comes swiftly to the Great Red Spot of Jupiter. This spot, which might have been observed by Robert Hooke in May 1664 — and might be the spot observed by Giovanni Cassini from 1665 to 1713 (initially, in July 1665, near to the shadow of Ganymede) — has been reliably observed since 1831. These qualifiers are necessary: Hooke's observation seems to have been, from his writings, of something appearing in the North Equatorial Belt. While Cassini's observations are those of a skilled observer over many decades, there is nevertheless a curious gap in recorded observations from 1713 to 1831.

The Spot fluctuates in most every observable quantity: its size has shrunk about a third in length from its size in the 1890s. Its color has varied from the intense red which gave it is name to almost invisibility against the surrounding South Tropical Zone; it has not been noticeably red, in visible light, since the 1970s. It is conceivable that the Spots of Hooke and of Cassini were unrelated to the one now observed; it is conceivable that Cassini's at least was the present one and simply faded past detection for over a century. When the spot was observed again from 1831 it was seen primarily in its "hollow", the distortion of the bands of surrounding clouds. It would be in 1878-1881 that the spot grew dramatically more red and became famous as the Great Red Spot.

As very nearly the only long-lived object that is not simply a zonal band on Jupiter the spot has been a natural reference point to use in trying to define longitudes on the planet. Since 1892 and the establishment of A Marth's Invaluable Ephemerides there have several systems for establishing longitude. System I is used for atmospheric features within ten degrees of the equator, and is based on the rotation of features around the axis of the planet every nine hours, 50 minutes, thirty seconds. System II is used outside that band and its motion is based on the average speed of the Great Red Spot. Its coordinates rotate around the planet every nine hours, 55 minutes, 40.6 seconds. It is a touch unsettling that the Great Red Spot has been drifting eastward even in this reference frame. The rotation of the Spot also appears to be slowing as the spot shrinks. (There is also a longitudinal System III, tied to the motion of radio-detectable objects within Jupiter, with a rotation period of nine hours, 55 minutes, 29.7 seconds.)

Its latitude, however, remains reasonably constant, hovering within about one degree of its average position. This is an interesting physical property which may be subject to modelling in the statistical mechanics treatment.

Explaining such a long-lasting anticyclonic structure is a naturally tempting target for any equilibrium statistical mechanics model and we will try to form some understanding of it. Frustrating many efforts to explain the storm as a hurricane-like structure — Kuiper was inspired to use this to try explaining its structure and survival, and the hurricane is still used as a shorthand for explaining it — is the Spot's apparent lack of much of a hurricane's structure, most noticeably in the absence of an eye or eye-wall.

While the Great Red Spot is the most famous anticyclonic storm it is far from the only one: large, white ovals appear in the South Tropical Bounds and in the South-South Tropical Bands, and a long chain of them formed part of the captivating moving images of Jupiter as reconstructed from Pioneer and Voyager observations. The ovals in the South Tropical Band have been observed to last at least half a century, while those in the South-South Temperate Belt seem to survive — or at least to be detectible from Earth — for only a few years.

In the northern hemisphere are more anticyclonic white ovals appear in the North Equatorial Belt, in the North-North Temperate Belt, and in the North Temperate Belt. Curiously, these are short-lived phenomena compared to their southern counterparts. The North Equatorial Belt storms rarely last more than one or two years, and the others are shorter-lived still. Similarly Little Red Spots forming in the region between the North Equatorial Belt and the North Tropical Zone — the analogue, it would appear, to the Great Red Spot's location — form but typically expire in about a year.

An exciting recent development has been the forming of the Oval BA storm. This is roughly half the size of the Great Red Spot, and it was created from the merger of smaller white ovals in the South Temperate Belt between 1998 and 2000. Its darkening into the same color as the Great Red Spot by March 2006 reinforces that the forces which formed and sustain the Great Red Spot are not unique to that phenomenon, and that new physical models of it can be tested with current data. The idea of anticyclonic storms merging into larger structures more reminiscent of the Great Red Spot has been often explored, as for example in simulations by Andrew Ingersoll and P G Cuong.

1.4 Polar Vortices and Other Curiosities

Another interesting large-scale structure known to almost all the bodies with atmospheres is that of the polar vortex. On Earth there are vortices for both poles, with a growth or decay in strength corresponding to the season. These vortices became noteworthy in the popular imagination in the late 1980s and the 1990s in their correspondence to the ozone holes. The coldest air within the polar vortices allows for the depletion of ozone by sunlight and by chlorine-bearing compounds, and as there appears to be relatively little transport of air between the polar vortices and the atmosphere in general this produces a considerable depletion of ozone over either pole.

But the conditions which produce a polar vortex are not unique to Earth. Mariner 10 and then Pioneer Venus found evidence of a major vortex around the south pole of Venus, and the Venus Expression mission in 2006 reinforced not just the existence of this structure but indicated the existence of a dipole there. This feature is yet under investigation.

Mars, too, features a polar vortex, there complicated by the curious fact that much of the carbon dioxide in its atmosphere will condense out of the atmosphere and fall on the polar ice caps. In what appears to be a part of this cycle, atmospheric argon increases in the southern polar regions in autumn, and dissipate in winter and spring. While these are fascinating phenomena they require a level of detail to model — particularly in requiring a change in density and atmospheric composition, as well as relatively sophisticated ground effects — that put it for now beyond what we wish to study.

On Saturn, recent study by the Cassini probe suggests the existence of a super-hurricane, reaching approximately eight thousand kilometers in diameter and centered on the south pole. This is a storm clearly analogous to hurricanes on earth: it has the well-defined eye, and it is surrounded by a ring of clouds between thirty and eighty kilometers taller than the storm's center.

The north pole of Saturn meanwhile has a curious hexagonal cloud surrounding it. This storm was first seen in the images from Voyager 1 and 2, and its rotation period of 10 hours, 39 minutes, 24 seconds matches that of the variational period for the planet's radio emissions. Polygonal shapes are reproducible in spinning fluids in the laboratory, of course, and it is hard not to think of Thomson rings of vortices when hearing of them. Of course, a ring of six vortices is stable on the sphere only when the six vortices are at a pole; even allowing that Saturn's north pole is a bit flatter than a sphere would be, the fact that the polygon stretches over ten thousand kilometers across makes this yet another challenge.

And finally Saturn does have its share of anticyclonic storms reminiscent of the Great Red Spot, although these appear to be seasonal phenomena, appearing when the northern hemisphere is tilted sunwards. These Great White Spots were first observed in 1876 by Asaph Hall, who is also known to astronomers for his 1877 discovery of the two moons of Mars. He is also obscure to specialists in Monte Carlo for an 1873 paper in which he reported the results of performing Buffon's needle problem to experimentally estimate the value of π. Hall was able to use the Great White Spot to provide the first good estimates for the rotation rate of Saturn.

When Voyager 2 flew past Neptune in 1989 it observed a large anticyclonic storm in the southern hemisphere, featuring winds blowing as fast as 2400 kilometers per hour. However, by 1994, the storm had disappeared, according to observations made by the Hubble Space Telescope. It might be that the storm was a particularly transient phenomenon, a hole in the methane layer or the like; but a very similar spot, known as the Northern Great Dark Spot, has appeared in the northern hemisphere and has remained for years. There is also a Small Dark Spot, a southern and cyclonic spot observed during the Voyager 2 flyby.

One of the astronomical events of the past decades which drew considerable scientific and popular interest, the collision of comet Shoemaker-Levy 9 into Jupiter, produced short-lived "scars" on the outer atmosphere, and by its effects provided information about the structure of the inner atmospheric layers. However, these spots were small, short-lived, and ultimately lacked the structure of the cyclonic or anticyclonic spots in which we are interested. The information about properties such as the location of tropopause contribute to our numerical modeling, data which lets us more rigorously test how our model compares to the actual atmosphere.

1.5 Outline

There are two substantially different sorts of planetary atmosphere which this book attempts to understand: the first is the super-rotating atmosphere like that of Venus and Titan, with slowly rotating planet surfaces and fast atmosphere layers. For this we construct model based on a thin layer of a barotropic (non-divergent) fluid on a rotating planet. This model is informed by earlier work on the non-rotating planet described in some detail in [64]. The addition of planetary rotation to the model introduces energy in a way opening new physical considerations. Most noticeably in the non-rotating planet when superrotation occurs is that it may (as expected) form an "axis of vorticity" in any arbitrary direction, while on the rotating planet there are energy considerations encouraging alignment parallel or antiparallel with the axis of rotation. Furthermore there is evidence of multiple phase transitions as a function of the statistical mechanics temperature.

Most of the material in this part of the book is based on new results obtained by the senior author and Dr. Xueru Ding, in collaboration with Rajinder Singh Mavi (chapter 8), Zhu Da and Nuwan Indurugwege. Included in this part is the exact closed-form solutions for the phase transitions of the Barotropic Vorticity Model by Lim, motivated by the discoveries, uncovered by Ding's simulations, of a significant asymmetry between super-rotating and anti-rotating vertically-averaged barotropic flows. The statement of this discovery, prediction and theorem is: a slowly-rotating planet can support a super-rotating barotropic atmosphere at high enough energies, but not an anti-rotating one; a necessary condition for anti-rotation of a barotropic atmosphere is sufficiently fast planetary spin. Only a few important physical quantities are needed as input in this theory, namely, in addition to planetary parameters such as spin-rate and radius, we need to input the relative enstrophy of the atmosphere, and a narrow range of averaged energy-momentum levels of the associated reservoir.

The multi-faceted discussions, mean-field solutions, exact integration by spherical model method based on the device that the enstrophy constraint is a higher-dimensional sphere and simulated super-rotating and anti-rotating end-states, in the first part of this book, goes beyond providing pedagogical completeness and an easy entry point for the interested reader, especially planetary astronomers, towards a resolution of a continuing enigma in the atmospheric dynamics of terrestrial planets and major moons [87].

The Metropolis-Hastings Monte Carlo algorithm proves useful in producing statistical equilibrium end-states which allow the gathering of numerical evidence for these transitions. That we want to use a Metropolis-Hastings procedure will encourage us to look for several quantities which can be kept microcanonically and a relevant energy function which we can allow to vary canonically in order to find stable equilibriums in positive and in negative temperature regions. This will be the topic of chapter 6, followed by two chapters employing respectively a simple mean-field theory and the Bragg mean-field theory, on variants of the Barotropic Vorticity Model where the enstrophy constraint for example might be relaxed to an inequality. In chapter 9 we return to the Barotropic Vorticity Model with its microcanonical constraints on total circulation and relative enstrophy, treating the latter as a spherical constraint in an application of Kac's spherical model to obtain exact or closed-form solutions for the phase transitions to super- and sub-rotating barotropic flows on a massive rotating sphere. This body of calculations will show that the mean-field approach is justified for the problem of barotropic flows on a rotating sphere although it should be emphasized that the Monte Carlo simulations and spherical model method in respectively chapter 6 and 9 are performed without any assumptions of mean-field. On the other hand, there is as yet no convincing evidence that a mean-field approach will do for the more complex divergent models known as the Shallow Water Models discussed in the second part of chapter 2 and in chapters 10 and 11.

The second type of planetary atmosphere we mean to model is that of the Jovian atmospheres, with rapidly-rotating planets where the surface height of the active fluid layer is dynamic. We have in mind possible simple explanations for an atmospheric layer divided into alternating zones and belts of varying vorticity (or velocity, or atmospheric pressure — these all prove to be relevant quantities) and the appearance of cyclonic or anticyclonic storms. In mind through this model construction will be the Great Red Spot, serving as an example of a large anticyclonic storm in the southern hemisphere which has high rim velocities and which also allows for a collection of other, smaller anticyclonic storms which appear in the same hemisphere. At issue here are the on-going debates about the anticyclonic predominance and the north-south asymmetry that exists on Jupiter [24], [46]. Most of the material for this part of the book is based on the recent work of the senior author and Dr Xueru Ding.

To model the Jovian atmospheres, we will build a Shallow-Water Model, in which the rapid spinning of the planet and the strong horizontal and non-quasi-geostrophic nature of the flows will help explain, in terms of simple physical quantities such as the fluid's angular momentum and its changing moment of inertia due to varying surface heights, the key large-scale features of these atmospheres. In this case we will look for cyclonic and anticyclonic spots, with size, location, and predominance of cyclonic or anticyclonic spots proving to be dependent on enstrophies and on the rotation rate of the planet. And as in the Barotropic Vorticity Model and the super-rotation of Venus and Titan there is evidence for phase transitions in both the positive and negative temperature ranges. Once again Metropolis-Hastings proves to be a good tool for visualizing these states and for finding evidence of phase transitions, as discussed in chapters 10 and 11. At this point, it is not known whether a mean-field approach will work for the shallow water problem. Furthermore, no exact solutions like those for the barotropic problem are known.

These numerical experiments will in turn indicate that the angular momentum of the atmosphere — itself a reflection of the energy derived from the rotation of the planet — is a critical component to the formation of Great Red Spot-like storms, and for that matter in the formation of the prominent features which motivated these models. The models also surprisingly capture details of the planetary atmospheres not explicitly in mind when the physical models or the numerical simulations for them were constructed. This indicates we have constructed robust models with physical significance that call for more study.

Some background material in the fine points of spin-lattice models and their analytic implications, as well as the topics in statistical mechanics most directly relevant to the questions we mean to ask, are included following the introduction of the barotropic and the Shallow-Water Models which grow to dominate the book.

A point of emphasis of the book is the formulation of a simple and powerful unified statistical mechanics theory for the modelling of the emergence of large-scale coherent structures in planetary atmospheres through phase transitions. One significant point is that the general unified theory encompasses both the Barotropic Vorticity Model for super-rotating and sub-rotating vertically averaged barotropic flows on slowly-spinning terrestrial planets and major moons, and the Shallow-Water Model for strongly-divergent, non-quasi-geostrophic shallow flows on rapidly-rotating Gas Giants. The reader should keep in mind that, as he explores the many-faceted aspects of these theories, the powerful methods on which they are based, and the good qualitative agreement of their theoretical predictions with recent observations obtained by space missions of NASA and the ESA, the overall objective of this book's models is not to replicate with high fidelity the results of intensive numerical simulations on dynamical rotating Shallow-Water Equations models. These important works have been organized and discussed by amongst others, Ingersoll, Del Genio, Salmon, Shepherd, Schubert, Young and their collaborators in too many seminal papers to be adequately referenced in this small monograph, and they form a highly informative and valuable background for the discerning reader. The reader should also read several excellent texts on the relevant background on geophysical fluid dynamics, such as Holton [43], Pedlosky, and more recently Vallis.

Chapter 2

Barotropic and Shallow-Water Models

2.1 The Physical Model

How do we translate these physical inspirations into a model with which to calculate? The simplest model is to start by supposing an infinitely massive, rotating rigid sphere, the planet, with radius R around which is a thin shell of fluid, the atmosphere. The atmosphere we suppose to be inviscid with respect to itself, but that it has some ability to exchange angular momentum and kinetic energy with the planet through mountain torque or topographical stress.

By assuming the planet to be infinitely massive, we avoid the complication of transferring rotation back from the atmosphere to the planet. While conservation laws make clear that rotation in the atmosphere must have some effect on the rotation of the planet, we know from the scales of the angular momentums involved that the effect is tiny and, for real planets, considerably smaller than other factors which influence the planet's spin.

Assume the atmosphere is barotropic, its pressure depending only on its density; and that the atmosphere is non-divergent, so that the atmosphere has uniform thickness and density. We therefore do not start with the complications of gravitational potential energy or an irregular surface to the top of the atmosphere. Furthermore we assume the atmosphere is in radiative balance, in the net neither gaining nor losing energy from incoming solar radiation (insolation). The model is simple, but it is robust enough to capture the atmospheric super-rotation phenomenon. Phenomena like the Great Red Spot and similar spots will require we change these assumptions, however, and those will be explained as we start.

Under what conditions super-rotation happens will depend on the angular momentum of the atmosphere as well as other parameters. The angular momentum in turn depends obviously on the rotation of the planet and how that rotation is transferred to and from the atmosphere. (Already we see the exchange of a variable quantity with an infinite bath of the quantity that makes for thermodynamics.) Obviously important physical properties will be the energy and the enstrophy of the atmosphere, and for the atmosphere only the kinetic energy is left to study.

As we are interested in the fluid's kinetic energy and we know the density to be uniform we can instead study its velocity. This velocity we can look at as having two components, one the portion due to the planet's rotation — the planetary velocity — and then the remainder — the relative velocity. Let ψ be the relative velocity stream function on the surface of the sphere; past experience with inviscid dynamics on the non-rotating sphere and on the plane suggest that it is useful to look at the vorticity, the curl of the velocity, which we can study through a spectral analysis (as in section 2.5.3) or by approximating the vorticity as a set of point particles (as in section 6.4).

Particularly convenient as coordinates is a variation of spherical coordinates in which we track the cosine of the colatitude (angle from the North pole) θ as well as the longitude ϕ. This pair $(\cos(\theta), \phi)$ has the advantage of being a sympletic pair of variables which makes Hamiltonian dynamics for this system easier to write and to manipulate when we do look at the point particle problem.

Let the planetary spin rate be Ω and assume it to be oriented along the z-axis. Then the planetary vorticity due to this spin at any colatitude θ will be $2\Omega\cos(\theta)$. If we represent at any time t the total vorticity as q, then we can decompose this into the relative and the planetary vorticities:

$$q(t; \cos(\theta), \phi) \equiv \Delta\psi + 2\Omega\cos(\theta) \tag{2.1}$$

where $\omega \equiv \Delta\psi$ will be the relative vorticity. Here Δ is the operator equal to negative one times the Laplace-Beltrami operator for the unit sphere S^2 which arises naturally in the study of vortices on the sphere.

We have here set up a model for the atmosphere that is distinguished from that of many other works. The first distinguishing feature is that the angular momentum of the atmosphere is not conserved in line with a relaxational explanation for the super-rotation seen in the atmosphere of Venus and Titan. On the basis of the standard model for barotropic flows on a rotating sphere that has some nontrivial topography, the inviscid mechanism known as mountain torque causes the non-conservation of atmospheric angular momentum — unlike the classical energy-enstrophy theories in which we do not find any phase transitions in the range of temperatures which are valid for the resulting Gaussian models [34] [35].

The second distinguishing feature is that we treat the energy and the angular momentum reservoirs for the atmosphere as a single reservoir quantity. The kinetic energy of the atmosphere is the only way for energy to be put into or removed from it — there is no gravitational or chemical potential energy, for example, considered in this model. A change in the kinetic energy of the atmosphere will be reflected in a change in its angular momentum and vice-versa, justifying this simplification. After the chapters on statistical mechanics and Monte Carlo methods, this can be viewed as a reservoir for the enthalpy. Equivalently we can also view the special combination of kinetic energy and angular momentum to be the Lagrangian for the Barotropic Vorticity Equation on a rotating sphere.

The third distinguishing feature of this model is that it fixes the relative enstrophy,

$$Q \equiv \int_{S^2} dx\, \omega^2 \tag{2.2}$$

of the atmosphere which has the important mathematical consequence of producing an exactly-solvable spherical model that is nonetheless non-Gaussian. This part of the book is based largely on [20] [21] [22].

In the inviscid barotropic model, we see that the total energy — the energy as measured from a rest-frame — of the atmosphere and the planet are conserved. Since we assume the planet to have infinite mass, then all there is to track is the kinetic energy of the barotropic fluid composing the atmosphere. Since the atmosphere is non-divergent, there is no gravitational potential energy to track: the atmosphere has a uniform thickness and density and the upper atmosphere is effectively a lid.

If we study the freely-decaying or forced-damped barotropic problems under the assumption of small viscosity, then the usual principle of selective decay for periodic domains, which holds that enstrophy decays at a faster rate than energy, needs modification in order to apply to the nearly inviscid quasi-two-dimensional flow in complex boundaries. In this case the enstrophy and total energy decay considerably slower at small scales — and somewhat faster through Ekman dissipation at the surface of the planet, the only significantly viscous portion of the atmosphere, but still slower — than are energy and angular momentum transferred towards the largest scales in the problem.

Since the change in enstrophy caused by the atmosphere's viscosity against the planetary surface is so slow relative to the fast time-scale transfer of energy and angular momentum, we can treat the enstrophy as fixed even in the freely-decaying problems, and much more so in the forced-damped problems which are the main focus in this text. It is important, however, to recognize that the forced-damped nature of this class of problems does not mean that one needs to fix both the total energy and the enstrophy. To see this, one needs to look no further than the fact that only in the final asymptotic stage of a damped-driven process, are energy and enstrophy stationary in a statistical sense. The real questions – of uppermost significance in this book — is the relationship between the stationary values of the physical quantities in end-stage damped-driven processes, and how to calculate them for a range of planetary-atmospheric models.

Furthermore, one can fix the relative enstrophy without fixing the total mechanical energy, or the Lagrangian of the Barotropic Vorticity Equation, or the Shallow-Water Equations, since there are many parts to the rest-frame kinetic energy of the atmosphere. While some of this energy should be fixed in the forced-damped context, there are other terms — as we will see — that are naturally allowed to change, that provide convenient measures of long-range order in the atmosphere, or in other words, they are order parameters in the statistical mechanics models.

This idea of using the Lagrangian of the underlying dynamical problem, instead of the Hamiltonian, in the action of the partition function (the path integral) is one of the main points of departure between our approach and previous studies.

2.2 Voronoi Cells and the Spin-Lattice Approximation

A regular feature of this book is the numerical approximation of a vorticity field $\omega(\vec{x})$, which is defined on the surface of the unit sphere. One obvious numerical treatment is to look to the spectral decomposition of the vorticity, using the orthonormal set of spherical harmonic functions $\{\psi_{l,m}\}$:

$$\omega(\vec{x}) = \sum_{l=1}^{\infty} \sum_{m=-l}^{l} \alpha_{l,m} \psi_{l,m} \tag{2.3}$$

This discretization can be truncated by limiting the maximum l considered.

The other obvious numerical treatment is the lattice model: build a discrete approximation $q(\vec{x})$ to the original $\omega(\vec{x})$. We will need to show that this model satisfies two essential requirements, based on the size or the order of the approximation, understanding that as the size of the approximation grows infinitely large, the approximation itself must become indistinguishable from the continuous fluid flow that we mean to study.

The first requirement is that the resulting family of finite-dimensional models must converge to the correct energy-functional and constraints of the problem. We will show that in this section.

The second requirement is that the thermodynamic limit — in this case, the non-extensive continuum limit — of the family of models must exist. This requirement turns out to be true if the exact solutions to the spherical models themselves yield valid free energy expressions, in terms of the associated saddle points in the non-extensive continuum limit. These solutions can be obtained by the Kac-Berlin method of steepest descent, as shown in [59]. For now, we will let the validity of this assumption be subsumed under the assumption that the mean-field theory for this class of problems is asymptotically exact for coupled barotropic flows on a rotating sphere.

We start by selecting a mesh M, consisting of a set of N fixed mesh sites $\vec{x}_j$ distributed reasonably uniformly over the surface of the sphere S^2. From this mesh on the surface of the sphere we build the Voronoi diagram by partitioning the sphere into N convex polygons D_j. The criterion for the polygons is that every point within the polygon D_j is nearer to the mesh site $\vec{x}_j$ than it is to any other mesh site $\vec{x}_k$. (This leaves the boundary lines out of consideration, but as this is a set of measure zero it does not impair our approximation.)

Next define the indicator functions $H_j\left(\vec{x}\right)$, which are equal to 1 if the point $\vec{x}$ is within the polygon D_j and is zero otherwise. Given the fixed mesh points $\vec{x}_j$ for $j = 1, 2, 3, \cdots, N$, we define a set of site strengths s_j for the same $j = 1, 2, 3, \cdots, N$.

Then we can approximate the relative vorticity with the piecewise level function

$$\omega\left(\vec{x}\right) = \sum_{j=1}^{N} s_j H_j\left(\vec{x}\right) \tag{2.4}$$

where the spin

$$s_j \equiv \omega\left(\vec{x}_j\right) \in \left(-\infty, \infty\right) \tag{2.5}$$

and where H_j is the indicator function on the Voronoi cell D_j centered at $\vec{x}_j$, that is,

$$H_j\left(\vec{x}\right) = \begin{cases} 1 & \text{for } \vec{x} \in D_j \\ \\ 0 & \text{for } \vec{x} \notin D_j \end{cases} \tag{2.6}$$

An obvious question is what to regard the discrete s_j values as representing — are they the vorticity of the continuous flow just at the point $\vec{x}_j$, or are they mean vorticities over the Voronoi cell D_j, or some other form of discretizing the continuous flow? We can — and will — view them as the coarse-grained or block-averaged vorticity, the result from a single-step renormalization procedure outlined in [61] — which is conveniently suited to a mean field approach. (Another viewpoint, treating the real-valued spin states $\{s_j\}$ as macrostates, is in the book [64].)

As the Voronoi cell D_j is all the points in S^2 which are nearer to $\vec{x}_j$ than to any other point in the mesh M, these cells have the essential property of being a disjoint cover for S^2, that is:

$$D_j \bigcap D_k = \emptyset \text{ when } j \neq k \tag{2.7}$$

$$\bigcup_{j=1}^{N} D_j = S^2 \tag{2.8}$$

(except for a set of measure zero, the boundary lines of the Voronoi cells).

Because the mesh M is uniform, we have another essential property: the areas A_j of the cells are equal,

$$A_j = |D_j| = \frac{4\pi}{N} \tag{2.9}$$

Now, we will look at the rest-frame kinetic energy, given in terms of variables in the frame which is rotating at the same fixed angular velocity Ω of the planet. In that frame, as seen in the previous chapter, that kinetic energy is

$$L = -\frac{1}{2}\int_{S^2} dx\, \psi q \tag{2.10}$$

$$= -\frac{1}{2}\int_{S^2} dx\, \left(\omega + 2\Omega\cos\left(\theta\right)\right) G\left[\omega\right] \tag{2.11}$$

making use of the fundamental solution of the Laplace-Beltrami operator on S^2,

$$\psi\left(\vec{x}\right) = G\left[\omega\right] = \int_{S^2} dx^{'}\, \log\left|1 - \vec{x}\cdot\vec{x}^{'}\right| \omega\left(\vec{x}^{'}\right) \tag{2.12}$$

We can find the truncated, or lattice approximate, energy L_N by putting into the above formula for rest-frame kinetic energy our approximation to the relative vorticity ω. From this,

$$\begin{aligned}
L_N &= -\frac{1}{2}\int_{S^2} dx \left(\sum_{j=1}^{N} s_j H_j\left(\vec{x}\right) + 2\Omega\cos\left(\theta\right) \right) G\left[\sum_{k=1}^{N} s_k H_k\left(\vec{x}\right) \right] & (2.13) \\
&= -\frac{1}{2}\sum_{j=1}^{N}\sum_{k=1}^{N} \left[\int_{S^2} dx\, H_j\left(\vec{x}\right) G\left[H_k\left(\vec{x}\right)\right] \right] s_j s_k & \\
&\quad -\Omega \sum_{k=1}^{N} \left[\int_{S^2} dx\, \cos\left(\theta\right) G\left[H_k\left(\vec{x}\right)\right] \right] s_k & (2.14) \\
&\to L \text{ as } N \to \infty & (2.15)
\end{aligned}$$

following the rules of Lebesgue integration.

By defining the interactions

$$J_{j,k} \equiv \int_{S^2} dx\, H_j\left(\vec{x}\right) G\left[H_k\left(\vec{x}\right)\right] \tag{2.16}$$

and the external fields

$$F_k \equiv \Omega \int_{S^2} dx\, \cos\left(\theta\right) G\left[H_k\left(\vec{x}\right)\right] \tag{2.17}$$

then the truncated energy takes on the form of a spin-lattice model:

$$L_N = -\frac{1}{2}\sum_{j=1}^{N}\sum_{k\neq j}^{N} J_{j,k} s_j s_k - \sum_{k=1}^{N} F_k s_k \tag{2.18}$$

The interactions $J_{j,k}$ are logarithmic in terms of the distance between points $\vec{x}_j$ and $\vec{x}_k$ and they are, therefore, long-range. The external fields F_k are non-uniform and they are linear in the planetary rotation $\Omega \geq 0$. These represent the coupling between the local relative vorticity, or spin, s_j and the planetary vorticity field $\Omega\cos\left(\theta\right)$. This external field energy is zero for the single-layer inviscid vortex dynamics on the non-rotating sphere; it is this inhomogenous term when $\Omega > 0$ that produces the more abundant mathematical and physical properties of the coupled barotropic flow on a rotating sphere.

When we evaluate the interaction strengths $J_{j,k}$ we find

$$\begin{aligned}
J_{j,k} &= \int_{S^2} dx\, H_j\left(\vec{x}\right) \int_{S^2} dx^{'}\, \log\left|1 - \vec{x}\cdot\vec{x}^{'}\right| H_k\left(\vec{x}^{'}\right) & (2.19) \\
&\to \frac{16\pi^2}{N^2}\log\left|1 - \vec{x}_j\cdot\vec{x}_k\right| \text{ as } N \to \infty & (2.20)
\end{aligned}$$

The external fields meanwhile are

$$F_k = \Omega \int_{S^2} dx \, \cos(\theta) \int_{S^2} dx' \, \log\left|1 - \vec{x} \cdot \vec{x}'\right| H_k\left(\vec{x}'\right) \tag{2.21}$$

$$= \Omega \int_{S^2} dx' \, H_k\left(\vec{x}'\right) \int_{S^2} dx \, \cos(\theta) \log\left|1 - \vec{x} \cdot \vec{x}'\right| \tag{2.22}$$

from the symmetry of G, the inverse Laplace-Beltrami operator on S^2. Following this,

$$F_k = \Omega \| \cos(\theta) \|_2 \int_{S^2} dx' \, H_k\left(\vec{x}'\right) \int_{S^2} dx \, \psi_{10}(\vec{x}) \log\left|1 - \vec{x} \cdot \vec{x}'\right| \tag{2.23}$$

$$= -\frac{1}{2} \Omega \| \cos(\theta) \|_2 \int_{S^2} dx' \, H_k\left(\vec{x}'\right) \psi_{1,0}\left(\vec{x}'\right) \tag{2.24}$$

$$\rightarrow -\frac{2\pi}{N} \Omega \| \cos(\theta) \|_2 \psi_{1,0}(\vec{x}_k) \text{ as } N \rightarrow \infty \tag{2.25}$$

using as in section 2.5.3 the L_2 norm for the function $\cos(\theta)$ and the spherical harmonic function $\psi_{1,0}$ which is also the relative vorticity of solid-body rotation.

The truncated relative enstrophy is given again by evaluating the enstrophy with our approximation as in equation (2.4):

$$\Gamma_N = \int_{S^2} dx \, \omega(\vec{x})^2 = \int_{S^2} dx \left(\sum_{j=1}^{N} s_j H_j(\vec{x}) \right)^2 \tag{2.26}$$

$$= \frac{4\pi}{N} \sum_{j=1}^{N} s_j^2 \rightarrow \Gamma \text{ as } N \rightarrow \infty \tag{2.27}$$

And finally the truncated total circulation is also given by putting the approximation of equation (2.4) into the integral for circulation:

$$TC_N = \int_{S^2} dx \, \omega(\vec{x}) = \int_{S^2} dx \sum_{j=1}^{N} s_j H_j(\vec{x}) \tag{2.28}$$

$$= \frac{4\pi}{N} \sum_{j=1}^{N} s_j \rightarrow TC \text{ as } N \rightarrow \infty \tag{2.29}$$

2.3 The Solid Sphere Model

In developing the variational method to be discussed in detail in the following chapter as a prelude to the statistical models that form the backbone of this book, we build up from the basic model of the thin and nearly inviscid atmosphere on a rotating planet described in section 2.1. In this chapter we decompose the relative vorticity ω into its spectral components. One question which comes immediately to mind is in what space of functions should we consider ω to be? There are some physical properties of the relative vorticity which drive our choice. In particular we know the circulation and the enstrophy of the atmosphere are properties we want to measure. The circulation — which is equivalent to the integral, over the sphere, of ω — is zero. This is required by the Stokes Theorem: there are no boundaries on the atmospheric layer in the problems we wish to do and therefore the integral of the circulation over the entire domain must be zero.

The other physical property that we know we will want to include in our models is the enstrophy of the atmosphere. This is the integral over the sphere of the square of the vorticity, indicating directly that we want a square-integrable vorticity ω. And therefore we want a function space which is at least square-integrable on the unit sphere. And as square-integrable functions are analytically familiar and useful we make $L^2\left(S^2\right)$, the square-integrable functions on the unit sphere, our function space.

We will want to decompose the relative vorticity into spectral components; this requires a suitable basis set. The obvious choice is the spherical harmonic functions.

The operator Δ referred to in equation (2.1) is (-1) times the Laplace-Beltrami operator for the unit sphere S^2, and it is one of the critical operators of this book. It naturally guides much of our thinking. The eigenfunctions of the Laplace-Beltrami operator on the unit sphere are the spherical harmonics

$$\psi_{l,m} \text{ for } m = -l, -l+1, -l+2, \cdots, l-2, l-1, l \tag{2.30}$$

with eigenvalues equal to

$$\lambda_{l,m} = l\,(l+1) \tag{2.31}$$

Δ will naturally have the same eigenfunctions and eigenvalues which are (-1) times those of the Laplace-Beltrami operator. The spherical harmonics are mutually orthonormal, and so will form a convenient set of basis functions for $L^2\left(S^2\right)$.

Now, consider any function f defined on the unit sphere S^2, and make use of the inverse G to the operator Δ:

$$G\left[f\left(\vec{x}\right)\right] = \int_{S^2} dx' \ \log\left|1 - \vec{x}\cdot\vec{x}'\right| f\left(\vec{x}'\right) \tag{2.32}$$

With this operator we can give as the solution to the problem

$$\Delta\psi = f\left(\vec{x}\right) \tag{2.33}$$

as

$$\psi\left(\vec{x}\right)=\Delta^{-1}\left(f\right)=G\left[f\left(\vec{x}\right)\right]=\int_{S^2}dx^{'}\,\log\left|1-\vec{x}\cdot\vec{x}^{'}\right|f\left(\vec{x}^{'}\right)\tag{2.34}$$

and therefore we can work with the vorticity distribution. This is convenient analytically and numerically, and then convert that vorticity distribution back into a fluid velocity field and therefore a kinetic energy for the atmosphere.

Since G is the inverse of the Laplace-Beltrami operator Δ on the unit sphere, we know that the eigenfunctions of the operator G are the eigenfunctions of the Laplace-Beltrami operator [9] [97], the spherical harmonics

$$\psi_{l,m}\text{ for }m=-l,-l+1,-l+2,\cdots,l-2,l-1,l\tag{2.35}$$

Its eigenvalues will equally be

$$\lambda_{l,m}=-\frac{1}{l\left(l+1\right)}\tag{2.36}$$

This is therefore a convenient orthonormal basis set for $L^2\left(S^2\right)$, the set of square-integrable functions defined on the unit sphere. We can expand the relative vorticity in the spherical harmonics:

$$\omega\left(\vec{x}\right)=\sum_{l\geq1}^{\infty}\sum_{m=-l}^{l}\alpha_{l,m}\psi_{l,m}\left(\vec{x}\right)\tag{2.37}$$

In the frame rotating with the planet we can see that the $\alpha_{1,0}\psi_{1,0}$ mode contains all of the angular momentum in the relative flow parallel to the planet's spin. However, the "rest-frame" is the reference frame which we will use to measure the kinetic energy:

$$L_T\left[q\right]=\frac{1}{2}\int_{S^2}dx\,\left(\left(u_r+u_p\right)^2+v_r^2\right)\tag{2.38}$$

$$=\frac{1}{2}\int_{S^2}dx\,\left(u_r^2+v_r^2+2u_ru_p\right)+\frac{1}{2}\int_{S^2}dx\,u_p^2\tag{2.39}$$

$$=-\frac{1}{2}\int_{S^2}dx\,\psi q+\frac{1}{2}\int_{S^2}dx\,u_p^2\tag{2.40}$$

where u_r is the zonal or latitudinal component of the relative velocity, v_r is the meridional or longitudinal component of the relative vorticity, u_p is the zonal component of the planetary vorticity. Since the planetary vorticity, representing the planet's rotation, is necessarily zonal, it follows that meridional component of the planetary vorticity is zero. ψ is the relative velocity's stream function as above.

But the second term of equation (2.40) is fixed given that the planetary spin rate Ω is fixed: we assume the vorticity in the atmosphere does nothing to alter the planet's rotation. So it is convenient to work with a pseudo-energy which omits this planetary rotation term and treats what remains as the energy functional:

$$\begin{aligned} L\left[\omega\right] &= -\frac{1}{2}\int_{S^2} dx\, \psi q &(2.41)\\ &= -\frac{1}{2}\int dx\, \psi\left(\vec{x}\right)\left[\omega\left(\vec{x}\right) + 2\Omega\cos\left(\theta\right)\right] &(2.42)\\ &= -\frac{1}{2}\int dx\, \psi\left(\vec{x}\right)\omega\left(\vec{x}\right) - \Omega\int dx\, \psi\left(\vec{x}\right)\cos\left(\theta\right) &(2.43)\\ &= -\frac{1}{2}\left\langle \omega, G\left[\omega\right]\right\rangle - \Omega C\left\langle \psi_{1,0}, G\left[\omega\right]\right\rangle &(2.44)\end{aligned}$$

where $C \equiv \|\cos\left(\theta\right)\|_2$. (In section 3.2 one will find that it is more convenient to rewrite this again, in a form which makes it positive-definite in the Fourier coefficients of the spectral expansion in spherical harmonics of the relative vorticity ω.)

The integral operator G is a self-adjoint operator. Because of this, and since we know the eigenvalues of G, we can find the net angular momentum associated with the relative vorticity $\omega\left(\vec{x}\right)$. We make an additional assumption, without loss of generality, that the fluid density is a uniform 1:

$$\begin{aligned} -C\left\langle \psi_{1,0}, G\left[\omega\right]\right\rangle &= -C\left\langle G\left[\psi_{1,0}\right], \omega\right\rangle &(2.45)\\ &= \frac{1}{2}C\left\langle \psi_{1,0}, \omega\right\rangle = \frac{1}{2}\int_{S^2} dx\, \omega\left(\vec{x}\right)\cos\left(\theta\right) &(2.46)\end{aligned}$$

which gives as net angular momentum:

$$\Lambda\left[\omega\right] \equiv -C\left\langle \psi_{1,0}, G\left[\omega\right]\right\rangle = \frac{1}{2}C\alpha_{1,0} \qquad (2.47)$$

In this approach we have not fixed the angular momentum $\Lambda\left[\omega\right]$. Neither have we fixed the kinetic energy H. The coefficient $\alpha_{1,0}$ is unfixed.

Since the kinetic energy of relative motion can be written as the operator

$$E\left[\omega\right] \equiv -\frac{1}{2}\left\langle \omega, G\left[\omega\right]\right\rangle = -\frac{1}{2}\int dx\, \psi\left(\vec{x}\right)\omega\left(\vec{x}\right) \qquad (2.48)$$

an obvious — although not useful for our immediate purposes — way to rewrite the pseudo-energy is to put it in the form

$$\begin{aligned} L\left[q\right] &= -\frac{1}{2}\int_{S^2} dx\, \psi q &(2.49)\\ &= E\left[\omega\right] + \Omega\Lambda\left[\omega\right] &(2.50)\end{aligned}$$

which suggests the energy-momentum functional that other variational methods would use in rotational problems.

From the Stokes Theorem on the surface of the sphere we have the consequence

$$\int dx\, q = \int dx\, \omega = 0 \tag{2.51}$$

so that total circulation is zero. The circulation being zero has nothing to do with the inviscid nature of the barotropic flow.

The kinetic energy functional H however cannot be well-defined without some constraint on its argument $\omega\left(\vec{x}\right)$. An obvious constraint is that it have a finite square norm, or relative enstrophy, which lets a variational analysis be done wholly within the $L^2\left(S^2\right)$ Hilbert space. But — is there a better constraint possible, or is there a better reason than computational convenience that could be brought to it?

Consider the total enstrophy for the flow q:

$$\Gamma\left[q\right] = \int_{S^2} dx\, q^2 \tag{2.52}$$

$$= \int_{S^2} dx\, \left[\omega + 2\Omega\cos\left(\theta\right)\right]^2 \tag{2.53}$$

$$= \int_{S^2} dx\, \omega^2 + 4\Omega \int_{S^2} dx\, \omega \cos\left(\theta\right) + 4\Omega^2 C^2 \tag{2.54}$$

The last term in equation (2.54) is fixed: it is the square of the L^2 norm of the fixed planetary vorticity. The second term in equation (2.54) is proportional to the potentially varying net angular momentum of the atmosphere relative to the rotating frame. The first term in equation (2.54) is the relative enstrophy. In the Barotropic Vorticity Equation both the total enstrophy and relative enstrophy can — depending on the particular context of the problems — in principle be conserved in the coupled fluid-sphere model. Are they?

From equation (2.54), in this model, no: we are not forced to suppose they are both conserved. We can assume one or the other is fixed, but then the other is forced to change with the net angular momentum. In fact, so far we have found no grounds for saying that either the relative or the total enstrophy is conserved. They could both vary along with the net angular momentum in the event the bottom topography is nontrivial, such as in the presence of mountain torque.

Choosing the relative enstrophy as a constraint is natural, and it is necessary to complete the analysis we mean to do in this chapter, but it is a new assumption and not one based on any constraints previously introduced. So how do we justify this?

Consider the principle of minimum enstrophy. Under this rule, neither the enstrophy nor the energy are directly relevant to our analysis of a quasi-steady-state two-dimensional fluid flow. What is important is the ratio of enstrophy to energy. And this ratio we find tends toward whatever is the minimum value needed to satisfy a particular geometry. So if we limit the relative enstrophy, then we can trust our statistical equilibrium will have an energy appropriate to minimizing the ratio. This useful principle is dual to the way that flows in two dimensions can be characterized by iso-energy manifolds.

On the other hand, in the class of forced-damped problems which we focus on in this text, the above principle of selective decay is not as relevant. This is because instead of the enstrophy decaying somewhat faster in inverse cascades, we face the situation of having to fix the relative enstrophy and suitable components of the kinetic energy.

In equation (2.54) the second term is equal to 4Ω times the variable angular momentum density of the relative fluid motion. (Its value has units of $\frac{m^4}{s}$.) Assuming that the fluid density is a constant ρ, then the fluid's angular momentum is

$$\rho \int_{S^2} dx\, \omega \cos(\theta) = \rho \langle \omega, \cos(\theta) \rangle \tag{2.55}$$

As a result of this, the only mode in the eigenfunction expansion of ω that contributes to the net angular momentum is $\alpha_{1,0}\psi_{1,0}$, the component that is the first nontrivial spherical harmonic. This movement is the form of solid-body rotation's vorticity.

What of the higher-order moments of the vorticity, $\int dx\, q^n$ for n greater than two? These are typically found in many physical theories of fluid motions to be less important than circulation and enstrophy are. In the absolute equilibrium statistical mechanics model and in variational problems they are relatively less importance than circulation and enstrophy. They are not irrelevant, though [65].

2.4 The Shallow-Water Equations on the Rotating Sphere

The model which is at the center of this monograph is based on the total mechanical energy of the Shallow-Water Equations on a rotating sphere. This model, the Shallow-Water Model will hopefully provide interesting results about anticyclonic storms — those like the Great Red Spot of Jupiter —and the zonal bands in Monte Carlo simulation. This is a generalization of the statistical Barotropic Vorticity Model [35] [101] [20] to the class of rotating flows for a single layer of fluid undergoing divergent flows [21] [22].

The non-divergent Barotropic Vorticity Model describes an inviscid fluid layer with, effectively, a rigid lid. This model we will see is successful [58] [20] in predicting aspects of the super-rotation of planetary atmospheres and can be checked against the atmospheres of Venus and of Titan [37] [36]. In particular they succeed in showing why slowly-rotating planetary atmospheres may super-rotate but are not expected to anti-rotate, and in explaining why a rapid planetary spin is necessary but not sufficient for atmospheric anti-rotation. But it does not represent the formation of giant coherent spots in an atmosphere such as appear in Jupiter's atmosphere [70] [24] — and for obvious reasons, as these atmospheric structures involve substantial variations in the height of the fluid's surface.

So the Shallow-Water Flows [24] modelled here will be familiar enough quasi-two-dimensional, weakly damped-driven or freely-decaying systems, with energy and enstrophies injected at intermediate scales, as a result of non-uniform insolation and the resulting baroclinic instability, except that the bottom topography is trivial here.

Because this model will be quasi-two-dimensional we expect that it supports some sort of (truncated) inverse cascades of energy and enstrophy into self-organized flows, and possibly forward cascades of energy and enstrophy, as will be shown to be the case in chapter 11 for the low energy, large-enstrophy, strongly-divergent flows. These flows we may expect to have scales significant in comparison to the planetary scale, where that scale is represented by the planetary radius R. These sorts of cascades, and the coherent structures which result from them, we see in many numerical studies of the dynamical Barotropic Vorticity Equation and of the Shallow-Water Equation models [13] [48].

We begin formulating the Shallow-Water Equation model by supposing the atmosphere is a thin, homogenous layer of an incompressible fluid, with a free surface, and which moves under the influences of gravity and of Coriolis forces [18]. In the rotating frame, the inviscid, unforced Shallow-Water Equations have the form

$$\frac{D}{Dt}\vec{u} = -g\nabla h - f\vec{k} \times \vec{u} \tag{2.56}$$

$$\frac{D}{Dt}h = -h\nabla \cdot \vec{u} \tag{2.57}$$

where $\vec{u} \equiv (u, v)^t$ is the horizontal velocity field relative to the rotating frame and u and v are the zonal and the meridional components of the velocity, and h is the height of the fluid wrapping the planetary sphere. This height $h \ll R$ where R is the planetary radius. The gravitational constant is g, while f is the Coriolis parameter, representing the effect of the planet's spin. Finally

$$\frac{D}{Dt} = \frac{\partial}{\partial t} + \vec{u} \cdot \nabla \tag{2.58}$$

is the material time derivative, and $\vec{k}\,(\vec{x})$ is the unit normal at $\vec{x}$.

From [18] — and from earlier works to which that refers — we know that the inviscid, unforced Shallow-Water Equation on a rotating sphere, with nontrivial topography can be derived from Hamilton's Principle of Least Action. In that we use, as Lagrangian L (equations 70-71 in [18]) the total or absolute mechanical energy $(KE + PE)$, kinetic energy plus potential energy, in the rotating frame variables, seen in equation (2.85).

It is possible to modify the gravity component g to include the centrifugal forces, which we will not do. One advantage of this is that it fits more naturally with the spherical geometry of the problem; another is that it makes the terms of equation (2.85) similar to the traditional form for the rotating Shallow-Water Equation Lagrangian.

The Shallow-Water Equations which are the Euler-Lagrange equations for L themselves conserve potential vorticity and a reduced energy, $H = (KE_r + PE)$, instead of the total mechanical energy L in equation (2.85). KE_r is the kinetic energy due purely to relative motions of the fluid, the $\vec{u} \cdot \vec{u}$ term in equation (2.60). This is true even when the topography is not trivial [18].

This is an important point: the angular momentum around the planetary spin axis — this is equivalent to the zonal component of linear momentum in [18] — is not generally conserved. Since the reduced energy $(KE_r + PE)$ is conserved this tells us the traditional Shallow-Water Equations on a rotating sphere with a nontrivial topography will not conserve the mechanical energy L, and therefore when we look to the statistical mechanics models we should not use a microcanonical constraint on L. The part of the mechanical energy L which varies in time is the sum of the fluid's moment of inertia and its angular momentum, $IM + AM = L - H$.

In the Shallow-Water Equation model we have two forms of mechanical energy: kinetic energy and potential energy. We describe the kinetic energy first. If we accept that the fluid density ρ is constant and that the fluid's motion is described by its horizontal velocity, then the total kinetic energy KE in the rotating-frame variables is

$$KE = \frac{1}{2}\rho \int_{S^2(R)} d\vec{x} \left[\left(\vec{u} + \vec{u}_p \right)^2 \right] \int_{h_B}^{h(\vec{x})} dz \tag{2.59}$$

$$= \frac{1}{2}\rho \int_{S^2(R)} d\vec{x} \left(h\left(\vec{x}\right) - h_B \right) \left[\vec{u} \cdot \vec{u} + 2\vec{u} \cdot \vec{u}_p + \vec{u}_p \cdot \vec{u}_p \right] \tag{2.60}$$

where $S^2(R)$ is the surface of the sphere with radius R, where h_B is the height of the bottom of the atmosphere — and for our use here we will model the bottom of the atmosphere as flat and therefore set $h_B = 0$ — and where $\vec{u}_p$ is the planetary velocity.

This planetary velocity $\vec{u}_p$ has only the zonal component, of size $\Omega R \sin(\theta)$, where Ω is the spin rate of the planet, where θ is the colatitude, and therefore $R \sin(\theta)$ is the perpendicular distance from any given point on the sphere to the axis of rotation.

We can use Helmholtz's Theorem to decompose the relative velocity into a purely rotational part and a purely divergent part, so that $\vec{u} = \vec{u}_\psi + \vec{u}_\Phi$. Here $\nabla \cdot \vec{u}_\psi = 0$ and $\nabla \times \vec{u}_\Phi = 0$. This further allows us to set the relative vorticity ζ and δ, which we write as $\zeta = \nabla \times \vec{u} = \nabla \times \vec{u}_\psi = \Delta\psi$ and $\delta = \nabla \cdot \vec{u} = \nabla \cdot \vec{u}_\Phi = \Delta\Phi$, where ψ is the stream function and where Φ is the velocity potential. And all this allows us to write the relative velocity in terms of the stream function ψ and the velocity potential Φ:

$$\vec{u} = \vec{k} \times \nabla\psi + \nabla\Phi \tag{2.61}$$

The Shallow-Water Equation energy function is cubic: the integrand is quadratic in the velocities (or equivalently in the gradients of the stream function and the velocity potential), and is linear in the height h.

Since we are going to represent this model with a spatial lattice formation where the generalized spins are relative vorticity, horizontal, and surface height, we will integrate by parts the kinetic energy expression in order to get cubic terms that are linear in the stream function or in the velocity potential, linear in the Laplacian of these potentials — the relative vorticity ζ and the horizontal δ — and linear in h. How do we know that?

Consider constructing K, the kinetic energy per unit mass, without planetary rotation; provided we know the stream function ψ and the velocity potential Φ:

$$
\begin{aligned}
K &= \frac{1}{2}\vec{u}\cdot\vec{u} && (2.62)\\
&= \frac{1}{2}\left[\left(\vec{k}\times\nabla\psi+\nabla\Phi\right)\cdot\left(\vec{k}\times\nabla\psi+\nabla\Phi\right)\right] && (2.63)\\
&= \frac{1}{2}\left[\nabla\psi\cdot\nabla\psi+\nabla\Phi\cdot\nabla\Phi\right]+\vec{k}\cdot\left(\nabla\psi\times\nabla\Phi\right) && (2.64)\\
&= \frac{1}{2}\left\{\left[\nabla\cdot\left(\psi\nabla\psi\right)-\psi\zeta\right]+\left[\nabla\cdot\left(\Phi\nabla\Phi\right)-\Phi\delta\right]\right\}\\
&\qquad +\vec{k}\cdot\left(\nabla\psi\times\nabla\Phi\right) && (2.65)
\end{aligned}
$$

Integrate by parts once. This provides the kinetic energy of the Shallow-Water Equation without planetary rotation, and it is uniquely given in terms that are linear in h and those that are linear in ∇h:

$$
\begin{aligned}
KE_r &= \rho\int_{S^2(R)} d\vec{x}\,h\left(\vec{x}\right)K && (2.66)\\
&= \frac{1}{2}\rho\int_{S^2(R)} d\vec{x}\,h\left(\vec{x}\right)\left\{\nabla\cdot\left(\psi\nabla\psi\right)-\psi\zeta+\nabla\cdot\left(\psi\nabla\psi\right)\right.\\
&\qquad \left.-\Phi\delta+2\vec{k}\cdot\left(\nabla\psi\times\nabla\Phi\right)\right\} && (2.67)\\
&= -\frac{1}{2}\rho\int_{S^2(R)} d\vec{x}\left[\psi\left(\vec{x}\right)\Delta\psi h\left(\vec{x}\right)+\psi\left(\vec{x}\right)\nabla\psi\cdot\nabla h+\Phi\left(\vec{x}\right)\Delta\Phi h\left(\vec{x}\right)\right.\\
&\qquad \left.+\Phi\left(\vec{x}\right)\nabla\Phi\cdot\nabla h+2\Phi\left(\vec{x}\right)\nabla^t\psi\cdot\nabla h\right] && (2.68)
\end{aligned}
$$

From this we conclude that we can rewrite the total kinetic energy from equation (2.60) as

$$
\begin{aligned}
KE = KE_r &+ \rho\int_{S^2(R)} d\vec{x}\,h\left(\vec{x}\right)\vec{u}\cdot\vec{u}_p\\
&+\frac{1}{2}\rho\int_{S^2(R)} d\vec{x}\,h\left(\vec{x}\right)\vec{u}_p\cdot\vec{u}_p && (2.69)
\end{aligned}
$$

The second term in equation (2.69) — dub it KE_2 — we can rewrite uniquely in stream function-velocity potential form, using terms which are linear in h and terms which are linear in ∇h, by

$$\begin{aligned}
KE_2 &= \rho \int_{S^2(R)} d\vec{x}\, h(\vec{x})\, \vec{u} \cdot \vec{u}_p && (2.70)\\
&= \rho \int_{S^2(R)} d\vec{x}\, h(\vec{x}) \left(\vec{k} \times \nabla\psi + \nabla\Phi\right) \cdot \vec{u}_p && (2.71)\\
&= \rho \int_{S^2(R)} d\vec{x}\, h(\vec{x})\, \nabla\psi \cdot \vec{k} \times \vec{u}_p + \rho \int_{S^2(R)} d\vec{x}\, h(\vec{x})\, \nabla\Phi \cdot \vec{u}_p && (2.72)\\
&= -\rho \int_{S^2(R)} d\vec{x} \left(\psi(\vec{x})\, \nabla h \cdot \vec{k} \times \vec{u}_p + \psi(\vec{x})\, h(\vec{x})\, \nabla \cdot \vec{k} \times \vec{u}_p\right)\\
&\quad -\rho \int_{S^2(R)} d\vec{x} \left(\Phi(\vec{x})\, \nabla h \cdot \vec{u}_p + \Phi(\vec{x})\, h(\vec{x})\, \nabla \cdot \vec{u}_p\right) && (2.73)\\
&= -\rho \int_{S^2(R)} d\vec{x} \left[\left(\psi(\vec{x})\, \vec{u}_p + \Phi(\vec{x})\, \vec{u}_p\right) \cdot \nabla h\right.\\
&\qquad\qquad \left. + \psi(\vec{x})\, h(\vec{x})\, \Omega \cos(\theta)\right] && (2.74)
\end{aligned}$$

The simplifications of the last line follow because $\nabla \cdot \vec{k} \times \vec{u}_p = \Omega \cos(\theta)$ and $\nabla \cdot \vec{u}_p = 0$.

The last term in equation (2.69), which we dub KE_3, is

$$\begin{aligned}
KE_3 &= \frac{1}{2}\rho \int_{S^2(R)} d\vec{x}\, h(\vec{x})\, \vec{u}_p \cdot \vec{u}_p && (2.75)\\
&= \frac{1}{2}\rho \int_{S^2(R)} d\vec{x}\, h(\vec{x})\, \Omega^2 R^2 \sin^2(\theta) && (2.76)
\end{aligned}$$

by similar reasoning.

As a result the total kinetic energy in the rotating-frame variables can now be described in unique terms linear in h and in ∇h:

$$\begin{aligned}
KE = -\frac{1}{2}\rho \int_{S^2(R)} d\vec{x}\\
\left[\begin{pmatrix} \psi(\vec{x})\, \nabla\psi + \Phi(\vec{x})\, \nabla\Phi + 2\Phi(\vec{x})\, \nabla^t\psi \\ +2\left(\psi(\vec{x})\, \vec{u}_p + \Phi(\vec{x})\, \vec{u}_p\right) \end{pmatrix} \cdot \nabla h \right.\\
\left. + \begin{pmatrix} \psi(\vec{x})\, \Delta\psi + \Phi(\vec{x})\, \Delta\Phi \\ +2\psi(\vec{x})\, \Omega \cos(\theta) \\ -\Omega^2 R^2 \sin^2(\theta) \end{pmatrix} \right] h(\vec{x}) \qquad (2.77)
\end{aligned}$$

We can simplify this, and we can arrive at a locally exact expression for the Shallow-Water Equation Lagrangian, in view of the results in [66]. Provided the Shallow-Water Equation flows satisfy the condition that

$$\int_{S^2(R)} d\vec{x}\, \nabla\psi \cdot \nabla h \neq 0 \qquad (2.78)$$

there will exist a suitable choice of the stream function such that the surface integral of all the terms containing ∇h will vanish identically.

This condition holds for the planetary atmospheres which we find interesting such as the Jovian atmospheres. Consider:

$$\int_{S^2(R)} d\vec{x}\,\nabla\psi\cdot\nabla h = \int_{S^2(R)} d\vec{x}\,\Delta\psi h \tag{2.79}$$

$$= \int_{S^2(R)} d\vec{x}\,\zeta h \tag{2.80}$$

We can find, a posteriori, that this integral will not be zero for the class of Shallow-Water Equation flows which are hemispherically or north-south asymmetric. And this quantity is conserved dynamically by the Shallow-Water Equation since it is equivalent to the potential vorticity.

Therefore we can write the kinetic energy, in terms of the appropriate stream function and the velocity potential, as

$$\begin{aligned} KE = & -\frac{1}{2}\rho\int_{S^2(R)} d\vec{x}\,\psi\left(\vec{x}\right)\zeta\left(\vec{x}\right)h\left(\vec{x}\right) \\ & -\rho\Omega\int_{S^2(R)} d\vec{x}\,\psi\left(\vec{x}\right)\cos\left(\theta\right)h\left(\vec{x}\right) \\ & -\frac{1}{2}\rho\int_{S(R)} d\vec{x}\,\Phi\left(\vec{x}\right)\delta\left(\vec{x}\right)h\left(\vec{x}\right) \\ & +\frac{1}{2}\rho\Omega^2R^2\int_{S^2(R)} d\vec{x}\,\sin^2\left(\theta\right)h\left(\vec{x}\right) \end{aligned} \tag{2.81}$$

The four terms here have distinct physical meanings. The first term we can label KE_ζ: it represents the part of the kinetic energy which comes from the relative vorticity. The second term is proportional to the fluid's excess angular momentum, past what it has from the rotation of the planet, and therefore we can dub it AM. The third term is the part of the kinetic energy which comes from the fluid, and therefore fits the label KE_δ. The final term, labelled IM, is related to the moment of inertia of the fluid within the rotating system. These separate labels will be convenient. The potential energy in the Shallow-Water Equation is given by

$$PE = \rho\int_{S^2(R)} d\vec{x}\,g\int_0^{h(\vec{x})} dz\,z \tag{2.82}$$

$$= \frac{1}{2}\rho g\int_{S^2(R)} d\vec{x}\,h^2\left(\vec{x}\right) \tag{2.83}$$

where the flat bottom of the atmosphere is taken to be the zero-reference level for the potential energy. For solid planets we generically lack enough information to justify using any particular topography for the bottom. For gas giants we make the assumption that beneath the topmost, active, layer of weather modelled by the Shallow-Water Equation is a quiescent higher-density fluid which provides a locally flat bottom. Other approaches based on one-and-one-half layer models require a special procedure to parameterize the flow in the deep layer from observations of the surface of the upper layer [24], and are therefore less predictive of some of the zonal features such as the Limaye bands on Jupiter. Nonetheless, if the main aim of the project does not include predicting the Limaye zonal velocity profile, then the procedure in [24] yielded a reduced gravity Shallow-Water Model with zonal bottom topography which produced an internal velocity distribution for the Red Spot that is more accurate than the trivial topography models.

Finally, the total mechanical energy L, in terms of the velocity potential, and a suitable choice of the stream function which served to eliminate the energy terms in equation (2.77) that are linear in ∇h, has the form

$$\begin{aligned}
L &= KE + PE && (2.84)\\
&= -\frac{1}{2}\rho \int_{S^2(R)} d\vec{x}\, \psi\left(\vec{x}\right) \zeta\left(\vec{x}\right) h\left(\vec{x}\right) - \rho\Omega \int_{S^2(R)} d\vec{x}\, \psi\left(\vec{x}\right) \cos\left(\theta\right) h\left(\vec{x}\right) \\
&\quad -\frac{1}{2}\rho \int_{S^2(R)} d\vec{x}\, \Phi\left(\vec{x}\right) \delta\left(\vec{x}\right) h\left(\vec{x}\right) + \frac{1}{2}\rho\Omega^2 R^2 \int_{S^2(R)} d\vec{x}\, \sin^2\left(\theta\right) h\left(\vec{x}\right) \\
&\quad +\frac{1}{2}\rho g \int_{S^2(R)} d\vec{x}\, h^2\left(\vec{x}\right) && (2.85)\\
&= KE_\zeta + AM + KE_\delta + IM + PE && (2.86)
\end{aligned}$$

Since we treat the fluid as incompressible we may assume for convenience that $\rho = 1$ and allow that to factor out.

2.5 The Spin-Lattice Shallow-Water Model

The equilibrium statistical mechanics model for the Shallow-Water Equation, the Shallow-Water Model, which we develop in this book is based on a Gibbs ensemble that will be canonical in energy and microcanonical in several of the circulations and enstrophies. This updates and extends classical energy-enstrophy theories [50] for planar and inviscid fluids to the more complicated quasi-two-dimensional flow in a bounded domain [92] [41] without falling prey to the Gaussian low-temperature defect [64].

Part of transforming equation (2.85) into a spin-lattice model requires the choice of further constraints, guided by the physics being modelled, and partially based on what is computationally convenient. The choices made for computational convenience or technical ease we can justify by comparing the results of numerical models to the actual behavior of planetary atmospheres. Further support for our specific constraints will therefore come from work on the non-quasi-geostrophic and the anticyclonic aspects of the model which resemble key Jovian features.

We also will justify a posteriori the selection of a model that is canonical-in-L, microcanonical-in-circulations, and microcanonical-in-enstrophies by considering the stability of the mean values of several key order parameters, particularly H and potential vorticity, in the equilibrated portion of the Monte Carlo simulations. An a priori motivation for this formulation comes from the path-integral method for deriving Gibbs partition functions, where the action is based on the corresponding Lagrangian in the problem [82].

There is an obvious alternative, a model which was microcanonical in H, in circulations, and in potential vorticities. This we avoid due to the technical difficulties and the computational costs in simulating it, and this aversion will be justified in the study of the order parameters mentioned above.

Accepting for the moment that we choose an ensemble canonical in L without constraints on the potential vorticity: how do we justify other constraints on the model?

The first and easiest constraint to justify is the microcanonical, or fixed constraint which sets the circulations of relative vorticity to be zero. This we can conclude from the spherical geometry of the flow domain: Stokes' Theorem given this domain implies both circulations will be zero.

How do we justify the microcanonical constraint on the total height of the fluid layer? The fluid is incompressible by one of our original assumptions. The mass of the fluid is also conserved, an assumption which has a strong basis in physics considerations. The fixed nature of the total height of the fluid layer follows from both.

It is the microcanonical constraints based on enstrophies which require less obvious motivations. Suppose we placed no constraint on enstrophy: then the Lagrangian L could be made to take on arbitrarily large values in the space of functions (ζ, δ, h), which would give us a variational problem that was not well-defined.

But we do not need to specifically constrain the height of the fluid layer (as opposed to the total height): the gravitational potential energy term in the Lagrangian, itself canonically constrained, will serve as a canonical constraint on square-norm of the height field.

Also justifying to us these microcanonical constraints is our desire to have a unified statistical mechanics theory which is able to predict phase transitions. In particular we want to be able to observe phase transitions at arbitrarily low statistical temperatures. That desire discourages us from using Gaussian models, based on canonical constraints, because we know these cease to be well-defined at low temperatures.

There is one other point. We assume that there exist fast-dissipation and slow-dissipation time scales. We know these exist in the damped-driven and freely-decaying Shallow-Water Equation, where there is Ekman damping at the boundary of the domain and viscous dissipation on the interior. The viscous dissipation on the interior takes place on a slower time-scale than does the relatively fast relaxation of energy toward large spatial scales in the quasi-two-dimensional flow. Therefore we allow ourselves to fix the enstrophies because we assume we are looking at the equilibrium after a short interval on the slow-dissipation time-scale.

The potential vorticity q we define as the height-average of the relative vorticity of the fluid and the vorticity of the planetary rotation projected on the local unit normal: $q = \frac{1}{h}\left(\zeta + f\right)$. If there is no dissipation, then this is a conserved quantity while following the motion of fluid parcels. The potential vorticity can be treated as an invariant quantity therefore — [48] does — but we will not constrain it for the Shallow-Water Model.

One reason for this decision is convenience: it is difficult to describe this particular conservation in the spin-lattice model. Another reason is that we already have microcanonical constraints on circulation and enstrophy of the relative vorticity. Adding a further microcanonical constraint on potential vorticity seems to risk overdetermining the system. And simulation will reveal that the potential vorticity turns out to be a stable quantity even if we do not explicitly conserve it, providing us with confidence that the choice was reasonable.

So this model has canonical constraints on mechanical energy, which allow the angular momentum of the fluid to change in response to inviscid topographical stresses, and is microcanonical in the relative vorticity circulation, in the circulation, in the total fluid height, in the relative vorticity enstrophy, and in the enstrophy.

Background experience in the selective decay of enstrophy and on multiple time-scales in the Shallow-Water Equations suggest that all of the enstrophies — including the higher vorticity moments and the reduced energy H — are dissipated by viscosity in the freely-decaying and the forced-damped systems. But we also know that only the quadratic enstrophies will be nearly constant in the fast time-scale, that of the inverse cascade of total mechanical energy towards longer wavelengths in which we work. Therefore we treat the higher vorticity moments as irrelevant in the forced-damped and freely-decaying Shallow-Water System. This supports the choice of fixing just the linear circulations and the quadratic enstrophies microcanonically in this Shallow-Water Model.

Directly calculating the partition function for the Shallow-Water Model is daunting and therefore we introduce a lattice approximation to the Shallow-Water Equation's Lagrangian. As described in section 2.2 we will decompose the surface of the planet $S^2(R)$ into a set of N domains, and approximate each of the continuous fields for the relative vorticity ζ, the field δ, and the fluid height h with functions that are piecewise continuous over each specific domain [64] [63] [20] [21] [22].

Using the notation ζ_j for the value of our piecewise approximation to ζ for all points within Voronoi cell j, and similarly δ_j for the discretized field and h_j for the fluid height, and the base stream function with standard long-range logarithmic kernel, we construct a spin-lattice model for the total mechanical energy or Lagrangian of the Shallow-Water Equation that holds when the potential vorticity, $\int_{S^2(R)} d\vec{x}\,\zeta h$, does not vanish:

$$\begin{aligned} L_N = & -\frac{1}{2}\sum_{j,k}^{N} J_{j,k} h_j \zeta_j \zeta_k + \frac{4\pi R^4}{N}\Omega \sum_{j=1}^{N} \cos(\theta_j)\, h_j \zeta_j \\ & -\frac{1}{2}\sum_{j,k}^{N} J_{j,k} h_j \delta_j \delta_k + \frac{2\pi R^4}{N}\Omega^2 \sum_{j=1}^{N} \sin^2(\theta_j) \\ & +\frac{2\pi g R^2}{N}\sum_{j=1}^{N} h_j^2 + c\int_{S^2(R)} d\vec{x}\,\zeta h \end{aligned} \tag{2.87}$$

where the interactions term $J_{j,k}$ has the form

$$J_{j,k} = \frac{16\pi^2 R^4}{N^2}\left(\log\left|R^2 - \vec{x}_j \cdot \vec{x}_k\right| - \log\left(R^2\right)\right) \tag{2.88}$$

and either the double summation skips the terms where $k = j$ or we set $J_{j,j} = 0$. The last term comes from further fixing the gauge to remove the terms in the energy equation (2.77) that are linear in ∇h from the Shallow-Water Equations Lagrangian L, as discussed above. It appears here because the choice of the suitable stream function needed to eliminate these ∇h terms has been partially fixed by the use of the desired logarithmic kernel in the last equation, leading to a final, remaining freedom of an arbitrary constant c in front of the last integral which is essentially the potential vorticity that is dynamically conserved by the Shallow-Water Equations.

2.5.1 *Circulation Constraints*

Stokes's Theorem dictates that the circulation of relative vorticity must be zero:

$$\int_{S^2(R)} d\vec{x}\, \zeta\left(\vec{x}\right) = 0 \tag{2.89}$$

The truncated discretization of relative vorticity, where we have divided the domain into subdomains D_j and where $H_j\left(\vec{x}\right)$ is the characteristic function for the domain D_j is

$$\zeta\left(\vec{x}\right) = \sum_{j=1}^{N} \zeta_j H_j\left(\vec{x}\right) \tag{2.90}$$

and therefore the truncated circulation of relative vorticity has the form

$$\begin{aligned} \int_{S^2(R)} d\vec{x}\, \zeta\left(\vec{x}\right) &= \int_{S^2(R)} d\vec{x} \sum_{j=1}^{N} \zeta_j H_j\left(\vec{x}\right) \\ &= \sum_{j=1}^{N} \zeta_j A_j = \frac{4\pi R^2}{N} \sum_{j=1}^{N} \zeta_j = 0 \end{aligned} \tag{2.91}$$

where A_j is the area of the subdomain D_j. As noted by equation (2.9), given the way we have chosen to construct subdomains each of these areas will be approximately $\frac{4\pi R^2}{N}$.

The circulation of it is constructed similarly. The theorem itself tells us

$$\int_{S^2(R)} d\vec{x}\delta\left(\vec{x}\right) = \int_{S^2(R)} d\vec{x}\, \left(\nabla \cdot \vec{u}\right) = 0 \tag{2.92}$$

and the truncated circulation of it is

$$\begin{aligned} \int_{S^2(R)} d\vec{x}\, \delta\left(\vec{x}\right) &= \int_{S^2(R)} d\vec{x} \sum_{j=1}^{N} \delta_j H_j\left(\vec{x}\right) \\ &= \sum_{j=1}^{N} \delta_j A_j = \frac{4\pi R^2}{N} \sum_{j=1}^{N} \delta_j = 0 \end{aligned} \tag{2.93}$$

The linear constraint of the total depth of the fluid layer

$$\int_{S^2(R)} d\vec{x}\, h\left(\vec{x}\right) = Q_h > 0 \tag{2.94}$$

which as noted is equivalent to the conservation of mass of the incompressible fluid we truncate using a similar approach again:

$$\int_{S^2(R)} d\vec{x} h\left(\vec{x}\right) = \frac{4\pi R^2}{N} \sum_{j=1}^{N} h_j = Q_h > 0 \quad \left(h_j \geq 0\right) \tag{2.95}$$

2.5.2 *Enstrophy Constraints*

Merely having these three constraints does not suffice to make the total energy functional, our discretized mechanical energy, L_N have a bounded value [64] [67] [20]. We also need to fix the relative vorticity enstrophy and the enstrophy, and as discussed in the main section we mean the quadratic enstrophy.

The relative vorticity enstrophy Q_{ζ^2} we discretize is as follows:

$$\begin{aligned}\int_{S^2(R)} d\vec{x}\, \zeta^2\left(\vec{x}\right) &= \int_{S^2(R)} d\vec{x} \left(\sum_{j=1}^{N} \zeta_j H_j\left(\vec{x}\right)\right)^2 \\ &= \sum_{j=1}^{N} \zeta_j^2 A_j = \frac{4\pi R^2}{N} \sum_{j=1}^{N} \zeta_j^2 = Q_{\zeta^2} \qquad (2.96)\end{aligned}$$

By a perfectly similar construction the enstrophy Q_{δ^2} is discretized:

$$\begin{aligned}\int_{S^2(R)} d\vec{x}\, \delta^2\left(\vec{x}\right) &= \int_{S^2(R)} d\vec{x} \left(\sum_{j=1}^{N} \delta_j H_j\left(\vec{x}\right)\right)^2 \\ &= \sum_{j=1}^{N} \delta_j^2 A_j = \frac{4\pi R^2}{N} \sum_{j=1}^{N} \delta_j^2 = Q_{\delta^2} \qquad (2.97)\end{aligned}$$

When we get to consider the formation of Great Red Spot-like structures in gas giants, and particularly when we try to understand the predominance of anticyclonic vorticity in them we will need to understand the effects of the relative vorticity enstrophy Q_{ζ^2} and the enstrophy Q_{δ^2} on the self-organization of large-scale structures.

2.5.3 *Gibbs Ensemble*

Looking ahead to the chapter on statistical mechanics and Monte Carlo methods, the Gibbsian statistics of our Shallow-Water Model are completely described by sampling the system according to the Gibbs probability. In our discretized form this probability at the inverse statistical mechanics temperature β is

$$\begin{aligned}P_G = {} & \frac{1}{Z_N}\exp\left(-\beta L_N\right)\\ & \cdot\delta\left(0 - 4\pi R^2 \sum_{j=1}^{N} \zeta_j\right) \delta\left(0 - 4\pi R^2 \sum_{j=1}^{N} \delta j\right) \delta\left(NQ_h - 4\pi R^2 \sum_{j=1}^{N} h_j\right)\\ & \cdot\delta\left(NQ_{\zeta^2} - 4\pi R^2 \sum_{j=1}^{N} \zeta_j^2\right) \delta\left(NQ_{\delta^2} - 4\pi R^2 \sum_{j=1}^{N} \delta_j^2\right) \qquad (2.98)\end{aligned}$$

where the functions $\delta\left(\cdot\right)$ represent the microcanonical constraints. The Gibbs partition function Z_N is

$$\begin{aligned}Z_N = {} & \sum_{\vec{s}}\exp\left(-\beta L_N\right)\\ & \cdot\delta\left(0 - 4\pi R^2 \sum_{j=1}^{N} \zeta_j\right) \delta\left(0 - 4\pi R^2 \sum_{j=1}^{N} \delta j\right) \delta\left(NQ_h - 4\pi R^2 \sum_{j=1}^{N} h_j\right)\\ & \cdot\delta\left(NQ_{\zeta^2} - 4\pi R^2 \sum_{j=1}^{N} \zeta_j^2\right) \delta\left(NQ_{\delta^2} - 4\pi R^2 \sum_{j=1}^{N} \delta_j^2\right) \qquad (2.99)\end{aligned}$$

for a sum taken over the entire phase space of lattice spin. The lattice spin vector $\vec{s}$ has the components (ζ, δ, h).

Applying equilibrium statistical mechanics to vortex flows depends on the minimization of the free energy $F = U - TS$ which is given in terms of the internal energy U and the information-theoretical entropy S. Monte Carlo simulations based on the Metropolis-Hastings algorithm [63] [20] efficiently sample this probability distribution and its equilibrated macrostates after a large number of sweeps are done, and so can find at least local minimums or maximums of the free energy. The free energy can be minimized through making the internal energy small, or making the entropy large, or both.

The internal energy is essentially an averaged total mechanical energy of the underlying dynamical PDEs and is resolved only for lattice scales. In other words, quantities of the macroscopic flow that varies on scales smaller than the UV-cutoff of the lattice are not resolved, and for 1000 lattice points on Venus, this could be 100 km in wavelength, way above the molecular scales of the traditional applications of equilibrium statistical mechanics. Thus, the temperature of such a Gibbs canonical ensemble is more an averaged energy-momentum level of the corresponding reservoir, which consists of the sub-grid scales, the baroclinic scales for injection of mechanical energy into the shallow flows due to convection, insolation and the planet's internal heat sources, and the bulk angular momentum of the massive planet, rather than any notion related to molecular kinetic energies.

The Shannon or information-theoretic entropy is mainly an expression of the degeneracy or number of re-arrangements of the piecewise constant values of the relative vorticity, surface height and horizontal consistent with given values of the bulk or macrostate variables, such as energy, moment of inertia, various total circulations, enstrophies and angular momentum of the fluid [22].

Chapter 3

Dynamic Equilibria of the Barotropic Model — Variational Approach

3.1 Energy-Relative Enstrophy Variational Theory

In this chapter, we begin the variational analyses of the Barotropic Vorticity Model. It provides through the Direct Method of the Calculus of Variations, existence and stability of the relative equilibria in the dynamical Barotropic Vorticity Equation. We will show that these dynamical equilibria of extremal total kinetic energy have maximal angular momentum on iso-enstrophy manifolds. Signifiantly, this variational analysis of the dynamical barotropic partial differential equation already show the asymmetry between the (maximal energy) super-rotating and sub-rotating states, with the type of the dynamical equilibria changing from minimal to saddle-point in the sub-rotating case. This asymmetry and the complexity that belongs to it is inherited by the energy-enstrophy statistical mechanics model for the barotropic partial differential equation, namely the Barotropic Vorticity Model, and will be further examined in the following chapters. The methods discussed here can be extended directly to the Shallow-Water Equations total mechanical energy functional under suitable constraints on total circulations and enstrophies or square-norms.

What vorticity field $w\left(x\right)$ makes the atmosphere's rest-frame kinetic energy an extremal, if we add the constraint that the relative enstrophy, the square-norm of $w\left(x\right)$, is fixed? It turns out that the answer is physically relevant. The relative vorticity field $w_0\left(x\right)$ which finds an extremum of $H\left[q\right]$ will also maximize the net angular momentum $\Lambda\left[q\right]$. This means that the extremal states under this constraint will be either super-rotating or sub-rotating states, as according to the sign of $\alpha_{1,0}$ in the expansion of equation (2.37).

We already know something for the special case when the planet does not rotate, that is, when $\Omega = 0$. An analysis similar to this one shows the kinetic energy $H[w] = E[w]$ is maximized for a fixed relative enstrophy by a pro-rotating solid-body flow. That is, one where $w_0(x) = \alpha_{1,0}\psi_{1,0}(x)$ where $\alpha_{1,0} > 0$. This is also the state that maximizes the net angular momentum, $\Lambda[w]$. This gives the first proposition:

Proposition 3.1. *For a fixed planetary rotation $\Omega > 0$, the kinetic energy $H[q]$ is maximized under a fixed relative enstrophy by the solid-body flow $w_0(x)$ which also maximizes the relative or the net angular momentum $\Lambda[w_0]$.*

Not obvious and requiring considerable study is showing there is an asymmetry between the relative vorticity states which minimize and which maximize the energy. The minimum angular momentum state corresponds to the counter-rotating solid body flow, $w_1(x) = \alpha_{1,0}\psi_{1,0}(x)$ where $\alpha_{1,0} < 0$, which also maximizes the energy $E[w]$ (the energy operator is even in w), will be a minimizer of $H[q]$ when the relative enstrophy is small compared to the planetary rotation Ω. But when the relative enstrophy is larger this state will become a saddle point.

In setting up the variational treatment we will ignore the higher vorticity moments, $\int dx\, q^n$ where $n > 2$, as might be expected from earlier variational problems. But in addition to this we will not constrain the total enstrophy

$$\int_{S^2} dx\, w^2 + 4\Omega \int_{S^2} dx\, w \cos(\theta) \tag{3.1}$$

nor will we constrain the angular momentum

$$\int_{S^2} dx\, w \cos(\theta) \tag{3.2}$$

What we do constrain are the circulation, set (as necessary) to zero,

$$\int_{S^2} dx\, w = 0 \tag{3.3}$$

and the relative enstrophy Q_{rel}, set to a positive value:

$$\int_{S^2} dx\, w^2 \equiv Q_{rel} > 0 \tag{3.4}$$

What are the effects of constraining the circulation and the relative enstrophy? With these constraints we will look for extremal vorticity flows w within the subspace V_{rel} which is defined by

$$V_{rel} = \left\{ w \in L^2\left(S^2\right) \middle| \Gamma_{rel}[w] = \|w\|_2 = Q_{rel} > 0;\ \int_{S^2} dx\, w = 0 \right\} \tag{3.5}$$

An extremum for w in V_{rel} leaves the angular momentum, as defined in equation (3.2), as something constrained only by an inequality. With the relative enstrophy and the relative circulation fixed the result is, in principle, a model in which energy extrema have their super- or sub-rotations bounded above.

Lemma 3.1. *Given $w \in L^2\left(S^2\right)$, with the circulation of w constrained as in equation (3.3), and the relative enstrophy constrained as in equation (3.4). Then the angular momentum as in equation (3.2) is constrained by an inequality, specifically,*

$$\left| \int_{S^2} dx\, w \cos\left(\theta\right) \right| \leq C\sqrt{Q_{rel}} \tag{3.6}$$

where $C > 0$ is a constant which does not depend on w.

Proof. Let

$$C^2 \equiv \int_{S^2} dx\, \left(\cos\left(\theta\right)\right)^2 \tag{3.7}$$

The result follows from the Cauchy-Schwarz inequality.

∎

Lemma 3.2. *The upper bound on the angular momentum given by equation (3.6) will be achieved only for the relative vorticity field*

$$w = k\cos\left(\theta\right) \tag{3.8}$$

for a constant k.

Proof. Let $w = k\cos\left(\theta\right)$. Then

$$\left| \int_{S^2} dx\, w \cos\left(\theta\right) \right| = |k| \left| \int_{S^2} dx\, \cos^2\left(\theta\right) \right| = |k|\, C^2 \tag{3.9}$$

and

$$\|w\|^2 = \int_{S^2} dx\, w^2 = k^2 C^2 = Q_{rel} \tag{3.10}$$

and therefore

$$\left| \int_{S^2} dx\, w \cos\left(\theta\right) \right| = C\sqrt{Q_{rel}} \tag{3.11}$$

So this state is the upper bound for equation (3.6). What remains to be shown is that the upper bound for equation (3.6) must be satisfied by equation (3.8).

Suppose that

$$w = k \cos(\theta) + a\psi_{l,m} \tag{3.12}$$

where $a \neq 0$, and where $(l, m) \neq (1, 0)$. In that case

$$\left| \int_{S^2} dx\, w \cos(\theta) \right| < C\|w\| \tag{3.13}$$

so an upper bound must be the relative vorticity field of equation (3.8).

∎

When we look for constrained extremals in the form of Euler-Lagrange equations we have [21] available the tools of the Lagrange multiplier method for a Hilbert space. This gives us the necessary conditions for such an extremal. In explicit forms the Lagrange multipliers provide the physical relationships we would like to have to find the spin, energy, and relative enstrophy. More, the Lagrange multiplier method can be extended to geometrically prove both the existence and the nonlinear stability of constrained energy extremals when the constraint is fixed relative enstrophy.

In trying to construct an augmented energy-relative enstrophy functional that follows the Lagrange multiplier method for an unconstrained optimization problem we find the necessary conditions to find the extremals to the constrained optimization problem. These necessary conditions are well-expressed in terms of their Euler-Lagrange equations or Gâteaux derivative.

The Gâteaux derivative is a generalized form of the directional derivative, defined on locally convex topological vector spaces, and it has the unusual property of being nonlinear: Given a function F defined at a point u and a direction v, the Gâteaux derivative is

$$dF(u, v) \equiv \lim_{\tau \to 0} \frac{F(u + \tau v) - F(u)}{\tau} = \left. \frac{d}{d\tau} F(u + \tau v) \right|_{\tau = 0} \tag{3.14}$$

provided the limit exists.

The necessary conditions for the extremals of the augmented functions will take on the form of inhomogenous linear equations built around G, the inverse of the Laplace-Beltrami operator. The extremals of the augmented energy functional will generally take on different types in different regimes of the Lagrange multiplier values, and the borders of these values will be marked by bifurcation values of the Lagrange multipliers. From the spectrum of G we will be able to read off the bifurcation values of the multipliers.

The constraint on relativeenstrophy means that we will have the constrained optimization problem — and it is convenient for later reference to put it on its own equation line —

Constraint 1.

$$\text{to extremize } H\left[w\right] \text{ in the space } V_{rel} \text{ defined in equation (3.5).} \tag{3.15}$$

Through the Lagrange multiplier method then the energy-relative enstrophy-functional

$$E_{rel}\left[w;\Omega,R\right] = H\left[w\right] + \lambda\Gamma_{rel}\left[w\right] \tag{3.16}$$

becomes the augmented objective functional for the unconstrained optimization problem corresponding to the constrained optimization problem.

According to the Euler-Lagrange multiplier theorem, if we let $w_0 \in V_{rel}$ be an extremal of $H\left[w\right]$ then at least one of these conditions must hold:

(1) $\delta\Gamma_{rel}\left(w_0\right) = 0$
(2) $\delta E_{rel}\left(w_0\right) = \delta H\left(w_0\right) + \lambda\delta\Gamma_{rel}\left(w_0\right) = 0$

This is how we apply the Euler-Lagrange multiplier theorem: first, find a set of relative vorticity $w \in V_{rel}$ that satisfies $\delta\Gamma_{rel}\left(w\right) = 0$. Next, find a second set of relative vorticity $w \in V_{rel}$ that satisfies $\delta H\left(w\right) + \lambda\delta\Gamma_{rel}\left(w\right) = 0$ for some multiplier λ. Now the set of constrained extremals of $H\left[w\right]$ will be contained in the union of this first and second sets. The value of λ will be determined from the value of the fixed, constant $\Gamma_{rel}\left[w\right] = Q_{rel} > 0$.

To do this requires first computing the variational or Gâteaux derivative

$$\delta\Gamma_{rel}\left(w,\Delta w\right) = 2\int_{S^2} dx\, w\Delta w \tag{3.17}$$

By selecting $\Delta w = w$ we can see that this variation does not vanish for any w, that is,

$$\delta\Gamma_{rel}\left(w\right) \neq 0 \tag{3.18}$$

Therefore, the Euler-Lagrange multiplier theorem requires that any extremal w_0 of the constrained variational problem of equation 1 must satisfy the second condition,

$$\delta E_{rel}\left(w_0\right) = \delta H\left(w_0\right) + \lambda\delta\Gamma_{rel}\left(w_0\right) = 0 \tag{3.19}$$

for some value of λ.

Solving for the vanishing of the Gâteaux derivative of the augmented functional E_{rel} will give the Euler-Lagrange equation for the unconstrained problem, and this is solved in the next section.

3.2 The Augmented Energy Functional

We want here to characterize the conditions under which extremal vorticities occur in the atmosphere of a rotating planet, and also to identify when these are solid-body rotations. This we do by taking the augmented energy functional and decomposing the relative vorticity of the atmosphere using the set of spherical harmonics as basis functions. The Lagrange multiplier method, looking for extremals based on a fixed relative enstrophy for the atmosphere, leads to the characterization we want.

The spherical harmonics are eigenfunctions of the Laplace-Beltrami operator on the sphere and therefore also of the inverse Laplace-Beltrami operator so important in translating a vorticity field back into fluid velocities, which makes their use as basis set difficult to resist. One particular eigenfunction, $\psi_{1,0} = a\cos(\theta)$, with the eigenvalue $\lambda_{1,0} = -2$ will be particularly important in describing the zonal steady states.

Since the inverse Laplace-Beltrami operator G is linear and since we can expand the relative vorticity w as

$$w = \sum_{l\geq 1} \sum_{m=-l}^{l} \alpha_{l,m}\psi_{l,m} \tag{3.20}$$

when we have the total circulation $\int_{S^2} dx\, w = 0$, then the Lagrangian functional we can expand in the spherical harmonics to the form

$$\begin{aligned} H &= -\frac{1}{2}\left\langle w, G\left[w\right]\right\rangle - \Omega C \left\langle \psi_{1,0}, G\left[w\right]\right\rangle & (3.21)\\ &= -\frac{1}{2}\sum_{l\geq 1;m} \frac{\alpha_{l,m}^2}{\lambda_{l,m}} + \frac{1}{2}\Omega C \alpha_{1,0} & (3.22)\end{aligned}$$

with the double sum over l and then m now written, as is common, as a single summation.

Written this way it is easy to see coupling between the planetary vorticity and the relative vorticity will happen through the eigenfunction $\psi_{1,0}$ mode, which is after all the one that matches solid-body rotational flow.

It is convenient to have a Lagrangian written in a quadratic form, and so we will change it by a constant with loss of generality:

Lemma 3.3. *For a fixed spin $\Omega > 0$, the energy H for relative vorticity w which satisfies*

$$\int_{S^2} dx\, w\left(x\right) = 0 \tag{3.23}$$

is modulo the constant

$$H_0 = -\frac{1}{4}\Omega^2 C^2 \tag{3.24}$$

equal to the positive definite quadratic form — again denoted by H —

$$H = \frac{1}{4}\left[\alpha_{1,0} - (-\Omega C)\right]^2 + \frac{1}{4}\left[\alpha_{1,1}^2 + \alpha_{1,-1}^2\right] - \frac{1}{2}\sum_{l>1;m}\frac{\alpha_{l,m}^2}{\lambda_{l,m}} \tag{3.25}$$

Proof. This is shown simply by completing the square:

$$H = -\frac{1}{2}\sum_{l\geq 1;m}\frac{\alpha_{l,m}^2}{\lambda_{l,m}} + \frac{1}{2}\Omega C\alpha_{1,0} \tag{3.26}$$

$$= \frac{1}{4}\alpha_{1,0}^2 + \frac{1}{2}\Omega C\alpha_{1,0} - \frac{1}{2}\sum_{l\geq 1;m}\frac{\alpha_{l,m}^2}{\lambda_{l,m}} \tag{3.27}$$

$$= \frac{1}{4}\left[\alpha_{1,0}^2 + 2\Omega C\alpha_{1,0} + \Omega^2 C^2\right] + \frac{1}{4}\left[\alpha_{1,1}^2 + \alpha_{1,-1}^2\right] - \frac{1}{2}\sum_{l>1;m}\frac{\alpha_{l,m}^2}{\lambda_{l,m}} - \frac{1}{4}\Omega^2 C^2 \tag{3.28}$$

$$= \frac{1}{4}\left[\alpha_{1,0} - (-\Omega C)\right]^2 + \frac{1}{4}\left[\alpha_{1,1}^2 + \alpha_{1,-1}^2\right] - \frac{1}{2}\sum_{l>1;m}\frac{\alpha_{l,m}^2}{\lambda_{l,m}} - \frac{1}{4}\Omega^2 C^2 \tag{3.29}$$

∎

All of the extremals w^0 have the form of solid-body rotations, that is, they are of the form

$$w^0 = k\psi_{1,0} \tag{3.30}$$

for the appropriate k. So the following result — simple enough that the proof is left to the reader — is useful to state; figures showing equations (3.32) and (3.33) are also included.

Lemma 3.4. *The energy and the relative enstrophy of the extremals $w^0 = \alpha_{1,0}\psi_{1,0}$ take the form*

$$H\left[\alpha_{1,0}\psi_{1,0}\right] = \frac{1}{4}\left(\alpha_{1,0} + \Omega C\right)^2 \tag{3.31}$$

$$Q_{rel} \equiv \Gamma_{rel}\left[\alpha_{1,0}\psi_{1,0}\right] = \alpha_{1,0}^2 \tag{3.32}$$

Furthermore, for a fixed H,

$$Q_{rel} \pm 2\Omega C\sqrt{Q_{rel}} + \Omega^2 C^2 = 4H \tag{3.33}$$

with the solutions

$$Q_{rel} = \left(\pm\Omega C + \sqrt{4H}\right)^2 \tag{3.34}$$

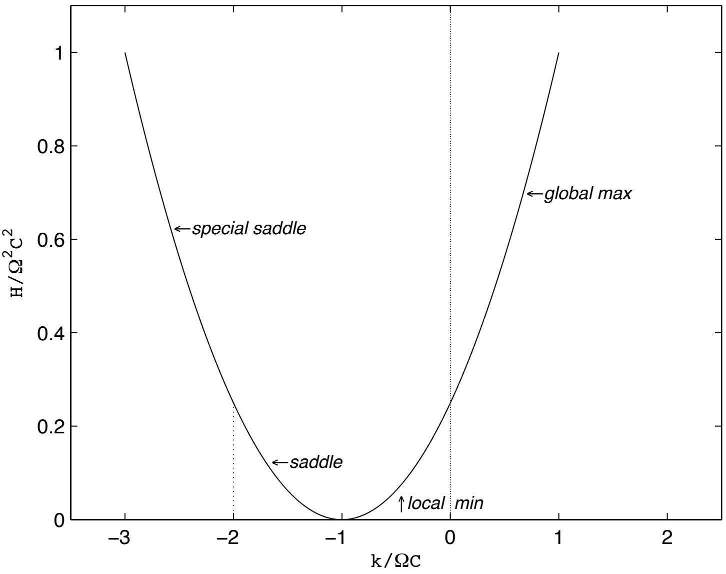

Fig. 3.1 Graph of energy H versus coordinates $k = \alpha_{1,0}$ of extremals as in equations (3.31) and (3.32).

Now we are ready to build the constrained variational model based on a fixed relative enstrophy constraint of V_{rel}. By a theorem from [91], we know that the variational problem of equation 1 can be reformed in terms of the extremals of the augmented functional:

$$E_{rel}\left[w;\Omega\right] = H\left[w\right] + \lambda_{rel}\Gamma_{rel}\left[w\right] \tag{3.35}$$

$$\Gamma_{rel}\left[w\right] = \int_{S^2} dx\, w^2 \tag{3.36}$$

Expanding the relative enstrophy $\Gamma_{rel}\left[w\right]$ in its spherical harmonic components as in equation (3.20) and using equation (3.25) yields

$$\begin{aligned} E_{rel}\left[w;\Omega\right] = {} & \frac{1}{4}\left[\alpha_{1,0} - (-\Omega C)\right]^2 + \frac{1}{4}\left[\alpha_{1,1}^2 + \alpha_{1,-1}^2\right] \\ & -\frac{1}{2}\sum_{l>1;m}\frac{\alpha_{l,m}^2}{\lambda_{l,m}} + \lambda_{rel}\sum_{l\geq 1;m}\alpha_{l,m}^2 \end{aligned} \tag{3.37}$$

The Gâteaux derivative of $E_{rel}\left[w;\Omega\right]$ taken with respect to w gives us the Euler-Lagrange equation:

$$\left[G - 2\lambda_{rel}\right]\left(w^0\right) = \frac{1}{2}\Omega C\psi_{1,0} \tag{3.38}$$

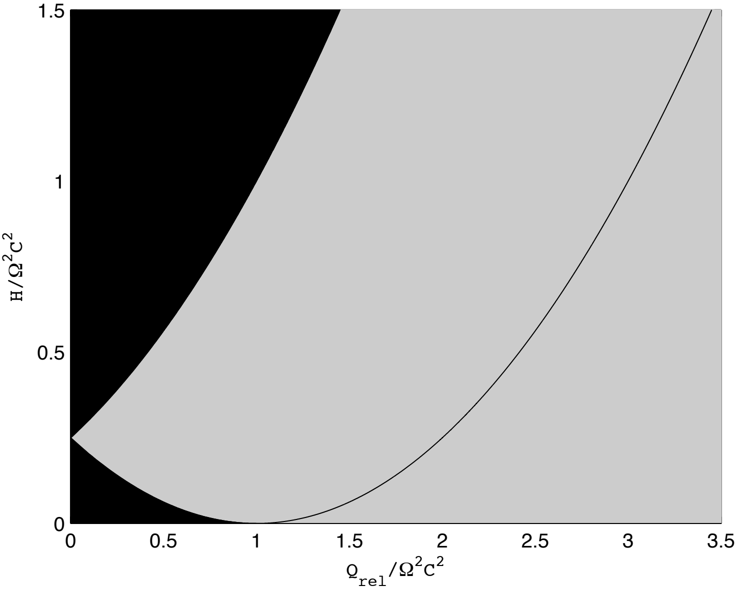

Fig. 3.2 Energy H-relative enstrophy Q_{rel} space. The black region denotes un- permitted values. The gray region denotes non-extremal permitted values. The curves denote values at extremals as in equation (3.33).

giving us a linear inverse-operator problem.

The Fredholm alternative dictates that equation (3.38) either (a) has solutions for all values of the right-hand side; or (b) has infinitely many solutions when the right-hand side is orthogonal to the kernel of the operator $[G - 2\lambda_{rel}]$.

We know that all the eigenvalues of G are negative and form an increasing sequence $\lambda_{l,m}^{-1}$. These will be divisible into three interesting cases: case (1), when $\lambda_{rel} \in \left(-\infty, -\frac{1}{4}\right)$; case (2), when $\lambda_{rel} \in \left(-\frac{1}{4}, \infty\right)$ and $\lambda_{ref} \neq -\frac{1}{2l(l+1)}$ for any l; and case (3), when $\lambda_{rel} = -\frac{1}{2l(l+1)} \in \left[-\frac{1}{4}, 0\right)$. These cases are themselves divided by the broader classes of whether the kernel of $[G - 2\lambda_{rel}]$ is trivial.

Since the Euler-Lagrange equation (3.38) is linear the results of this theorem will be easy to demonstrate, and equations (3.39) and (3.42) are plotted as well. The results also have clear physical interpretations and significance. The value of k as used in equation (3.30) is also plotted.

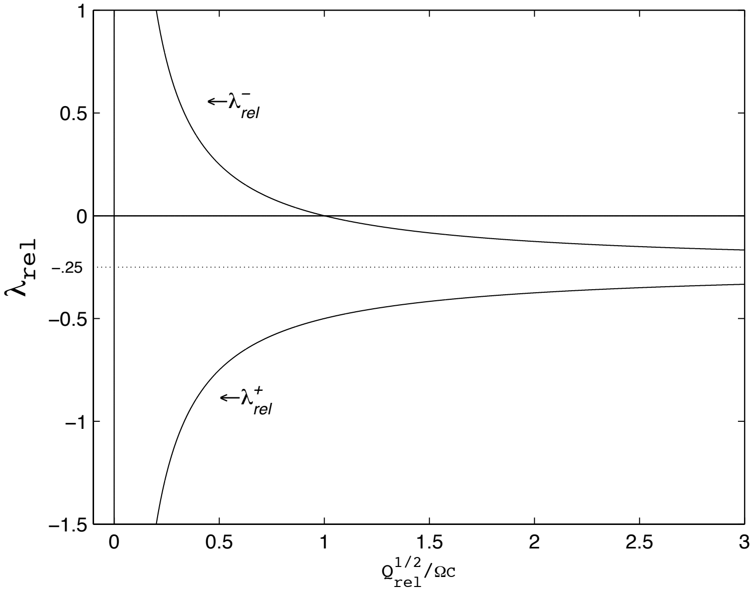

Fig. 3.3 Graph of Lagrange Multipliers $\lambda^{\pm}_{rel}$ versus the square root of the relative enstrophy, Q_{rel}, for a fixed spin $\Omega > 0$, as in equations (3.47) and (3.48).

Theorem 3.1.

(1) Only when $\lambda_{rel} \in \left(-\infty, -\frac{1}{4}\right)$ *can extremal vorticity in the form of solid-body rotation in the same direction of planetary vorticity — prograde — arise.*

(2) For $\lambda_{rel} \in \left(\frac{1}{4}, \infty\right)$ *with* $\lambda_{rel} \neq -\frac{1}{2l(l+1)}$*, the extremal vorticity — if it exists — is solid-body rotation in the opposite — retrograde — direction of planetary vorticity.*

(3) Only when $\lambda_{rel} = -\frac{1}{2l(l+1)} \in \left[\frac{1}{4}, 0\right)$ *can the spherical harmonics* $\psi_{l,m}$ *for* $(l, m) \neq (1, 0)$ *contribute to the extremal vorticity.*

The proof is most easily done in the two subcases, first where the kernel of $(G - 2\lambda_{rel})$ is empty as it is in parts (1) and (2) of the theorem, and second where this kernel is nonempty, as in part (3).

(i) $\lambda_{rel} \in \left(-\infty, -\frac{1}{4}\right)$.

In this regime, the kernel of $[G - 2\lambda_{rel}]$ is necessarily empty. As a result we can find the extremal vorticity easily, as this is a familiar sort of inverse operator problem. This implies for λ_{rel} within these bounds:

$$w^0 = -\frac{\Omega C}{2\left(\frac{1}{2} + 2\lambda_{rel}\right)}\psi_{1,0} \tag{3.39}$$

and therefore: as $\lambda_{rel} \to -\infty$

$$w^0 = k\psi_{1,0} \text{ with } k \to 0^+ \tag{3.40}$$

while as $\lambda_{rel} \to -\frac{1}{4}$,

$$w^0 = k\psi_{1,0} \text{ with } k \to \infty \tag{3.41}$$

That is, there is a pole-like singularity at $\lambda_{rel} = -\frac{1}{4}$. This proves part (1) of the theorem.

Part (2) of the theorem is most conveniently proved by splitting the range of λ_{rel} at zero and considering a negative λ_{rel} and positive one separately.

(ii-negative) $\lambda_{rel} \in \left(-\frac{1}{4}, 0\right)$ with $\lambda_{rel} \neq -\frac{1}{2l(l+1)}$.

In this case, given the range in which λ_{rel} appears and that it is not the reciprocal of any eigenvalue then

$$w^0 = -\frac{\Omega C}{2\left(\frac{1}{2} + 2\lambda_{rel}\right)}\psi_{1,0} \tag{3.42}$$

(ii-positive) $\lambda_{rel} \geq 0$.

Since all of the eigenvalues of G are negative, it follows that the kernel of $[G - 2\lambda_{rel}]$ must be empty when $\lambda_{rel} > 0$. So to equation (3.38) set $w^0 = k\psi_{1,0}$, and we find that

$$k = -\frac{\Omega C}{(1 + 4\lambda_{rel})} \tag{3.43}$$

This implies, then, that as $\lambda_{rel} \to \infty$ then

$$w^0 = k\psi_{1,0} \text{ with } k \to 0^- \tag{3.44}$$

and also that as $\lambda_{rel} \to 0^+$ then

$$w^0 \to -\Omega C\psi_{1,0} \tag{3.45}$$

The special solution $w^0 = -\Omega C\psi_{1,0}$ holds when the constraint on V_{rel} is not applied and we look only at the unconstrained optimization of the energy H.

And so between the cases of (ii-negative) and (ii-positive) we have proved part (2) of the theorem.

(iii) $\lambda_{rel} \in \left[-\frac{1}{4}, 0\right)$ and $\lambda_{rel} = -\frac{1}{2l(l+1)}$.

For $l = 2, 3, 4, \cdots$ the values of $\lambda_{rel} = -\frac{1}{2l(l+1)}$ will form bifurcation values. We can have an extremal relative vorticity for which

$$w^0 = -\frac{\Omega C}{2\left(\frac{1}{2} - \frac{1}{l(l+1)}\right)}\psi_{1,0} + \sum_{m=-l}^{l} \alpha_{l,m}\psi_{l,m} \tag{3.46}$$

That is, this is the only case in which higher spherical harmonics than the mode $(l, m) = (1, 0)$ are able to contribute to the extremal vorticity.

∎

So far, we have formed a variational problem to find extremal relative vorticity states for the atmosphere around a planet, and we have shown that using the Euler-Lagrange multiplier method implies certain physical properties about any extremals that do exist. What we have not yet done is to show that these extremal states do exist, nor have we found the multipliers λ_{rel} for which they appear. This is the objective of the next section.

3.3 Extremals: Existence and Properties

We have a fixed relative enstrophy $Q_{rel} > 0$ as part of our atmospheric model. By using this we can find the value of the Euler-Lagrange multiplier λ_{rel} discussed so much above. One of the consequences of finding this multiplier is that we will become able to determine the physical properties of the extremal relative vorticity w^0 and describe them in terms of the relative enstrophy Q_{rel} and the planetary spin rate Ω. Equations (3.47) and (3.48) are plotted to show the dependence of the Lagrange multipliers on the relative enstrophy.

Lemma 3.5. *The Lagrange multipliers λ_{rel} of the extremals of the variational problem 1 are given in terms of the planetary spin rate $\Omega \geq 0$ and of the relative enstrophy $Q_{rel} > 0$ by*

$$\lambda_{rel}^{+} = -\frac{1}{4}\left[1 + \frac{\Omega C}{\sqrt{Q_{rel}}}\right] \tag{3.47}$$

and

$$\lambda_{rel}^{-} = -\frac{1}{4}\left[1 - \frac{\Omega C}{\sqrt{Q_{rel}}}\right] \tag{3.48}$$

Proof. We start with the solution, given in equation (3.39), for the Euler-Lagrange equation. Put this into the constraint in V_{rel}:

$$\|w^0\|^2 = \frac{\Omega^2 C^2}{4\left(\frac{1}{2} + 2\lambda_{rel}\right)^2} = Q_{rel} > 0 \tag{3.49}$$

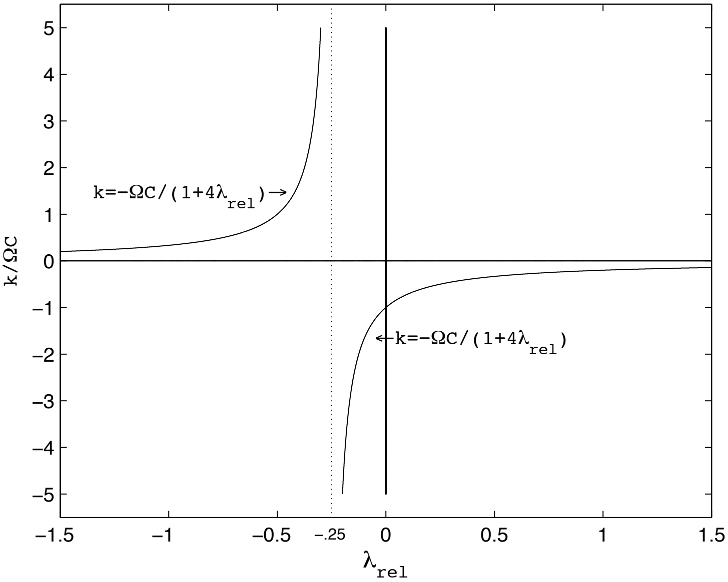

Fig. 3.4 A graph of extremal coordinates k versus Lagrange Multipliers $\lambda^{\pm}_{rel}$ for a fixed spin $\Omega > 0$ as in equations (3.39) and (3.42).

Solve this for $\lambda^{\pm}_{rel}$.

The special solutions given in equation (3.46) correspond to a countable set of bifurcation values.

∎

The next lemma is given without proof, but the evaluation necessary is straightforward.

Lemma 3.6. *The first branch of solutions described in Lemma 3.5, where*

$$\lambda^{+}_{rel} < -\frac{1}{4} \tag{3.50}$$

with a corresponding extremal relative vorticity

$$w^{0}_{Max} = \sqrt{Q_{rel}}\psi_{1,0} \tag{3.51}$$

are associated with solid-body rotation in the direction of spin Ω. In terms of the original kinetic energy

$$H_{Max}\left[\alpha_{1,0}\psi_{1,0}\right] = -\Omega^2 C^2 \frac{\left(1+8\lambda_{rel}^{+}\right)}{16\left(\frac{1}{2}+2\lambda_{rel}^{+}\right)^2} \tag{3.52}$$

$$= \frac{1}{4}Q_{rel} + \frac{1}{2}\Omega C\sqrt{Q_{rel}} \tag{3.53}$$

The second branch of solutions described in Lemma 3.5, where

$$\lambda_{rel}^{-} \in \left(-\frac{1}{4}, \infty\right) \text{ while } \lambda_{rel}^{-} \neq -\frac{1}{2l\left(l+1\right)}, l = 2, 3, 4, \cdots \tag{3.54}$$

with a corresponding extremal relative vorticity

$$w_{min}^{0} = -\sqrt{Q_{rel}}\psi_{1,0} \tag{3.55}$$

are associated with solid-body rotation opposite the direction of spin Ω. In the terms of the original kinetic energy

$$H_{min}\left[\alpha_{1,0}\psi_{1,0}\right] = -\Omega^2 C^2 \frac{\left(1+8\lambda_{rel}^{-}\right)}{16\left(\frac{1}{2}+2\lambda_{rel}^{-}\right)^2} \tag{3.56}$$

$$= \frac{1}{4}Q_{rel} - \frac{1}{2}\Omega C\sqrt{Q_{rel}} \tag{3.57}$$

all for a given relative enstrophy Q_{rel} and spin Ω.

The Euler-Lagrange multiplier method gives necessary conditions for an extremal to exist; it does not give sufficient conditions. The traditional method to show this sufficiency is the direct method of the calculus of variations, and it follows in two steps. First, show the unconstrained extremals of an augmented objective functional exist; second, show these unconstrained extremals are the constrained extremals of the original objective functional. We will show this later on. In this section, we mean to show the sufficiency by an argument in the geometry of the energy and relative enstrophy manifolds, an infinite-dimensional geometric argument which is no less rigorous but which may be more intuitive.

Suppose one means to find an extremal of H subject to the constraint Γ. This extremal must be within the set of points p which share common tangent spaces on some level curve of H and of Γ simultaneously. But it is only the points in p where one level curve remains on the same side of the other level curve within a neighborhood of the point that can be a constrained energy maximizer or minimizer.

Let p_{Max} be the slightly leading name for one of these points where the level curves share a tangent space and where both curves locally stay on the same side of the other within the neighborhood. If the level curve of H is on the outside of the curve of Γ in a full neighborhood of p_{Max}, measuring inside and outside with respect to the point $p_0 = (-\Omega C, 0, 0, 0, \cdots, 0)$ in the subspace of $L^2\left(S^2\right)$ which is defined by equation (3.20), then p_{Max} is a constrained energy maximizer. Similarly, for another leadingly named point p_{min}, if the level curve of H is on the inside of the level curve of Γ in a full neighborhood of p_{min}, again with respect to the same point $p_0 = (-\Omega C, 0, 0, 0, \cdots, 0)$ in the same subspace of $L^2\left(S^2\right)$, then p_{min} must be a constrained energy minimizer.

The lemmas and theorems established above support the necessary conditions. These facts and Lemma 3.3 will come together to form an existence proof, giving sufficient conditions for the constrained extremals we want in terms of the geometry of the objective and of the constraint functionals.

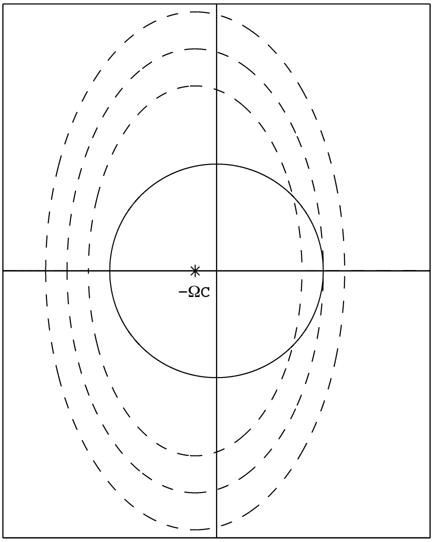

Fig. 3.5 Projections of the energy ellipsoid and the enstrophy sphere showing the common tangent at global maximizer w^0_{Max} when energy exceeds H_c.

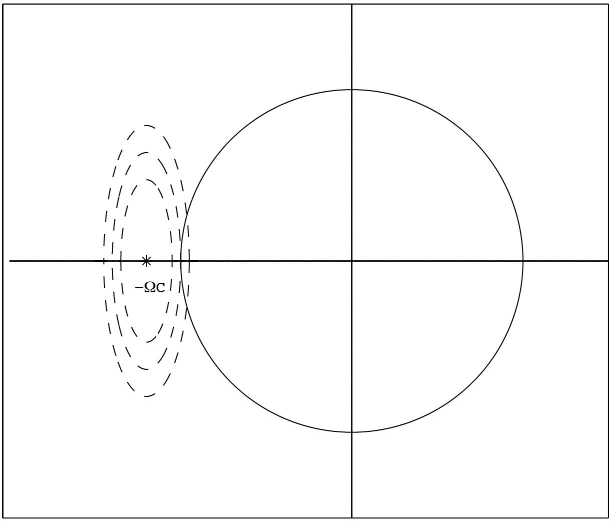

Fig. 3.6 Projections of energy ellipsoid and enstrophy sphere showing the common tangent at local minimizer $w^0_{\min}$ when equation (3.60) holds.

Theorem 3.2.

(1) The first branch of solutions $w^0_{Max} = \sqrt{Q_{rel}}\psi_{1,0}$ *in Lemmas 3.5 and 3.6 are global energy maximizers for any relative enstrophy* Q_{rel} *and any spin* Ω*.*

(2) For the second branch of solutions $w^0_{min} = -\sqrt{Q_{rel}}\psi_{1,0}$ *in Lemmas 3.5 and 3.6 these statements hold:*

(1) If the relative enstrophy is large compared to the spin, i.e.,

$$Q_{rel} > 4\Omega^2 C^2 \tag{3.58}$$

then w^0_{min} *is a special saddle point: it is a local energy maximum in all eigendirections except for span* $\{\psi_{1,\pm 1}\}$*, in which it is a local minimum.*

(2) If the relative enstrophy satisfies

$$\Omega^2 C^2 < Q_{rel} < 4\Omega^2 C^2 \tag{3.59}$$

then w^0_{min} *is a constrained energy saddle point.*

(3) If the relative enstrophy is small compared to the spin, i.e.,

$$Q_{rel} < \Omega^2 C^2 \tag{3.60}$$

then w^0_{min} *is a constrained energy minimum.*

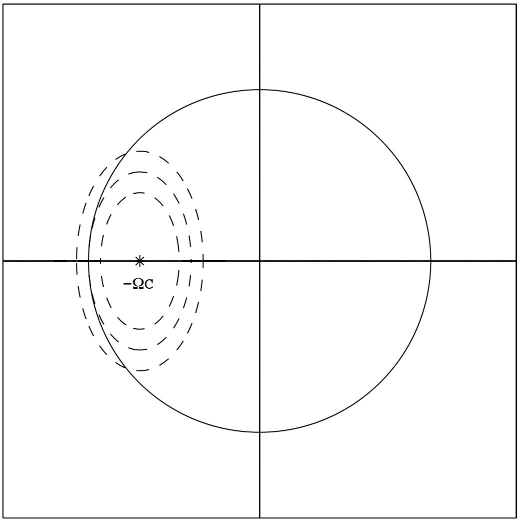

Fig. 3.7 Projections of an energy ellipsoid and enstrophy sphere showing the saddle point $w^0_{\min}$ as a local minimum when equation (3.59) or (3.58) hold.

Proof.

For part (1), we know from the eigenvalues $\lambda_{l,m} = -l\,(l+1)$ and the fact that the spherical harmonics $\psi_{l,m}$ diagonalize the energy H and furthermore from Lemma 3.3 — cf. equation (3.25) — that H must be positive definite in $L^2\left(S^2\right)$. Furthermore, its level surfaces are infinite-dimensional ellipsoids centered at $p_0 = (-\Omega C, 0, 0, 0, \cdots, 0)$ with the properties that

$$\begin{aligned}&\text{the shortest semi-major axes of equal lengths are in}\\ &\mathit{span}\,\{\psi_{1,0}, \psi_{1,-1}, \psi_{1,1}\}\end{aligned} \tag{3.61}$$

and

$$\begin{aligned}&\text{all other semi-major axes —}\\ &\text{associated with azimuthal wave number } l > 1\\ &\text{— have lengths } L\,(l) \text{ quadratic in } l\\ &\text{and independent of the wave number } m\end{aligned} \tag{3.62}$$

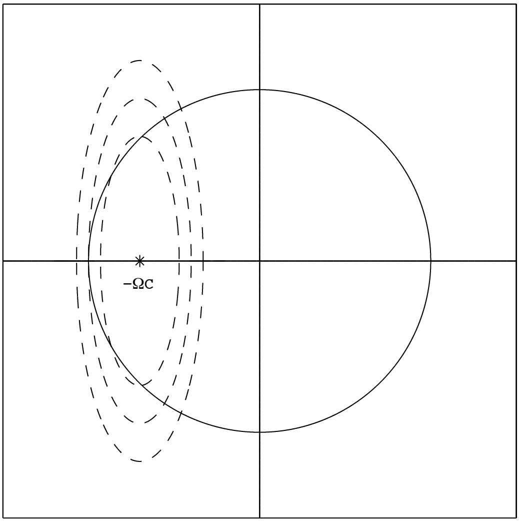

Fig. 3.8 Projections of an energy ellipsoid and enstrophy sphere showing the saddle point w^0_{min} as a local maximum.

The level surfaces of relative enstrophy are noncompact but concentric spheres centered on 0 in $L^2\left(S^2\right)$,

$$\|w\|_2^2 = \sum_{l,m} \alpha_{l,m}^2 = Q_{rel} > 0 \tag{3.63}$$

Taken together, this implies that the level surface of H is on the outside — with respect to p_0 — of the relative enstrophy level surface for a fixed Q_{rel} in the neighborhood of the point $w^0_{Max}\left(Q_{rel}\right) = +\sqrt{Q_{rel}}\psi_{1,0}$. Therefore, $w^0_{Max}\left(Q_{rel}\right)$ is a global constrained energy maximizer.

Part (2) we will take in three segments, as the statement of the theorem suggests we should. The first is part C, where the relative enstrophy is small compared to the planetary spin,

$$Q_{rel} < \Omega^2 C^2 \tag{3.64}$$

In this case at the common point $w^0_{min} = -\sqrt{Q_{rel}}\psi_{1,0}$ the relative enstrophy level surface hypersphere is on the outside of the energy level surface ellipsoid with respect to the point p_o. (Both surfaces are locally convex with respect to their individual centers.) Therefore, in this case w^0_{min} is a constrained energy minimum.

Now to the first case, where the relative enstrophy is large compared to the spin,

$$Q_{rel} > 4\Omega^2 C^2 \tag{3.65}$$

Here it becomes convenient to split the common tangent space of the energy level-surface ellipsoid and the enstrophy level-surface hypersphere at w^0_{min} into two orthogonal components,

$$\text{(a)}\mathit{span}\left\{\psi_{1,\pm 1}\right\}, \text{ and } \text{(b) } \mathit{span}\left\{\psi_{l,m}\right\}, l > 1 \tag{3.66}$$

From what we know through equation (3.61) and equation (3.58), we know the semi-major axes in *span* $\{\psi_{1,0}, \psi_{1,1}, \psi_{1,-1}\}$ of the energy ellipsoid at w^0_{min} will have equal lengths:

$$L = \left| -\sqrt{Q_{rel}} + \Omega C \right| > \Omega C \tag{3.67}$$

Meanwhile, the enstrophy hypersphere at the same point has radii of equal lengths

$$L_{rel} = \left| -\sqrt{Q_{rel}} \right| > 2\Omega C \tag{3.68}$$

The center of the energy level-surface ellipsoid is at $p_0 = -\Omega C \psi_{1,0}$. The center of the enstrophy level-surface hypersphere is at the origin. Therefore,

$$L < L_{rel} \tag{3.69}$$

Consequently, in case (a), then inside *span* $\{\psi_{1,\pm 1}\}$ of the common tangent space (3.66) at w^0_{min}, it follows that the energy ellipsoid is inside the enstrophy hypersphere with respect to p_0 and therefore w^0_{min} is a local energy minimum within this subspace.

However, using equation (3.62), we conclude that the ellipsoid is outside the sphere with respect to p_0, which implies that w^0_{min} is a local energy maximum within this subspace. Therefore, w^0_{min} is a special saddle point in the case of (3.58), a local maximum except within the *span* $\{\psi_{1,\pm 1}\}$.

Finally, in the intermediate case where

$$\Omega^2 C^2 < Q_{rel} < 4\Omega^2 C^2 \tag{3.70}$$

it follows from property (3.61) and the unboundedness property (3.62) of the energy level-surface ellipsoid that there is a critical value of the azimuthal wave number, l_{crit}, such that part (a),

$$\mathit{span}\left\{\psi_{l,m}, l \leq l_{crit}\right\} \tag{3.71}$$

of the common tangent space at w^0_{min} has the energy ellipsoid within the enstrophy hypersphere with respect to p_o; but in the orthogonal complement of part (b),

$$span\,\{\psi_{l,m}, l > l_{crit}\} \tag{3.72}$$

the energy ellipsoid is outside the enstrophy hypersphere with respect to p_o. Therefore, w^0_{min} is a constrained saddle point in the case (3.59).

∎

The variational analyses discussed in some detail in this chapter can be extended to the total mechanical energy functional of the Shallow-Water Equations given in chapter 2, the only changes being the choice of constraints. In this case, it is natural to fix the two square norms – relative and enstrophies – and three total circulations for relative vorticity, horizontal and surface height, making the technicalities in the corresponding variational analyses, substantial. Another possible set of constraints — although unlikely to change the physical outcome of the associated variational problem — is to enforce a fixed total potential vorticity as well as potential vorticity enstrophy or square-norm, and relax the two prior constraints on relative vorticity.

Chapter 4

Statistical Mechanics

4.1 Introduction

Statistical mechanics is a formalism in which we aim to explain the physical properties of matter, in bulk, on the basis of the dynamical behavior of its components, the microscopic quantities [94], [64], [14]. In the context here of forced-damped and freely-decaying bounded quasi-two-dimensional flows in single-layer fluids with multiple time and spatial scales, the bulk refers precisely to the symmetry-breaking in order parameters such as net angular momentum, moment of inertia of the fluid, gravitational potential energy amongst several other physical quantities. For us, the microscopic quantities are –in the Eulerian or lattice picture — patches of vorticity, horizontal divergence and fluid height — in other words, the local spatial-temporal distributions of the dynamical variables in the shallow water equations given in chapter 2 that are governed by the microscopic dynamical equations (2.56, 2.57).

Being able to make macroscopic predictions based on microscopic properties is one of the primary advantages to the statistical mechanics approach over a thermodynamic one. Both approaches are governed, most importantly, by the study of entropy. However, from the thermodynamic approach we know entropy only as an empirically measured quantity. From a statistical mechanics point of view the entropy is a function, known from the distribution of a system into its microstates.

Our fundamental postulate for statistical mechanics is based on an isolated system which is in thermal equilibrium. Our fundamental assumption is that this system will be found, with an equal probability, in each of its accessible microstates. That is to say, a system in equilibrium has no preference for any of its available microstates.

What the postulate allows us to do is to conclude that given a system at equilibrium, the thermodynamically observed state which corresponds to the greatest number of microstates will be the most probable macrostate. This is the microcanonical picture which forms the basis of the other ensembles such as canonical and grand-canonical ones, modulo possible non-equivalences between them.

The picture that is most useful in this book is the canonical one of a two-dimensional lattice of vectorial spins interacting self-consistently with other spins and with unresolved degrees of freedom / spins relegated to the energy-momentum reservoir. For instance, in the shallow water model, the energy-momentum reservoir consists of subgrid scales information in the form of relative vorticity, horizontal divergence and surface heights modes that changes spatially at wavelengths smaller than the lattice cutoff. For a grid of 10000 points on the Jupiter, 2000 km could already be subgrid. Furthermore, the energy-momentum reservoir consists significantly of the unresolved and unmodelled angular momentum and other forms of mechanical energy residing within the massive planet. The main physical mechanisms transferring energy and momentum between the fluid and the massive planet reside in the planetary boundary or Ekman layer - it could also be at the interface between the active upper layer and the deep lower layer in two-layer models [24]– and comprise inviscid ones such as topographical stresses or mountain torques which act through pressure difference and viscous ones such as the relatively thin shear layers. Other ways of transferring energy and momentum are through the energy injection mechanisms which operate at intermediate scales through baroclinic or convective instability and insolation or the planet's internal heat. Between the lattice scales and the subgrid scales, the main mechanisms at work for exchanging energy and enstrophies are the well-known forward enstrophy cascade in many quasi-two-dimensional flows and the less well-known direct energy cascade that operates in tandem with the inverse energy cascade to intensify small-scales turbulence even as the large-scale coherent structures emerge. Indeed we will discuss a new link between the statistical mechanics picture of most probable statistical equilibria and of asymptotic statistically stationary flow states in damped-driven quasi-two-dimensional bounded flows which demonstrates this dual cascade indirectly– the discovery of first order phase transitions at the heart of self-organization of long-range and large-scale order means that significant amounts of mechanical energy is dumped into the energy-momentum reservoir at subgrid scales through the known latent heat effect [94].

4.2 Microstates and Macrostates

As we have already used the terms microstate and macrostate casually to describe properties about a statistical equilibrium it is important to pause and to give these more precise definitions. A **microstate** is a finely detailed description of the state of a system, one in which we list all of the relevant component values. The **macrostate** is a coarser description in which we describe the aggregate totals of properties such as energy for the entire system but refrain from specifying the component variables. These components are for a single macrostate allowed to take any configuration which satisfies the specific aggregate or bulk variables.

The macrostate is, logically, composed of multiple microstates. The number of microstates consistent with any specific value of energy (or for any number of fixed quantities) is the **degeneracy**. For a fixed energy E we denote this degeneracy as $W\left(E\right)$. If the probability that the system will be in one of the microstates with energy E is itself $P\left(E\right)$, then the probability of observing the system to have energy E will be $W\left(E\right) \times P\left(E\right)$ [64].

4.3 Entropy

Entropy is one of the greatest concepts of statistical mechanics, one of the scientific notions to have captured the public fancy. For our needs entropy is a function of the state of the system, and it is dependent on the degeneracy of the system's macrostate. Ludwig Boltzman established in the study of gases a working definition for the entropy S which we still rely on:

$$S = k_B \log\left(W\left(E\right)\right) \tag{4.1}$$

where k_B is the Boltzmann constant, approximately $1.38066 \times 10^{-23} JK^{-1}$. $W\left(E\right)$ is the degeneracy of the macrostate as introduced above.

Claude Shannon, in his definitive papers on Information Theory, proposed a definition of entropy which was based on the probability of encountering a system in each of its possible configurations. Letting P_j represent the probability that we will find the system in state j and given a complete roster of all possible configurations we can say the entropy of the system is:

$$S = \sum_j P_j \log\left(P_j\right) \tag{4.2}$$

where the logarithm is taken with respect to a convenient base. In the case of digital electronics the desire to represent information by binary digits drives the use of base two logarithms. However, the definition is as valid for any convenient base, and is equivalent — up to a multiplicative constant — to the Boltzmann definition for the entropy.

Therefore we will find it convenient to often rely on the Shannon information-theory entropy definition, using the natural logarithm rather than base-two logarithm.

4.4 Partition Functions

Suppose a macroscopic system is in thermal equilibrium with its environment. Then the probability P_j that the system will be in the microstate j, with energy E_j, will be given by the Boltzmann distribution:

$$P_j = \frac{\exp\left(-\beta E_j\right)}{\sum_k \exp\left(-\beta E_k\right)} \tag{4.3}$$

where the summation is taken over all the possible microstates, and where β is the **inverse temperature**: $\beta = \frac{1}{k_B T}$, where T is the temperature of the gas (in Kelvin) and k_B the Boltzmann constant.

While we are not interested in the measurement of heat in our work, we are certainly interested in the entropy and in the internal energy of our systems. Since we can measure the change in entropy with respect to the internal energy, we can calculate a quantity identical to the temperature encountered in the dynamics of gas particles, and therefore we continue talking about temperature and inverse temperature [64].

In order for this probability P_j to be meaningfully defined, the sum of all the probabilities of the various microstates must add to 1. This sum, the normalization factor in the probability, is the **canonical partition function**:

$$Z = \sum_k \exp\left(-\beta E_k\right) \tag{4.4}$$

where E_k is the energy of state k. The partition function measures, in its way, the number of states accessible to a system at a given temperature T through its inverse temperature β.

We must use the canonical partition function Z as a normalization factor in evaluating the probabilities of various states appearing, and so we will see notations such as defining the probability of finding a system at inverse temperature β to be in a state with energy E_j as

$$P_j = \frac{1}{Z} \exp\left(-\beta E_j\right) \tag{4.5}$$

We can use the partition function to find the expectation values, the averages, for bulk property of the system. As an example, the expected value for the energy E we can view as the microscopic definition of the thermodynamic internal energy U, and we can find that by taking the derivative of the partition function with respect to the temperature. In fact,

$$\langle E \rangle = \frac{\sum_j \exp\left(-\beta E_j\right)}{Z} \tag{4.6}$$

$$= -\frac{1}{Z}\frac{dZ}{d\beta} \tag{4.7}$$

implies, if we interpret $\langle E \rangle$ as U, this microscopic definition of the internal energy:

$$U = -\frac{d \log\left(Z\right)}{d\beta} \tag{4.8}$$

The entropy of the system we can calculate using the Shannon information-theory definition of entropy:

$$S = -k_B \sum_j P_j \log\left(P_j\right) \tag{4.9}$$

$$= k_B \sum_j \frac{\exp\left(-\beta E_j\right)}{Z}\left(\beta E_j + \log\left(Z\right)\right) \tag{4.10}$$

$$= k_B \left(\log\left(Z\right) + \beta U\right) \tag{4.11}$$

which implies

$$-\frac{\log\left(Z\right)}{\beta} = U - TS = F \tag{4.12}$$

is the free energy of the system. Or, in other words,

$$Z = \exp\left(-\beta F\right) \tag{4.13}$$

4.5 Free Energies

The entropy of an isolated system cannot decrease. From this we can conclude the entropy of an isolated system in equilibrium must be a maximum. However, there is not much experimental interest in an isolated system: we want to consider a more typical case in which the system is connected to a heat bath which has properties not changing significantly.

The Helmholtz free energy, the amount of thermodynamic energy in system which at a constant temperature can be converted into work, is given by

$$F = U - TS \tag{4.14}$$

where F is the Helmholtz free energy, and U is the internal energy of the system, with T the temperature and S the entropy.

The approach we use of applying equilibrium statistical mechanics principles to the study of two-dimensional flows centers on finding extremal values of the free energy. Because we are interested in exploring the whole range of possible flow mechanical energies we needed the extension of Planck's Theorem (theorem 4.1) to cover negative temperatures.

4.6 Planck's Theorem in Negative Temperatures

When a system has a maximum possible energy, we will generally see the degeneracy $W(E)$ decreasing as the system's energy approaches that maximum. So there must be some energy, below the maximum possible energy, at which the degeneracy and therefore the entropy is maximized.

When the system energy exceeds this maximum energy, then, further increases in energy will decrease the entropy and therefore the temperature becomes negative [64]. A system with a negative temperature is a hotter one than a system with positive temperature, which in this case means that were we to connect a system at negative temperatures to one with positive temperatures, heat would flow from the negative-temperature system to the positive-temperature one.

These highly energetic systems we will see correspond to many interesting and highly structured systems.

In these analyses we will very often rely on a representation of vorticity, and with a fixed relative enstrophy this means we will have a phase space for possible vorticity distributions among the points which is bounded in the square-norm measure. As a result, we can expect that at the highest possible kinetic energies we will see the phenomenon of negative temperatures: an increase in energy will see a decrease in the entropy of the system. Ever since Lars Onsager's seminal 1949 paper [80] we have known that two-dimensional vortex statistics are characterized by the existence of negative temperatures at the highest values of the flow's kinetic energy. And therefore we know we will need to consider the extension of Planck's Theorem extended to cover negative temperatures T, as we rely on this to find the most probable configuration of vorticity on a given isotherm.

Theorem 4.1. ***Extended Planck's Theorem.*** *The most probable (thermodynamically stable) state at a negative [positive] temperature T corresponds to maxima [minima] of the Gibbs free energy per site*

$$F = U - TS \tag{4.15}$$

where

$$U = \langle L \rangle \tag{4.16}$$

is the internal energy per site (L representing the Lagrangian describing the system) and where

$$S = -k_B \int ds\, p(s) \log(p(s)) \tag{4.17}$$

is the mixing entropy per site, given in terms of the probability distribution $p(s)$ for the site value s. k_B is the Boltzmann constant.

Remark 4.1. It follows that the most probable state — also a thermodynamically stable state — is not necessarily the state $m^{'}$ which maximizes $W = \exp\left(\frac{1}{k_B} S\right)$.

Instead it will be the state which maximizes the product $W \exp(-\beta U)$ where $\beta \equiv \frac{1}{k_b} T$.

However, at temperatures T where $|T|$ is small, it becomes likely that the state extremizing the Gibbs free energy per site F is close to the state m which maximizes U, rather than the state $m^{'}$ which maximizes S. At temperatures T where $|T|$ is large, it is likely the state which extremizes F is closer to the $m^{'}$ that maximizes S rather than the state m that maximizes U. This immediately foreshadows a feature of section 6.4, namely, can we characterize the differences between states that maximize S compared to those that maximize U, and will there be obvious transitions between those states?

Another significant property is that, for systems which support the existence of negative temperatures, in particular barotropic flows, the specific heat will be positive even when the temperature is negative.

4.7 Latent Heat and Orders of Phase Transitions

The models in this book will be shown to support both first and second order phase transitions. Ising and Heisenberg models for the Barotropic Vorticity problem have well-defined second order phase transitions, many aspects of which have been rigorously worked out by the exact solutions of the corresponding Kac's spherical models. The newer class of lattice Shallow-Water Models discussed in chapters 2, 10 and 11 are essentially Potts models and are well-known to have first order phase transitions where latent heat is either absorbed or given out. In the case of the Shallow-Water Model at positive temperatures, most suitable for modelling the Jovian atmospheres, the emergence of organized coherent structures with long-range order through a first order transition, ejects latent heat in the form of mechanical energy and entropy into the canonical reservoir comprising the small eddies below the lattice ultraviolet-cutoff. This phenomemon provides a new and significant link between the statistical mechanics approach highlighted in this book and the energy cascades, long known to be central to stationary forced-damped quasi-two-dimensional flows, in the form of dual energy cascades between intermediate scales on one hand, and large-scales through the self-organization of large coherent structures and also sub-grid scales through a forward energy cascade that intensifies the turbulence at small-scales even as the large-scales are organized. The reader can find out more about phase transitions and their long history in scientific applications in Stanley's book, [94].

As predicted by the extension of Planck's theorem to negative temperatures, phase transitions in systems that exhibit negative temperatures are anomalous in several key aspects. In the case of the first-order transition at negative T_c in the Shallow-Water Model, a sharp decrease in the entropy occurs in passing to the high energy phase. In standard latent heat calculations such as in the case of boiling water, the high energy phase — vapor in this case — is associated with a higher entropy. By this anomaly, a first-order phase transition at negative temperatures is therefore shown to increase the long-range order even as the associated energy increases.

The verification of a first-order transition indicated in the numerical results in chapters 10 will be based on an extension of Planck's theorem to negative temperatures [64]. Unlike the standard minimization of free energy in the traditional statement of Planck's theorem which holds for positive temperatures, the equivalent result for negative temperatures is the maximization of free energy. It is interesting to note that in both versions

- applicable to canonical and grand-canonical Gibbs statistical mechanics — the free energy $F = U - TS$ does not usually have a jump discontinuity at a first-order transition point denoted herein by T_c. It is customary to see a cusp-type singularity at which the free energy remains continuous across the transition. The internal energy U of the preferred macrostate, on the other hand, displays a clear and significant jump discontinuity at the transition. In passing from a more negative temperature through T_c to a less negative temperature, corresponding to an increase δ in energy, the entropy is expected - as is easily shown in greater detail below - to decrease by the amount $\delta \ / \ T_c$.

Chapter 5

The Monte Carlo Approach

5.1 Introduction

What do we find if we measure the energy of a system? This relatively simple question provides the motive for introducing the numerical technique of the Metropolis-Hastings, Markov Chain, Monte Carlo simulation, and this is a computationally simple yet powerful tool for finding statistical equilibrium configurations of the sorts of spin-lattice problems which are a focus of this book.

In this chapter we start by considering the expectation value of any random variable. This may be the energy or may be another property. But we start with the energy, since much of what we will want to study is either the Hamiltonian or the Lagrangian of a system.

We expect that a measurement of energy should find the most probable energy. And we know the probability of state j appearing as it derives from the partition function:

$$P(E_j) = \frac{\exp\left(-\beta E_j\right)}{\sum_s \exp\left(-\beta E_s\right)} \tag{5.1}$$

Since the denominator is constant we can maximize $P\left(E\right)$ by minimizing βE. Assuming that β is positive, then the maximum probability is found by minimizing the energy.

The solution is simple, direct, and almost useless. The first flaw is that we need a more exact definition of what it is to be in a state; do we mean the microstate or the macrostate? This affects what the expectation value of the energy is.

We need to represent fairly all the states of a system, and to find a way to select representative slate of these states for a numerical estimate.

For an analytically simple enough system we can write out its partition function and degeneracy and calculate them exactly. But few interesting systems are simple enough to be understood this way. The three-dimensional Ising model is a fine example of an interesting and simply described system, yet it is one not yet analytically solved.

So we resort to the numerical techniques. We can identify all the N possible states for the system, calculate their energies, and take the expectation value.

$$\langle E \rangle = \frac{1}{N} \sum_{s} E(s) \tag{5.2}$$

This algorithm enjoys simplicity of design, but it is impractical; there are too many states for any interesting system to ever complete. But the essence of numerical simulation is that we do not need to calculate all of them. The law of large numbers indicates that the system will almost certainly be in one peak of most probable configurations, and anything too far from that peak may be ignored without making an intolerable error.

Yet if we knew the most probable states we would not need to estimate the most probable states. What we want is a representative sampling of the various states, chosen so that the expectation value for this sampling also equals the expectation value for the universe of all possible states. How do we create this representative sample? We begin, as many numerical methods do, by taking a wild guess.

5.2 Markov Chains

This initial guess serves the same role the first guess at a root in Newton-Raphson iterations does: it is an arbitrary starting point for a process which eventually reaches the desired solution. In fact, unlike Newton-Raphson iterative methods we do not look particularly for a single solution, but rather look for a chain of states which are around the statistical equilibrium of whatever system we mean to study. Once we have reached a statistical equilibrium we can sample a number of these equilibrium states and find whatever system property we mean to study. From our starting state we will generate a Markov chain of new states, which will cluster around the most probable states.

We explore the set of all possible states of a system by a stochastic process, one which relies on a certain randomness in how it will evolve. In a Markov chain the probability of moving to another state depends only on the current state, and not on any other factors. Note that this decision means we are not attempting to represent the evolution in time of any system; the only mechanical properties we find interesting are the total energy or whatever other property it is we use to construct the Markov chain or the terms describing how to move from one configuration to another, which we will describe shortly.

We represent this with a transition matrix. This is a square matrix of size N — where N is the number of possible states — and in which the entry at row j, column k is the probability of the system moving from the state j to the state k in one iteration. The sum of the terms in any one column must be 1 — the system must be in some state at the end of the iteration. Each entry in this transition matrix must be nonnegative, and must be at most 1.

Let $\vec{x}_0$ be the probability vector, a vector with N dimensions, representing the starting point for our set of configurations. Each state is represented by a different component of this vector, and the value of element j in the vector is the probability the system is in state j. Each term is necessarily between zero and one inclusive, and the sum of all components is one.

We can represent the effect on a probability vector of of running our stochastic process by left-multiplication the vector by the the transition matrix M. As a consequence the probability of being in the various possible states after each of the first several iterations is

$$\vec{x}_1 = M\vec{x}_0 \tag{5.3}$$

$$\vec{x}_2 = M\vec{x}_1 = M^2\vec{x}_0 \tag{5.4}$$

$$\vec{x}_3 = M\vec{x}_2 = M^2\vec{x}_1 = M^3\vec{x}_0 \tag{5.5}$$

$$\vdots$$

$$\vec{x}_{j+1} = M\vec{x}_j = M^j\vec{x}_0 \tag{5.6}$$

The probability of getting from microstate j to microstate k in a single step is $M_{j,k}$. The chance of making it in two steps is $M^2_{j,k}$, and the chance of making it in n steps is $M^n_{j,k}$. The chance of ever getting from j to k is $\sum_{n=1}^{\infty} M^n_{j,k}$.

State j is called a recurrent state if $\sum_{n=1}^{\infty} M^n_{j,j}$ equals one — that is, if the system run long enough has probability one of returning. If $M^n_{j,j}$ is nonzero only when n is a whole multiple of some integer p, then state j has the period p. If p is 1 the state is aperiodic.

If it is always possible, given enough time, to get from any j to any k and back again — there are some p and q so that $M^p_{j,k} > 0$ and $M^q_{k,j} > 0$ — then M is an irreducible Markov chain. An irreducible aperiodic chain will justify Markov chain Monte Carlo in section 5.6.

After a great many iterations, the system settles to a statistical equilibrium, with the components no longer significantly changing. This equilibrium is the vector for which

$$\vec{x} = \lim_{i \to \infty} M^i \vec{x}_0 \tag{5.7}$$

which ought to be reached independently of whatever the initial vector $\vec{x}_0$ is.

Another interpretation of the statistical equilibrium vector is that it is the eigenvector of M with eigenvalue 1. If the vector $\vec{x}$ from (5.7) exists, then

$$\vec{x} = M\vec{x} \tag{5.8}$$

Note that the method of picking an arbitrary starting point and repeating matrix multiplication is one numerical method for finding a matrix's largest eigenvalue and its eigenvector.

The random walk is probably the best-known example of a Markov chain (though the self-avoiding random walk is not — its moves depend on its previous states), and we can view our Markov chains as a form of random walk through all possible states. Assuming that the phase space of possible states of a system does not have any traps, it should be possible to get from any one state to any other state eventually.

Using these iterative or eigenvector methods seems to make the problem worse. Now we need not justify all the states but the chance of transferring between them — and finding eigenvalues and eigenvectors of large, mostly nonzero, matrices is extremely computationally costly. We need to reduce this overhead.

5.3 Detailed Balance

We know something about the statistical equilibrium of a system. In equilibrium the probability of being in the state j has to be

$$\pi(j) = \frac{1}{Z} \exp(-\beta E_j) \tag{5.9}$$

with Z the partition function and a normalizing factor, so that $\sum_j \pi(j) = 1$.

Detailed balance, a principle holding for any time-reversible system, holds that at statistical equilibrium the rate at which any process occurs equals the rate at which its inverse occurs. The chance of the transition from state A to B equals the chance of the transition from B to A occurring. In chemical reactions — which may offer an intuitive guide to the property — it means the rate at which the components combine to form the product equals the rate at which some of the product breaks back down to its components.

Let $P_{A,B}$ represent the probability of state A evolving to B. The chance of observing A turning to B is the product $\pi(A) \times P_{A,B}$ — the probability we began in A *and* changed to B. To be in detailed balance means for all A and B

$$\pi(A)P_{A,B} = \pi(B)P_{B,A} \tag{5.10}$$

From equation (5.10) and from the probability of states occurring from equation (5.9) we can find the probability of observing the transition from A to B, in terms of the probability of observing the transition from B to A. The challenge is then to construct a Markov chain of states which reach this detailed balance.

$$\pi(A)P_{A,B} = \pi(B)P_{B,A} \tag{5.11}$$

$$P_{A,B} = P_{B,A}\frac{\pi(B)}{\pi(A)} \tag{5.12}$$

$$P_{A,B} = P_{B,A}\frac{\frac{1}{Z}\exp\left(-\beta E(B)\right)}{\frac{1}{Z}\exp\left(-\beta E(A)\right)} \tag{5.13}$$

$$P_{A,B} = P_{B,A}\exp\left(-\beta(E(B) - E(A))\right) \tag{5.14}$$

5.4 The Metropolis Rule

The term Monte Carlo describes a collection of probability-based methods. The name is meant to evoke gambling: any one event is unpredictable, but the averages over many events are certain. The use of statistical methods to find exact results goes back centuries at least. Likely the best-known and startling example is Buffon's needle problem, in which short needles are dropped across an array of parallel straight lines. The chance of a needle intersecting one of the lines is proportional to the width of the lines, the length of the needle, and π, which provides an experimental (but inefficient) way to calculate π.

Modern Monte Carlo studies problems from numerical quadrature, to random walks, to polymer and crystal growth, to neutral network growth and decay. Some techniques allow the solution of differential equations by these methods. Monte Carlo methods — and the name— came about after 1944, in the effort to simulate the diffusion of neutrons in fissionable materials [39].

There are many techniques, but the typical approach starts with an arbitrary state. We experimentally adjust that solution, making small changes at random. Steps that improve the solution are accepted, and steps which worsen it are rejected with a probability that depends on how much worse the change would be. This process continues until the detailed balance is met.

The Metropolis Rule for Monte Carlo, introduced by Nicholas Metropolis, A W Rosenbluth, M N Rosenbluth, A H Teller, and Edward Teller in a 1953 paper, "Equations of state calculations by fast computing machines," (J. Chem. Phys. 21, 1087-1092) is one of the great algorithms of the 20th century.

The algorithm is powerful and flexible; it can be used for problems from the absorption of neutrons by atomic nuclei to the growth of crystals to the travelling salesman problem. To customize it to the needs of the vortex problems we address here we fill in only a few details. What we will use is the Hastingsrule, and so this particular method is often called the Metropolis-Hastings algorithm.

We begin with state A. Typically Monte Carlo programs will try to change as few components as possible, for example by moving one particle. The desire to change as few variables as possible is a computational convenience. We need to calculate the difference in energy (and other quantities) between the new state and the old, and fewer changes make those calculations faster.

So we find a modified state B. We then determine whether to accept or reject it. The probability of moving from state A to state B is $\exp\left(-\beta\left(E_B - E_A\right)\right)$, so we find $\Delta E = E_B - E_A$ and our inverse temperature β. Draw a random number r from a uniform distribution on the interval $[0, 1]$; if $r < \exp\left(-\beta \Delta E\right)$ then the experiment is accepted. Repeat the process until an equilibrium is reached. (Note that if $\beta \Delta E < 0$ then the change is always accepted. The interpretation that in this case the probability of moving from A to B is greater than one is quietly ignored; the probability cannot be more than one.)

That this rule obeys the detailed balance principle is clear: the chance of the process moving the system from state A to state B in one iterate is $\pi(A) \cdot \exp\left(\beta\left(E\left(B\right) - E\left(A\right)\right)\right)$.

The thermodynamic origins of statistical mechanics give us a metaphor, of placing the system into a heat reservoir at inverse temperature β. The

Metropolis-Hastings algorithm simulates what happens if a system is given access to an unlimited reservoir from which to draw, or into which to dump, heat. For the system of gas particles, the average kinetic energy at detailed balance equals to the average kinetic energy at the temperature $T = \frac{1}{k_B \beta}$ (with k_B the Boltzmann constant). Reaching a statistical equilibrium may be referred to as reaching thermal equilibrium.

There are other criteria that may be applied: the detailed balance is satisfied if experiments are approved whenever the r drawn from $[0, 1]$ is less than $\left[\exp\left(\beta \Delta E\right) + 1\right]^{-1}$ instead. While this alternate acceptance criteria will accept and reject slightly different states than the above rule does, they will produce a Markov chain with similar properties.

The Markov chain settles around a few states around the peak where the product of the probability and degeneracy reaches a maximum. Assuming β is positive, then if we start from a state with higher than the most-probable energy we will see any states lowering energy approved, while few states increasing it are permitted. Thus we get a chain of states with, usually, decreasing energy whenever we are above the most-probable energy.

If we begin from below the most-probable energy, while the Metropolis-Hastings process would try to decrease the energy, the degeneracy of these lower-energy states is small enough the algorithm cannot find many. More moves increasing the energy are approved. The only energy at which the number of moves increasing the energy will equal the number decreasing is that most-probable energy state — which is another way of saying the system settles at the energy where detailed balance is satisfied.

5.5 Multiple Canonical Constraints

We have looked at systems in which several quantities, such as energy and circulation, affect the probability of a microstate appearing. When the probability depended only on its energy, its probability of appearing at a particular β was $\frac{1}{Z}\exp\left(-\beta E\right)$. With several quantities, such as energy E and enstrophy Γ, we had an inverse temperature β and a chemical potential μ, and the probability of microstate A was

$$\pi(A) = \frac{\exp\left(-\beta E_A - \mu \Gamma_A\right)}{\sum_j \exp\left(-\beta E_j - \mu \Gamma_j\right)} \tag{5.15}$$

with Z the partition function, the sum of $\exp\left(-\beta E\left(j\right) - \mu \Gamma\left(j\right)\right)$ over all possible microstates j.

The kinetic theory of gases defines the enthalpy of a system to be the sum of the energy and of the pressure times the volume. We will appropriate the name enthalpy and modify it to be

$$H_A = E_A + \frac{\mu}{\beta}\Gamma_A \tag{5.16}$$

with Γ_A the new canonically constrained quantity. The Metropolis-Hastings algorithm we rewrite with enthalpy in place of energy.

Given the current microstate j, we generate a new microstate k, and calculate the change in enthalpy $\Delta H = \Delta E + \frac{\mu}{\beta}\Delta\Gamma$. We draw a random number r uniformly from the interval $(0, 1)$ and accept the move whenever

$$r \leq \exp\left(-\beta\Delta H\right) = \exp\left(-\beta\Delta E - \mu\Delta\Gamma\right) \tag{5.17}$$

and reject the move otherwise.

(Some books and articles introduce enthalpy as $H = E + \mu\Gamma$, which is a different scaling of μ. Whether to use this definition or that of (5.16) is a personal preference.)

This enthalpy can be extended. Each new conserved quantity Ξ requires its own chemical potential, but the algorithm remains the same, with

$$H_A = E_A + \frac{\mu_1}{\beta}\Gamma_A + \frac{\mu_2}{\beta}\Xi_A \tag{5.18}$$

and the decision to accept or reject a proposed move being based on whether or not the randomly drawn number r satisfies

$$r \leq \exp\left(-\beta\Delta H\right) = \exp\left(-\beta\Delta E - \mu_1\Delta\Gamma - \mu_2\Delta\Xi\right) \tag{5.19}$$

As with the metaphor of Metropolis-Hastings simulation as placing the system in a heat reservoir at inverse temperature β, we can regard multiple canonical constraints as giving a system access to several reservoirs from which to draw or into which to dump energy, enstrophy, or whatever is interesting.

5.6 Ensemble Averages

We use the Markov chain of Metropolis-Hastings produced sequences to find an average of the property x. With M such states, and $x\left(j\right)$ the property measured at state number j, the mean value of x is

$$\bar{x} = \frac{1}{M}\sum_{j=1}^{M} x\left(j\right) \tag{5.20}$$

This number will approximate the expectation value of x, the average over all possible states. Given the probability of any state j occurring at inverse temperature β is $\frac{1}{Z} \exp\left(-\beta H\left(j\right)\right)$ then this expectation value, if there are a discrete set of N possible states, will be

$$\langle x \rangle = \frac{\sum_{j=1}^{N} x\left(j\right) \exp\left(-\beta H\left(j\right)\right)}{\sum_{j=1}^{N} \exp\left(-\beta H\left(j\right)\right)} \tag{5.21}$$

or, if there is a continuum of possible states,

$$\langle x \rangle = \frac{\int x(\vec{s}) \exp\left(-\beta H(\vec{s})\right) d\vec{s}}{\int \exp\left(-\beta H(\vec{s})\right) d\vec{s}} \tag{5.22}$$

The ergodic hypothesis says if one takes a single system and constructs a long enough chain of microstates, then the averages of any measured quantity taken over these microstates will approximate the average the quantity would have over all of phase space. The fraction of "time" spent in any macrostate consisting of a certain energy range will be proportional to the fraction of the volume of phase space that is in that energy range macrostate.

Consider an irreducible aperiodic Markov chain. This sequence of states can explore all phase space without becoming trapped forever in one region — it is irreducible, so the chance of getting from one microstate to another is never zero. It can concentrate on the most probable microstates — an aperiodic chain may repeat its position. A long enough chain should explore phase space and spend approximately as much "time" — have as many links — in each macrostate as the whole phase space does.

Given an irreducible aperiodic Markov chain, $\pi\left(j\right)$ the probability the current microstate is j, and $M_{j,k}$ the probability of moving to k then

$$\pi\left(k\right) = \sum_{j} M_{j,k} \pi\left(j\right) \tag{5.23}$$

when the steady state distribution has been found, and the summation is taken over all microstates. (If we have a continuum of states, rather than a discrete set, this becomes an integral.) If we satisfy this (and the requirements $\pi\left(k\right) > 0$ and $\sum_{j} \pi\left(k\right) = 1$) then

$$\lim_{n \to \infty} M_{j,k}^{n} = \pi\left(k\right) \tag{5.24}$$

The choice of j is irrelevant: the statistical equilibrium does not depend on the initial state. We can find an equilibrium even by multiplying M by itself repeatedly. Every column of M^{n} approaches the equilibrium (if it exists).

The approach of Metropolis et al — well-presented by J M Hammersley and D C Handscomb [39] — is to build a transition matrix P with elements $P_{j,k}$ that will eventually satisfy the equilibrium distribution. Assume $P_{j,k} > 0$ for all j and k, and that P is a regular transition matrix: $\sum_k P_{j,k} = 1$ and $P_{j,k} = P_{k,j}$. We know the relative probability $\frac{\pi j}{\pi k}$ at equilibrium: $\exp\left(-\beta\left(H_j - H_k\right)\right)$. From this we build the elements of the transition matrix M.

Define $M_{j,k}$ by the rule:

$$M_{j,k} = \left\{ \begin{array}{ll} P_{j,k}\frac{\pi(k)}{\pi(j)} & \text{if } \frac{\pi(k)}{\pi(j)} < 1 \\ P_{j,k} & \text{if } \frac{\pi(k)}{\pi(j)} \geq 1 \end{array} \right\} \text{if } j \neq k \tag{5.25}$$

$$M_{j,j} = P_{j,j} + \sum_k{}' P_{j,k}(1 - \frac{\pi\left(k\right)}{\pi\left(j\right)}) \tag{5.26}$$

where $\sum_k'$ means a summation over all states k for which $\frac{\pi(k)}{\pi(j)} \geq 1$. As one last bit of notation let $\sum_k''$ represent the summation over all $k \neq j$ for which $\frac{\pi(k)}{\pi(j)} \geq 1$, which will let us conveniently find $M_{j,k}$:

$$\begin{aligned} \sum_j M_{j,k} &= P_{j,j} + \sum_k{}' P_{j,k}\left(1 - \frac{\pi\left(k\right)}{\pi\left(j\right)}\right) \\ &\quad + \sum_k{}' P_{j,k}\frac{\pi\left(k\right)}{\pi\left(j\right)} + \sum_k{}'' P_{j,k} && (5.27) \\ &= P_{j,j} + \sum_k{}' P_{j,k} + \sum_k{}'' P_{j,k} && (5.28) \\ &= P_{j,j} + \sum_{k\neq j} P_{j,k} && (5.29) \\ &= \sum_j P_{j,k} && (5.30) \\ &= 1 && (5.31) \end{aligned}$$

which means the matrix M is a regular matrix with nonzero terms as demanded. We have remaining only to show that equation (5.23) holds and the Markov chain Monte Carlo will be fully justified.

The assumption of detailed balance means the chance of observing a move from j to k is equal to the chance of observing the reverse: $\pi\left(j\right) M_{j,k} = \pi\left(k\right) M_{k,j}$. We claim this is satisfied by this matrix. Suppose for the states j and k, $\pi(j) = \pi(k)$. From equation (5.25) then

$$M_{j,k} = P_{j,k} = P_{k,j} = M_{k,j} \tag{5.32}$$

$$\pi(j) M_{j,k} = \pi(k) M_{k,j} \tag{5.33}$$

which satisfies the balance if $\pi(j) = \pi(k)$. If they are not equal, then — taking without loss of generality — suppose $\pi(k) < \pi(j)$. Then, again from (5.25) and our assumption that $P_{j,k} = P_{k,j}$ we have

$$M_{j,k} = P_{j,k} \frac{\pi(k)}{\pi(j)} = P_{k,j} \frac{\pi(k)}{\pi(j)} = M_{k,j} \frac{\pi(k)}{\pi(j)} \tag{5.34}$$

$$\pi(j) M_{j,k} = \pi(k) M_{k,j} \tag{5.35}$$

and a similar argument will hold if $\pi(j) < \pi(k)$. Finally,

$$\sum_j \pi(j) M_{j,k} = \sum_j \pi(k) M_{k,j} \tag{5.36}$$

$$= \pi(k) \sum_j M_{k,j} \tag{5.37}$$

$$= \pi(k) \times 1 \tag{5.38}$$

which is equation (5.23).

And this explains finally the method of the Metropolis-Hastings rule. From any microstate j some new microstate k is picked. We accept or reject that move, with probability $\frac{\pi(k)}{\pi(j)}$, which number[1] can be calculated knowing only microstates j and k. The resulting chain of states are distributed as the entire phase space is. Ensemble averages over a long enough chain will approximate averages over the whole of phase space [39].

We have the question of how long is a long enough chain. The expectation value of the difference between the ensemble average and the Markov chain average for N states is proportional to $\sqrt{\frac{1}{N}}$. What that proportion is depends on a constant called the correlation time, a measure of how many attempted changes have to be made before we have two independent states. Its value is not obvious before calculations are done, though. Worse, critical slowing down occurs: the correlation time grows longer if β is close to the inverse temperature of a phase transition. We will return to this phenomenon.

By tracking the expectation values of the quantity $f(i)$ and of the quantity $f^2(i)$ we can estimate the correlation time and from that the error

---

[1] Properly, the probability is $\min\left(1, \frac{\pi(k)}{\pi(j)}\right)$.

margin of any measurement. If $f(N)$ is the value of the measured quantity after N links and $f(N+t)$ is its value after t more links are created, then

$$\frac{\langle f(N+t)f(N)\rangle}{\langle f^2\rangle - \langle f\rangle^2} \sim \exp\left(-\frac{t}{\tau}\right) \tag{5.39}$$

with τ the correlation time. The estimate of the error in f after N links is

$$\Delta f \sim \sqrt{\langle f^2\rangle - \langle f\rangle^2}\sqrt{\frac{\tau}{N}} \tag{5.40}$$

[39] [81]. $\sqrt{\langle f^2\rangle - \langle f\rangle^2}$ is sometimes called the spread of f.

Often good practice is running several examples for as long a time as possible, with the energy (and other interesting properties) measured often, to examine their evolution. This provides some feel for the correlation time, and how long simulations need to be for fluctuations to grow sufficiently small.

5.7 Metropolis-Hastings Monte Carlo Algorithm

Throughout this book we will see Metropolis-Hastings Monte Carlo approaches used to approximate the equilibrium for a system at a particular temperature for both the barotropic flow model and for the Shallow-Water Model. In these cases we start with a set of some convenient number of mesh sites distributed approximately uniformly over the surface of the sphere. They are only approximately uniformly distributed, in part because we do wish to reduce the possibility of mesh artifacts. More critically, there is no general solution for how to uniformly distribute an arbitrary number of points on the surface of the sphere. There are solutions for some select numbers of points only. Conveniently, another Metropolis-Hastings Monte Carlo algorithm allows for the convenient generation of nearly uniform mesh sites on a closed domain: the mesh sites can be treated as the locations of uniform-strength point-particle vortices in the vortex gas problem [64].

With a mesh site provided for we initially assign site values arbitrarily, taking care only to satisfy whatever microcanonical constraints on our model should be. Most often this will be the circulation — the sum of mesh sites — being zero and the enstrophy — the sum of squares of mesh sites — being a convenient constant.

Starting from a particular initial state A we wish to vary site values to explore all possible configurations which preserve the circulation and relative enstrophy. In general, Monte Carlo algorithms change as few components as possible at once for the computational convenience this offers. The smallest changes which do anything more than swapping site values (site swaps of course preserve circulation and relative enstrophy, but are unsatisfying ways to explore all possible configurations) involve three mesh sites.

So from the mesh site A we will choose three distinct sites, and attempt to change the site strengths s_1, s_2, and s_3 to new values $s_1^{'}$, $s_2^{'}$, and $s_3^{'}$ by the formula:

$$s_1^{'} = s_1 - \delta - \epsilon \tag{5.41}$$

$$s_2^{'} = s_2 + \delta \tag{5.42}$$

$$s_3^{'} = s_3 + \epsilon \tag{5.43}$$

with the requirement that

$$\delta = \frac{(K+1) \cdot s_1 - s_2 - K \cdot s_3}{K^2 + K + 1} \tag{5.44}$$

$$\epsilon = K \cdot \delta \tag{5.45}$$

for a value of K chosen at random from $[-1, 1]$ [64].

With the site values changed we have a new configuration B. Whether to accept these changes, making the next state in the Markov Chain B, or to reject them, making the next state A, depends on the inverse temperature β and on the change in system energy $\Delta E \equiv E_B - E_A$.

Should $\beta \Delta E$ be less than zero (which is not equivalent to the change in energy being negative, since the temperature may also be negative) then the new configuration B is always accepted. Should $\beta \Delta E$ be greater than zero, then the new configuration B will be accepted with a probability $\exp(-\beta \Delta E)$. (We draw a random number r uniformly from $(0, 1)$, and accept the change if $r < \exp(-\beta \Delta E)$.) Otherwise, we take configuration A as the next state in the Markov Chain.

And we repeat these experiments and selections of mesh sites until an equilibrium is finally reached. These simulations are convenient and rapid ways to find equilibrium configurations for a given mesh over a wide selection of parameters.

Chapter 6

Phase Transitions of the Energy-Relative Enstrophy Theory for the Barotropic Vorticity Model on a Rotating Sphere

6.1 Introduction

In this chapter we set about finding phase transitions for the atmospheric flow by numerically simulating a version of Kac's spherical model, one which is microcanonically constrained in the total circulation and in the relative enstrophy of the fluid. But we also know about such models as that of Kraichnan [50], which for two-dimensional macroscopic flows are based on a Gibbs partition function canonical both in energy and in enstrophy. One can also examine a doubly canonical energy-enstrophy theory for barotropic flows, as per Frederiksen and Sawford [35], on a rotating sphere that is set to conserve both relative enstrophy and angular momentum separately. However, this canonical constraint on relative enstrophy and on angular momentum does not support phase transitions.

In this chapter's energy-relative enstrophy theory, we relax the constraint on angular momentum, and apply the relative enstrophy constraint microcanonically instead. This lets us see that treating the coupled barotropic fluid-massive rotating sphere system, and the relaxation of the angular momentum constraint, has significant physical consequences. In particular, we now find two phase transitions between disordered, or mixed, vorticity states and organized, or unmixed, flows in both super-rotating and sub-rotating patterns, with physically significant asymmetry between the two.

The equilibrium statistical mechanics of barotropic vorticity dynamics on a rotating sphere are formed on the basis of a canonical constraint in the total kinetic energy, a microcanonical constraint on the relative enstrophy, and the setting of the total circulation to zero. This microcanonical constraint on the relative enstrophy means we have a spherical model, as per Berlin and Kac's ferromagnetic models [8]. At small absolute values of the statistical temperature for the macroscopic flow the free energy of this model is closely approximated by the internal energy, which was studied by a variational approach in chapter 3.

The partition function for the energy-relative enstrophy spherical model is

$$Z_N = \int \left(\prod_{j=1}^{N} ds_j \right) \delta \left(N\Gamma_N - 4\pi \sum_{j=1}^{N} s_j^2 \right) \exp\left(-\beta H_N\right) \qquad (6.1)$$

where H_N is the spin-lattice Lagrangian, not the usual Hamiltonian in ferromagnetism, but the total kinetic energy of the Barotropic Vorticity Equations, where Γ_N is the relative enstrophy, where s_j is the vorticity for site j, N is the number of mesh sites distributed uniformly over the sphere, β is the inverse temperature, and δ is the Dirac delta function, all of which is in line with the spin-lattice model we have set up previously. Using the Lagrangian instead of the Barotropic Vorticity Equation's conserved Hamiltonian is a point of departure for the models in this book from previous statistical mechanics models of macroscopic atmosphere dynamics. However, it is not new, having been used in the context of a Feynman path-integral approach for the partition function. After all, the Lagrangian of the Barotropic Vorticity Equation is just the enthalpy discussed in chapter 5 on Markov Chain Monte Carlo simulations.

The Gibbs canonical-microcanonical probability for any particular configuration $\vec{s}$ is

$$P_G\left(\vec{s}\right) = \frac{1}{Z_N} \exp\left(-\beta H_N\left(\vec{s}\right)\right) \delta \left(N\Gamma_N - 4\pi \sum_{j=1}^{N} s_j^2 \right). \qquad (6.2)$$

6.2 Classical and Recent Energy-Enstrophy Theories

The Gibbs canonical ensemble and the corresponding partition function for the spherical model of energy-enstrophy theory for barotropic vorticity dynamics on a rotating sphere (which is discussed below and in chapter 9) are closely related to path integrals and they are difficult expressions to evaluate in closed form. The spin-lattice approximations allow us to obtain both analytic and numeric solutions.

To provide context and perspective for the Monte Carlo simulations in this chapter, the mean-field theories in chapters 7 and 8, and the exact solution of the energy-enstrophy theory by Kac's spherical model methods in chapter 9, it is worth taking time to review the main theories used to investigate the statistical relationships between energy, angular momentum and enstrophy in macroscopic flows. Both of these theories derive from Kac's inventions around 1952. The first is the Gaussian model, in which enstrophy is held as a canonical constraint, which forms the basis of all the classical energy-enstrophy theories. The second is the spherical model, in which enstrophy is a microcanonical constraint, versions of which are in the energy-enstrophy-circulation models Lim first introduced in 2000, and which is detailed in [64]. Several papers and conference proceedings have been devoted to the formulation, solutions and applications of these models to atmospheric problems; the interested reader will find them under Lim and co-authors in the references and online.

6.2.1 *Gaussian Model*

Most early papers on the Gaussian model use a spectral formulation, establishing a truncated set of orthonormal eigenfunctions on the flow domain. Many of the authors using this approach present results on the applications of this theory which cover a wide range of topics in geophysical flows, including two-layer flows over nontrivial bottom topographies, and quasi-geostrophic f-plane and β-plane flows. We will present a spatial lattice formulation instead.

The classical energy-enstrophy theory is identical to the well-known Gaussian model for ferromagnetism introduced by Berlin and Kac [8] and which is exactly solvable.

The classical energy-enstrophy theory, written using a spatial discretization, is given in terms of the truncated energy H_N(equation (2.18)) and the relative enstrophy Γ_N (equation (2.27)) by the Gaussian partition function

$$Z_N = \left(\frac{b}{2\pi}\right)^{\frac{N}{2}} \int \left[\prod_{j=1}^{N} ds_j\right] \exp\left(-b\sum_{j=1}^{N} s_j^2\right) \exp\left(-\beta H_n\left[S;\Omega\right]\right) \quad (6.3)$$

in terms of the spin (vorticity) state

$$S = \{s_1, s_2, s_3, \cdots, s_N\} \quad (6.4)$$

$$s_j \in (-\infty, \infty) \quad (6.5)$$

In this model, the standard deviation of the above Gaussian distribution is given in terms of the parameter

$$b = \frac{4\pi\mu}{N} \tag{6.6}$$

where μ is the chemical potential, or Lagrange multiplier, associated with the relative enstrophy constraint. The factor $\left(\frac{b}{N}\right)^{\frac{N}{2}}$ is needed in order to make

$$W[S] = \left(\frac{b}{2\pi}\right)^{\frac{N}{2}} \exp\left(-b\sum_{j=1}^{N} s_j^2\right) \tag{6.7}$$

a probability distribution.

The exact solution of this Gaussian model — where it is well-defined — is the base for much work on statistical equilibrium in geophysical flows (cf Salmon, Holloway, and Hendershott [86]; Frederiksen and Sawford [35]; and Carnevale and Frederiksen [12] among others).

The Gaussian model, however, does suffer from a low-temperature defect: it is not defined for certain temperatures. One approach which avoids this problem is the spherical model, which is well-defined for all temperatures, positive and negative.

6.2.2 *Spherical Model for Coupled Barotropic Flows*

The choice of a canonical constraint on the total kinetic energy $H[q]$ and a microcanonical constraint on the relative enstrophy Γ results in the spherical model formulation, which is difficult to solve analytically, but is quite amenable to numerical simulations and to mean-field methods.

The change of the canonical constraint on relative enstrophy to a microcanonical constraint yields a version of Kac's spherical model for the spin-lattice model. The spherical model formulation of an equilibrium statistical energy-enstrophy theory for the barotropic flows on a rotating sphere starts with the spin-lattice partition function

$$Z_N = \int \left(\prod_{j=1}^{N} ds_j\right) \delta\left(NQ_r - \sum_{j=1}^{N} s_j^2\right) \exp\left(-\beta H_N\right) \tag{6.8}$$

where H_N, $J_{j,k}$, and the external fields F_j are as given in equations (2.18), (2.20), and (2.25). Q_r is the desired value of the relative enstrophy, and δ is the Dirac delta function.

In the Laplace integral form the microcanonical enstrophy constraint can be written

$$Z_N = \frac{1}{4\pi\imath}\int\left(\prod_{j=1}^{n} ds_j\right) \cdot \int_{a-\imath\infty}^{a+\imath\infty} d\eta \left[\frac{1}{2}\eta N Q_r - \frac{1}{2}\left\langle S\left|K\right|S\right\rangle\right] \exp\left[\beta\sum_{j=1}^{N} F_j s_j\right] \tag{6.9}$$

in terms of the matrix

$$K_{j,k} \equiv \eta - \beta J_{j,k} \tag{6.10}$$

and the spin vector

$$S = \{s_1, s_2, s_3, \cdots, s_N\} \tag{6.11}$$

6.3 Monte Carlo Simulations of the Energy-Relative Enstrophy Model

We want here to perform numerical simulations to find relative equilibriums at different inverse temperatures. One tool which is quite useful and almost irresistible for this sort of problem — in which we have an enormous configuration space of possible site vorticity distributions $\vec{s}$ and a complicated function H_N which we want to extremize — is that of Markov Chain Monte Carlo simulation, based on the Metropolis-Hastings algorithm [64] [39] discussed in chapter 5.

The Monte Carlo simulation which provides the equilibriums we want will begin with a mesh of N points distributed uniformly over the surface of the sphere. Producing that mesh we will discuss shortly, after we describe what we do with it. We initialize the site values s_j for each mesh site $\vec{x}_j$ by assigning to the sites a randomly assigned value, with the assignments adjusted so as to satisfy the circulation constraint (this is easily done by finding the mean of the initial set and then subtracting this mean from all the sites s_j), and then to satisfy the enstrophy constraint (this is easily done by taking the sum of squares of the adjusted site values, and finding the constant by which they must all be multiplied so as to set the proper enstrophy).

Now that we have a distribution of site vorticities which satisfies the circulation and the enstrophy constraints we begin a set of many, many experiments in altering them. From the existing configuration, we attempt changing several of the site vorticities — in practice, this is conveniently done by changing three at a time, which allows for the conservation of circulation and enstrophy without restricting us to simply permuting site vorticity assignments — and allowing these experimental changes to be accepted or rejected on the basis of the Metropolis-Hastings rule. That is, we accept changes which reduce the value of $-\beta H_N$, and accept changes which increase $-\beta H_N$ only if another randomly selected number r drawn uniformly from the range $(0, 1)$, is less than $\exp(-\beta \Delta H_N)$.

These Monte Carlo simulations are a convenient and rapid way to find statistical equilibriums for the lattice system over a wide range of values for the inverse temperature β, for the relative enstrophy Γ_N, and for the planetary rotation Ω.

There are a variety of diagnostic tools which allow us to find evidence of phase transitions from these Monte Carlo simulations. One useful tool is to find a set of spherical harmonic amplitudes which interpolate the mesh site vorticities we derive. This will let us support the claim that states are super-rotating and sub-rotating flows with more or with less (respectively) angular momentum than the same fluid shell rotating at the planetary spin rate.

It was mentioned that we need a mesh site of N points uniformly distributed on the surface of the sphere. In general of course we do not know of a uniform distribution or a most-nearly-uniform distribution, but conveniently, a preliminary round of Markov chain Monte Carlo simulation lets us find a good distribution.

In this mesh-generating round we use the vortex gas problem: we scatter a set of N points $\vec{x}_j$ on the surface of the sphere with no regard for anything other than that we wish no points to overlap. Treat each of these points as a vortex with uniform strength 1; there is therefore an energy which we can evaluate as

$$H_M = \frac{1}{4\pi} \sum_{j=1}^{N} \sum_{k \neq j}^{N} \log |1 - \vec{x}_j \cdot \vec{x}_k| \tag{6.12}$$

although in practice we do not care about the scale of the energy, merely its size.

This vortex gas problem is unrelated to the atmospheric flows in which we are actually interested (which is something obvious in considering that the total circulation of this problem is N rather than zero).

For in this mesh-generating Monte Carlo step we will not vary vortex strength but rather vortex position: we pick a site at random, and move it a bit. With a positive statistical mechanics temperature β_M, then, we find whether we have decreased the value of $-\beta_M H_M$ — in which case we accept the move of this one vortex position — or else we see whether a number drawn at random and uniformly from $(0, 1)$ is less than $\exp(-\beta_M \Delta H_M)$. If it is, we accept the move; if it is not, we reject the move.

By repeating this experiment with any positive β_M we find the collection of mesh sites to spread out over the surface of the sphere. With a larger M the spreading to a uniform distribution is faster, requiring fewer experiments, and the uniformity appears to be slightly better. In any case we get for any desired mesh size N a reasonably uniformly distributed mesh.

(A negative β_M is of no obvious practical use here as it produces a clustering of mesh sites around a few points.)

Note that the mesh-generating inverse temperature β_M has absolutely no connection to the inverse temperature β for our simulations. β_M is simply a convenient tool in the event one has not already got a mesh to use, and it is discarded once one begins the process of generating a statistical equilibrium. Indeed, although the simulations discussed here do not use it, further applications of the mesh-generation or particle Monte Carlo moves, alternating with the lattice Monte Carlo moves, will be the basis of a spin-glass lattice model for the Barotropic Vorticity Equation on a rotating sphere. This is in the realm of current and future cutting-edge methods for Monte Carlo simulations that could possibly speed up the traditional Metropolis-Hastings algorithm and avoid the classic critical slowdown.

Super-rotation

When do we expect to see super-rotation, or any organized states? We can start by considering the spin-lattice Lagrangian or total kinetic energy of the Barotropic Vorticity Equation,

$$\begin{aligned} H_N\left[q\right] = -\frac{8\pi^2}{N^2} \sum_{j=1}^{N} \sum_{k=1}^{N} \log\left|1 - \vec{x}_j \cdot \vec{x}_k\right| s_j s_k \\ + \frac{2\pi\Omega}{N} \sum_{j=1}^{N} \cos\left(\theta_j\right) s_j \end{aligned} \tag{6.13}$$

The first term of equation (6.13) suggests that vortices surrounded by vortices of the same sign will have a higher energy than vortices surrounded by vortices of the opposite sign. The second term suggests that sites near the north pole should have the most positive values in order to maximize the energy, while sites near the south pole will maximize energy when they are the most negative. This suggests what we already suspected from the mean-field theories, that negative temperatures should see these unmixed or highly organized states, while they will be unlikely in positive temperatures. More, to maximize the energy, this solid-body rotation should be super-rotating, that is, going in the direction of the planet's rotation.

In Monte Carlo simulations we find the most probable vorticity distributions generated do indeed have the form, as in Figure 6.10, suggested by this heuristic argument. The unmixed is a high energy state, and the form of these macrostates are close to those of the unique global energy maximizer [55]. The most probable state for negative β is, as pictured in the example of Figure 6.10, one with super-rotating solid-body flow.

We have mentioned the use of spectral analysis to determine in what state a system is. For these solid-body rotations we expect that there should be a considerable energy within the ground state modes, the various $\psi_{1,m}$ components. So, let us calculate the spherical harmonic components $\alpha_{l,m}$ for a field which interpolates these mesh points, which we can do thanks to the harmonics $\psi_{l,m}$ themselves forming an orthonormal basis set for the space of square-integrable functions defined on the unit sphere:

$$\alpha_{l,m} = \left\langle \omega\left(x\right), \psi_{l,m}\left(x\right)\right\rangle \tag{6.14}$$

$$= \frac{4\pi}{N}\sum_{j=1}^{N} \omega\left(\vec{x}_j\right)\psi_{l,m}\left(\vec{x}_j\right) \tag{6.15}$$

The components for one typical equilibrium are plotted in Figure 6.10b. What we see is that in the super-rotating flow the spherical harmonic with the largest amplitude is the one corresponding to the $\psi_{1,0}$ state. In fact its amplitude approaches $\sqrt{\Gamma_N}$, the square root of the relative enstrophy and thus nearly the entire enstrophy of the equilibrium. And this is as we projected: solid-body rotation is one of the $l = 1$ modes, and the super-rotating state is one with $m = 0$.

Sub-Rotation

What about sub-rotation, that is, the case when most of the energy of the system will be found in a solid-body state, and yet the direction of the solid-body rotation is opposite that of the planet? Solid-body rotation is a high energy state, but the sub-rotation mode is of lower energy than super-rotation would be. This implies that we should look in high energy states that fall short of the highest possible energies, and that we will probably want to look where the planetary rotation is fast so that there is a significant difference between super-rotation and sub-rotation energies.

When the inverse temperature β is large and positive, while the relative enstrophy Γ_N is less than $\Omega^2 C^2$, the numerically generated relative vorticity distribution is one as in Figure 6.11. As a specific example plotted there is the selection of $\beta = 2$, $\Omega = 60$, and $\Gamma_N = 128$, so that $\Gamma_N < \Omega^2 C^2$. This combination produces the statistical equilibrium state of the figure.

The macrostate is largely a counter-rotating flow. We see it associated with a nonlinearly stable state that achieves a local minimum energy. In the variational theory discussed in chapter 3, we see $w^0_{min}\left(\Gamma_N\right) = -\sqrt{\Gamma_N}\psi_{1,0}$ for this state [55]. The largest component of the sub-rotating relative vorticity is, again, the harmonic $\psi_{1,0}$ — it is a spherical harmonic — but the amplitude is negative — it rotates opposite the planetary spin.

Phase transitions

So we have seen different modes predominating at different inverse temperatures. Naturally the expectation is that we might find phase transitions, and that these transitions may depend on properties such as the planetary rotation and the relative enstrophy. We look ahead to chapters 7 and 8 where two versions of mean-field analyses will be discussed on variants of the energy-enstrophy theory for the Barotropic Vorticity Equation, to provide points of comparison with the Monte Carlo simulations results here and also to provide enough pedagogical details of the important class of mean-field methods. The mean-field analyses in these chapters suggested there exist phase transitions to sub-rotation, allowed only when planetary rotation is large enough, and which provides logical grounds to search for the same consequence numerically.

And in fact simulations on a wide range of these parameters suggest that there are two phase transitions. One of them is at a negative critical temperature regardless of the planetary rotation. The other is in a positive temperature but only when the planetary rotation is large enough, where "large enough" itself depends on the relative enstrophy.

We can show this numerically by trying a planetary rotation set at $\Omega = 60$ and relative enstrophy $\Gamma_N = 128$. With the number of lattice sites $N = 512$ equal to that used in finding super-rotation and sub-rotation we can experiment with various β values and seek phase transitions.

Figure 6.12 shows examples of equilibrium states with $\beta = -0.01$ and with $\beta = 0.02$. The energies in these cases do not settle, and in fact fluctuate

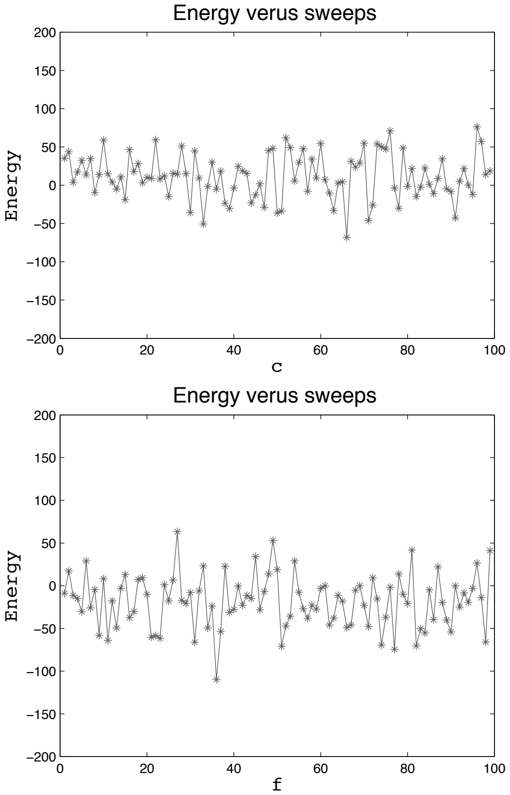

Fig. 6.1 The energy of the distributions producing most probable states when $\beta = -0.01$ and $\beta = 0.02$ for 512 mesh points on a Monte Carlo run of $10,000$ sweeps.

wildly during simulation runs. Comparing these energy results with those of Figures 6.10 and 6.11 suggest the state of the equilibrium changes, for these parameters, between $\beta = -0.01$ and $\beta = -2$ and between $\beta = 0.02$ and $\beta = 2$.

So here we invoke a tool [64] useful in identifying possible phase transitions. As suggested by examining equation (6.13) an important property of the energy is likely to be whether sites are more likely to be surrounded by sites of the same or of the opposite sign. We saw this in the Bragg-Williams approximations as the order parameter within a domain; here, though, we have not introduced any domains or partitioning of the sphere and we are not going to start.

N	128	256	512	1024
C^{+}	0.42	0.34	0.26	0.20
C^{-}	0.84	0.82	0.75	0.60
β_c^{+}	0.15	0.22	0.35	0.45
$\frac{\beta_c^{+}}{N}$	0.0012	0.00086	0.00068	0.00044
β_c^{-}	-0.07	-0.13	-0.18	-0.35
$\frac{\beta_c^{-}}{N}$	-0.00055	-0.00051	-0.00035	-0.00034

What we do instead is to construct a new descriptive variable which corresponds to the likeliness of neighboring sites sharing the same orientation. Start by defining the parity of any pair of sites to be the product of the signs of the vorticities of the sites: that is, it will be $+1$ if both sites are positive or both negative; it will be -1 if one site is positive and the other negative; it will be 0 if at least one site has zero vorticity.

For each site j there is some site k nearer to it than any other site is. The nearest-neighbor parity is the parity of site j with its nearest neighbor k.

Let the mean nearest-neighbor parity be the arithmetic mean of the nearest-neighbor parities for all nearest-neighbor pairs.

This simple-to-calculate property provides an excellent measure of the structure of site vorticities. When site vorticities are strongly organized, the magnitude of the mean nearest-neighbor parity is close to 1. When the sites are mixed, the parity is close to 0. Now we can search for evidence suggesting phase transitions as the temperature changes.

Figure 6.2 shows one experiment, in which we fix the relative enstrophy Γ_N and the planetary rotation Ω, but allow the mesh size N to vary. For this we see the mean nearest neighbor parity drop to zero both in negative and positive inverse temperatures. This leads us to suspect two phase transitions, with one in both the positive and the negative temperature domains.

If we allow that the mean nearest neighbor parity at a given temperature (and fixed other parameters) is a measure of the phase, then we can plot the dependence of this measure as a function of temperature, $m(\beta)$. Rapid changes in the mean nearest neighbor parity as β changes are then suggestive of phase transitions.

So, let us take the mean nearest neighbor parity at various temperatures, and attempt to interpolate a curve through these points. Since we expect

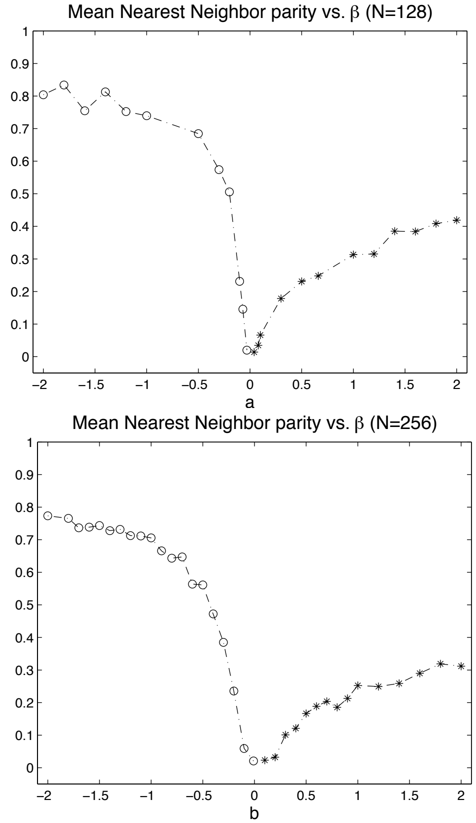

Fig. 6.2 These plots are of the mean nearest neighbor parity, used as a measure of organization, versus the inverse temperature β for different mesh sizes on a range from $\beta = -2 \cdots 2$ with relative enstrophy fixed to $Q_{rel} = 128$ and planetary rotation $\Omega = 60$.

a phase transition we will assume the function $m(\beta)$ will have the form

$$m(\beta) = C^{\pm}\left(1 - \left(\frac{\beta_c^{\pm}}{\beta}\right)\right)^{\alpha} \tag{6.16}$$

where part of the interpolation will be determining the constants $C^{\pm}$. Table 6.1 contains examples of estimated values for these curves for a variety of mesh sizes.

In all these cases we find that $\alpha = 1$ fits well as an exponent, as seen in Figure 6.4. This fit suggests that the mean-field theory should be exact for this sort of problem [94] [73].

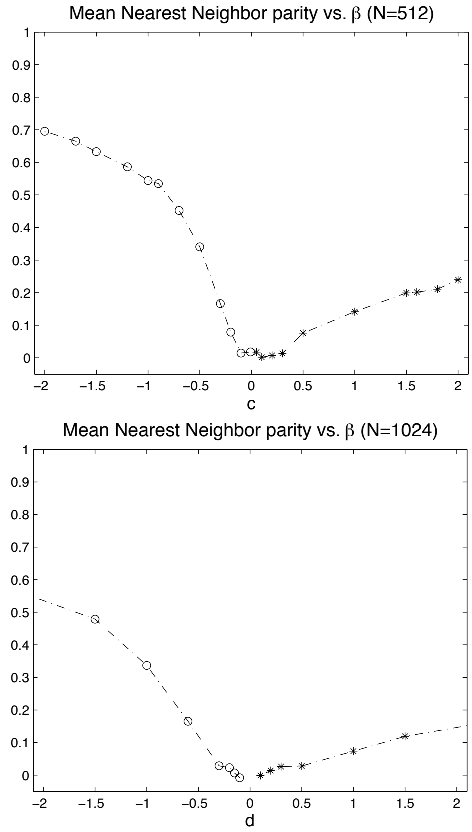

Fig. 6.3 These plots are of the mean nearest neighbor parity, used as a measure of organization, versus the inverse temperature β for different mesh sizes on a range from $\beta = -2 \cdots 2$ with relative enstrophy fixed to $Q_{rel} = 128$ and planetary rotation $\Omega = 60$.

But we have another and a more classically familiar parameter to indicate phase transitions, and that is the specific heat. While there is no specific heat in the molecular sense relevant to our problems any more than there is a molecular-sense temperature, the statistical mechanics definition of temperature obviously applies, and it is from that which we draw the specific heat. The specific heat can be estimated by a numerical differentiation of the internal energy with respect to the temperature:

$$C_v \left(\frac{k_B T_{n+1} - k_B T_n}{2} \right) = \frac{U\left(k_B T_{n+1}\right) - U\left(k_B T_n\right)}{k_B T_{n+1} - k_B T_n} \tag{6.17}$$

where $U\left(k_B T_n\right)$ is the internal energy at the temperature $k_B T_n$.

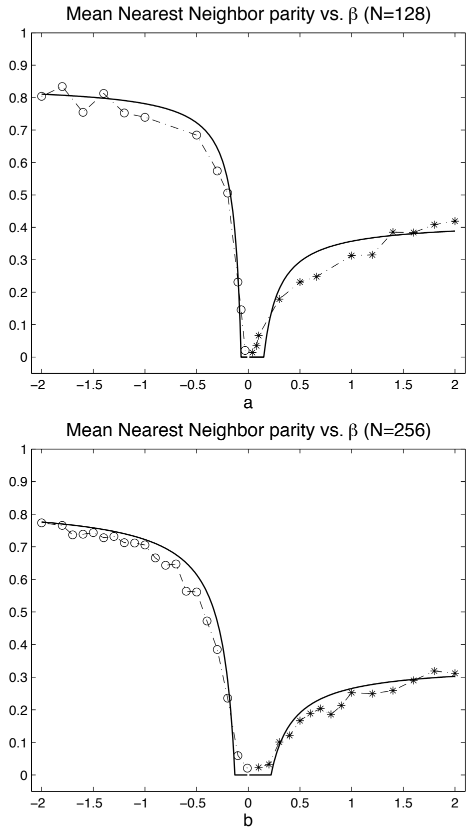

Fig. 6.4 The mean nearest neighbor parity versus inverse temperature along with the fitting curves for different mesh sizes N.

Figure 6.6 shows the internal energy and the specific heat as functions of temperature for the cases where $N = 512$ and where $N = 1024$. The dashed lines of Figures 6.6b and 6.6d show there appear to be discontinuities in the first derivative of specific heat with respect to temperature. This corresponds to two phase transitions, as expected from above one at positive and one at negative temperatures. These results, as in Table 6.2, agree very well with the inverse critical temperatures $\beta_c^{\pm}$ shown in Table 6.1.

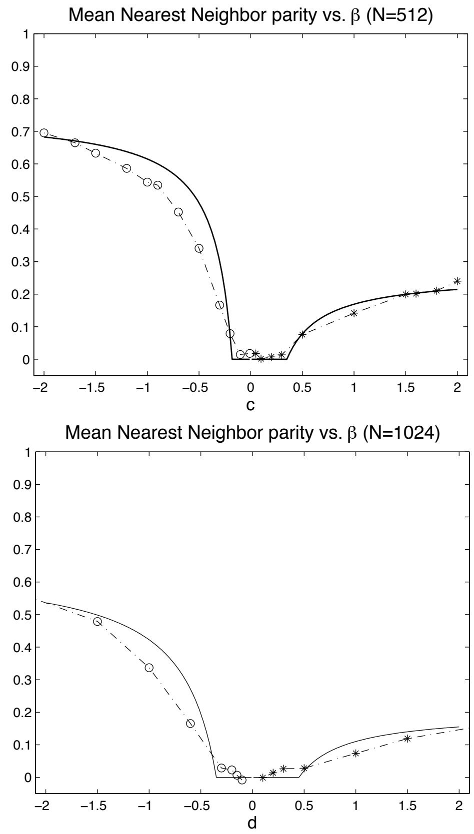

Fig. 6.5 The mean nearest neighbor parity versus inverse temperature along with the fitting curves for different mesh sizes N.

N	512	1024
$k_BT_c^+$	2.8	2.2
$k_BT_c^-$	-5.7	-2.8

6.4 Free Energy

The Monte Carlo method is an algorithm quite capable of the numerical estimation of any quantity writable as the average of a state function. Estimating the entropy is more difficult: there is no state function whose

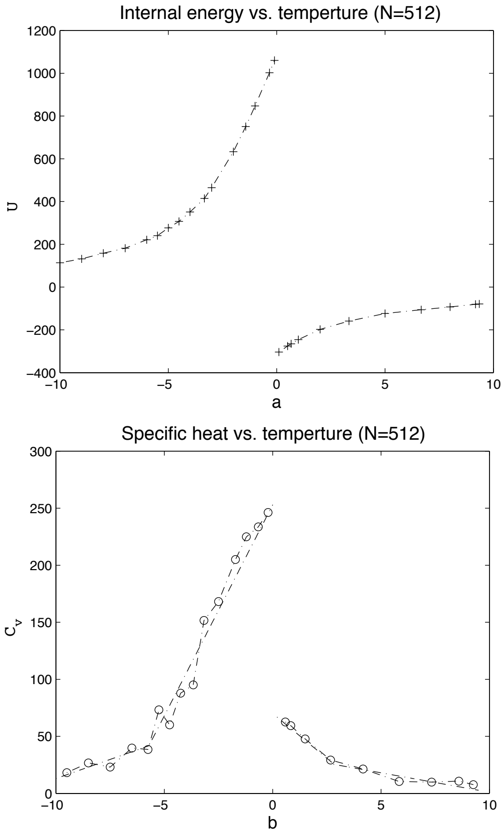

Fig. 6.6 The internal energy U and the specific heat C_v plotted against temperature $k_B T$ for a mesh of 512 points.

average is the entropy. A similar problem therefore extends to the free energy, much as we would like to calculate that. We overcome this by introducing a method which estimates the entropy of the spin-lattice system by a Monte Carlo simulation.

Consider the probability distribution of states, where the probability of occurrence of a configuration with energy E is proportional to $\exp(-\beta E)$. As per the normal Metropolis-Hastings Monte Carlo procedure, the probability of moving from state A, with energy E_A, to state B, with energy E_B, is defined as $\exp(-\beta(E_B - E_A))$.

But when we set $\beta = 0$ the probability of moving from state A to

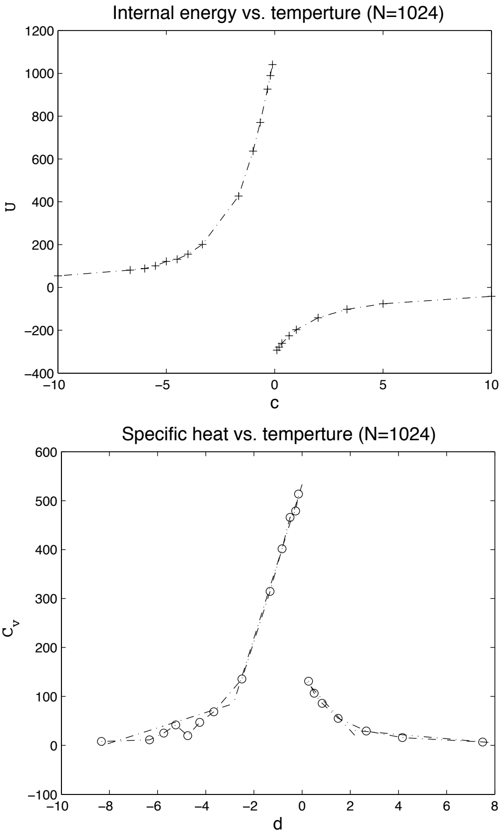

Fig. 6.7 The internal energy U and the specific heat C_v plotted against temperature k_BT for a mesh of 1,024 points.

state B is equal to 1 regardless of the magnitude or sign of the change in energy $(E_B - E_A)$. All new states will be invariably accepted. So this simulates the system with the same probability for all states. And therefore after enough sweeps this $\beta = 0$ Monte Carlo simulation is a random walk through all regions of the system's energy space.

Now consider indexing the different states of the system by their energy. We divide the range of energy into 20 levels between the lowest and the highest possible values, and count how many of the possible configurations fit into each band. (There is nothing particularly special about 20; it is simply a convenient number of bands with which to work. The reasoning applies to any number of such bands.) The entropy $S(E)$ is proportional to the logarithm of the degeneracy of the energy macrostate, as per Boltzmann's entropy equation:

$$S(E) = k_B \log(W) \tag{6.18}$$

where W is the degeneracy of a given macrostate, or, as we have set it up, a given band of energy.

In Figure 6.8 we see the degeneracy and entropy (taking for convenience $k_B = 1$), which both decline as the energy approaches the maximum. This confirms numerically the existence of negative temperature states: these are the domains where the derivative of entropy with respect to energy is negative.

Figure 6.9 shows Helmholtz's free energy formula $F = U - TS$ and this entropy estimation method used to yield an estimate to the free energy. We have seen in Monte Carlo simulations a super-rotating most-probable state with extremely high energy and low entropy. We have also seen a projection of a sub-rotating most-probable state with very low energy and low entropy when the relative enstrophy is small in comparison to the planetary rotation. This suggests the maximal kinetic energy steady-state from two zero-temperature variational theory [55] should be related to the most-probable flow state predicted by Monte Carlo simulation at hot enough negative temperatures.

Similarly the minimal kinetic energy steady-states from that theory are related to the most-probable flow state at low positive temperatures. At temperatures with sufficiently small absolute values and provided the entropy-energy reltionship in this problem is as depicted in Figure 6.9 this correspondence between the variational theory and the statistical equilibrium theory follows directly from the form of the Helmholtz free energy $F = U - TS \simeq U$.

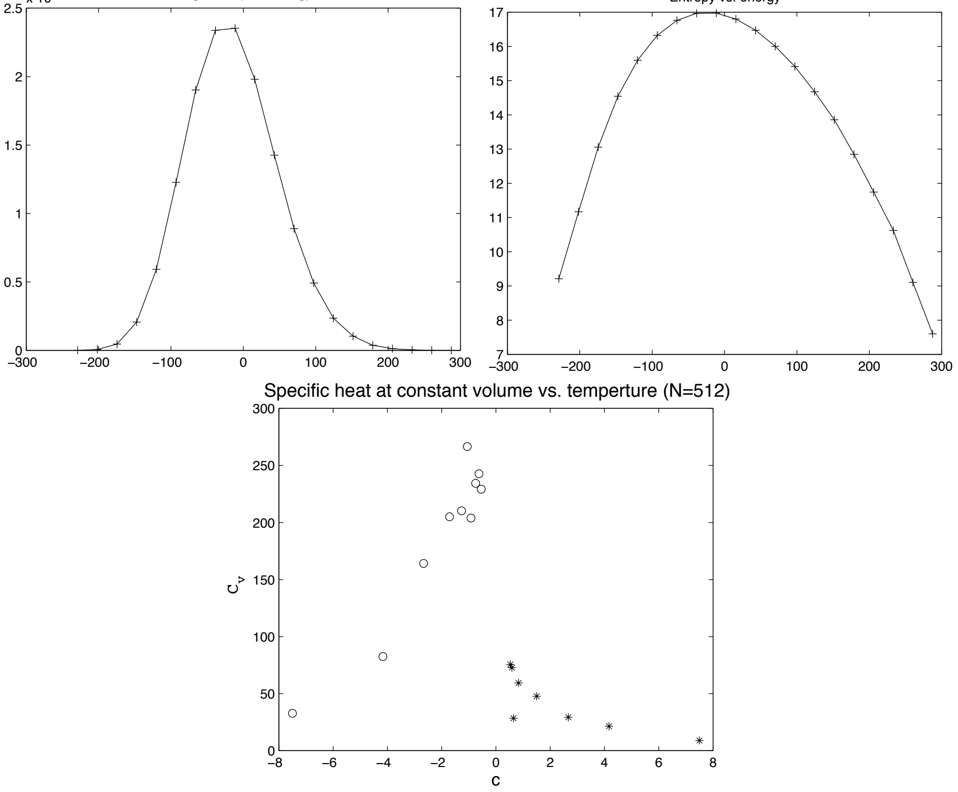

Fig. 6.8 The numerically estimated degeneracy, the plot of entropy versus energy, and the specific heat at constant volume, which serves as confirmation of the existence of negative temperatures.

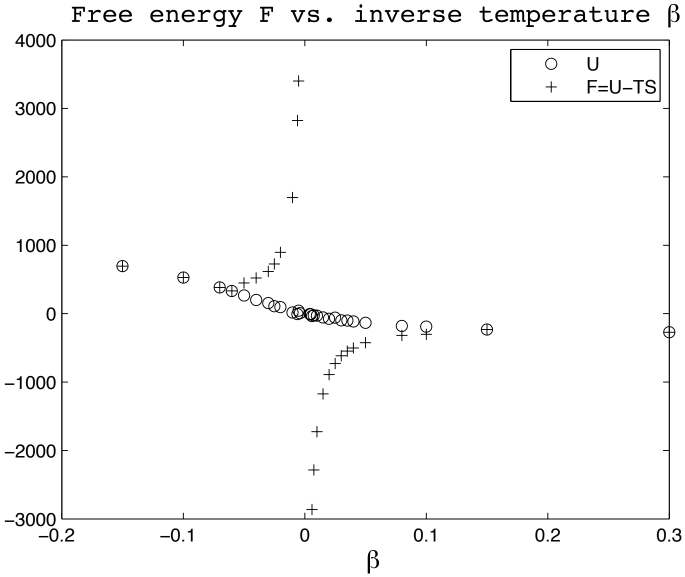

Fig. 6.9 The free energy F and the internal energy U plotted against the inverse temperature.

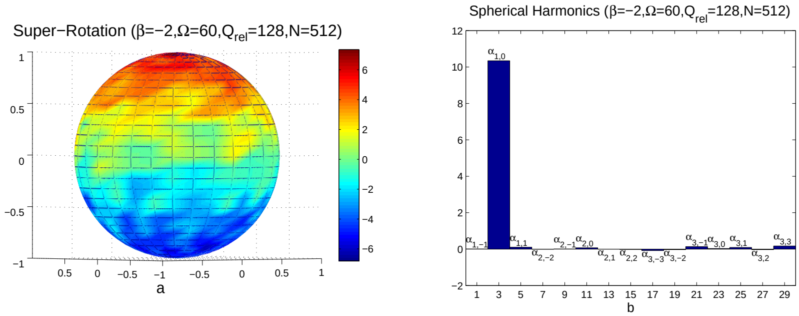
Super−Rotation (β=−2,Ω=60,Q_{rel}=128,N=512)

Spherical Harmonics (β=−2,Ω=60,Q_{rel}=128,N=512)

Fig. 6.10 Negative β — a super-rotating state. In this example there are 512 points, the inverse temperature $\beta = -2$, and the Monte Carlo simulation is run for $10,000$ sweeps.

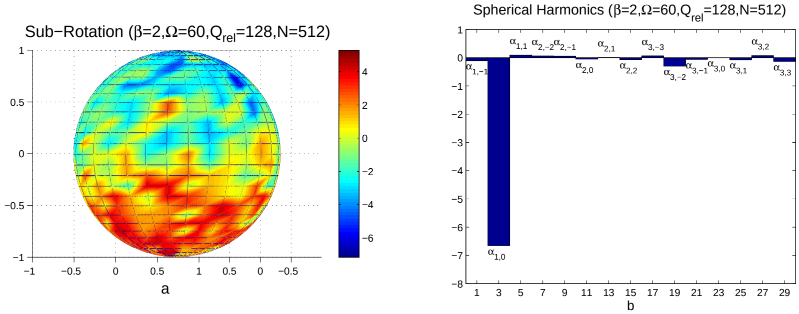
Sub−Rotation (β=2,Ω=60,Q_{rel}=128,N=512)

Spherical Harmonics (β=2,Ω=60,Q_{rel}=128,N=512)

Fig. 6.11 Positive β — a sub-rotating state. In this example there are 512 points, the inverse temperature $\beta = 2$, and the Monte Carlo simulation is run for $10,000$ sweeps.

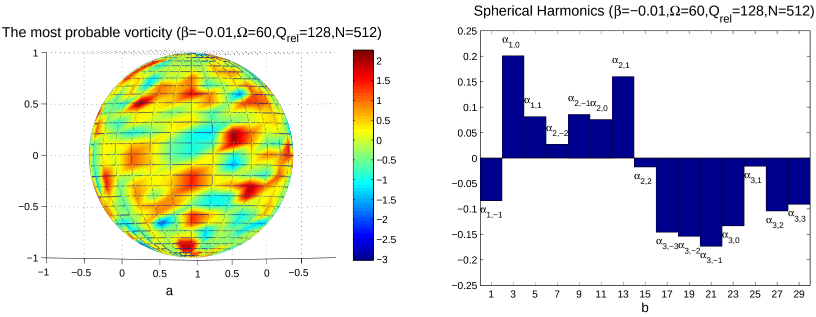

Fig. 6.12 The most probable vorticity distribution, in vorticity and spherical harmonics, for $\beta = -0.01$, with 512 mesh points, on a Monte Carlo run of $10,000$ sweeps.

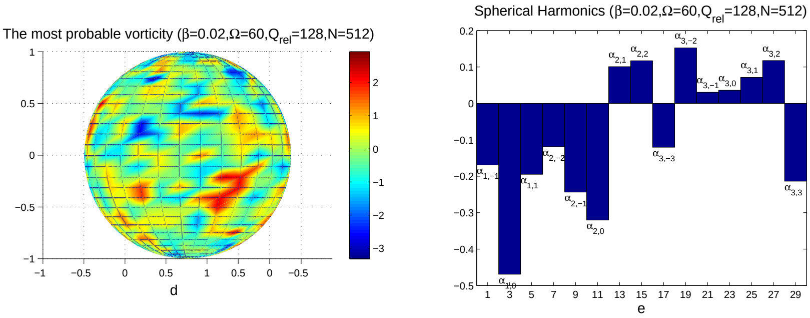

Fig. 6.13 The most probable vorticity distribution, in vorticity and spherical harmonics, for $\beta = 0.02$, with 512 mesh points, on a Monte Carlo run of $10,000$ sweeps.

Chapter 7

Extremal Free Energy in the Mean-Field Theory

7.1 Introduction

In this chapter we again look at the system of a rotating, high-mass planet, a sphere of radius R, around which is a thin atmosphere of a free barotropic fluid. The atmosphere is again inviscid, apart from its ability to exchange angular momentum and energy with the planet. And again we will look at the relative vorticity of the atmosphere. We present a mean-field approach this time where one possible viewpoint is to model the coarse-grained relative vorticity as a distribution or count of point vortices with fixed strengths in fixed mesh cells. The detailed pairwise particle interactions are subsumed under a coarse-grained or renormalized cell-to-cell interaction in a mean-field theory, from which we can study the phase transitions of the fluid with respect to a few key parameters.

Of particular interest is that we will be able to characterize two particularly special macrostates in the atmosphere, a disordered vorticity state and then highly ordered state representing a rigidly rotating atmosphere, and that by examining the difference in the Gibbs free energy between these states we will become able to find critical temperatures.

Ultimately, in chapter 9, we like to study a spherical model in which the relative enstrophy of the atmosphere is fixed to a constant, but this is a difficult problem to solve in closed form, and best postponed until we have gained some analytical experience using mean-field methods. Thus we take alternatives: the simple mean-field theory approach used here, for example, in which we conserve an averaged relative enstrophy. A second alternative discussed in chapter 6 was what motivated and generated current interest in these new energy-enstrophy models of the senior author: the problem is quite amenable to being modeled in a Monte Carlo simulation of the spherical model, with the relative enstrophy a microcanonical constraint of the simulation. A third approach, the Bragg mean field model, which is based on an intermediate mean-field method, will be examined in chapter 8. In that we get a renormalized expression for the free energy in terms of the coarse-grained barotropic non-divergent vorticity and do not use a relative enstrophy constraint. This approximate expression for the free energy produces values for both the positive and the negative critical temperatures that are consistent with this chapter's mean-field methods, and are also consistent with the Monte Carlo simulations in chapter 6 and as expected, will be found to be in total agreement with the closed-form solutions given in chapter 9.

For the statistical mechanics studied here it will be convenient, like before, to have a temperature and an entropy; we need to have some idea of what they are as there are no molecules and little resembling the kinetic theory of gases present. But the statistical definition of temperature for macroscopic flows has been well-established and is widely recognized. The macroscopic flow temperature is a measure, not of the average kinetic energy of molecular motion, but of the average kinetic energy contained in eddies of vorticity which potentially vary over a wide range of length scales. Given a macroscopic flow state or a macrostate vorticity distribution we have a suitable flow temperature which depends on the average energy of the eddies in that flow. So we have energy reservoirs instead of heat baths, and we will see transfers of energy and angular momentum at complex boundaries producing changes in the kinetic energy and angular momentums of the large, organized, eddies and changes in the kinetic energy and entropy of the smaller eddies.

7.2 Equilibrium Statistical Mechanics

Since we are making a lattice representation of the relative enstrophy, and are using a mean-field theory with the intention of finding most probable states at different temperatures — and we make the assumption the entire atmosphere has finite energy and will enjoy the same statistical-mechanics temperature — we know to expect the existence of negative statistical-mechanics temperatures and therefore will need the extended Planck's Theorem as outlined in section 4.6.

There is a precise correspondence between the statistical equilibrium properties of barotropic flows and the dynamical properties of barotropic flows. We can describe this correspondence by using the Minimum Enstrophy Principle — or its equivalent, the Extremal Kinetic Energy Principle — which form a pair of dual variational principles for the steady-states of barotropic flows.

What is the maximal-kinetic energy steady-state of a barotropic flow? What is the minimal-kinetic energy steady-state? Can we see either in the statistical mechanics models?

Consider the Helmholtz free energy, $F = U - TS$, at a temperature which is sufficiently close to zero. Then $F \simeq U$ regardless of the sign of T. In this case, then, the maximal-kinetic energy steady-state corresponds to the most probable flow at the hottest negative temperatures, the maximizing of both U and F, while the minimal-kinetic energy steady-state is the most probable flow at the coldest positive temperatures.

The Gibbs canonical ensemble consists, in general, of the standard form for this probability measure:

$$P_G\left(w\right) = \frac{1}{Z\left[\beta, \mu\right]} \exp\left(-\beta H\left[w\right] - \mu \Gamma\left[w\right]\right) \tag{7.1}$$

where $H\left[w\right]$ is the energy and β is an inverse temperature; and $\Gamma\left[w\right]$ is a quantity we wish to conserve and μ is a chemical potential, or Lagrange multiplier, conjugate to $\Gamma\left[w\right]$. The partition function, or configurational integral, $Z\left[\beta, \mu\right]$ provides the normalization required so that $P_G\left(w\right)$ will be a probability measure.

Customarily, we include only the key conserved quantities as the canonical constraints $\Gamma\left[\mu\right]$. In the case of quasi-two-dimensional turbulence we have an infinity of conserved quantities to select. All of the higher-order moments of the relative vorticity $\int dx\, w^n$ for integer n are conserved. But we do not need to include all of them as canonical constraints in the Gibbs probability P_G. In practice we will be interested only in conserving the circulation and the enstrophy. Analytically this is enough to provide a model that is tractable and still resembles what we believe the physical properties being modelled require; numerically, this allows us to use tools such as Monte Carlo simulation to find equilibriums that do not make too complicated the constraints we need to put on site vorticity alterations.

7.3 Mean-Field Theory

It is hard to solve the spherical model for the energy-enstrophy theory of rotating barotropic flows, so we postpone that until chapter 9. We will first attempt to use a mean-field method to find thermal properties for the spin-lattice model:

$$H_N = -\frac{1}{2}\sum_{j=1}^{N}\sum_{k=1}^{N} J_{j,k} s_j s_k - \sum_{j=1}^{N} F_j s_j \tag{7.2}$$

This will give us physically significant phase transitions for the energy-relative enstrophy theory of coupled barotropic flows on the rotating sphere. The major step in this mean-field theory is to calculate the change in the free energy per site between the two fundamentally different vorticity states, which are straightforward to characterize and which can be distinguished by their distributions.

The first state is the mixed macrostate: in this, the vorticities are arranged so that a site has equal probability of having positive or negative sign regardless of its location. It is unlikely to see many large-scale structures — regions of uniform vorticity sign, for example — and the vorticity distribution would look mixed or even chaotic to the eye. The second state is the unmixed macrostate, in which the coarse-grained vorticity is arranged so that the opposite signs are separated into hemispheres — so that a site has either probability 0 or probability 1 of being negative — or positive — entirely dependent of which hemisphere it is in. This is highly organized and we may consider whole hemispheres — the whole domain, in fact — to be one large-scale structure.

We will make some simplifications for the convenience of computation. Assume the coarse-grained site vorticity $s(x_j)$ for each mesh site x_j will be one of the pair $\{s_0, -s_0\}$ for an appropriate s_0. We also will suppose that for every mesh site there are z other sites in its neighborhood. The neighborhood is the set of sites which have direct influence on the simplified mean spin value.

For the energy-enstrophy spin-lattice model the actual neighborhood $N(j)$ of mesh site x_j is all the other sites in the mesh. Obviously the entire globe interacts with each site x_j, as we see in the energy function H_N. But there is still a short-range interaction: the integral of interactions over all sites is finite. The consequence to this is that the mean-field properties will not depend on z. This simplification of introducing a neighborhood does not have an important loss of accuracy or precision in the results which follow.

Simplifying the mean spin values so they are exactly $\pm s_0$ appears to be a more serious restriction, as it makes our problem more clearly an Ising-type model. However, the binary spin models developed from this can be shown

— by a single step of spatial renormalization or by block spin averaging — to produce a mean-field theory equivalent to the original.

7.3.1 *Setting Up Coupled Barotropic Flows*

We have these relationships which are satisfied by the coarse-grained spin or vorticity $s(x)$:

$$\Gamma = \int_{S^2} dx\, s^2(x) = Q \tag{7.3}$$

$$0 = \int_{S^2} dx\, s(x) = TC \tag{7.4}$$

For the mean-field theory we will assume the existence of a site-dependent **volume fraction** or **probability distribution function**, $\nu_x(s)$ with the properties that

$$\int_{-M}^{M} ds\, \nu_x(s) = 1 \tag{7.5}$$

where M denotes the limiting values of the coarse-grained spin $s(x)$ over S^2, and where

$$\int_{S^2} dx \int_{-M}^{M} ds\, \nu_x(s)\, s^2 = Q \tag{7.6}$$

$$\int_{S^2} dx \int_{-M}^{M} ds\, \nu_x(s)\, s = 0 \tag{7.7}$$

Next, we will set a convenient notation for the mixed state and for the unmixed field states, as we will need to compare various properties of the two. Let m denote for the mixed state where the mean spins $s_0(x)$ are independent of their neighbors; and n denote the unmixed state where the mean spins $s_0(x)$ are dependent and, in fact, are equal for an entire hemisphere. Therefore we will write, for example, S_m to describe the entropy of the mixed state, and S_n for the entropy of the unmixed state, and these subscripts will carry across to all the quantities describing a flow which we examine. We will also use a notation like $v = m$ to mean describing the mixed state and $v = n$ the unmixed.

Another useful bit of notation will be to describe the subsets of mesh sites. Let x^+ represent all the lattice sites which are in the positive hemisphere of the unmixed state n, and let x^- represent all the lattice sites which are in the negative hemisphere of the unmixed state. We do not make the assumption that these hemispheres correspond to any particular latitudes: it will be interesting to see if these unmixed hemispheres will or will not line up with the rotation of the planet.

These two states we can characterize the probability distribution functions ν by, for the mixed state m,

$$\nu_x^m\left(\pm s_0\right) = \frac{1}{2} \text{ for all } x \in S^2 \tag{7.8}$$

(which is to say that positive and negative vorticities are equally likely everywhere on the sphere), and for the unmixed state n,

$$\nu_{x^+}^n\left(s_0\right) = 1 \text{ for all } x^+ \in S^2 \tag{7.9}$$

$$\nu_{x^-}^n\left(s_0\right) = 0 \text{ for all } x^- \in S^2 \tag{7.10}$$

$$\nu_{x^+}^n\left(-s_0\right) = 0 \text{ for all } x^+ \in S^2 \tag{7.11}$$

$$\nu_{x^-}^n\left(-s_0\right) = 1 \text{ for all } x^- \in S^2 \tag{7.12}$$

(which is to say in one hemisphere positive vorticities are certain and in the other negative vorticities are).

By $N\left(j\right)$ we signify the neighborhood of site j, that is, all the lattice sites k which are connected to site j. We are, at least implicitly, supposing that we can set up a graph with the mesh sites as vertices and edges drawn to some subset of the entire mesh. Note that this is not the sort of graph we would draw for a finite element approximation to fluid vorticity: we do not have any interest in creating elements or in maximizing the isometry of whatever elements could be derived from this. The edges we draw to establish the neighborhood of j are simply to the points which we want to consider short-range interactions. They need not even be exclusively the nearest mesh sites to j.

We let $z \equiv \left|N\left(j\right)\right|$ be the common size of neighborhoods $N\left(j\right)$, what is, the **coordination number** for the lattice. By altering z we are able to model interactions at different ranges in a variety of spin-lattice models.

Now let ϵ represent the **interaction energy scale** for H_N. We find this by averaging $J_{j,k}$ over $N\left(j\right)$. For energy-enstrophy theories, this ϵ is negative: it represents an anti-ferromagnetic interaction. This is enough to give us a spin-lattice approximation for H_N.

The other quantity we will need is a lattice approximation model for the per-site mixing entropy. Using the approach of equation (2.20) for $J_{j,k}$ and of equation (2.25) for F_j then we can derive this lattice approximation for the total mixing entropy:

$$S\left[w\right] = -k_B \int_{S^2} dx \int_{-M}^{M} ds\, \nu_x\left(s\right) \log\left(\nu_x\left(s\right)\right) \tag{7.13}$$

$$\simeq -k_B \sum_{j=1}^{N} \int_{S^2} dx\, H_j\left(x\right) \int_{-M}^{M} ds\, \nu_x\left(s\right) \log\left(\nu_x\left(s\right)\right) \tag{7.14}$$

$$= -\frac{4\pi k_B}{N} \sum_{j=1}^{N} \int_{-M}^{M} ds\, \nu_{x_j}\left(s\right) \log\left(\nu_{x_j}\left(s\right)\right) \tag{7.15}$$

We will use this for both the mixed and the unmixed states, and when rotation of the planet is considered will see three logical ways that the unmixed state may appear.

7.3.2 *Proofs for a Non-Rotating Planet*

What are we able to say about the barotropic flows for a non-rotating planet? Are we able to predict at what temperatures the various configurations will occur, and at what critical temperatures the preferred configuration will change from the unmixed state n to the mixed state m? And does this guide us in evaluating the similar regions of preferred configurations and critical temperatures when we move on to rotating planets?

We start by considering the per-site entropy for the mixed state, $v = m$, where the sign of vorticity is uncorrelated with position:

$$S_m = -\frac{4\pi k_B}{N} \int_{-M}^{M} ds\, \nu_x \log\left(\nu_x\right) \tag{7.16}$$

$$= \frac{4\pi k_B}{N} \log\left(2\right) \tag{7.17}$$

The per-site entropy in the unmixed state, $v = n$, where the vorticity is divided into two hemispheres of uniform sign is neatly enough

$$S_n = 0 \tag{7.18}$$

since, by definition, neighboring mean values s_0 are perfectly correlated.

Now, calculate the per-site internal energy for the mixed state $v = m$:

$$u_m = -\frac{1}{2}\epsilon \int_{-M}^{M} ds\, \nu_x\left(s\right) \int_{-M}^{M} ds^{'}\, \nu_{x^{'}}\left(s^{'}\right) ss^{'} z \tag{7.19}$$

$$= -\frac{1}{2}\epsilon z \left[\int_{-M}^{M} ds\, \nu_x\left(s\right) s\right]^2 \tag{7.20}$$

$$= 0 \tag{7.21}$$

And finally calculate the per-site internal energy in the unmixed state. There is a key to making this simple. In the unmixed state we know that neighboring mean spins s_{x_k} satisfy

$$s\left(x_k\right) = s\left(x_j\right) = \pm s_0 \text{ for all } k \in N\left(j\right) \tag{7.22}$$

$$\left|N\left(j\right)\right| = z \text{ for all } j = 1, 2, 3, \cdots, N \tag{7.23}$$

Therefore, in this mean-field theory,

$$u_n = -\frac{1}{2}\frac{\epsilon z}{N}\int_{S^2} dx \int_{-M}^{M} ds_0\, \nu_x s_0^2 \tag{7.24}$$

$$= -\frac{\epsilon z}{2}\int_{-M}^{M} ds_0\, \nu_x s_0^2 \tag{7.25}$$

$$= -\frac{\epsilon z}{8\pi} Q \tag{7.26}$$

For a given enstrophy $Q > 0$ and a given temperature T, and treating as if they were free parameters the state $v = m, n$ as well as the mean spin distribution ν_x, then we can calculate the isothermal per-site free energy difference between the mixed and unmixed states:

$$\Delta f = f_m - f_n \tag{7.27}$$

$$= \left(u_m - u_n\right) - T\left(S_m - S\right) n \tag{7.28}$$

$$= \frac{\epsilon z}{8\pi} Q - \frac{4\pi k_B T}{N}\log\left(2\right) \tag{7.29}$$

Equivalently,

$$f_m = u_m - T S_m \tag{7.30}$$

$$= -\frac{4\pi k_B T}{N}\log\left(2\right) \tag{7.31}$$

while

$$f_N = u_n - T S_n \tag{7.32}$$

$$= -\frac{\epsilon z}{8\pi} Q \tag{7.33}$$

This, together, comes to nearly prove a mean-field result for the non-rotating barotropic flows. Using the extension of Planck's theorem for negative temperatures $T < 0$, which tells us that thermodynamically stable statistical equilibriums correspond to maximizers of the free energy, and a maximum mean spin entropy S_{ms}, and the interaction energy scale ϵ:

Theorem 7.1. *If* $\epsilon < 0$*, then:*

(i) For all $T > 0$ *the mixed state* $v = m$ *is preferred.*

For $\epsilon < 0$ and $T < 0$ there is a finite N-dependent critical temperature

$$T_c\left(N\right) = \frac{\epsilon z N}{8\pi S_{m,s}} Q < 0 \tag{7.34}$$

such that

(ii) if

$$0 > T > T_c\left(N\right) \tag{7.35}$$

then the unmixed state $v = n$ is preferred, and

(iii) if

$$T < T_c\left(N\right) < 0 \tag{7.36}$$

then the mixed state $v = m$ is preferred, with maximum mean spin entropy

$$S_{ms} = 4\pi k_B \log\left(2\right) \tag{7.37}$$

(iv) In the non-extensive continuum limit — assumed to exist — as $N \to \infty$, then $T_c\left(N\right)$ tends to a finite negative critical temperature:

$$T_c\left(Q\right) = \frac{1}{S_{ms}}\left(\frac{Q}{2}\int_{S^2} dx\,\psi_{1,0}\left(x\right)\int_{S^2} dx^{'}\,\psi_{1,0}\left(x^{'}\right)\log\left|1 - x\cdot x^{'}\right|\right) \tag{7.38}$$

$$= \frac{1}{S_{ms}}\left(\frac{Q}{2}\int_{S^2} dx\,\psi_{1,0}\left(x\right)G\left(\psi_{1,0}\right)\left(x\right)\right) \tag{7.39}$$

$$= \frac{1}{S_{ms}}\left(-\frac{Q}{4}\int_{S^2} dx\,\psi_{1,0}^2\left(x\right)\right) \tag{7.40}$$

$$= -\frac{Q}{4S_{ms}} < 0 \tag{7.41}$$

such that if

$$0 > T > T_c \tag{7.42}$$

then the unmixed state $v = n$ is preferred and if

$$T < T_c < 0 \tag{7.43}$$

then the mixed state $v = m$ is preferred.

Proof.

The proof of part (i) follows directly from the calculations done leading to it: what are the maximizers of the Gibbs probability function?

To prove parts (ii) and (iii), compare the per-site free energy in the mixed state $v = m$

$$f_m\left(max\right) = -\frac{T}{N} S_{ms} > 0 \tag{7.44}$$

with the per-site free energy in the unmixed state $v = n$

$$f_n\left(max\right) = -\frac{\epsilon z}{8\pi} Q > 0 \tag{7.45}$$

When

$$-\frac{T}{N} S_{ms} < -\frac{\epsilon z}{8\pi} Q \tag{7.46}$$

— that is, when $0 > T > T_c\left(N\right)$ — then (ii) $v = n$ the unmixed state is preferred, and vice-versa for (iii). Since the interaction energy scale ϵ is negative (due to the positive-termperature antiferromagnetic nature of the logarithm interaction at short ranges), and the enstrophy Q is positive, and by definition the maximum mean spin entropy S_{ms} is positive, then the critical temperature $T_c\left(N\right)$ must be negative.

The proof of part (iv) follows by considering the free energy under the non-extensive continuum limit:

$$\frac{\epsilon z N}{8\pi} Q \rightarrow \frac{Q}{2} \int_{S^2} dx\, \psi_{1,0}\left(x\right) \int_{S^2} dx^{'}\, \psi_{1,0}\left(x^{'}\right) \log\left|1 - x \cdot x^{'}\right| \tag{7.47}$$

$$= -\frac{Q}{4} < 0 \tag{7.48}$$

∎

Remark 7.1. When the interaction energy scale ϵ is negative, there is a negative-temperature transition between the mixed state at the hot temperatures $T < T_c < 0$ and the unmixed state at extremely hot temperatures $T_c < T < 0$.

Remark 7.2. The mixed state per-site free energy f_m is entirely entropic. The unmixed state per-site free energy f_n is purely an internal energy term, and it is linear in the enstrophy Q.

7.3.3 *Mean-Field Theory on a Rotating Sphere*

While the non-rotating case provides some experience in the sorts of calculations we wish to do, it is the rotating planet which we want to study here. Since the energy function for the rotating planet can be written as a pairwise particle interaction added to an interaction between points and the rotating planet, we have reason to expect that the decomposition of energy into the pairwise interactions and into the planetary interactions will be likely to provide the answers we want. The pairwise particle interactions will produce internal energy and free energy and other quantities which look like those of the non-rotating planet; the new features come in from the particle-planet interaction. Again we will look for where the most probable state changes from an unmixed to a mixed state. And furthermore we have the interesting question of whether, in an unmixed state, the positive hemisphere will correspond with the north, or the south, or with no particular rotational hemisphere of the planet.

We decompose the energy H_N into the pairwise particle interactions $H_N^{(1)}$ and the interaction of particles with the rotating sphere $H_N^{(2)}$, which we describe as

$$H_N = H_N^{(1)} + H_N^{(2)} \tag{7.49}$$

$$H_N^{(1)} = -\frac{1}{2}\sum_{j=1}^{N}\sum_{k=1}^{N} J_{j,k} s_j s_k \tag{7.50}$$

$$H_N^{(2)} = \frac{2\pi\Omega}{N}\sum_{j=1}^{N} s_j \cos\left(\theta_j\right) \tag{7.51}$$

This suggests a similar natural decomposition of the internal energies:

$$u_m = u_m^{(1)} + u_m^{(2)} \tag{7.52}$$

$$u_n = u_n^{(1)} + u_n^{(2)} \tag{7.53}$$

for the different states which we have designated m and n. We know, from equations (7.21) and (7.26) some of these internal energy components — specifically, that

$$u_m^{(1)} = 0 \tag{7.54}$$

$$u_n^{(1)} = -\frac{\epsilon z}{8\pi} Q_r \tag{7.55}$$

We have previously introduced the mixed state denoted by $v = m$, and the unmixed mean field state denoted by $v = n$. We will also be able to divide the unmixed states into two particular cases: $v = n_u$ in which the steady-state rotation is prograde, moving with the rotation of the planet; and $v = n_d$, in which the steady-state rotation is retrograde, moving opposite the rotation of the planet. Each of these states, mixed and unmixed, can be characterized by the correlations between sites and their neighboring site spins, $s\left(x\right) = s\left(x'\right) \in \left\{s_0^{\pm}\right\}$.

In the unmixed states $v = n$, $v = n_u$, and $v = n_d$, the correlations are by hemispheres: opposite sides of the globe hold the equal values s_0^+ and s_0^-, where

$$s_0^+ + s_0^- = 0 \tag{7.56}$$

$$2\pi\left(\left(s_0^+\right)^2 + \left(s_0^-\right)^2\right) = Q_r \tag{7.57}$$

These equations imply

$$s_0^+ = -s_0^- = \sqrt{\frac{Q_r}{4\pi}} \tag{7.58}$$

The prograde and retrograde unmixed states $v = n_u$ and $v = n_d$ are also characterized by the hemispherical correlations of the spins $s_0^\pm$ which will turn out to satisfy equations (7.80) and (7.81) respectively: they are aligned and anti-aligned with the northern and southern hemispheres as defined by the rotation of the planet $\Omega > 0$.

Entropy is calculated the same way as it is when the planetary spin is zero because the entropies S_m and S_n depend only on the statistical distribution $v_x\left(s_0\right)$ of the mean field relative vorticity s_0. The planetary rotation does not directly contribute to the atmosphere's entropy.

What are the per-site internal energies $u_m^{(2)}$ and $u_n^{(2)}$ which result from the nonzero planetary rotation $\Omega > 0$?

For the mixed state $v = m$ by its definition:

$$\begin{aligned}
u_m^{(2)} &= \frac{2\pi\Omega}{N^2}\left\langle \sum_{j=1}^{N} s_j \cos\left(\theta_j\right)\right\rangle &(7.59)\\
&= \frac{2\pi\Omega}{N^2}\sum_{j=1}^{N}\cos\left(\theta_j\right)\left\langle s_j\right\rangle &(7.60)\\
&= \frac{2\pi\Omega}{N^2}\left(\int_{-M}^{M} ds\, v_x\left(s\right) s\right)\sum_{j=1}^{N}\cos\left(\theta_j\right) &(7.61)\\
&= 0 &(7.62)
\end{aligned}$$

since, in the mixed state,

$$v_x^m\left(\pm s_0\right) = \frac{1}{2} \tag{7.63}$$

For the unmixed state $v = n$ it will be convenient to use our notation $x_j^\pm$ for lattice sites which fall within the positive hemisphere and which in the negative, and to establish a similar one for the co-latitudes in each vorticity hemisphere. (These vorticity hemispheres, we reiterate, are not necessarily aligned with the hemispheres of the planet's rotation.) For the s_0^+ hemisphere we will use x_j^+ and θ_j^+ for sites and for co-latitude. For the s_0^- hemisphere we use x_j^- and θ_j^- for sites and for co-latitudes. From this we calculate:

$$u_n^{(2)} = \frac{2\pi\Omega}{N^2}\left\langle \sum_{j=1}^{N} s_j \cos\left(\theta_j\right)\right\rangle \tag{7.64}$$

$$= \frac{2\pi\Omega}{N^2}\sum_{j=1}^{N} \langle s_j\rangle \cos\left(\theta_j\right) \tag{7.65}$$

$$\equiv \frac{2\pi\Omega}{N^2}\left\{\left(\sum_{j=1}^{\frac{N}{2}} \left\langle s\left(x_j^+\right)\right\rangle \cos\left(\theta_j^+\right)\right) + \left(\sum_{k=1}^{\frac{N}{2}} \left\langle s\left(x_k^-\right)\right\rangle \cos\left(\theta_k^-\right)\right)\right\} \tag{7.66}$$

$$= \frac{2\pi\Omega}{N^2}\left(s_0^+ \cos\left(\theta_j^+\right) + s_0^- \sum_{k=1}^{\frac{N}{2}} \cos\left(\theta_k^-\right)\right) \tag{7.67}$$

Now, what are the per-site free energies for the mixed and the unmixed states? Going back to definitions:

$$f_m = u_m - TS_m \tag{7.68}$$

$$= \frac{4\pi k_B T}{N}\log\left(2\right) \tag{7.69}$$

for the mixed state; for the unmixed state,

$$f_n = u_n - TS_n \tag{7.70}$$

$$= -\frac{\epsilon z}{8\pi}Q_r + \frac{2\pi\Omega}{N^2}\left(s_0^+ \sum_{j=1}^{\frac{N}{2}} \cos\left(\theta_j^+\right) + s_0^- \sum_{k=1}^{\frac{N}{2}} \cos\left(\theta_k^-\right)\right) \tag{7.71}$$

This allows us to calculate the per-site change in free energy in going from the unmixed to the mixed states at a constant temperature, which is given by:

$$\Delta f \equiv f_m - f_n \tag{7.72}$$

$$= \frac{4\pi k_B T}{N}\log\left(2\right) + \frac{\epsilon z}{8\pi}Q_r - \frac{2\pi\Omega}{N^2}\left(s_0^+ \sum_{j=1}^{\frac{N}{2}} \cos\left(\theta_j^+\right) + s_0^- \sum_{k=1}^{\frac{N}{2}} \cos\left(\theta_k^-\right)\right) \tag{7.73}$$

Remark 7.3. To apply this formulation to the non-rotating barotropic flows on the sphere at both positive and negative temperatures requires the consideration of the non-extensive continuum limit. Under this limit,

$$\epsilon z = \epsilon\left(N\right) z\left(N\right) \rightarrow O\left(N^{-1}\right) < 0 \tag{7.74}$$

$$\frac{2\pi}{N^2}\sum_{j=1}^{\frac{N}{2}} s_0^+ \cos\left(\theta_j^+\right) + \frac{2\Omega}{N^2}\sum_{k=1}^{\frac{N}{2}} s_0^- \cos\left(\theta_k^-\right) \rightarrow O\left(N^{-1}\right) \tag{7.75}$$

So we know per-site free-energies. What are the preferred states at different temperatures, then, and what are the critical temperatures, in both the positive and negative temperature ranges? We start in positive temperatures.

7.3.4 *Positive Temperatures*

For $T > 0$ we need to compare the minimum free energy per site for the mixed state $v = m$ with that of the unmixed state $v = n$. These are:

$$f_m\left(min\right) = -\frac{T}{N}S_{ms} = \frac{4\pi k_B T}{N}\log\left(2\right) \tag{7.76}$$

for the maximum mean spin entropy S_{ms}, and

$$f_n\left(min\right) = -\frac{\epsilon z}{8\pi}Q_r + \frac{2\pi\Omega}{N^2}\left(s_0^+\sum_{j=1}^{\frac{N}{2}}\cos\left(\theta_j^+\right) + s_0^-\sum_{k=1}^{\frac{N}{2}}\cos\left(\theta_k^-\right)\right) \tag{7.77}$$

The extreme value of $f_n\left(min\right)$ we will find at the most negative values of

$$\frac{2\pi\Omega}{N^2}\left(s_0^+\sum_{j=1}^{\frac{N}{2}}\cos\left(\theta_j^+\right) + s_0^-\sum_{k=1}^{\frac{N}{2}}\cos\left(\theta_k^-\right)\right) \tag{7.78}$$

which we will find when the hemispheres associated with the correlated means $s_0^{\pm}$ are anti-correlated with those corresponding to the planetary rotation $\Omega > 0$, that is, when the greatest positive vorticity is also where the planetary spin is most negative.

Whenever the temperature is positive, if

$$\frac{2\pi\Omega}{N^2}\left(s_0^+\sum_{j=1}^{\frac{N}{2}}\cos\left(\theta_j^+\right) + s_0^-\sum_{k=1}^{\frac{N}{2}}\cos\left(\theta_k^-\right)\right) > \frac{\epsilon z}{8\pi}Q_r - \frac{T}{N}S_{m,s} \tag{7.79}$$

then the mixed state $v = m$ is preferred. Should the inequality be reversed then the unmixed state $v = n$ is preferred.

If the interaction energy scale $\epsilon < 0$, then for all positive temperatures $T > 0$ and for all positive relative entrophies $Q_r > 0$ the right-hand side of equation (7.79) is negative. This implies that the mixed state $v = m$ therefore will be preferred over the $v = n_u$ state, where the hemispheres associated with the means $s_0^{\pm}$ are correlated with those of the planetary rotation $\Omega > 0$ — that is, when

$$\frac{1}{N}\left(s_0^{+}\sum_{j=1}^{\frac{N}{2}}\cos\left(\theta_j^{+}\right) + s_0^{-}\sum_{k=1}^{\frac{N}{2}}\cos\left(\theta_k^{-}\right)\right) > 0 \tag{7.80}$$

How do the energies of the mixed state $v = m$ compare with those of the unmixed state $v = n_d$ where the means $s_0^{\pm}$ are anti-correlated with the planetary rotation, that is, where

$$\frac{1}{N}\left(s_0^{+}\sum_{j=1}^{\frac{N}{2}}\cos\left(\theta_j^{+}\right) + s_0^{-}\sum_{k=1}^{\frac{N}{2}}\cos\left(\theta_k^{-}\right)\right) < 0 \tag{7.81}$$

instead? With again $\epsilon < 0$ and the fixed relative enstrophy $Q_r > 0$ then there is some positive finite critical temperature, which depends also on Ω and on Q_r, for each N,

$$T_c\left(\Omega, Q_r; N\right) = \frac{2\pi\Omega I_0 - \frac{\epsilon z}{8\pi}NQ_r}{-S_{m,s}\left(Q_r\right)} > 0 \tag{7.82}$$

where

$$-\infty < I_- \equiv \min_{s_0^{\pm}}\frac{1}{N}\left(s_0^{+}\sum_{j=1}^{\frac{N}{2}}\cos\left(\theta_j^{+}\right) + s_0^{-}\sum_{k=1}^{\frac{N}{2}}\cos\left(\theta_k^{-}\right)\right) < 0 \tag{7.83}$$

provided the planetary rotation Ω is large enough compared to the relative vorticity — specifically, that

$$\Omega > \Omega_+\left(Q_r\right) = \frac{\epsilon z}{16\pi^2 I_-}NQ_r \tag{7.84}$$

This converges to a finite limit as $N \to \infty$.

The minimum I_- introduced in equation (7.83) is the minimum over all possible orientations of the hemispheres associated with $s_0^{\pm}$, and from equation (7.58),

$$I_- = O\left(\sqrt{Q_r}\right) \tag{7.85}$$

In summary: when $T > T_c\left(N\right) > 0$, the mixed state $v = m$ will be preferred over any unmixed state $v = n_u$ or $v = n_d$. When $0 < T < T_c\left(N\right)$, the unmixed state $v = n_d$ satisfying equation (7.81) is preferred over the mixed state $v = m$.

In the non-extensive continuum limit as $N \to \infty$, the positive finite size N critical temperature

$$T_c\left(\Omega, Q_r; N\right) \to T_c\left(\Omega, Q_r\right) < \infty \tag{7.86}$$

and furthermore if

$$\Omega > \Omega_+\left(Q_r\right) = \frac{\epsilon z}{16\pi^2 I_-} N Q_r \tag{7.87}$$

holds true then

$$T_c\left(\Omega, Q_r\right) > 0 \tag{7.88}$$

Remark 7.4. There is a positive-temperature phase transition provided the planetary rotation is large enough.

As there is no positive-temperature phase transition when the planet is not rotating, it is reassuring to see that very slight rotations would agree with this lack of a phase transition.

7.3.5 *Negative Temperatures*

We know from the extension of Planck's theorem to negative temperatures that when $T < 0$ we will see as most probable a state in which the free energy is maximized. So we again compare the per-site free energies of the mixed state $v = m$ and for the unmixed states $v = n_u$ and $v = n_d$:

$$f_m\left(max\right) = -\frac{T}{N} S_{m,s} \tag{7.89}$$

$$f_n\left(max\right) = -\frac{\epsilon z}{8\pi} Q_r + \frac{2\pi\Omega}{N^2}\left(s_0^+ \sum_{j=1}^{\frac{N}{2}} \cos\left(\theta_j^+\right) + s_0^- \sum_{k=1}^{\frac{N}{2}} \cos\left(\theta_k^-\right)\right) \tag{7.90}$$

For $T < 0$,

$$-\frac{\epsilon z}{8\pi} Q_r + \frac{2\pi\Omega}{N^2}\left(s_0^+ \sum_{j=1}^{\frac{N}{2}} \cos\left(\theta_j^+\right) + s_0^- \sum_{k=1}^{\frac{N}{2}} \cos\left(\theta_k^-\right)\right) > -\frac{T}{N} S_{m,s} > 0 \tag{7.91}$$

which implies that the unmixed states will be preferred. The inequality can be solved for the finite size N critical temperature. This yields:

$$T_c^-\left(\Omega, Q_r; N\right) = \frac{2\pi\Omega I_+ - \frac{\epsilon z}{8\pi} N Q_r}{-S_{m,s}} < 0 \tag{7.92}$$

where

$$\infty > I_{+} \equiv \max_{s_0^{\pm}} \frac{1}{N}\left(s_0^{+}\sum_{j=1}^{\frac{N}{2}}\cos\left(\theta_j^{+}\right)+s_0^{-}\sum_{k=1}^{\frac{N}{2}}\cos\left(\theta_k^{-}\right)\right)=-I_{-}>0 \tag{7.93}$$

and

$$I_{+}=O\left(\sqrt{Q_r}\right) \tag{7.94}$$

In this case, then $T < T_c^{-}(N)$, the mixed state $v = m$ will be preferred over any aligned unmixed state $v = n_u$ and so also over any anti-aligned unmixed state $v = n_d$ as well. The left-hand side of equation (7.91), evaluated in the retrograde unmixed state $v = n_d$ and in the prograde unmixed state $v = n_u$, satisfies

$$\begin{aligned}&\left[-\frac{\epsilon z}{8\pi}Q_r+\frac{2\pi\Omega}{N^2}\left(s_0^{+}\sum_{j=1}^{\frac{N}{2}}\cos\left(\theta_j^{+}\right)+s_0^{-}\sum_{k=1}^{\frac{N}{2}}\cos\left(\theta_k^{-}\right)\right)\right](n_d)\\ &<\left[-\frac{\epsilon z}{8\pi}Q_r+\frac{2\pi\Omega}{N^2}\left(s_0^{+}\sum_{j=1}^{\frac{N}{2}}\cos\left(\theta_j^{+}\right)+s_0^{-}\sum_{k=1}^{\frac{N}{2}}\cos\left(\theta_k^{-}\right)\right)\right](n_u)\\ &<-\frac{T}{N}S_{m,s}\end{aligned} \tag{7.95}$$

When $T_c^{-}(N) < T < 0$, the aligned unmixed state $v = n_u$ will be preferred over the mixed state $v = m$. Notice that a negative finite size N critical temperature $T_c^{-}(\Omega, Q_r; N) < 0$ exists for every planetary rotation $\Omega > 0$. This is quite unlike the positive finite size critical temperature $T_c(N)$, which exists only for rapid enough planetary rotations, those that satisfy equation (7.84).

Remark 7.5. Under the non-extensive continuum limit $N \to \infty$,

$$T_c^{-}(\Omega, Q_r; N) \to T_c^{-}(\Omega, Q_r) < \infty \tag{7.96}$$

$$T_c^{-}(\Omega, Q_r) < 0 \tag{7.97}$$

because in equation (7.92), the denominator is negative (by definition) and does not depend on N, while the numerator tends to a finite positive limit due to Remark 7.3. In consequence, there is a negative temperature phase transition for all values of the planetary rotation.

Since the numerator of equation (7.92) contains the positive term $-\frac{\epsilon z}{8\pi} N Q_r$ (positive, assuming $\epsilon < 0$), we can define a second negative critical temperature:

$$T_c^{--}(\Omega, Q_r; N) = \frac{2\pi\Omega I_- - \frac{\epsilon z}{8\pi} N Q_r}{-S_{m,s}} < 0 \tag{7.98}$$

provided the planetary rotation $\Omega > 0$ is small enough. Small enough is when

$$\Omega < \Omega_+(Q_r) = \frac{\epsilon z}{16\pi^2 I_-} N Q_r \tag{7.99}$$

Notice that $T_c^{--}(\Omega, Q_r; N) < 0$ and $T_c(N) > 0$ in equation (7.82) are the same expression, corresponding to the two sides of the equality in equation (7.99).

When $T < T_c^{--}(N) < 0$, the mixed state $v = m$ will be preferred to the anti-aligned unmixed state $v = n_d$.

When $T_c^{--}(N) < T < 0$, the anti-aligned unmixed state $v = n_d$ is preferred to the mixed state $v = m$.

Comparing equation (7.92) to equation (7.98) we can conclude that when the planetary rotation Ω satisfies equation (7.99),

$$T_c^{-}(N) < T_c^{--}(N) < 0 \tag{7.100}$$

By comparing the per-site free energies of unmixed states $v = n_u$ and $v = n_d$ when the temperature is negative (and, specifically, when $T_c^- < T < T_c^{--} < 0$ and when $T_c^- < T_c^{--} < T < 0$):

$$f_n^u(max) = -\frac{\epsilon z}{8\pi} Q_r + \frac{2\pi\Omega}{N} I_+ \tag{7.101}$$

$$f_n^d(max) = -\frac{\epsilon z}{8\pi} Q_r + \frac{2\pi\Omega}{N} I_- \tag{7.102}$$

In consequence, the aligned unmixed state $v = n_u$ will always be preferred over the anti-aligned unmixed state $v = n_d$ for negative temperatures.

Remark 7.6. Under the non-extensive continuum limit $N \to \infty$,

$$T_c^{--}(N) \to T_c^{--} < \infty \tag{7.103}$$

and

$$T_c^{-} < T_c^{--} < 0 \tag{7.104}$$

provided the planetary spin is small enough, that is,

$$\Omega < \Omega_+(Q_r) = \frac{\epsilon z}{16\pi^2 I_-} N Q_r \tag{7.105}$$

We can collect the above calculations and summarize the phase transitions they imply for this simple mean-field theory into a convenient form:

Theorem 7.2. *(A) For large enough planetary rotations $\Omega > 0$, the anti-aligned unmixed state $v = n_d$ changes into the mixed state $v = m$ at $T_c(\Omega, Q_r) > 0$.*

(B) This mixed state $v = m$ will then be preferred for positive temperatures $T > T_c$ as well as for negative temperatures $T < T_c^-$, changing to the aligned unmixed state $v = n_u$ at $T_c^-(\Omega, Q_r) < 0$.

(C) (i) For large enough rotations Ω, the unmixed state $v = n_u$ persists for all temperatures such that $T_c^- < T < 0$.

(ii) For small enough spins $\Omega < \Omega_+(Q_r)$ the state $v = n_u$ persists as the preferred state for temperatures where $T_c^- < T < 0$; but for temperatures where $T_c^{--} < T < 0$ the anti-aligned state $v = n_d$ will be preferred over the mixed state $v = m$ but not the aligned unmixed state $v = n_u$.

In the non-extensive continuum limit the mean-field critical temperatures of the energy-relative enstrophy theory for this problem are

$$\infty > T_c(\Omega, Q_r) = \lim_{N\to\infty} \frac{2\pi\Omega I_- - \frac{\epsilon z}{8\pi} N Q_r}{-S_{m,s}} \tag{7.106}$$

$$= \frac{1}{-S_{m,s}} \left(\min_{w,Q_r} \int_{S^2} dx\, \Omega C \psi_{1,0} G\left[w\left(x'\right)\right] + \frac{1}{4} Q_r \right) \tag{7.107}$$

$$= \frac{1}{S_{m,s}} \left(\frac{1}{2} \Omega C \sqrt{Q_r} - \frac{1}{4} Q_r \right) > 0 \tag{7.108}$$

precisely when

$$\Omega > \Omega_+^{\infty}(Q_r) = \frac{\sqrt{Q_r}}{2C} \tag{7.109}$$

$$> 0 \tag{7.110}$$

and for all planetary rotations $\Omega > 0$

$$-\infty < T_c^-(\Omega, Q_r) = \lim_{N\to\infty} \frac{2\pi\Omega I_+ - \frac{\epsilon z}{8\pi} N Q_r}{-S_{m,s}} \tag{7.111}$$

$$= \frac{\max_{w,Q_r} \int_{S^2} dx\, \Omega \cos(\theta(x))\, G\left[w\left(x'\right)\right] + \frac{1}{4} Q_r}{-S_{m,s}} \tag{7.112}$$

$$= \frac{-\frac{1}{2} \Omega C \sqrt{Q_r} - \frac{1}{4} Q_r}{S_{m,s}} < 0 \tag{7.113}$$

where $I^{\pm}$ are given by equations (7.83) and (7.93), where $C = \sqrt{\int_{S^2} dx\, \cos^2(\theta)}$, the minimum (or maximum) is taken over all relative *vorticity distributions $w(x)$ with the same fixed relative enstrophy Q_r, and the total entropy is*

$$S_{m,s} \equiv -4\pi k_B \log(2) > 0 \tag{7.114}$$

Proof. We have the definitions of the interaction energy scale $\epsilon(N)$, and of the size of the interaction neighborhood $z(N)$. So the term $-\frac{\epsilon z}{8\pi} N Q_r$ which appears in the numerator of $T_c(N)$, which is the finite-dimensional representation of the per-site spin-spin interaction energy in the unmixed states $v = n_u$ and $v = n_d$ (as opposed to being the spin-rotation Ω interaction energy), will tend to

$$-\frac{Q_r}{2}\int_{S^2} dx\, \psi_{1,0}(x) \int_{S^2} dx'\, \psi_{1,0}\left(x'\right) \log\left|1 - x \cdot x'\right| = \frac{Q_r}{4} > 0 \tag{7.115}$$

So, from the definition of the minimum I_-, and the derivation of the spin-lattice models H_N from the rest frame pseudo-kinetic energy H of the coupled barotropic flows, the finite N critical temperature

$$T_c(\Omega, Q_r; N) = \frac{2\pi\Omega \min_{s_0^\pm} \frac{1}{N} \begin{pmatrix} s_0^+ \sum_{j=1}^{\frac{N}{2}} \cos\left(\theta_j^+\right) \\ +s_0^- \sum_{k=1}^{\frac{N}{2}} \cos\left(\theta_k^-\right) \end{pmatrix} - \frac{\epsilon z}{8\pi} N Q_r}{-S_{m,s}} \tag{7.116}$$

$$\to \frac{\min_{w,Q_r}\left(\int_{S^2} dx\, \Omega \cos(\theta(x))\, G\left[w\left(x'\right)\right]\right) - \frac{1}{4} Q_r}{-S_{m,s}} \tag{7.117}$$

where the denominator has no dependence on N.

The minimum in the numerator is taken over all relative vorticities $w(x)$ with the desired fixed relative enstrophy Q_r, and is a well-defined, finite, negative quantity that is proportional to Ω and to $\sqrt{Q_r}$:

$$\min_{w,Q_r}\left(\int_{S^2} dx\, \Omega C \psi_{1,0} G\left[w\left(x'\right)\right]\right) = \int_{S^2} dx\, \Omega C \psi_{1,0} G\left[\sqrt{Q_r}\psi_{1,0}\right] \tag{7.118}$$

$$= -\frac{1}{2}\Omega C \sqrt{Q_r} \int_{S^2} dx\, \psi_{1,0}^2 \tag{7.119}$$

$$= -\frac{1}{2}\Omega C \sqrt{Q_r} \tag{7.120}$$

Since

$$\Omega_+(Q_r) = \frac{\epsilon z}{16\pi^2 I_-} N Q_r \tag{7.121}$$

$$\to \Omega_+^\infty(Q_r) = \frac{-Q_r}{\min_{w,Q_r}\left(\int_{S^2} dx\, 4C\psi_{1,0} G[w(x)]\right)} > 0 \tag{7.122}$$

when $\Omega > \Omega_+^\infty(Q_r)$, the mean-field critical temperature

$$T_c(\Omega, Q_r) > 0 \tag{7.123}$$

We similarly prove the existence of the continuum limit of T_c^- on the basis

$$\max_{w, Q_r}\left(\int_{S^2} dx\, \Omega C \psi_{1,0} G\left[w\left(x'\right)\right]\right) = \int_{S^2} dx\, \Omega C \psi_{1,0} G\left[-\sqrt{Q_r}\psi_{1,0}\right] \tag{7.124}$$

$$= \frac{1}{2}\Omega C \sqrt{Q_r} \tag{7.125}$$

This completes the proof.

∎

So now let us restate and reorganize the various phase transitions into two categories, based on the planetary rotation.

Theorem 7.3. *When the planetary spin $\Omega < \Omega_+(Q_r)$,*

(i) there is no positive temperature phase transition and the mixed state $v = m$ is preferred for all $T > 0$.

(ii) There is a negative temperature phase transition at $T_c^- < 0$ — which exists irrespective of the value of the planetary rotation — where the preferred mixed state $v = m$ for all $T < T_c^- < 0$ changes into the aligned unmixed state $v = n_u$, which is preferred over both the mixed state $v = m$ and the anti-aligned unmixed state $v = n_d$ for all $T_c^- < T < 0$.

(iii) There is a secondary transition at the hotter temperature $T_c^{--} < 0$ (where $T_c^- < T_c^{--}$) where the intermediate state $v = n_d$ changes place with $v = m$ in order of thermal preference. Letting the symbol $\prec$ represent "has smaller free energy than", we can summarize the state preference for the state $\Omega < \Omega_+(Q_r)$:

$$n_d \prec n_u \prec m \text{ for } T < T_c^- < 0 \tag{7.126}$$

$$n_d \prec m \prec n_u \text{ for } T_c^- < T < T_c^{--} \tag{7.127}$$

$$m \prec n_d \prec n_u \text{ for } T_c^{--} < T < 0 \tag{7.128}$$

When the planetary spin $\Omega > \Omega_+(Q_r)$, (iv) there is a positive critical temperature $T_c(\Omega, Q_r)$ given by equation (7.82) at which the preferred state changes from $v = n_d$ for $0 < T < T_c$ to $v = m$ for all $T > T_c$ and for all negative $T < T_c^- < 0$.

(v) There is a negative critical temperature $T_c^- < 0$, that exists irrespective of the value of the planetary rotation, at which the preferred state changes from $v = m$ to $v = n_u$ for all negative $T > T_c^-$. We can summarize the state preference for the case $\Omega > \Omega_+(Q_r)$:

$$n_d \prec n_u \prec m \text{ for } T < T_c^- < 0 \tag{7.129}$$

$$n_d \prec m \prec n_u \text{ for } T_c^- < T < 0 \tag{7.130}$$

Chapter 8

Phase Transitions of Barotropic Flow

8.1 Introduction

We saw in section 6.4 a model for the barotropic flow on a rotating sphere in which phase transitions are detected by Monte Carlo simulations. In that model we allow the angular momentum of the atmosphere to change while holding fixed the values of the total circulation and of the relative enstrophy of the atmosphere. The result is, as we see, a set of sub-rotational and super-rotational macrostates which have different ranges in which they are preferred.

In this chapter we will look at the same problem but develop it by the Bragg mean-field theory. In this model, we continue to allow angular momentum of the atmosphere to change. More than that, we now have the relative enstrophy constrained only by an inequality, although the total circulation is still held fixed at zero. The results of this change can be numerically validated in Monte Carlo simulations on the logarithmic-potential spherical model, and have been for both the non-rotating case and the rotating case.

Previously we have had a spherical model, in that the microcanonical constraint on the relative enstrophy becomes a spherical constraint in the style introduced by Berlin and Kac [8]. Here, we use instead a simplified model in which the possible values of vortex spins are discretized, and this allows us to use the Bragg method to approximate the free energy. In turn this lets us find an analytic solution to the coarse-grained stream function in the resulting mean field theory. Closed form solutions of the partition function in the spherical model required considerable analytical effort, which we can sidestep for now.

Qualitatively, this model is not very different from the circulation-relative enstrophy spherical model, or from the simple mean-field model. There do remain differences in the detailed predictions of these models, however. Looking to the atmosphere of Venus for inspiration shows little reason to select one over another: the current state of observational data is not refined enough to distinguish between these physical models. One will need to perform detailed, direct numerical simulations of coupled geophysical flows in order to gather enough data to allow for selection among the three models. They are included here for pedagogical reasons.

Our discretized vorticity model is a set $X = \{\vec{x}_j\}$ of some $2N$ sites randomly distributed on the sphere with a uniform distribution. Each site has a spin $s_j \in \{+1, -1\}$, and each site has an interaction energy with every other site as a function of distance. Each spin further interacts with the planetary rotation, which again serves a role analogous to that of the external magnetic field from the Ising model. The sum of this interaction between spin and planetary rotation is proportional to the (potentially variable) net angular momentum of the fluid in the frame of reference of the planety's daily rotation.

The contribution to the kinetic energy of the atmosphere from the planetary spin varies zonally, so that this "external field" is inhomogeneous and so is difficult to treat analytically. Bragg and Williams [44] used a one-step renormalization to allow them to examine properties of order and disorder in the Ising model of a ferromagnetic. Since the discretized model for barotropic flows coupled to a rotating sphere is similar to the Ising model of a ferromagnet in an inhomogeneous external field we can use the Bragg-Williams technique and from this infer the order-disorder properties of the atmosphere.

We have already seen that systems of constrained vortices may have both positive and negative-temperatures. This model has them as well. By using the simplest two-domains partition of the surface of the sphere we find a positive temperature continuous phase transition to the sub-rotating ordered state for decreasing temperatures if the planetary spin is large enough. If there is no rotation then we find no phase transition in positive temperatures. There is a transition to a super-rotating ordered state when the temperature is negative and has a small absolute value: these are the very highest energies.

8.2 Statistical Mechanics of Macroscopic Flows

What are some important properties in the application of a statistical equilibrium approach to macroscopic flows? The atmospheric flows which we deal with here — largely two-dimensional flows — are in reality non-equilibrium phenomena even when the fluid is nearly inviscid, an assumption which is mainly correct for the interior of geophysical flows. So how is it we can apply equilibrium statistical mechanics methods?

The main reason is that we have two separate time scales in the microdynamics of two-dimensional vorticities, which is best formulated as the well-known physical principle of selective decay, at least for freely-decaying flows. This principle states that the slow time scale, given by the overall decay rates of enstrophy and of kinetic energy in damped and unforced fluid flows, is sufficiently different from the fast time scale, given by the inverse cascade relaxation of kinetic energy from small to large spatial scales. So several relaxation periods fit within a unit of slow time. Therefore, the total kinetic energy — and enstrophy — may be considered fixed in the time which it takes for the eddies to reach statistical equilibrium.

Furthermore, the principle of selective decay states the asymptotic properties of the damped two-dimensional flow will be characterized by a minimal enstrophy-toenergy ratio, which depends on the geometry of the flow domain. One of the key properties of the enstrophy, known as the square-norm of the vorticity field, then implies that these minimum enstrophy states are associated with large-scale ordered structures, such as domain scale vorticities. In this model, these coherent structures are the super- and the sub-rotating solid-body flows.

The specific properties of a given flow problem [69] will decide which of the many statistical equilibrium models [50] [68] [74] [84] [80] is most suitable. Since we have a coupled flow, in which angular momentum and energy are transferred between the atmosphere and the rotating planet, all the particle and vortex gas models [68] [80] on the surface of the sphere S^2 are not suitable because they conserve angular momentum, as dictated by Noether's theorem.

In general, none of the vorticity moments are conserved in the coupled flows, other than the total circulation which is fixed at zero (by the Stokes Theorem), independently of the coupling between the atmosphere and the rotating planet.

So we start with the classical Kraichnan models, also known as absolute equilibrium models, and their variants such as those used in [35]. But there are two sets of problems: first, they model a two-dimensional fluid flow which is uncoupled to any boundary or which has periodic boundaries and therefore a fixed angular momentum, unsuitable for our needs. Second, they are equivalent to the Gaussian models and therefore can be shown easily not to have a well-defined partition function at low temperatures.

One solution, taken up in [58] [59], is to replace the canonical enstrophy constraint with a microcanonical one, which results in a version of Kac's spherical model. Combined with the total circulation fixed at zero and allowing the angular momentum to fluctuate — that is, the coupling of the barotropic fluid to an infinitely-massive rotating solid sphere — this approach yields exact partition functions and closed-form expressions for phase transitions to self-organized or condensed super- and sub-rotating flows. These results agree perfectly with Monte Carlo simulations of the spherical model in [19] [20] [63].

It demands an argument similar in style to the above discussion of the Principle of Selective Decay to justify the choice of a microcanonical (and therefore spherical) constraint on relative enstrophy in this class of coupled flows, while the zero-total-circulation constraint requires none since it is implied by topological arguments: it follows from the Stokes Theorem on the sphere. The spherical model, unlike the Bragg model used in this chapter, is not based on a mean field assumption.

Instead, one of the objectives in this chapter is to study the effects on solutions by relaxing the enstrophy constraint. We impose neither a canonical enstrophy constraint as in [50] nor a microcanonical enstrophy constraint as in [19] [20] [58] [59] [63] and then derive a physically sound mean-field theory for a relatively simple geophysical problem. The relative enstrophy in the Bragg mean-field theory, we will show, is constrained instead by an upper bound.

One more objective in this chapter is to show the Bragg method extends to this coupled flow where the kinetic energy is a Lagrangian functional but not a Hamiltonian of the barotropic flow. The original Bragg method formed for the Ising model of ferromagnetism was developed for a Hamiltonian. Lim reported in [19] [20] [59] that the kinetic energy of the atmosphere component of the coupled fluid-rotating sphere system cannot be a Hamiltonian for the evolution of the vorticity field. If it were, then its $SO\,(2)$ symmetry — a property which is easy to demonstrate holds — would imply the conservation of the angular momentum of the fluid component.

8.3 Bragg-Williams Approximation

The Bragg-Williams approximation to the Barotropic Vorticity Equation begins with a discrete approximation to the pseudo-kinetic energy, one which looks very much like what we have used before, except that here we suppose there are $2N$ sites on the mesh, N of them with positive spin and N of them with negative spin:

$$H_N = -\frac{1}{2}\sum_{j=1}^{2N}\sum_{k=1}^{2N} J_{j,k} s_j s_k - \Omega \sum_{j=1}^{2N} F_j s_j \tag{8.1}$$

where the $2N$ mesh sites $\vec{x}_j$ are distributed uniformly over the sphere, where Ω is the planet's rotation, and where

$$J_{j,k} = \frac{16\pi^2}{N^2} \log\left(1 - \vec{x}_j \cdot \vec{x}_j\right) \tag{8.2}$$

$$F_j = -\frac{2\pi}{N} \cos\left(\theta\left(\vec{x}_j\right)\right) \tag{8.3}$$

with the notes that $J_{j,j} \equiv 0$ for all j, and where $\theta\left(\vec{x}_j\right)$ is the co-latitude for the mesh site $\vec{x}_j$. Furthermore, each mesh site vorticity s_j is either positive or negative one, the direction of the spin of the node.

We want to replace the internal energy of a state with its long-range order.

This is central to the Bragg-Williams approximation [44]. This is a familiar sort of problem to study, however: the ferromagnetism models which inform our treatment adapt naturally to this problem, and were part of what inspired our discrete model with its uniform magnitude for the vorticity and its separation into equal numbers of positive and negative signs.

In the Bragg-Williams model of a ferromagnet, in a flat, square lattice with uniform spacing between “rows” and “columns” of mesh sites, we consider the division of a lattice into two regions, and the length of the “wall” separating the upward from the downward spins. The energy of this domain wall will be proportional to the length of the wall and the energy required to flip any one lattice site from one orientation to the other. The entropy for a domain wall is proportional also to the length of the wall, and a wall might start from any lattice site. From this, we can derive the free energy associated with the division of a lattice into two domains. Having that free energy lets us predict at what statistical mechanics temperature it becomes energetically favorable to allow domain formation, or what temperatures resist this formation. This will not be invariably correct, but it gives us guidance to what phase transitions to expect and where they might be found with an analysis that remains straightforward for the information derived.

Some adaptations are required to go from a uniform square lattice on a flat surface to the uniform yet non-columnar mesh on the surface of the sphere. The energy of the domain walls is a particularly more complicated expression, no longer simply linearly proportional to its length. The planetary rotation we can treat as an external magnetic field, but it is necessarily an inhomogeneous one. What we must do is estimate the internal energy based on the local order as seen on the domains of the sphere.

We have to define a partition of the sphere into domains, or blocks, which we label $\{\xi\}$. Within each domain there are, at least in principle, many of the original lattice sites. In the thermodynamic limit for lattice models we typically take the number of sites to grow infinitely large. This we must do on the surface of the sphere.

We are not, however, making the assumption right now that these domains are of uniform vorticity: they may be expected to have a combination of some positive and some negative sites. For each of these domains we define N_ξ^+ to be the number of sites within domain ξ which have positive vorticity, and N_ξ^- to be the number of sites within domain ξ which have negative vorticity. Obviously, $N_\xi = N_\xi^+ + N_\xi^-$.

For each domain ξ we define the local order parameter σ_ξ:

$$\sigma_\xi \equiv 2\frac{N_\xi^+}{N_\xi} - 1 \tag{8.4}$$

There are many important quantities we want to know, or at least to estimate. We are going to approximate them by replacing the original discrete spin values with the local probability for the spin values. This probability is itself based on the local order parameter, how probable it is that a particular sign will be observed for the vortex. This is precisely the sort of substitution which allows the Bragg-Williams approximation for ferromagnetism to be as useful as it is, and so it is no surprise that it appears here.

The probability of any particular spin s within the domain ζ being positive is

$$P_\zeta^+ \equiv Prob\{s = +1\,|s \in \zeta\} = \frac{1+\sigma_\zeta}{2} \tag{8.5}$$

while the probability of the spin being negative is

$$P_\zeta^- \equiv Prob\{s = -1\,|s \in \zeta\} = \frac{1-\sigma_\zeta}{2} \tag{8.6}$$

These definitions characterize the macrostate, defining it by the local order.

The energy is the coupling of the spin domains. The entropy we can calculate through the Shannon information entropy over the local orders, and will do so shortly.

Since we have made all the vortex magnitudes uniform in strength there are only three types of pairwise interaction. In any pair of sites both sites may be positive $(++)$, both may be negative $(--)$, or one may be positive and the other negative $(+-)$. The probabilities of spin distribution, our coarse-grained variables, are what we use to provide the probabilities of the different spin interactions. These probabilities themselves will depend on the respective domains of the interacting sites.

Consider the edge which divides the domains ξ and $\xi^{'}$. The probabilities of the pairwise interactions across this edge, with one site in ξ and the other in $\xi^{'}$, are therefore by definition

$$P^{++}_{\xi,\xi'} \equiv Prob\left\{ s_j = +1; s_k = +1 \;\middle|\; \vec{x}_j \in \xi; \vec{x}_k \in \xi^{'} \right\} \tag{8.7}$$

$$P^{--}_{\xi,\xi'} \equiv Prob\left\{ s_j = -1; s_k = -1 \;\middle|\; \vec{x}_j \in \xi; \vec{x}_k \in \xi^{'} \right\} \tag{8.8}$$

$$\begin{aligned} P^{+-}_{\xi,\xi'} \equiv Prob\{ s_j = +1; s_k = -1 \quad &\text{or} \\ s_j = -1; s_k = +1 \Big| \; \vec{x}_j \in \xi; \vec{x}_k \in \xi^{'} &\Big\} \end{aligned} \tag{8.9}$$

And it follows — since we have identified all the possible alternatives — that

$$P^{++}_{\zeta,\zeta'} + P^{---}_{\zeta,\zeta'} + P^{+-}_{\zeta,\zeta'} = 1 \tag{8.10}$$

or, equivalently,

$$P^{++}_{\zeta,\zeta'} + P^{---}_{\zeta,\zeta'} - P^{+-}_{\zeta,\zeta'} = 1 - 2P^{+-}_{\zeta,\zeta'} \tag{8.11}$$

We will see the left-hand side of equation (8.11) again in equation (8.27): it will be the sole contribution of the pairwise order to the free energy.

What remains to calculate is the order probability $P^{+-}_{\zeta,\zeta'}$. This must be done in two cases: in the first, we take $\zeta^{'} \neq \zeta$. Then

$$P^{+-}_{\zeta,\zeta'} = \frac{N^{+-}_{\zeta,\zeta'}}{N_\zeta N_{\zeta'}} \tag{8.12}$$

$$= \frac{N^{+}_{\zeta}}{N_\zeta} \frac{N^{-}_{\zeta'}}{N_{\zeta'}} + \frac{N^{-}_{\zeta}}{N_\zeta} \frac{N^{+}_{\zeta'}}{N_{\zeta'}} \tag{8.13}$$

$$= \frac{1 + \sigma_\zeta}{2} \frac{1 - \sigma_{\zeta'}}{2} + \frac{1 + \sigma_{\zeta'}}{2} \frac{1 - \sigma_\zeta}{2} \tag{8.14}$$

$$= \frac{1 - \sigma_\zeta \sigma_{\zeta'}}{2} \tag{8.15}$$

It turns out to be useful that this gives us the relationship

$$1 - 2P^{+-}_{\zeta,\zeta'} = \sigma_{\zeta}\sigma_{\zeta'} \tag{8.16}$$

In the other case we take $\zeta^{'} = \zeta$, and so have

$$\begin{aligned}
P^{+-}_{\zeta\zeta} &= \frac{N^{+-}_{\zeta\zeta}}{\frac{1}{2}N_{\zeta}\left(N_{\zeta} - 1\right)} && (8.17)\\
&\approx \frac{N^{++}_{\zeta\zeta}}{\frac{1}{2}N^{2}_{\zeta}} && (8.18)\\
&= 2\frac{N^{+}_{\zeta}}{N_{\zeta}}\frac{N^{-}_{\zeta}}{N_{\zeta}} && (8.19)\\
&= 2\frac{1+\sigma_{\zeta}}{2}\frac{1-\sigma_{\zeta}}{2} && (8.20)\\
&= \frac{1-\sigma^{2}_{\zeta}}{2} && (8.21)
\end{aligned}$$

provided that N_{ζ} is sufficiently large. Notice that we made this assumption at the start of this section.

Now we can estimate interesting properties — like the internal energy or the free energy — in terms of the system's Bragg coarse-grained order. In the coarse-graining, we have made the enstrophy now merely an upper bound rather than a fixed value: we hold that $\sigma^{2}_{\xi} \leq 1$. Other models have constrained the enstrophy microcanonically, but we know from the Principle of Selective Decay for two-dimensional flows that any bound on the relative enstrophy is enough to allow a statistical mechanics model to be a well-defined model.

8.3.1 *Internal Energy*

The discrete approximation to the pseudo energy, as seen in equation (8.1), we can rewrite in a form in which we take the sums over pairs of domains and then over the sets of points within each of those domain pairs. This is equivalent, of course — we are still taking a sum over all the pairs of particles — but by rearranging things to pairs of domains as the first consideration we are taking advantage of our partitioning of the surface into domains and into our consideration of the boundaries between domains. In this form we have the pseudo energy as

$$H_N = -\frac{1}{2}\sum_{l,m}\sum_{(j,k)|(\vec{x}_j,\vec{x}_k)\in\xi_l\times\xi_m} J_{j,k}s_j s_k - \Omega\sum_{l}\sum_{j|x_j\in\xi_l} F_j s_j \tag{8.22}$$

We have not overlooked the edges which were described to great fanfare previously. They are simply already subsumed in the sums: each edge is already part of some particle pairs within the appropriate domain pair.

We have made the assumption that the distribution of the positive and negative sites within a single partition are homogeneous, that is, that we can describe the likelihood of each sign by the order parameters introduced already. Let $\{\sigma_{\xi}\}$ be the vector which represents all the order parameters. Then the Bragg internal energy we can write in terms of that vector:

$$H_N^B = -\frac{1}{2}\sum_{l,m}\left\langle \sum_{(j,k)|(\vec{x}_j,\vec{x}_k)\in\xi_l\times\xi_m} J_{j,k}s_j s_k \right\rangle_B - \Omega\sum_{l}\left\langle \sum_{j|x_j\in\xi_l} F_j s_j \right\rangle_B \tag{8.23}$$

where by the symbol $\langle \quad \rangle_B$ we mean a Bragg averaging. What we mean by a Bragg averaging will become clear in the next few paragraphs as we evaluate it in terms of the probabilities of different distributions of pairs and of area-averaged internal energies to a domain.

The mean energy of an edge, whether it connects two domains, or whether it is simply of a domain by itself, we can define in terms of the area average, thanks to the assumption we made that the domain will be homogeneous, or uniform, throughout:

$$K_{\xi,\xi'} = \left\langle \log\left(1 - \vec{x}\cdot\vec{x'}\right) \quad \middle| \left(x, x'\right) \in \xi\times\xi' \right\rangle \tag{8.24}$$

This mean is an average over the relevant domains: there is implicitly an area integral within this.

We will start calculating the pairwise interaction terms in the Bragg internal energy, H_N^B, and we will start that by considering the interactions between different domains, that is, where $\xi \neq \xi'$.

Useful in simplifying the calculation of pairwise interactions is the Dirac delta function. Since we have taken each s_j to be either positive or negative 1, this means that $\delta(1 - s_j s_k)$ will be 0 if they are of opposite sign. Meanwhile $\delta(1 + s_j s_k)$ will be 0 when both sites j and k are of the same sign.

We will use the Dirac delta function within this area-averaging bracket $\langle \quad \rangle$ to pick out the values of pairwise interactions. As mentioned above because this is an area integral our use of the Dirac delta is analytically justified; and, as we would hope for a particle-based discretization only the mesh sites will contribute to the internal energy.

So we add together the scale of the pairwise interaction $J_{j,k}$ when the sites are of the same sign which are picked out by $\delta(1 - s_j s_k)$, and subtract that when they are of opposite sign, which are picked out by $\delta(1 + s_j s_k)$.

This will then let us find the energy in terms of the probability $P^{++}_{\xi,\xi'}$ of pairs being both positive, the probability $P^{---}_{\xi,\xi'}$ of both being negative, and the probability $P^{+-}_{\xi,\xi'}$ of opposite signs:

$$\left\langle \sum_{(j,k)\left|(\vec{x}_j,\vec{x}_k)\in\xi\times\xi'\right.} J_{j,k}s_js_k \right\rangle_B \tag{8.25}$$

$$= \left\langle \sum_{(j,k)\left|(\vec{x}_j,\vec{x}_k)\in\xi\times\xi'\right.} J_{j,k}\delta\left(1-s_js_k\right) - \sum_{(j,k)\left|(\vec{x}_j,\vec{x}_k)\in\xi\times\xi'\right.} J_{j,k}\delta\left(1+s_js_k\right) \right\rangle_B \tag{8.26}$$

$$= \left(P^{++}_{\xi,\xi'} + P^{---}_{\xi,\xi'} - P^{+-}_{\xi,\xi'}\right) \left\langle \sum_{(j,k)\left|(\vec{x}_j,\vec{x}_k)\in\xi\times\xi'\right.} J_{j,k} \right\rangle \tag{8.27}$$

$$= \sigma_\xi \sigma_{\xi'} V_\xi V_{\xi'} K_{\xi,\xi'} \tag{8.28}$$

Equation (8.27) contains the coarse-graining approximation over the edges in $\xi \times \xi^{'}$. Equation (8.28) uses the relationship between the probabilities of the various pairs and the order parameters outlined in equations (8.11) and (8.16). V_ξ is the area of the domain ξ and it should not be surprising that an expression based on the area-average interaction between two domains and the order parameters within each domain requires multiplication by the domain areas to approximate the internal energy.

The other case which we needed to consider was the interaction of a domain ξ with itself. The approach for this is going to be essentially identical: we will write out the Bragg average for this internal energy, and then break up the sum this implies in terms of the interactions between pairs of the same sign, picked out by the Dirac delta function $\delta\left(1 - s_j s_k\right)$ again, and those of the opposite sign, once more marked by $\delta\left(1 + s_j s_k\right)$.

The only substantial difference between the interaction of a domain with itself and the interaction of a domain with another, from our perspective, is a multiplied factor of $\frac{1}{2}$. This difference accounts for what would otherwise be a double-counting of each pair. Keeping that in mind, then:

$$\left\langle \sum_{(j,k)|(\vec{x}_j,\vec{x}_k)\in\xi\times\xi} J_{j,k} s_j s_k \right\rangle_B \tag{8.29}$$

$$= \frac{1}{2} \left\langle \sum_{(j,k)|(\vec{x}_j,\vec{x}_k)\in\xi\times\xi} J_{j,k}\delta\left(1 - s_j s_k\right) - \sum_{(j,k)|(\vec{x}_j,\vec{x}_k)\in\xi\times\xi} J_{j,k}\delta\left(1 + s_j s_k\right) \right\rangle_B \tag{8.30}$$

$$= \frac{1}{2} \left(P^{++}_{\xi,\xi} + P^{---}_{\xi,\xi'} - P^{+-}_{\xi,\xi}\right) \left\langle \sum_{(j,k)\middle|(\vec{x}_j,\vec{x}_k)\in\xi\times\xi'} J_{j,k} \right\rangle \tag{8.31}$$

$$= \frac{1}{2}\sigma_\xi^2 V_\xi^2 K_{\xi,\xi} \tag{8.32}$$

This has given us the pairwise particle interactions among the various domains and for a non-rotating planet would be all that contributes to the pseudo energy. What remains to be considered is the external interaction, the component of the energy reflecting the interaction of the domains with the planetary rotation.

We need to introduce an area-weighted mean coupling of a site with an external field. This will allow us to perform the sort of averaging which we did for pairwise particles with the planetary rotation instead and still allow for the rotation being, on average, of different strengths in different domains. Once again using V_ζ to represent the area of the domain ζ, and using $\theta\left(\vec{x}_j\right)$ to represent the colatitude of the mesh site $\vec{x}_j$ this area-weighted mean coupling is:

$$L_\zeta = \int_\zeta dx\, \frac{1}{2V_\zeta} \cos\left(\theta\left(\vec{x}\right)\right) \tag{8.33}$$

This now allows us to estimate the mean coupling. That term, as written at the end of equation (8.22), we can evaluate:

$$\sum_l \left\langle \sum_{j|x_j\in\zeta_l} F_j s_j \right\rangle_B = \sum_\zeta N_\zeta \left\langle s_j \left| \vec{x}_j \in \zeta \right.\right\rangle \left\langle F_j \left| x_j \in \zeta \right.\right\rangle \tag{8.34}$$

$$= \sum_\zeta \sigma_\zeta \int_\zeta dx\, \frac{1}{2} \cos\left(\theta\left(\vec{x}\right)\right) \tag{8.35}$$

$$= \sum_\zeta \sigma_\zeta V_\zeta L_\zeta \tag{8.36}$$

That the energy of this mean coupling amounts to the volume of the domain times the mean point-rotation energy interaction times the order parameter, that is, the mean site value, is on reflection not surprising. This looks like what it would have to be.

So between the pairwise interactions and the particle-rotation interaction we can form a simple expression for the Bragg internal energy:

$$U = -\frac{1}{2} \sum_{j,k} \sigma_{\xi_j} \sigma_{\xi_k} V_{\xi_j} V_{\xi_k} K_{\xi_j,\xi_k} - \Omega \sum_{j} \sigma_{\xi_j} V_{\xi_j} L_{\xi_j} \tag{8.37}$$

8.3.2 *Entropy*

The entropy we will calculate from the Shannon information-theory definition of entropy, that is, the definition based on the probability distribution function of the spins. We are forced into this definition, in a sense: our mesh is based on a sphere of constant size and a fixed mesh on it. We do not have any extensive quantities, only intensive ones.

Since we have divided the sphere into domains ξ_j each of which has a homogeneous probability distribution function within, we need only take sums over the separate domains, with a weighting based on the area of each of these domains. Since we have taken the site vorticities to be either positive or negative a constant value, as well, the probability distributions amount to just the probabilities $P^{++}_{\xi,\xi'}$, $P^{---}_{\xi,\xi'}$, and $P^{+-}_{\xi,\xi'}$, which we know from equations (8.5) and (8.6) can be written in terms of the order parameters ρ_{ζ}.

$$S = -k_B \sum_{j} V_{\zeta_j} \left[\frac{1+\sigma_{\zeta_j}}{2} \log\left(\frac{1+\sigma_{\zeta_j}}{2} \right) + \frac{1-\sigma_{\zeta_j}}{2} \log\left(\frac{1-\sigma_{\zeta_j}}{2} \right) \right] \tag{8.38}$$

Now we have the internal energy and the entropy components required for calculating the Helmholtz free energy and the identification of phase transitions which we want.

8.3.3 *Helmholtz Free Energy*

The Helmholtz free energy is by definition

$$\Psi = U - TS \tag{8.39}$$

$$\begin{aligned} &= -\frac{1}{2}\sum_{j,k}\sigma_{\xi_j}\sigma_{\xi_k}V_{\xi_j}V_{\xi_k}K_{\xi_j,\xi_k} - \Omega\sum_j \sigma_{\xi_j}V_{\xi_j}L_{\xi_j} \\ &\quad + Tk_B\sum_j V_{\xi_j}\left[\frac{1+\sigma_{\xi_j}}{2}\log\left(\frac{1+\sigma_{\xi_j}}{2}\right)+\frac{1-\sigma_{\xi_j}}{2}\log\left(\frac{1-\sigma_{\xi_j}}{2}\right)\right] \end{aligned} \tag{8.40}$$

for the set of σ_ξ which satisfy the constraint

$$\sum_j V_{\xi_j}\sigma_{\xi_j} = 0 \tag{8.41}$$

What we look for are critical points of the free energy with respect to the set of order parameters $\left\{\sigma_{\xi_j}\right\}_{j=1}^{m}$ for the m domains within the sphere. Notice that this can be written as a vector, and that this vector is constrained to fit on the surface curve described by equation (8.41).

This means we have a problem amenable to solution by Lagrange multipliers. We need the critical points given by the simultaneous solution of the m equations

$$\lambda V_{\xi_j}\left\{\nabla_{\sigma_{\xi_j}}\sum_l \sigma_{\xi_l}\right\} = \left\{\nabla_{\sigma_{\xi_l}}\Psi\right\} \tag{8.42}$$

$$\begin{aligned} &= -V_{\xi_j}\Omega L_{\xi_j} - \sum_l \sigma_{\xi_j}V_{\xi_j}V_{\xi_l}K_{\xi_j,\xi_j} \\ &\quad + Tk_BV_{\xi_j}\left(\frac{1}{2}\cdot\frac{1+\sigma_{\xi_j}}{1-\sigma_{\xi_j}}\right) \end{aligned} \tag{8.43}$$

along with the constraint equation (8.41).

Equivalently, we write for all $j = 1, 2, 3, \cdots, m$ that

$$\sigma_{\xi_j} = \tanh\left[\beta\left(\Omega L_{\xi_j}+\lambda\right)+\beta\sum_l \sigma_{\xi_l}V_{\xi_l}K_{\xi_j,\xi_l}\right] \tag{8.44}$$

This is an m-dimensional fixed-point problem for $\left\{\sigma_{\xi_j}\right\}_{j=1}^{m}$. The challenge is to show that a well-defined continuum limit for this equation exists in the form of a fixed-point equation in the Hilbert space $L_2\left(S^2\right)$.

8.4 Polar State Criteria

The preceding section has given us the framework for the Bragg-Williams approximations. What we do now is to implement it, with a two-domain partition on the sphere, which is as simple a division as we can provide but which nevertheless allows interesting results.

What we find by this partitioning is that the order of the system varies continuously as function of the statistical mechanics temperature and of the planetary rotation. When the planet is not rotating, there will be a continuous phase transition of the second order at a critical temperature which proves to be negative. When the planetary rotation is large, we will find a continuous phase transition, between a weakly counter-rotating ordered or unmixed state and a mixed state, at a critical temperature that is positive.

Our partitioning will be into the northern and southern hemispheres, with the northern hemisphere labelled domain 1 and the southern hemisphere labelled 2. So we have only the order parameters σ_1 and σ_2, for the northern and the southern hemispheres respectively. Furthermore, since by the Stokes Theorem the net circulation must be zero, we know that $\sigma_2 = -\sigma_1$. The result of this is that the expression for the Helmholtz free energy becomes rather simple and so do the equations for critical points or fixed points already introduced. Making use of this partitioning for the free energy we find:

$$\begin{aligned}\Psi = {} & \sigma_1^2 V_1^2 \left(K_{1,2} - K_{1,1}\right) + 2\Omega\sigma_1 \\ & + k_b T 2\pi \left[\left(1+\sigma_1\right) \log\left(\frac{1+\sigma_1}{2}\right) + \left(1-\sigma_1\right) \log\left(\frac{1-\sigma_1}{2}\right) \right] \end{aligned} \tag{8.45}$$

To find the extremal values we need to solve the fixed point equations

$$\sigma_1 = \tanh\left[\beta\left(\Omega L_1 + \lambda\right) + \beta\sigma_1 V_1 \left(K_{1,1} - K_{1,2}\right)\right] \tag{8.46}$$

$$-\sigma_1 = \tanh\left[-\beta\left(\Omega L_1 - \lambda\right) - \beta\sigma_1 V_1 \left(K_{1,1} - K_{1,2}\right)\right] \tag{8.47}$$

which reduces to a fixed point equation in one variable:

$$\sigma_1 = \tanh\left[\beta\Omega L_1 + \beta\sigma_1 V_1 \left(K_{1,1} - K_{1,2}\right)\right] \tag{8.48}$$

In this case, $L_1 = -1$, and $V_1 = 2\pi$.

Finally we need an estimate for $K_{1,1}$ and $K_{1,2}$, that is, the mean energy of an edge. The precise value of this we know will depend on the number of mesh sites. It also depends a bit on the precise configuration of the mesh sites, but since we have assumed the mesh sites are uniform or nearly uniform on the sphere that will be a minor effect.

What is less dependent on the mesh size and is more closely what we find actually interesting is to look at $V_1^2 (K_{1,1} - K_{1,2})$, which appears in equation (8.48). We can estimate this, among other approaches, by using a Monte Carlo integrator, which finds that

$$K \equiv -V_1^2 (K_{1,1} - K_{1,2}) \approx 120 \tag{8.49}$$

This K we will use in the following subsections to consider first the case of a non-rotating planet and then the planet with rotation.

8.4.1 *The Non-Rotating Case*

The non-rotating case is addressed just as one might imagine, by setting the planetary rotation Ω to zero in equation (8.48):

$$\sigma_1 = \tanh [\beta \sigma_1 V_1 (K_{1,1} - K_{1,2})] \tag{8.50}$$

$$\approx \tanh [-120 \beta \sigma_1] \tag{8.51}$$

The free energy, with planetary rotation set to zero, becomes

$$\begin{aligned} \Psi &= \sigma_1^2 V_1^2 (K_{1,2} - K_{1,1}) \\ &\quad + k_b T 2\pi \left[(1 + \sigma_1) \log \left(\frac{1 + \sigma_1}{2} \right) + (1 - \sigma_1) \log \left(\frac{1 - \sigma_1}{2} \right) \right] \end{aligned} \tag{8.52}$$

There exists at least one solution to equation (8.50), and that is the obvious one: $\sigma_1 = 0$. This is the state in which the probability of any given mesh site in domain 1 being positive is $\frac{1}{2}$ and being negative is equally $\frac{1}{2}$. That is, the state is mixed. And as we have a two-domain problem and known σ_1, we also know $\sigma_2 = -\sigma_1 = 0$ and therefore positive and negative sites are equally probable in domain 2; thus, the mixed state is seen over the entire sphere.

The question is, is there another solution? For a positive temperature, which corresponds to positive β, we can answer this right away by considering the two sides of equation (8.50) as σ_1 is allowed to increase. The right-hand side of equation (8.50) decreases with increasing σ_1, while obviously the left-hand side increases. The conclusion is that the solution must be unique. In positive temperatures, then, we will see only the mixed state.

Now what of negative-temperatures, where $\beta < 0$? We still have, obviously, the solution $\sigma_1 = 0$ which is still the mixed state and will be seen in both domains. But are there other solutions, and if there are, then do they have a higher or lower free energy? We need that answer since in negative-temperatures the observed state is more likely to be the one which maximizes the free energy.

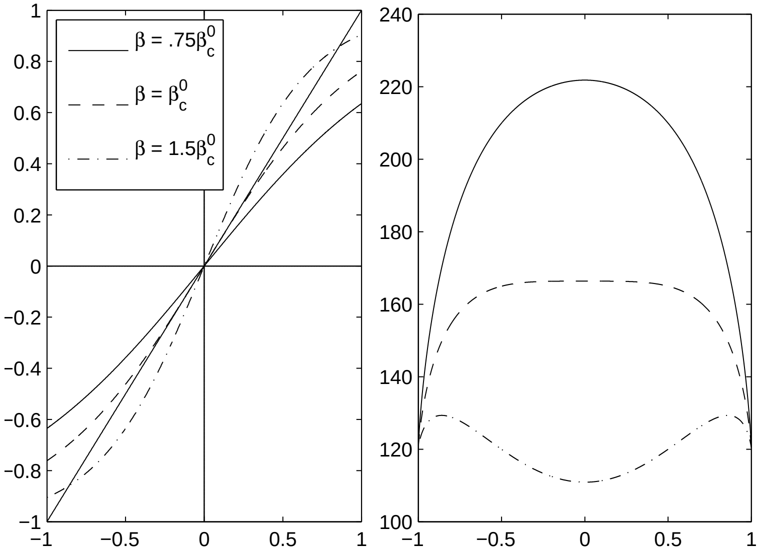

Fig. 8.1 On the left are the left-hand side and the right-hand sides of equations (8.48) for several values of β. On the right are the corresponding plots for the free energy. For all of these plots $\Omega = 0$.

Whether there is a second fixed point solution to equation (8.50) will depend on the slope of its right-hand side. Specifically, if the magnitude of the slope at its maximum is at least 1 then there will be at least one more solution, since the tanh function is bounded above and below. This consequence can be shown convincingly by inspecting a graph of the hyperbolic tangent function compared to the identity function.

The maximum slope, as a function of σ_1, will be found when $\sigma_1 = 0$, so that we can determine whether other solutions exist based entirely on the derivative of the right-hand side of equation (8.50) with respect to σ_1 evaluated at $\sigma_1 = 0$. This is the consideration which will give us a critical temperature and what information about phase transitions we can derive.

The slope of the right-hand side of equation (8.50) at $\sigma_1 = 0$ will be $\beta V_1 \left(K_{1,1} - K_{1,2}\right)$. The fixed point must exist when this slope is 1. And therefore we can find a critical temperature β_c^0: it must satisfy

$$\beta_c^0 V_1 \left(K_{1,1} - K_{1,2}\right) = 1 \tag{8.53}$$

and so the critical inverse temperature is

$$\beta_c^0 = -\frac{2\pi}{K} \tag{8.54}$$

If the inverse temperature β for our current statistical mechanics temperature is greater than the critical temperature β_c^0, but is still negative, then the slope of the right-hand side of equation (8.50) will be less than 1, and there will be no second fixed point. We have only the stationary point $\sigma_1 = 0$, the mixed state, just as we saw for the case of positive temperatures.

Now what if the inverse temperature β is less than the critical inverse temperature β_c^0? In this case the slope of the right-hand side of equation (8.50) is greater than 1 at its maximum, and therefore there will exist another fixed point. In fact, there must be two fixed points, a $\sigma_- < 0$ and a $\sigma_+ > 0$, each of which will be a non-zero maximizer of the free energy.

We know something further: the tanh function is odd in σ_1. And therefore σ^- must equal $-\sigma^+$. Furthermore, the free energy as in equation (8.52) is an even function in σ_1. Therefore we do not need to consider σ^- separately from σ^+, and all we need to consider are the energies at the fixed points σ^+ and σ^0.

Since σ^+ is positive, this corresponds to a state in which positive vorticities are more probable than negative vorticities are in domain 1. While the specific probability of this depends on β, we can still characterize this as the unmixed state or ordered state. The question is whether the free energy for σ^+ is greater or less than the free energy for σ^0.

It is easiest to estimate the free energy at σ^+ by looking at the Taylor series expansion for the free energy as expanded around $\sigma_1 = 0$. In this we have:

$$\Phi\left(\sigma\right) - \Phi\left(0\right) = \left(K + 2\pi k_B T\right)\sigma^2 + \frac{4\pi}{3} k_b T \sigma^4 + O\left(\sigma^6\right) > 0 \tag{8.55}$$

which indicates that the free energy at σ^+ will be greater than the free energy at σ^0.

Therefore, when $\beta < \beta_c^0 < 0$ it is statistically favorable to have the unmixed, or ordered, state: we expect to see solid-body rotating flow.

As a result we see that a standard symmetry-breaking phase transition is predicted by the fixed-point equation in the Bragg mean-field. Happily, this agrees with both the simple mean-field theory prediction [56] and with the spherical model [19] [20] [58] [59] [63].

So we have overall established the result:

Proposition 8.1. *In the non-rotating case of the Bragg model, there is a negative-temperature phase transition to a solid-body-rotating ordered state* *for* $\beta < \beta_c^0 = -\frac{2\pi}{K} < 0$*. For all other values of the temperature, both positive and negative, the most probable state is a mixed-vorticity state.*

8.4.2 *The Rotating Case*

The remaining case is that of the nonzero planetary rotation, and this is forced to be more complicated because we do not have the symmetries which reduced the number of cases we had to consider before. Nevertheless, we can still see that equation (8.48) must have at least one solution, and it may have as many as three, depending on the slope of its right-hand side. And the free energy will have a term which is not even in σ_1, but it is not seriously more complicated to approximate by a Taylor series expansion around $\sigma_1 = 0$, and we can still evaluate which of the fixed points will have the greatest or the least free energies.

So as with the non-rotating case we will look first at positive and then at negative-temperatures, identifying critical temperatures and then in each of these temperature regions finding fixed points for σ_1. With these we then compare free energies to see whether we may expect the most probable distribution to have σ_1 at zero, which would be the mixed state; to have σ_1 positive, which would be an unmixed solid-body rotation moving in the same direction as the planetary rotation; or to have σ_1 negative, which would be an unmixed solid-body rotation moving in the opposite direction as the planetary rotation.

This difference between the states requires some guiding principle: it is obvious that if σ_1 is just a little different from zero that we have what is essentially the mixed state; and if σ_1 is just slightly less than 1, or slightly greater than -1, we still have the unmixed state. Where should we put the dividing line between describing the system as being in the mixed state from being in the unmixed state if all we have to consider is the order parameter σ_1? It is arbitrary, but also convenient, to make the dividing line be where $|\sigma_1|$ equals $\frac{1}{2}$: if the magnitude of the order parameter is less than $\frac{1}{2}$, we have the mixed state; if the magnitude is greater than $\frac{1}{2}$ we have the unmixed state.

Consider the fixed-point equation, equation (8.48), which with nonzero rotation Ω will remain

$$\sigma_1 = \tanh\left[\beta\Omega L_1 + \beta\sigma_1 V_1\left(K_{1,1} - K_{1,2}\right)\right] \tag{8.56}$$

Regardless of whether the temperature is positive or negative, when the planetary rotation Ω is positive, the right-hand side of the fixed-point equation (8.48) will be zero at the value

$$\bar{\sigma}_1 = -\frac{2\pi\Omega}{K} < 0 \tag{8.57}$$

since $K > 0$. Furthermore, the zero $\bar{\sigma}_1$ satisfies

$$-1 < \bar{\sigma}_1 < 0 \tag{8.58}$$

if and only if the planetary rotation Ω satisfies the condition

$$0 < \Omega < \Omega_{cc} = \frac{K}{2\pi} \tag{8.59}$$

where Ω_{cc} is a critical rotation speed that is independent of the temperature. The condition is, therefore, that planetary rotation is not too fast. This condition proves to be significant for determining the fixed points of equation (8.48) in the rotating case.

When the planetary rotation Ω is positive, the free energy can be approximated in terms of σ by the Taylor series expansion

$$\begin{aligned} \Psi_{T,\Omega}(\sigma) = -4\pi k_B T \log(2) + 2\Omega\sigma + (K + 2\pi k_B T)\,\sigma^2 \\ + \frac{1}{3}\pi k_B T \sigma^4 + O\left(\sigma^6\right) \end{aligned} \tag{8.60}$$

Positive Temperatures

We start by considering positive temperatures and thus $\beta > 0$. The right-hand side of equation (8.48) is decreasing in σ_1, and it is bounded between -1 and $+1$, much as we saw in the non-rotating case. This dictates that there must be a fixed point σ_1 of equation (8.48), and that it must satisfy

$$-1 < \sigma_1 < 0 \tag{8.61}$$

Now further consider the shape of the right-hand side of equation (8.48), which is plotted in Figure 8.1. From it we know the fixed point must also satisfy

$$\bar{\sigma}_1 < \sigma_1 < 0 \tag{8.62}$$

And as the inverse temperature $\beta \to \infty$, it follows that σ_1 approaches, decreasing, the maximum of $\bar{\sigma}_1$ and -1.

Suppose the planetary rotation Ω is smaller than the threshold value

$$\Omega_c = \frac{K}{4\pi} > 0, \tag{8.63}$$

and furthermore that the zero $\bar{\sigma}_1$ satisfies

$$-\frac{1}{2} < \bar{\sigma}_1 < 0 \tag{8.64}$$

What, then, does equation (8.62) tell us about the fixed point? In this case, it must satisfty

$$-\frac{1}{2} < \sigma_1 < 0 \tag{8.65}$$

From the fixed-point equation (8.48) therefore we find a phase transition where $\sigma < -\frac{1}{2}$ at the positive critical temperature

$$T^+(\Omega)\, k_B = \frac{4\pi\Omega - K}{2\pi \log(3)} \tag{8.66}$$

Because Ω_c is independent of the inverse temperature $\beta > 0$, we have established this proposition:

Proposition 8.2. *(a) The most probable state in the Bragg model is the mixed -vorticity state for all positive temperatures when planetary spins are smaller than Ω_c. There are therefore no phase transitions in positive temperatures in this case. (This is shown in Figure 8.5 where the fixed points are plotted against temperature T for very small $\Omega < \Omega_c$.)*

(b) On the other hand, for planetary spins that are not small — that is

$$\Omega \geq \Omega_c = \frac{K}{4\pi} \tag{8.67}$$

— the fixed point $\sigma_1(\beta) \in (-1, 0)$ has continuously-increasing long-range order as the temperature decreases (see Figure 8.4) and below $T_c^+(\Omega) > 0$, the statistical equilibrium $\sigma_1 < -\frac{1}{2}$ is an organized counter-rotating physical flow.

This matches the results found in the simple mean-field theory in the case of positive temperatures [56]. The properties of this first threshold value of the planetary rotation are clearly shown in Figure 8.2 and Figure 8.3 where the fixed points σ and the free energy, respectively, are plotted against temperature T for planetary rotation $\Omega = \Omega_c$.

Transition Between Positive and Negative-Temperatures With Large $|T|$

For all planetary rotations Ω the most probable state changes smoothly through mixed states between high positive temperatures $T \gg 1$ and the large-absolute-valued negative-temperatures $T \ll -1$. At $T \gg 1$ the preferred mixed-state or fixed-point has a small negative angular momentum — it is a counter-rotating state, although only slightly. For $T \ll -1$ it is the reverse: the fixed-point is a mixed state which has a small positive angular momentum, or pro-rotation bias. These are shown in the plots of Figures 8.4 and 8.5 for several distinct values of rotation Ω.

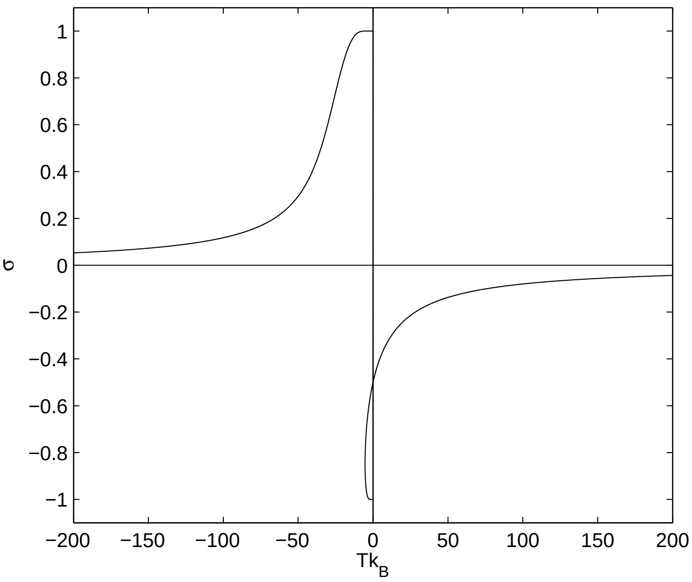

Fig. 8.2 A graph of σ versus $k_B T$ when $\Omega = \Omega_c$.

Negative-Temperature

With negative-temperatures we remember how the non-rotating problem found a critical temperature at which the single fixed point split into three fixed points. It is reasonable to suppose that this sort of critical temperature will exist for negative-temperatures when the planet is rotating. Therefore, we will look for two sub-cases to the negative-temperature case.

The first sub-case supposes that the fixed-point equation has the possibility of multiple fixed points. In the second sub-case we suppose the fixed point equation has exactly one fixed point. In both categories, as the negative T increases — that is, decreases in absolute value, drawing towards zero — and for all values of the planetary rotation the slightly pro-rotating mixed state gives way continuously to a strongly pro-rotating state at $\beta^{-}(\Omega) < 0$.

$\beta^{-}(\Omega)$ is chosen to be the value of β for which the fixed point $\sigma_1(\beta^{-}) = \frac{1}{2}$. We see this β depicted in Figures 8.2, 8.4, and 8.5 for several values of the planetary rotation.

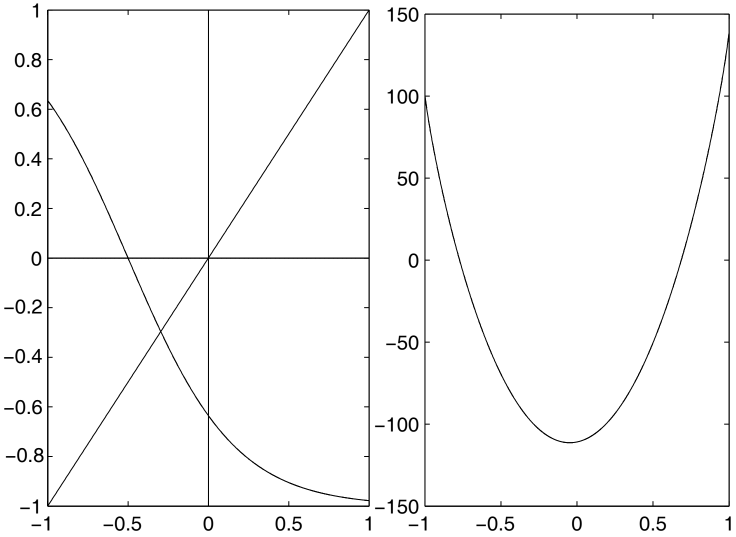

Fig. 8.3 On the left is a graph of the fixed point when $\beta = 0$ and $\Omega = \Omega_c$. On the right is the free energy.

Solving the fixed-point equation (8.48) for $k_B T$ gives

$$k_b T = \frac{2\pi\Omega + \sigma K}{\pi \log\left(\frac{1-\sigma}{1+\sigma}\right)} \tag{8.68}$$

and so therefore

$$\beta^-(\Omega) = -\frac{2\pi \log(3)}{4\pi\Omega + K} \tag{8.69}$$

But there is another temperature threshold, which we anticipate as a result of inspecting Figures 8.2, 8.4, and 8.5, at least when the spin is not too large. This threshold,

$$\beta_c^\Omega < 0 \tag{8.70}$$

is the value for which multiple fixed points appear when $\beta \leq \beta_c^\Omega$ and when $\Omega < \Omega_{cc}$. Both of these terms we will define shortly, so that we will finally know what to make of the Ω_{cc} asserted above to be important and independent of temperature.

We can estimate β_c^Ω. The critical value leading to the appearance of two more counter-rotating solutions of equation (8.48) is given by

$$0 = \frac{d\left(k_b T\right)}{d\sigma} = \frac{K\left(1-\sigma^2\right)\log\left(\frac{1+\sigma}{1-\sigma}\right) + 4\pi\Omega + \sigma 2K}{\pi\left(1-\sigma^2\right)\left(\log\left(\frac{1-\sigma}{1+\sigma}\right)\right)^2} \tag{8.71}$$

and from this it follows

$$\beta_c^\Omega = \left.\frac{-2\pi}{K\left(1-\sigma^2\right)}\right|_{\sigma=\sigma^\Omega} \tag{8.72}$$

Approximating the numerator on the right-hand side of equation (8.71) by a third-order polynomial in σ gives

$$\sigma^\Omega \approx -\left(\frac{3\pi\Omega}{K}\right)^{\frac{1}{3}} \tag{8.73}$$

and so we conclude

Lemma 8.1. *The critical temperature T_c^Ω is increasing in Ω.*

Its proof follows immediately from equations (8.72) and (8.73): σ^Ω increases with Ω, and β_c^Ω is proportional to the inverse of σ^Ω, and of course T_c^Ω is proportional to the inverse of β_c^Ω.

One Fixed Point

In the case of negative-temperatures the fact that there is a physical bound $|\sigma_1| \leq 1$ in the fixed-point equation, equation (8.48), implies that there is another threshold, this Ω_{cc}, on the planetary rotation rate. When

$$\Omega \geq \Omega_{cc} = \frac{V_1\left(K_{1,1} - K_{1,2}\right)}{L_1} = 2\Omega_c \tag{8.74}$$

there exist only pro-rotating solutions, $\sigma_1 > 0$, to the fixed-point equation. Any negative fixed-point $\sigma_1^- < 0$, if they existed, would have to satisfy

$$\sigma_1^- < \bar{\sigma}_1 < 0 \tag{8.75}$$

while the zero $\bar{\sigma}_1$ must satisfy

$$\bar{\sigma}_1 < -1 \tag{8.76}$$

to respect equations (8.58) and (8.59). This would lead to the contradiction $\sigma_1^- < -1$.

Therefore we have the result:

Proposition 8.3. *For large spins $\Omega > \Omega_{cc}$ there is a single negative-temperature transition at $\beta^-(\Omega) < 0$ between the mixed and the strongly pro-rotating state for $|T| \ll 1$.*

Multiple Fixed Points

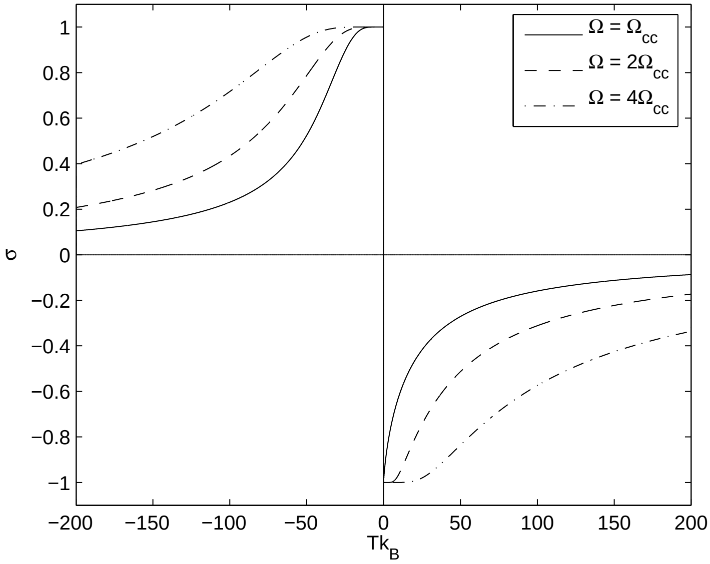

Fig. 8.4 A graph of σ versus $k_B T$ when $\Omega \geq \Omega_{cc}$.

When $\Omega < \Omega_{cc}$ it is possible for the argument of tanh in equation (8.48) to be zero at values of $\bar{\sigma}_1$ within the physical range $-1 < \bar{\sigma}_1 < 0$. In turn this makes it possible to have counter-rotating or mixed-state fixed points which satisfy

$$-1 \leq \sigma_1 < \bar{\sigma}_1 < 0 \tag{8.77}$$

provided that in addition the inverse temperature satisfies the condition

$$\beta \leq \beta_c^{\Omega} < 0 \tag{8.78}$$

In the case where $\Omega \leq \Omega_{cc}$ and $\beta \leq \beta_c^{\Omega}$ there are (generically) three fixed points, which is to be expected from the shape of the curve of tanh. One of these fixed states is pro-rotating. In general, there will be two other fixed points: one which is strongly counter-rotating; and one which is mixed, with a small counter-rotation. There is a degenerate case: these two will merge into a single mixed, counter-rotating solution when $\beta = \beta_c^{\Omega}$. This last threshold $\beta_c^{\Omega} < 0$ follows because the value of $-\beta$ determines the slope

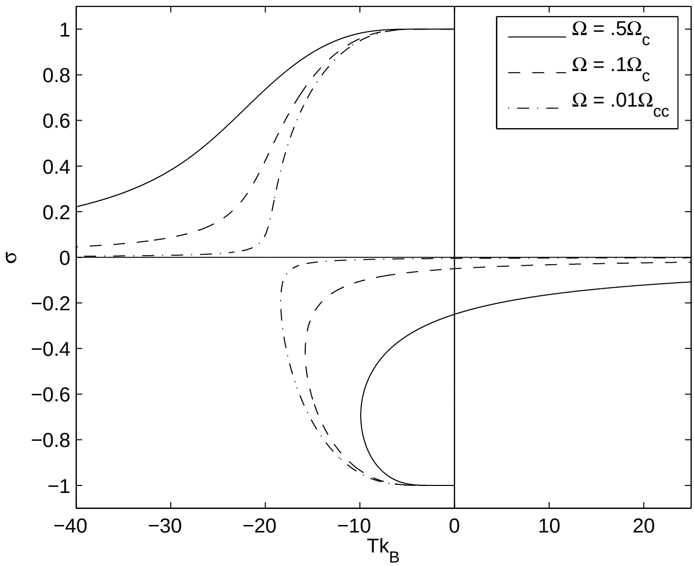

Fig. 8.5 A graph of σ versus $k_B T$ when $\Omega_c\, \Omega > 0$.

of tanh near zero, and we need a large enough slope in order for the graph of tanh to intersect the line of the identity function.

There is a transition at $\beta^-(\Omega) < 0$ between the mixed state and the strongly pro-rotating state, and there is another negative-temperature transition $\beta_c^\Omega < 0$ when $\Omega < \Omega_{cc}$ where the additional critical points are as defined by equation (8.60). The Bragg free energy has a simple form in this case, which can be used to see that the pro-rotating solution has a greater free energy than the counter-rotating solution in negative-temperatures close to zero. This is shown in Figure 8.6 for $\beta > \beta_c^\Omega$.

In the two-domain case, $\Omega > 0$ adds a linear term to the free energy functional:

$$\Psi_{T,\Omega}(\sigma) = \Psi_{T,0}(\sigma) + 2\Omega\sigma \tag{8.79}$$

We found in the non-rotating case that for $0 > T > T_c^0$ the free energy has two maximizers, which we denote here as $\bar{\sigma}^+$ and $\bar{\sigma}^-$ (we had previously labelled them σ^+ and σ^-). Since the free energy in the non-rotating case is even we knew $\bar{\sigma}^- = -\bar{\sigma}^+$. So from lemma 8.1 and from equation (8.79)

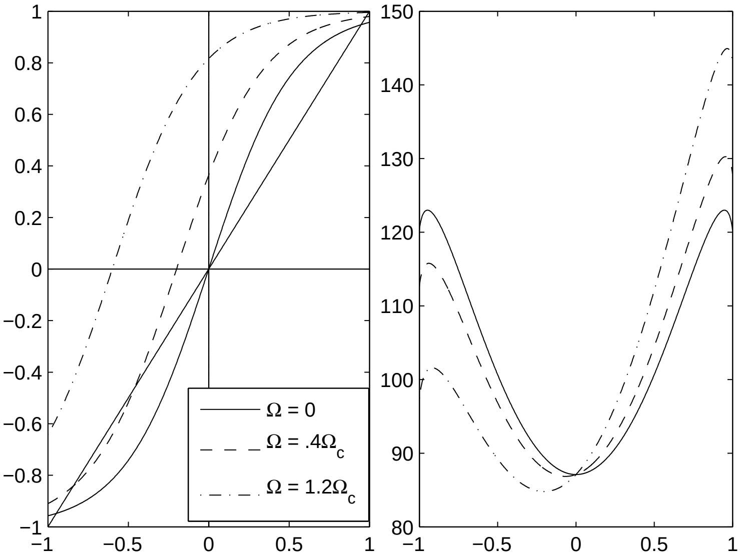

Fig. 8.6 On the left are plots of fixed points. On the right are plots of the corresponding free energies. Both plots are for the same value of $\beta < \beta_c^\Omega < 0$.

then

$$\Psi_{T,\Omega}\left(\bar{\sigma}^-\right) < \Psi_{T,\Omega}\left(\sigma^-\right) < \Psi_{T,\Omega}\left(\bar{\sigma}^+\right) < \Psi_{T,\Omega}\left(\sigma^+\right) \tag{8.80}$$

Interestingly, $\bar{\sigma}^- < \sigma^- < 0 < \bar{\sigma}^+ < \sigma^+$. Physically, this implies that the ordered state $\sigma_1^+ > 0$, in which positive relative vorticity determines the northern hemisphere, is more ordered than the symmetric solutions at $\Omega = 0$, which is in turn more ordered than the counter-rotating fixed point $\sigma_1^- < 0$. Thus we have demonstrated

Proposition 8.4. *For rotations not too fast, that is if $\Omega \leq \Omega_{cc}$, then for the hottest inverse temperatures, such that $\beta < \beta_c^\Omega < 0$, there are exactly three fixed points in the Bragg model. But the most probable state is pro-rotating such that $\sigma_1 \nearrow 1$.*

8.4.3 *Summary of Main Results*

To sum up: the simple two-domain case of the fixed-point equation predicts that in the rotating problem there are two critical values of the planetary rotation. The first is Ω_c as defined in equation (8.63), and the second is $\Omega_{cc} = 2\Omega_c$. Below Ω_c, there is no transition at positive temperatures, and the most probable flow state is mainly a mixed state (per equation (8.65)), with some small amount of counter-rotation. This counter-rotation vanishes as the temperature increases. For planetary rotations above Ω_c, there is a continuous positive-temperature transition from mixed states at $T > T_c^+(\Omega)$ to strongly counter-rotating barotropic states at lower positive temperatures.

For all values of planetary rotation, there is a smooth transition through mixed states at $\beta = 0$ between slightly counter-rotating mixed states for $T \gg 1$ and the slightly pro-rotating mixed states for negative T with $|T| \gg 1$. Once again, for all values of planetary rotation Ω, there is a continuous transition at $\beta^-(\Omega) < 0$ between mixed states for cooler negative $\beta > \beta^-(\Omega)$ and strongly pro-rotating states for hotter $\beta < \beta^-(\Omega)$. For the larger rotations $\Omega > \Omega_{cc}$ this is the only possible transition at negative-temperatures.

For intermediate-to-small values of the planetary rotation, $\Omega < \Omega_{cc}$, there is a negative threshold β_c^Ω at which we have the possibility of multiple — and for that matter metastable — thermodynamic equilibriums. When there are multiple fixed points the pro-rotating branch has the largest free energy and therefore it continues to be the thermodynamically stable macrostate. Therefore, for all rotations there is a single negative-temperature transition at $\beta^-(\Omega) < 0$ to the pro-rotating state for the hottest negative-temperatures (those with the smallest absolute values, corresponding to the largest kinetic energy).

8.5 The Infinite-Dimensional Non-Extensive Limit

This model has not got an extensive limit from which we can calculate intensive quantities. However, we have built directly a non-extensive model. We can support drawing conclusions about a continuum model by convergence theorems. The continuous case will look very much like the analog case; we need just a few constraints for analytic consideration.

Consider a set of domain systems all of which are built from the Voronoi cells on a uniform mesh, which allows us to assume that the coarse-grained domains will be spatially symmetric. What we will describe as a Bragg process will be the sequence of domain systems and their associated ensembles.

The limiting ensemble of a Bragg process is the $L_2\left(S^2\right)$ space of functions σ which map the unit sphere S^2 onto the interval $[-1, 1]$. This ensemble has a functional for the free energy which is analogous to the free energy formula in the discrete case:

$$\begin{aligned}\Psi\left[\sigma\right] = -\frac{1}{2}\int dx \int dy\, \sigma\left(x\right)\sigma\left(y\right)K\left(x,y\right) - \Omega\int dx\, \sigma\left(x\right)L\left(x\right) \\ +k_B T\int dx\left[\begin{array}{c}\left(\frac{1+\sigma(x)}{2}\right)\log\left(\frac{1+\sigma(x)}{2}\right) \\ +\left(\frac{1-\sigma(x)}{2}\right)\log\left(\frac{1-\sigma(x)}{2}\right)\end{array}\right]\end{aligned} \tag{8.81}$$

from which we can recover the analog to the fixed-point equation.

When we look for extremes of the free energy we need to limit our search to the subspace of functions which are constrained by Stokes's Theorem, the space

$$\Sigma = \left\{\sigma : S^2 \mapsto [-1, 1] \middle| \int_{S^2} dx\, \sigma\left(x\right) = 0\right\} \tag{8.82}$$

Another physical constraint, the bounded relative enstrophy, is implicit in the condition that $|\sigma| \leq 1$ in the fixed-point equation. The fixed-point equation can be derived, in the continuous case, in a form that is analogous to that of the discrete case:

$$\sigma\left(x\right) = \tanh\left[\beta\left(\Omega L\left(x\right) + \lambda\right) + \beta\int_{S^2} dy\, \sigma\left(y\right)K\left(x,y\right)\right] \tag{8.83}$$

From the definition of K as per equation (8.24) we recover the inverse Laplacian G, and so equation (8.83) can be rewritten as

$$\Delta\psi = \tanh\left[\beta\left(\Omega L\left(x\right) + \lambda + \psi\right)\right] \tag{8.84}$$

where ψ is the coarse-grained stream function. This form provides, given the conditions that $L\left(x\right)$ is proportional to the first spherical harmonic, and that $\langle\Delta\psi\rangle = 0$ we conclude that $\lambda = 0$. For any ψ, in fact, $\lambda = 0$ implies

$$\langle\tanh\left[\beta\left(\Omega L\left(x\right) + \lambda + \psi\right)\right]\rangle = 0 \tag{8.85}$$

and

$$\frac{d}{d\lambda}\langle\tanh\left[\beta\left(\Omega L\left(x\right) + \lambda + \psi\right)\right]\rangle = \left\langle\frac{d}{d\lambda}\tanh\left[\beta\left(\Omega L\left(x\right) + \lambda + \psi\right)\right]\right\rangle \tag{8.86}$$

$$= \left\langle\beta\cosh^{-2}\left[\beta\left(\Omega L\left(x\right) + \lambda + \psi\right)\right]\right\rangle \tag{8.87}$$

which must be the same sign as β and which therefore shows the average will be monotonic in λ.

The discrete model was limited in its degrees of freedom. Here, we have a continuum for the spin as the coarse-grained state is given by a bounded function, $\sigma(x)$ in $L_2(S^2)$, constrained to zero circulation, $\int_{S^2} dx\, \sigma(x) = 0$.

The Bragg estimation of the interaction energy became a very accurate one in the continuum model, at the cost — a cost which is common to all mean-field models — of an artifact in the entropy estimation. However, the Shannon entropy of a binary variable is what allows the derivation of the tanh fixed-point equation.

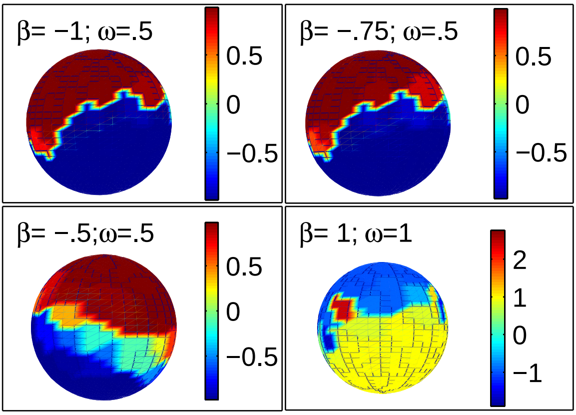

Fig. 8.7 These are several fixed point solutions.

In Figure 8.7 we have some spin states of some thermodynamic regimes calculated numerically.

Chapter 9

Phase Transitions to Super-Rotation — Exact Closed-Form Solutions

9.1 Introduction

We have been introduced to the mean-field theory approach to identifying phase transitions and extremal states for the barotropic flow of an inviscid fluid on a rotating sphere. Along the way, we have mentioned in a few spots that these models can be addressed by the spherical model, in which we constrain the enstrophy of the system microcanonically. We know from the mean-field theory treatment that we can expect to see mixed and organized states in negative and positive temperatures, with perhaps the critical temperatures between regions dependent on planetary rotation. It is rare and fortuitous that an exactly-solvable non-Gaussian model can be formulated for macroscopic flows on a sphere but the coincidence of the notions of relative enstrophy as square-norm and high-dimensional spherical constraint provides just such a rare chance to fully solve for and flesh out the details of the critical phenomena around the transitions to super-rotation and sub-rotation in a rapidly-spinning sphere. The focus of this chapter is to show how Kac's spherical model can be used to solve in closed-form the critical temperatures of phase transitions for barotropic flows on a non-rotating sphere, and to show how this approach differs from Gaussian models [58], leaving the reader to consult [59] for the corresponding exact solutions in the case of the rotating Barotropic Vorticity Model.

The main statement of the theorems in [59] confirms the MC simulations in [20], discussed in chapter 6, the mean-field results in [56], discussed in chapter 7 and in [61], discussed in chapter 8: there is a physically significant asymmetry between super-rotating and sub-rotating vertically-averaged barotropic, non-divergent flows on a rotating sphere, due chiefly to an energy gap in the angular momentum part of the energy functional, Lagrangian of the Barotropic Vorticity Equations, which anticipates the results in chapters 10 and 11 on the dichotomy between the cyclonic and anticyclonic flow states of the Shallow Water Model. Specifically, our exact solution of the rotating Barotropic Vorticity Model by Kac's spherical model methods, states that, no matter what the spin-rate, there is a high enough energy-to-relative enstrophy threshold, depending on spin-rate, above which, the most-probable statistical flow states comprise a largely super-rotating atmosphere. In contrast, it states that, only when the spin-rate is large enough, there is an energy-to-enstrophy threshold, below which, the most-probable state is a chiefly anti- or sub-rotating flow.

In our solar system, there are two data points of super-rotating atmospheres, Titan, the major moon of Saturn and Venus, both of which are slowly-rotating, in agreement with our rigorous results here, and have thick heavy aatmospheres that have very high zonal winds exceeding 100m/s.

In the next section, for the sake of completeness, we will give the formulation in terms of the full Barotropic Vorticity Model on a rotating sphere where the keystone of the model appears as a two-dimensional Ising-Heisenberg lattice model [58], [59].

9.2 The Rotating Sphere Model

As we have in earlier chapters we begin with spherical coordinates ϕ and $\cos(\theta)$ to describe points in the planetary atmosphere, which we assume to be thin enough not to require a third coordinate, and we let the planetary rotation be Ω. So the total vorticity q at any time t is a function

$$q\left(t; \cos(\theta), \phi\right) = \Delta\psi + 2\Omega\cos(\theta) \tag{9.1}$$

for a relative velocity stream function ψ, so that the relative vorticity $w = \Delta\psi$, and using the negative Laplace-Beltrami operator on the unit sphere Δ.

Suppose that we put a mesh of N points $\vec{x}_j$, distributed uniformly on the surface of the sphere, so that we can use the piecewise constant approximation for the relative vorticity w based on the Voronoi cells on a lattice. That is, at each mesh site $\vec{x}_j$ we represent the vorticity in the Voronoi cell around that point with the single spin s_j, as we began the mean-field theories. With this discretization, the truncated energy or pseudoenergy — it is not exactly the energy of the continuous flow which we want to approximate — has a standard form, pairwise interaction and point-planet interaction form, for a spin-lattice model:

$$H_N = -\frac{1}{2}\sum_{j=1}^{N}\sum_{k=1}^{N} J_{j,k} s_j s_k - \sum_{j=1}^{N} F_j s_j \tag{9.2}$$

where we define the interactions to be

$$J_{j,k} = \frac{16\pi^2}{N^2} \log |1 - \vec{x}_j \cdot \vec{x}_k| \tag{9.3}$$

(while $J_{j,j} \equiv 0$) between points and the external fields

$$F_j = -\frac{2\pi}{N}\Omega \| \cos(\theta) \|_2 \psi_{1,0}(\vec{x}_j) \tag{9.4}$$

to represent the point-planet coupling. In this case $\| \cos(\theta) \|_2$ is the L_2 norm of the function $\cos(\theta)$, and the spherical harmonic $\psi_{1,0}$ is the relative vorticity of solid-body rotation.

The truncated relative enstrophy, reflecting just the mesh sites in our particular discretization, is

$$\Gamma_N = \frac{4\pi}{N}\sum_{j=1}^{N} s_j^2 = \frac{4\pi}{N}\vec{s}\cdot\vec{s} \tag{9.5}$$

and for the spherical model this is fixed. The vector $\vec{s}$ is an ordered list of all the values of the vortex spin at the mesh sites.

The truncated circulation similarly we find by calculating

$$TC_N = \frac{4\pi}{N}\sum_{j=1}^{N} s_j \tag{9.6}$$

and it is also fixed, at zero. Having established this pairwise-particle interaction, we will shortly be getting rid of it, because it is vastly more convenient numerically to work with the spectral decomposition of a vorticity field which matches our discretization at the mesh sites.

A relative vorticity field can be expanded in terms of the spherical harmonics:

$$w(x) = \sum_{l\geq 1}^{\infty}\sum_{m=-1}^{l} \alpha_{l,m}\psi_{l,m}(x) \tag{9.7}$$

which will provide our spectral decomposition of the vorticity field. The spherical harmonics are particularly tempting to us not only because of their appealing properties as an orthonormal basis set for the set of square-integrable functions defined on the surface of the sphere, but also because we know they serve as Green's functions for the Laplace-Beltrami operator, and we therefore expect to see them in the analysis of functions modelling the vorticity of a fluid flow. Another appealing trait is that they automatically preserve the total circulation over the sphere at zero, so that we have this constraint without having to make any further explicit allowance for it.

The eigenvalues of the Green's function for the Laplace-Beltrami operator on the unit sphere are

$$\lambda_{l,m} = \frac{1}{l\left(l+1\right)} \text{ for } l = 1, 2, 3, \cdots; m = -l, -l+1, \cdots, 0, \cdots, l \tag{9.8}$$

We will find $\alpha_{l,m}$ to be the spectral components so that

$$s\left(\vec{x}_j\right) = \sum_{l=1} \sum_{m=-l}^{l} \alpha_{l,m} \psi_{l,m}\left(\vec{x}_j\right) \tag{9.9}$$

for each mesh site $\vec{x}_j$.

One of the consequences of this expansion is that the mode $\alpha_{1,0}\psi_{1,0}\left(x\right)$ contains all the angular momentum in the relative flow, as measured in the reference frame rotating at the fixed angular velocity Ω, that is, in the reference frame rotating with the planet.

Another consequence which is not obvious but which greatly simplifies our taking of the spectral decomposition is that we will want to only look at mesh sizes N which are perfect squares. In this way we can look at the spectral decomposition for the first harmonic number l starting at 1 and increasing to $\sqrt{N}$, with the second harmonic number m an index between $-l$ up to l. Analytically this is convenient; when running numerical simulations, this simply encourages one to look at even powers of two for the number of mesh sites.

9.3 Solution of the Spherical Model

What is the exact solution to the spherical model [8] for barotropic flows in the inertial frame? That is the objective for this section, and further details are provided in [58] and [59].

The partition function Z_N for the spherical model on N mesh sites has the form

$$Z_N \propto \int d\vec{s}\, D\left(\vec{s}\right) \exp\left(-\beta H_N\left(\vec{s}\right)\right) \delta\left(\Gamma_N \frac{N}{4\pi} - \sum_{j=1}^{N} \vec{s}_j \cdot \vec{s}_k\right) \tag{9.10}$$

where the integral in equation (9.10) is a path integral taken over all the microstates $\vec{s}$ where circulation is zero. The Dirac delta function is of course the microcanonical constraint on enstrophy. $D(\vec{s})$ is the degeneracy of the microstate $\vec{s}$, and $\exp(-\beta H_N)$ is the Gibbs factor based on the energy of the microstate as we might expect.

In the thermodynamic limit, the continuum limit, in which we consider this integral as $N \to \infty$ this partition function can be calculated by using the Laplace integral transformation, which changes the Dirac delta into a line integral in the complex plane:

$$Z_N \propto \int d\vec{s}\, D(\vec{s}) \exp\left((-\beta H_N(\vec{s}))\right) \delta\left(\Gamma_N \frac{N}{4\pi} - \sum_{j=1}^{N} \vec{s}_j \cdot \vec{s}_k\right) \tag{9.11}$$

$$= \int d\vec{s} D(s) \exp\left((-\beta H_N(\vec{s}))\right) \times \left(\frac{1}{2\pi\imath} \int_{a-\imath\infty}^{a+\imath\infty} d\eta \exp\left(\eta\left(\Gamma_N \frac{N}{4\pi} - \sum_{j=1}^{N} \vec{s}_j \cdot \vec{s}_k\right)\right)\right) \tag{9.12}$$

In order to solve this integral we change our form for writing the site vorticities $\vec{s}_j$ away from the explicit mesh-dependent form and into the form in terms of the spherical harmonics $\{\psi_{l,m}\}_{l=1}^{\infty}$, and we use this to diagonalize the interactions H_N:

$$Z_N \propto \int D(\alpha) \exp\left(-\frac{\beta}{2} \sum_{l=1} \sum_{m=-l}^{m} \lambda_{l,m} \alpha_{l,m}^2\right) \times \left(\frac{1}{2\pi\imath} \int_{a-\imath\infty}^{a+\imath\infty} d\eta \exp\left(\eta N\left(1 - \frac{4\pi}{\Gamma_N} \sum_{l=1} \sum_{m=-l}^{l} \alpha_{l,m}^2\right)\right)\right) \tag{9.13}$$

with $\lambda_{l,m}$ and $\alpha_{l,m}$ as defined in the previous section. For any particular mesh l will be taken only up to $\sqrt{N}$, but it does not confuse the analysis here if we simply let the upper bound on l go unstated in these formulas.

Our next step is to swap the order of integration in equation (9.13). This is analytically permitted, provided that a is positive and is large enough for the integrand to be absolutely convergent. What we gain by doing this is an innermost integral that is the product of a collection of Gaussian integrals, that is, ones which have the form of integrating the exponential of a squared quantity, the classic bell curve distribution. We know what these integrals are, provided that certain constraints on the scaling factors in the distribution are satisfied. These factors will themselves prove to be describable as physically significant conditions.

The next step will be to rescale the inverse temperature, defining the new $\beta^{'}N \equiv \beta$. This rescaling, after the change in the order of integration, yields

$$Z_N \propto \frac{1}{2\pi\imath}\int_{a-\imath\infty}^{a+\imath\infty} d\eta \exp\left(\begin{array}{c} \eta n\left(1-\frac{4\pi}{\Gamma_N}\sum_{l=1}\sum_{m=-l}^{l}\alpha_{l,m}^2\right) \\ -\frac{\beta^{'}N}{2}\sum_{m=-1}^{1}\lambda_{1,m}\alpha_{1,m}^2 \end{array}\right)$$
$$\times \int_{l\geq 2} D\left(\alpha\right)\exp\left(-\sum_{l=2}\sum_{m=-l}^{l}\left(\frac{\beta^{'}N\lambda_{l,m}}{2}+N\eta\frac{4\pi}{\Gamma_N}\right)\alpha_{l,m}^2\right) \quad (9.14)$$

This inner integral is the promised collection of Gaussian integrals. It is explicitly solvable despite being the product of many of them:

$$\int_{l\geq 2} D\left(\alpha\right)\exp\left(-\sum_{l=2}\sum_{m=-l}^{l}\left(\frac{\beta^{'}N\lambda_{l,m}}{2}+N\eta\frac{4\pi}{\Gamma_N}\right)\alpha_{l,m}^2\right)$$
$$=\prod_{l=2}^{\sqrt{N}}\prod_{m=-l}^{l}\left(\frac{\pi}{N\eta\frac{4\pi}{\Gamma_N}+\frac{\beta^{'}N}{2}\lambda_{l,m}}\right)^{\frac{1}{2}} \quad (9.15)$$

provided we satisfy this physically important condition:

$$\frac{\beta^{'}\lambda_{l,m}}{2}+\eta\frac{4\pi}{\Gamma_N}>0 \text{ for } l=2,3,4,\cdots,\sqrt{N}; m=-l,-l+1,\cdots,0,\cdots,l \quad (9.16)$$

Since we have evaluated the innermost integrals, we can rewrite equation (9.14) in a form which is longer and yet simpler:

$$Z_N \propto \int_{a-\imath\infty}^{a+\imath\infty} d\eta \exp\left(\begin{array}{l} \eta\left(1-\frac{4\pi}{\Gamma_N}\sum_{m=-1}^{1}\alpha_{1,m}^2\right) \\ \quad -\frac{\beta^{'}}{2}\sum_{m=-1}^{1}\lambda_{1,m}\alpha_{1,m}^2 \\ \quad -\frac{1}{2N}\sum_{l=2}\sum_{m}\log\left(N\eta\frac{4\pi}{\Gamma_N}+\frac{\beta^{'}N}{2}\lambda_{l,m}\right) \end{array}\right) \quad (9.17)$$

One approach we can use successfully to solve this is the saddle point method, or the method of steepest descent. To do this we will rewrite equation (9.17) in a suitable form:

$$Z \propto \lim_{N\to\infty}\frac{1}{2\pi\imath}\int_{a-\imath\infty}^{a+\imath\infty} d\eta \exp\left(NF\left(\eta,\Gamma_N,\beta\right)\right) \quad (9.18)$$

In the thermodynamic limit, as $N \to \infty$, the free energy per site, modulo a factor of $-\beta^{'}$, given by

$$F\left(\eta,\Gamma_N,\beta^{'}\right)=\eta\left(1-\frac{4\pi}{\Gamma_N}\sum_{m=-1}^{1}\alpha_{1,m}^2\right)-\frac{\beta^{'}}{2}\sum_{m=-1}^{1}\lambda_{1,m}\alpha_{1,m}^2$$
$$-\frac{1}{2N}\sum_{l=2}\sum_{m=-l}^{l}\log\left(N\eta\frac{4\pi}{\Gamma_N}+\frac{\beta^{'}N}{2}\lambda_{l,m}\right) \quad (9.19)$$

with one special note: we have here separated out the ground states $\psi_{1,0}$, $\psi_{1,-1}$, and $\psi_{1,1}$, which are a three-fold degenerate ground state which we will address shortly.

The saddle point condition, allowing us to find the extremum for this internal free energy, is

$$0 = \frac{\partial F}{\partial \eta} = \left(1 - \frac{4\pi}{\Gamma_N} \sum_{m=-1}^{1} \alpha_{1,m}^2\right) - \frac{2\pi}{\Gamma_N} \sum_{l=2}^{\sqrt{N}} \sum_{m=-l}^{l} \left(N\eta\frac{4\pi}{\Gamma_N} + \frac{\beta' N}{2}\lambda_{l,m}\right)^{-1} \tag{9.20}$$

We still have not settled the three ground states, where $l = 1$. To resolve them we need additional constraints. We get these from the equations of state for $m = -1, 0, 1$:

$$0 = \frac{\partial F}{\partial \alpha_{1,m}} = \left(\frac{8\pi\eta}{\Gamma_N} + \beta^{'}\lambda_{1,m}\right)\alpha_{1,m} \tag{9.21}$$

These three equations have as their solutions

$$\alpha_{1,m} = 0 \quad \text{or} \quad \frac{8\pi\eta}{\Gamma_N} + \beta^{'}\lambda_{1,m} = 0 \text{ for each } m \tag{9.22}$$

In order to have nonzero amplitudes in at least one of the ground, or condensed, states, we must have that

$$\frac{4\pi\eta}{\Gamma_N} = -\frac{\beta^{'}}{4} \tag{9.23}$$

which implies that the inverse temperature must be negative:

$$\beta^{'} < 0 \tag{9.24}$$

Notice that these are the only states which carry a non-zero angular momentum, which therefore gives us information about the angular momentum of the atmosphere and how it depends on the temperature.

In the modes where $l = 2$ the Gaussian equation, equation (9.16),

$$\frac{\beta^{'}}{12} - \frac{\beta^{'}}{4} > 0 \tag{9.25}$$

can be satisfied only by a negative temperature $\beta^{'} < 0$ when there is energy in the angular momentum containing the ground modes, that is, when equation (9.23) is satisfied.

So what does the saddle point condition (9.20) look like at this nonzero solution? Substitution produces

$$0 = \left(1 - \frac{4\pi}{\Gamma_N} \sum_{m=-1}^{1} \alpha_{1,m}^2\right) - \frac{2\pi}{\Gamma_N} \sum_{l=2}^{\sqrt{N}} \sum_{m=-l}^{l} \left(-\frac{\beta' N}{4} + \frac{\beta' N}{2} \lambda_{l,m}\right)^{-1} \tag{9.26}$$

$$= \left(1 - \frac{4\pi}{\Gamma_N} \sum_{m=-1}^{1} \alpha_{1,m}^2\right) - \frac{4\pi}{\Gamma_N} \frac{1}{\beta' N} \sum_{l=2}^{\sqrt{N}} \sum_{m=-l}^{l} \left(-\frac{1}{2} + \lambda_{l,m}\right)^{-1} \tag{9.27}$$

$$= \left(1 - \frac{4\pi}{\Gamma_N} \sum_{m=-1}^{1} \alpha_{1,m}^2\right) - \frac{\beta_c'}{\beta'} \tag{9.28}$$

The formulation gives us a strong suggestion for what a critical inverse temperature ought to be.

The critical inverse temperature is negative and has a finite large N limit, and it is inversely proportional to the relative enstrophy Γ_N:

$$-\infty < \beta_c' = \frac{4\pi}{\Gamma_N N} \sum_{l=2}^{\sqrt{2}} \sum_{m=-l}^{l} \left(\lambda_{l,m} - \frac{1}{2}\right)^{-1} < 0 \tag{9.29}$$

The saddle point equation gives a way to compute the equilibrium amplitudes for the ground modes for temperatures below the negative critical inverse temperature β_c'. For inverse temperatures β with $\beta < \beta_c' < 0$

$$\sum_{m=-1}^{1} \alpha_{1,m}^2 (\beta) = \frac{\Gamma_N}{4\pi} \left(1 - \frac{\beta_c'}{\beta}\right) \tag{9.30}$$

What this means is that at positive temperatures there can not be any energy in the solid-body rotating modes. Since the solid-body rotating modes are the $l = 1$ ground or condensed states this tells us there is only the mixed state in positive temperatures, and therefore, there will be no phase transition in positive temperatures.

This is the spin-lattice representation of the self-organization of barotropic energy into a large-scale coherent flow in very high energies. This organization takes the form of symmetry-breaking Goldstone modes.

These extremely high energy ground modes carry with them a nonzero angular momentum which can be directed along an arbitrary axis, a problem formulated in the inertial frame with planetary rotation $\Omega = 0$.

Another project that simulates and analyzes the statistical equilibriums of a layer of divergent fluid when coupled to a massive, rotating sphere using the spin-lattice models, generalizing the results given here, provides results which suggest that initially non-divergent flow states are thermodynamically unstable to divergent perturbations [19]. The key fact from these numerical experiments — that overall divergent statistical equilibriums have been found to have non-divergent parts, the relative vorticity, that are close to super- and sub-rotating solid-body barotropic flows — appears to justify the analysis of the spherical model for the coupled barotropic fluid-sphere system.

Chapter 10

The Shallow-Water Models — High Energy, Cyclonic Solutions

10.1 Introduction

The rotating Shallow-Water Equations have long been used as models for aspects of planetary atmospheres ([13] and its references), and the model supports the formation of robust large-scale coherent structures in studies based on forced-damped and freely-decaying dynamics. In sections 2.4 and 2.5 we introduced a Shallow-Water Model [21] based on a statistical equilibrium spin-lattice model, and in this chapter and the next we intend to discuss Monte Carlo simulations as well as analytical deductions of significant physical properties pertaining to the Jovian atmospheres from the form of the energy terms in the Shallow-Water Equation Lagrangian. These simulations suggest that long-lived, large-scale coherent structures in rapidly-rotating shallow flows can be formed following a first order phase transition. In this chapter we will examine the negative temperature domain associated with very high mechanical energy to entrophies ratio [21]; in the next chapter, positive temperatures associated with lower energy to entrophies ratio, with direct applications to the Jovian atmospheres [22].

The Shallow-Water Model as introduced in section 2.4 generalizes the statistical Barotropic Vorticity Model to rotating flows of a single layer of horizontally divergent fluid. Through sections 2.4 and 2.5 we became familiar with a model that is based on a canonical constraint on the mechanical energy L, microcanonical in the relative vorticity circulation ζ, in the circulation δ, in the total fluid height h, in the relative vorticity enstrophy Q_{ζ^2}, and in the enstrophy Q_{δ^2}. The construction of a Metropolis-Hastings Monte Carlo algorithm from this is clear, following the procedure for the Barotropic Vorticity Model.

Simulations of the Gibbs ensemble will require a Lagrange multiplier known as the inverse temperature β representing the averaged energy level of the energy-momentum reservoir, and this multiplier is directly related to the expected value of the total mechanical energy for the equilibrated system. In two-dimensional vortical problems it is well-known that the inverse temperature can be a negative quantity, which happens when the expected energy of a bounded system is very high.

Results in this chapter and the next show the results of performing many Monte Carlo runs at a range of fixed inverse temperatures β in parallel on a small cluster. The negative and positive inverse temperatures are run within a narrow range and selected values for the relative vorticity enstrophy and the enstrophy. Some of the windows of mean total energy and enstrophy will include evidence for a first-order phase transition between disorganized and highly-organized end-states. These Monte Carlo simulations also require fixing the values of the relative vorticity and horizontal enstrophies or square-norms, after the Jovian parameters are set at Jupiter's radius, spin-rate, surface gravitational constant, and an average uppermost weather layer thickness of 20 km. No other inputs are required in the Shallow-Water Model since the microcanonical constraint on the total surface height is fixed by the previous entry, and the remaining two microcanonical constraints on, respectively, the total sums of relative vorticity and horizontal, are set at zero by Stokes's theorem on the sphere.

In summary, the key Jovian features we want to be able to predict are (1) the high velocities in the circumferential bands of the Great Red Spot as observed by Voyagers 1 and 2 [6]; (2) the predominance of anticyclonic spots over cyclonic ones in the Jovian weather layer; (3) the north-south asymmetry locating the Great Red Spot in the southern Jovian hemisphere, and the latitudes of the Great Red Spot and (4) the Limaye bands. A non-quasi-geostrophic and strongly divergent aspect of the Shallow Water Model appears to be necessary to account for all these key features. That is the capstone of this book, to be discussed in the last chapter where it will be clear that not only do simulations predict these key features but analytical deductions from the form of the energy terms of the Shallow-Water Equations Lagrangian provide sound physical reasons for the presence of these features in the Jovian atmosphere.

Monte Carlo simulations indicate that the Shallow-Water Model we have introduced will provide evidence for all these key features in the proper parameter ranges. In negative temperatures, the highest mechanical energy range, we expect to see cyclonic structures arise as it is when the planetary spin is large enough that there appears a significant orientation-based asymmetry in the free energy of cyclonic compared to anticyclonic end-states that favors cyclonic states as particular statistically stable states with maximum free energy [64] [21]. The orientation asymmetry we find through the angular momentum term (labelled AM) in the Shallow-Water Equation Lagrangian L (equation (2.85)). With similar reasoning on the same physical factor of the angular momentum, we can predict that when the end-states have low energy-to-enstrophy ratios we will see anticyclonic storms favored as will be apparent in the next chapter and in [22].

It appears that we can characterize the cyclonic/anticyclonic choice for dominant vortex structures based on the energy-to-enstrophy ratios. In the quasi-geostrophic regime, corresponding to high energy-to-enstrophy ratios (and weakly divergent), statistically stationary flows in this model will generally show cyclonic spots. In the non-quasigeostrophic regions (intermediate-geostrophic and beyond [100], [70]), with low energy-to-enstrophy ratios and strongly divergent steady flows, we will see mainly anticyclonic-vorticity end-states.

And we will also want to predict the detailed velocity or vorticity profiles within the highest cyclonic vortices predicted by the Shallow-Water Model. Quasi-geostrophic simulations suggest the largest cyclonic spot will cover a large part of the hemisphere in which it arises, and, more, that the relative vorticity inside this vortex will have a nearly-concentric, slowly-decreasing profile from a peak value at the geometric center to zero at a distance of approximately one planetary radius.

That distribution complements the Bessel's function-like properties of the family of uniform-q potential vortices described in [70], which show high rim velocities and vorticity when the Rossby radius is much less than the semi-diameter of the vortex, and which have a Gaussian-like interior vorticity distribution indicative of solid-body rotations when the semi-diameter of the vortex is two to three times the Rossby radius. At lower energy-to-enstrophy ratios we have evidence suggesting that large coherent vortices will have velocity-vorticity profiles close to those of the uniform-q potential vortices.

10.2 First Order Transitions

The Shallow-Water Equation model has a bounded phase space, and a quasi-two-dimensional nature to its flow. Because of this the Shallow-Water Model shows negative temperatures, as does the original Onsager Point

Vortex Model on the plane [80] [68], and extensions [62] [10], and classical energy-enstrophy models [50] [27]. Temperature here is the derivative of entropy with respect to energy. As a result when there is a finite maximum energy or a compact phase space, as shown by Onsager [80] the macrostates with extremal energies will have the least entropy, while the intermediate macrostates have maximum entropy. This implies the existence of negative temperatures, where the energies exceed the threshold value corresponding to the maximum entropy.

Some of the properties of negative temperatures predicted by Planck's theorem have been described but it is worth refreshing one's memory. In the case of the first-order phase transition at a negative temperature T_c in the Shallow-Water Model there will be a sharp decrease in the entropy as the system passes into the high energy phase. In the standard, latent heat calculation for an example like the boiling of water, the high energy phase — a vapor, physically — corresponds to the higher entropy. The implication and the feature which we will look for in the negative temperatures is an increase in the long-range order as the associated energy increases as we observe a first-order phase transition.

We will verify the numerical evidence for a first-order phase transition based on the extension to the Planck's Theorem in negative temperatures [64]. In negative temperatures the equilibrium we observe will be a maximization of the free energy $F = U - TS$. This free energy will typically not show a jump discontinuity at a first-order transition temperature T_c. Customarily one sees a cusp-type singularity, with the free energy continuous across the transition.

It is the internal energy U of the preferred macrostate that shows a clear, significant jump discontinuity at the transition. In passing from a more negative temperature through the critical temperature T_c to a less negative temperature — an increase of δ in energy — the entropy can be expected to decrease by $\frac{\delta}{T_c}$.

10.3 Antipodal Symmetry

An important property of the main part of the Shallow-Water Equations Lagrangian, that is the part of L that does not depend on $grad(h)$ where h is the surface height, is antipodal symmetry which will be shown next. Precisely because of this property, this part of the Lagrangian, which is the basis for the main part of the Monte Carlo algorithm used to obtain the simulation results reported in this chapter, cannot distinguish, for example between an anticyclonic state with a highest southern anticyclonic spot and its antipodal state - to be defined next - which is again a predominantly anticyclonic state except that its highest anticyclonic spot is now in the northern hemisphere, in the antipodal position of the other spot.

It will turn out crucially for the correct prediction of one of the key Jovian features by the non-quasi-geostrophic, strongly divergent shallow water model to be discussed in the next chapter, that the part of the total mechanical energy that is uniquely dependent on the gradient of the surface height h, and which is represented through judicious choice of the gauge-freedom in the arbitrary constant of the stream function, by a term that is a multiple of the potential vorticity — see chapter 2 — is responsible for the north-south asymmetry that is clearly observed in the form of the largest and highest anticyclonic spot in the Jovian atmosphere being the Great Red Spot in the south hemisphere, along with other lower southern anticyclonic spots such as the White Ovals [22]. Significantly, these energy terms involving $grad(h)$ do not change the overall qualitative properties of the main discoveries discussed in this chapter of a robust most-probable cyclonic-vorticity end-state in the high energy, nearly-quasi-geostrophic and weakly divergent regime of the Shallow-Water Model.

On the surface of a sphere the point (x_j, y_j, z_j) has an antipodal point $(-x_j, -y_j, -z_j)$. We can go further: given a state S_1 which has the site values (ζ_j, δ_j, h_j) at the point (x_j, y_j, z_j), we can define the antipodal state S_2 which has site values $(-\zeta_j, \delta_j, h_j)$ at the point (x_j, y_j, z_j). An antipodal pair — a state and its antipodal state — has this **antipodal symmetry** when both states have the same total mechanical energy and free energy.

Figure 10.2 shows the relative vorticity field of a state S_1 and of its antipodal state S_2. The definition of antipodal symmetry can be worked out by examining the lattice form of the mechanical energy. The truncated spin-lattice energy for state S_1 is

$$\begin{aligned} L_{S_1} = & -\frac{1}{2}\sum_{j,k}^{N} J_{j,k} h_j \zeta_j \zeta_k + \frac{4\pi R^4}{N}\Omega \sum_{j=1}^{N} \cos\left(\theta_j\right) h_j \zeta_j \\ & -\frac{1}{2}\sum_{j,k}^{N} J_{j,k} h_j \delta_j \delta_k + \frac{2\pi R^4}{N}\Omega^2 \sum_{j=1}^{N} h_j \sin^2\left(\theta_j\right) \\ & +\frac{2\pi g R^2}{N}\sum_{j=1}^{N} h_j^2 \end{aligned} \tag{10.1}$$

while the truncated energy for the antipodal state S_2 is

$$\begin{aligned} L_{S_2} &= -\frac{1}{2}\sum_{j,k}^{N} J_{j,k}h_j\left(-\zeta_j\right)\left(-\zeta_k\right) + \frac{4\pi R^4}{N}\Omega\sum_{j=1}^{N}\left(-\cos\left(\theta_j\right)\right)h_j\left(-\zeta_j\right) \\ &\quad -\frac{1}{2}\sum_{j,k}^{N} J_{j,k}h_j\delta_j\delta_k + \frac{2\pi R^4}{N}\Omega^2\sum_{j=1}^{N} h_j\sin^2\left(\theta_j\right) \\ &\quad +\frac{2\pi g R^2}{N}\sum_{j=1}^{N} h_j^2 \\ &= L_{S_1} \end{aligned} \tag{10.2}$$

The truncated energies for these states are equal apart from the $grad(h)$ terms. Their entropies are also equal. As a result the probabilities of occurrence for these antipodal states are equal according to the reduced L without these terms. The implication is that we should be as likely to see one as the other — which we observe in the Monte Carlo simulations.

10.4 Monte Carlo Results

That we have a model canonical in mechanical energy and microcanonical in several circulations and enstrophies means we can easily set up a Metropolis-Hastings Monte Carlo algorithm. These numerical simulations are set up much the same as any Ising-type model. The only substantial difference is that to preserve both circulation and enstrophy it is no longer enough to select two sites and alter their values; we must select three, and choose a new set of potential values which stays on both the plane of constant circulation and the sphere of constant enstrophy [64].

As often happens with this sort of spin-lattice Monte Carlo simulation the computational requirements are not great: ordinary desktop computers or work stations are perfectly adequate and Monte Carlo runs of as few as a million sweeps will provide a satisfactory equilibrium. In this chapter and the next we will see results based on runs no more numerically intensive than those are. They will be enough to examine qualitatively the emergence of coherent spots and to describe the factors of orientation asymmetry in large enough spins and of the values of the enstrophies. There is also numerical evidence suggesting a phase transition between disordered lower energy flow states and self-organized higher energy states which typically show a large cyclonic vortex in the southern hemisphere.

Jupiter has a radius $R = 7.15 \times 10^7 m$, with rotation $\Omega = 1.76 \times 10^{-4} s^{-1}$, surface gravity $g = 22.9 ms^{-2}$, and a height of the weather layer, the outermost atmosphere, of about 40 kilometers. We will use an average atmospheric height $H = 2.0 \times 10^4 m$, the 20 kilometers of the topmost layer, which represents the cloud tops and omits the quiescent lower layer. With a negative temperature $\beta = k_B T = -90$, a very high energy system, we can see broad-based cyclonic structures.

These broad-based cyclonic structures form within a narrow range of very high mechanical energy at relatively low enstrophies, which indicates that these are results in the quasi-geostrophic, that is, weakly-divergent, regime.

Figure 10.3 indicates that the zero level-set for the relative vorticity is more than one planetary radius away from the geometric center of the vorticity distribution. This supports the idea that the internal vorticity profile of the large cyclonic vortex has a Gaussian-type distribution. And these are robust simulations, in that the large cyclonic spots appear consistently over many runs and with similar data. The large cyclonic vortex is as likely to be in the southern hemisphere as well as the northern, a result of the antipodal symmetry.

The fact of these cyclonic vortices in negative temperatures is interesting enough. The question to follow is why we do not see an anticyclonic vorticity distribution. That they consistently do not appear suggests these anticyclonic storms would be unstable at high values of the mechanical energy. We need to find a reason the cyclonic vortex state might have the (preferred) higher free energy than the anticyclonic vortex, and this reason will be one of the most notable differences between negative temperature and positive-temperature equilibriums.

Consider the angular momentum AM and the moment of inertia term IM. The angular momentum term is not symmetric with respect to the sign of the relative vorticity ζ. In terms of the action βL of the Gibbs partition function Z_N when the planetary spin is large, the internal energy U — that is, the mean value of the mechanical energy under the Gibbs probability measure — of any cyclonic vorticity distribution will be different from that of an anticyclonic vorticity distribution of the same magnitude.

This "energy gap" is not the full story, of course: but since the entropy of a cyclonic spot will be equal to that of an anticyclonic storm of the same magnitude and position their free energies will be different and we have the ability to select one over the other as a statistical equilibrium. If we are in a negative temperature domain we expect, through Planck's theorem in negative temperatures, that the thermodynamic stability of a macrostate implies the more probable or stable state is the one with a higher free energy.

We will also see in positive temperatures the other predictable consequence: at positive temperatures, that is where mechanical energy is very low relative to planetary spin, and when the relative vorticity enstrophy and the enstrophy are large, we will see anticyclonic vortices, like that of the Great Red Spot [24], [70].

The expression for mechanical energy used in this model indicates that a necessary condition for a high-pressure vortex to arise against a quiescent background is a depth-dependent potential energy PE.

A natural question is where — at least, at what latitude — will a large coherent vortex appear? This positioning is dependent on the ratio of the angular momentum AM and the moment of inertia IM terms within the kinetic energy, in relation to the size of the relative vorticity enstrophy. We can examine the effects relative vorticity enstrophy has on the emergence and on the latitude positions of these large coherent vortices Q_{ζ^2} as in Figure 10.4.

Qualitatively, what we observe is that a small Q_{ζ^2} permits a single large coherent vortex, which will be located near the equator. Numerically and analytically we can observe that the moment of inertia IM and potential energy PE terms dominate the total mechanical energy when Q_{ζ^2} and Q_{δ^2} are small. But both the IM and PE terms are relatively large when a single coherent vortex forms at or near the equator. Thus, since we expect the equilibrium to be one which maximizes or nearly maximizes the free energy we see the single equatorial spot.

As Q_{ζ^2} becomes larger the spot moves away from the equator, again seen in Figure 10.4. The ratio of angular momentum AM to moment of inertia IM grows larger with Q_{ζ^2}. To make AM larger the system would 'prefer' the spots move away from the equator; but to make the IM term larger the system 'prefers' spots stay near the equator — thus, we see the appearance of spots farther from the equator.

When the relative vorticity enstrophy is large enough we see, as in Figure 10.5, the single spot become replaced with a pair of spots in the relative vorticity field.

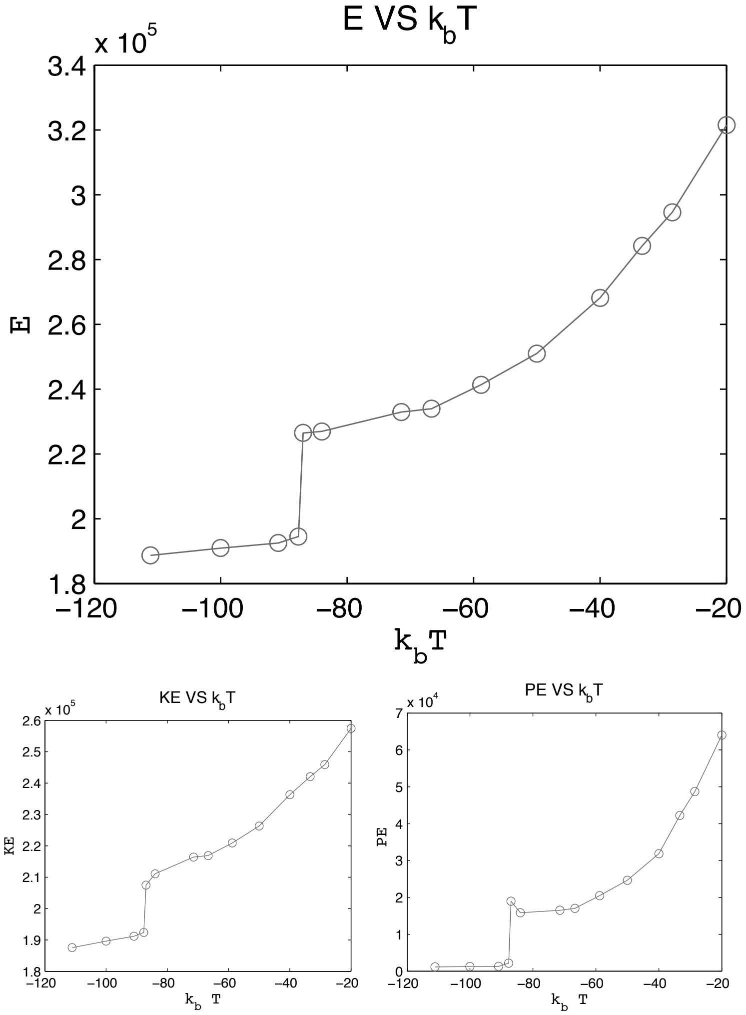

Fig. 10.1 Phase transition: Energy versus temperature.

10.5 Phase Transitions in Latent Heat

We see evidence of phase transitions in these extremely high energy, relatively-large planetary spin domains. As might be expected these transitions are different from what we see in the second-order phase transitions of the non-divergent barotropic model [20]. In a range of negative temperatures — remembering that a greater-magnitude negative temperature is cooler, that is, less energetic than a lesser-magnitude negative temperature — we can observe quantities like the energy (total energy, kinetic energy, or potential energy) as a function of temperature.

This we see in Figure 10.1. There is obviously evidence suggesting a jump in energy at a critical temperature T_c at somewhere around $k_b T = -85$, suggesting that there is a first-order transition.

In Figure 10.6 we see a large coherent spot appearing when the negative temperature is greater than this critical T_c, but that there is no coherent spot in the vorticity field of the equilibrium derived when the temperature is more negative than T_c. Here we see a "latent heat" of vortex formation.

10.6 Conclusion

With this Shallow-Water Model we have a model which looks likely to capture some of the interesting features of robust and long-lived vortical storms in gas giants and to understand why these storms can produce self-organizing structures in phase transitions. While we have not yet seen the anticyclonic structures we also have not yet examined positive temperature regions. We have seen evidence of some phase transitions associated with these atmospheric phenomena, but we have not built any specifically into the model proposed here. It is not clear a priori whether this statistical model will even support any phase transitions related to coherent vortex phenomena.

What we have identified is a key physical factor, the angular momentum, which seems to provide a way to discriminate between cyclonic and anticyclonic vorticities, and which explains why numerically we see a predominance of one over the other when the mechanical energy of the flows are large in comparison to enstrophy.

Based on a canonical constraint on the Lagrangian for the Shallow-Water Equation, with microcanonical constraints on the circulations, enstrophies, and total height, we do see already the Shallow-Water Model supports equilibriums with a single, broad-based cyclonic vortex at extremely high values of the total mechanical energy, at least when the planetary spin is large and when the relative vorticity enstrophy is large compared to the enstrophy. This indicates the quasi-geostrophic property of these flows. The formation of these coherent cyclonic spots appears to be associated to a first-order phase transition with a significant "latent heat".

Left unexplored yet is the domain in which there are low energy-to-enstrophy ratios, and unobserved are sets of parameters in which we see anticyclonic spots under Jupiter-like physical parameters. But we know also that we have not yet explored the positive temperature range, and this provides us with the final research and experiments to conduct.

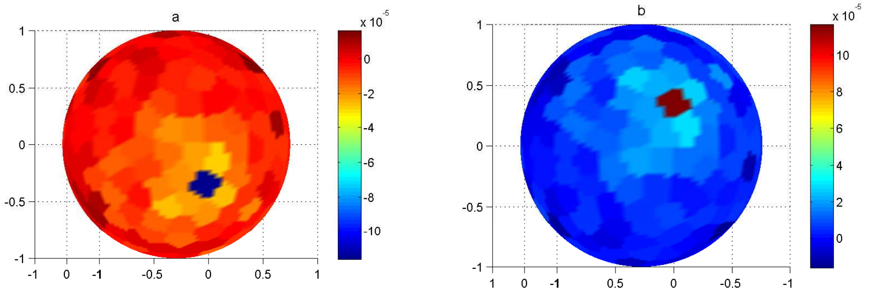

Fig. 10.2 Antipodal Symmetry: the relative vorticity field plots for the microstate S_1 (a) and its antipodal state S_2 (b).

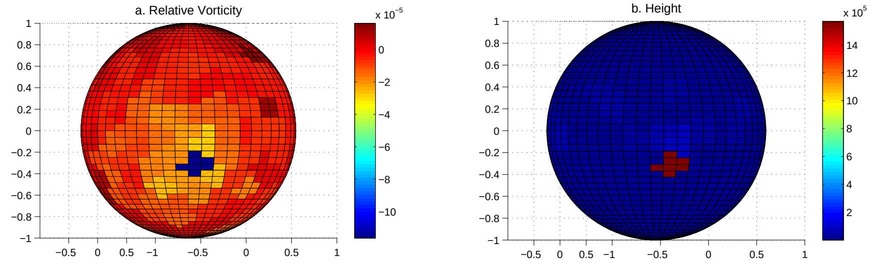

Fig. 10.3 A coherent cyclonic spot: the relative vorticity field (left) and the fluid height field (right).

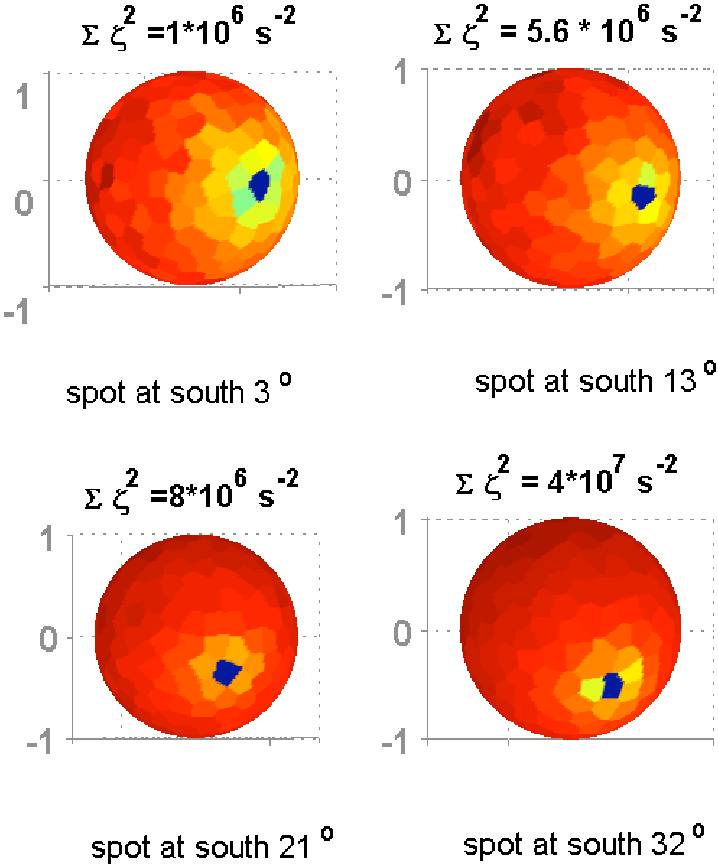

Fig. 10.4 The location of cyclonic spots moves as relative vorticity enstrophy changes.

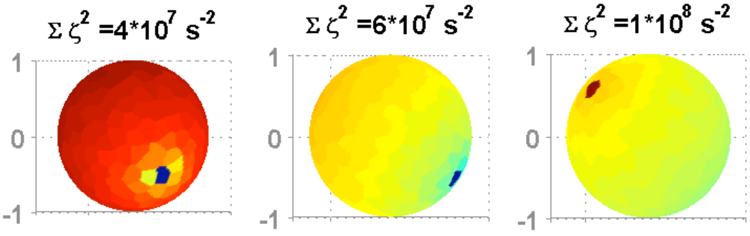

Fig. 10.5 One spot becomes two spots when relative vorticity enstrophy is too large.

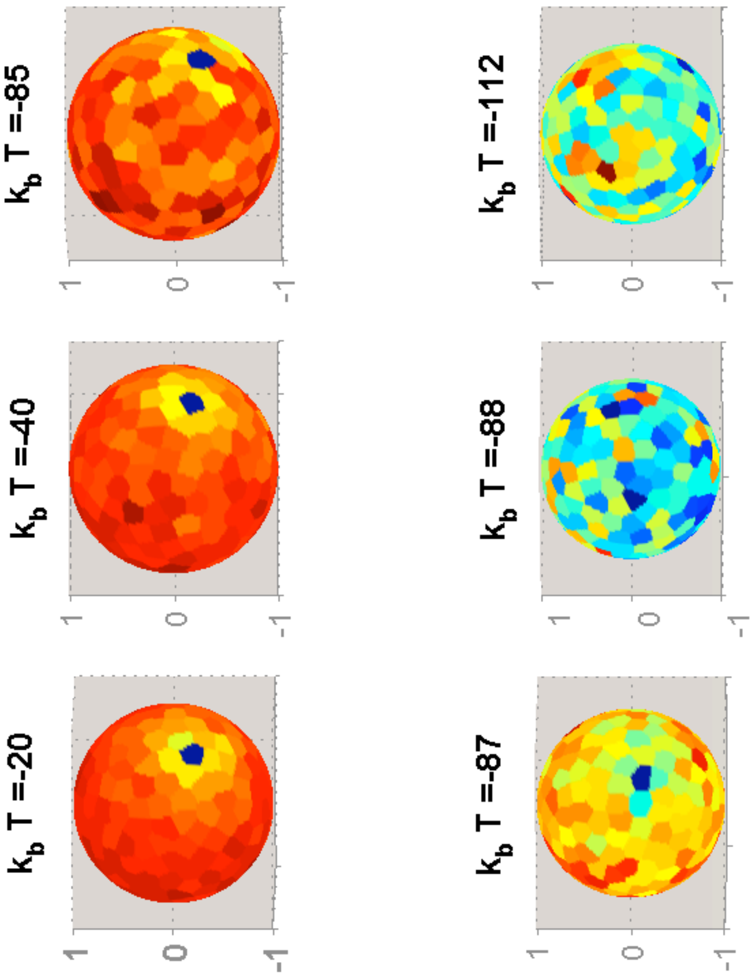

Fig. 10.6 Phase Transition: Relative Vorticity versus Temperature.

Chapter 11

The Shallow-Water Model — Strongly Divergent, Anticyclonic, Low Energy Solutions

11.1 Introduction

We have in the Shallow-Water Model [21] [22], introduced in sections 2.4 and 2.5 and expanded upon in section 9.3, presented a unified statistical theory on the formation and the robustness of large-scale coherent structures in planetary atmospheres through phase transitions [64] [67] [20] [94] which lends itself to straightforward Monte Carlo simulation. Always in mind in this subject is the continued fascinating existence of the Great Red Spot, a persistent, anticyclonic spot at about 22 degrees south latitude in the atmosphere of Jupiter. An anticyclonic spot, meteorologically, is one moving counterclockwise in the southern hemisphere; it would be clockwise in the northern hemisphere.

Including the Red Spot, it is widely accepted that the key features of Jupiter's atmosphere are (1) the high velocities in the circumferential bands of the Great Red Spot as observed by Voyagers 1 and 2 [6]; (2) the predominance of anticyclonic spots over cyclonic ones in the Jovian weather layer; (3) the north-south asymmetry locating the Red Spot in the southern Jovian hemisphere, and the latitudes of the Red Spot and (4) the Limaye bands. A non-quasi-geostrophic model appears to be necessary to account for all these key features and that is the capstone of this book.

Earlier statistical equilibrium and dynamical theories for large-scale coherent structures [70] [25] [46] successfully generate some of the aspects of the Great Red Spot and of the Limaye zonal bands. A soliton intermediate-geostrophic theory [100] may predict such a spot's anticyclonic state, while a quasi-geostrophic model predicts the internal vorticity distributions well but also predicts a predominance of cyclonicity [70]. But so far these quasi-geostrophic and intermediate-geostrophic dynamical and statistical theories, including recent one-and-a-half layer models [70] [25] [46] do not correctly predict all four key features of the Jovian atmosphere without further inputs.

An important work [24] reported numerical solutions of a rotating Shallow-Water Equations model that has very accurate comparisons with the observed internal velocity profile of the Red Spot. However, based on an inverse procedure to deduce the nontrivial zonal bottom topography of an effective reduced gravity model that is equivalent to a one-and-one-half layer model, this model required inputs from the Limaye surface velocity data, and therefore, cannot predict the Limaye banded structures. It is explicitly stated in [24] that the physical factors for the unstable zonal surface velocity profile are largely unknown.

In the region of negative statistical mechanics temperatures we observed in the last chapter the formation of large cyclonic spots at latitudes dependent on several physical quantities, particularly the relative vorticity enstrophy and the enstrophy. These are akin to some of the cyclonic spots found by Sommeria et al [93] experimentally and numerically by Marcus [71] and Miller. Aspects of these solutions were reported in a series of Nature articles as possible candidates for the Red Spot but were hotly debated by Antipov et al [1] and Williams - Yamagata [100], [2] who correctly insisted that only anticyclonic flow states are suitable candidates for the Great Red Spot on Jupiter.

The important point is that the Shallow-Water Model presented in chapter 2 supports two main regimes of end-states at the same Jovian parameters set, namely, the high energy and low enstrophies, nearly quasi-geostrophic and weakly divergent statistical equilibria discussed in chapter 10, and the low energy - large enstrophies, non-quasi-geostrophic, strongly divergent solutions presented in this chapter.

In this chapter, we have obtained robust end-state vorticity distributions with four key features of the Jovian atmosphere, including those of a storm resembling the Great Red Spot, or other lesser coherent spots such as the White Ovals, an anticyclonic vortex with a high rim velocity, in addition to evidence of a Limaye zone-belt banded structure, all in the same robust end-state of a single Monte Carlo run.

The Shallow-Water Model is derived from the Shallow-Water Equations on a rotating sphere: we have not made intermediate-geostrophic or quasi-geostrophic approximations and therefore this model will include as special cases the intermediate-geostrophic and the quasi-geostrophic regimes. That we choose a large enstrophy in these simulations means we are working in a non-quasi-geostrophic study. These enstrophies are chosen to model as best we can observed Jupiter data, particularly in the extrema of the observed relative vorticity fields in the Great Red Spot and in the zonal bands, which may have wind speeds near $100\frac{m}{s}$.

With an exploration of positive temperature regimes we will find in the distinctly non-quasi-geostrophic regime under Jovian parameters that the preferred macrostate for the Shallow-Water Model shows a large anticyclonic, high-pressure vortex placed about twenty degrees south latitude, with a clear indication of uniformly high velocity in its circumferential band. There will also be smaller and lower spots, typically anticyclones in the southern hemisphere and cyclones in the northern, with a banded zonal structure showing zones or belts in the relative vorticity, and the height data. This serves as a posteriori justification for the constraints we made in forming the Shallow-Water Model.

What we have suggested by this is the possibility that the predominance of anticyclonic spots in Jupiter's atmosphere results from a combination of the orientational asymmetry within the Lagrangian, which is therefore found in the free energy as well, noticeable in the large spin rate of Jupiter with the low mechanical energy to relative enstrophies ratio. More, the unique circumferential jet at the rim of the Great Red Spot may be a result of the alternating radial structure of the eigenfunctions of the relative kinetic energy operator in the Shallow-Water Equations.

Further evidence that orientational asymmetry in the Lagrangian may play an important role in the characterization of the self-organized end-states and the statistically-steady states comes from the non-divergent Barotropic Vorticity Models explored earlier [64] [20] of this unified theory, which allowed us to provide simple but cogent explanations for the preference for super-rotational atmospheres over sub-rotational atmospheres as observed at the slowly-rotating Venus and Titan.

11.2 Theoretical Predictions of the Shallow-Water Model

The Shallow-Water Equation Lagrangian [22] describing the mechanical energy of the atmosphere allows us to make quite a few theoretical predictions before starting any Monte Carlo experimentation.

11.2.1 *The Energy Gap from Large Planetary Spin and Anticyclonic Spots*

The properties of statistical equilibriums for the Shallow-Water Model, or any other statistical mechanics model, are determined by the free energy $F = U - TS$. Any phase transitions observed will be derived from the competition between the long-range order 'favored' by the term U and the disorder 'favored' by the entropy S. From the form of the Lagrangian, equation (2.87), and the orientation asymmetry in the angular momentum AM term noted in section 10.4 we can expect a substantial energy gap between the anticyclonic state A and its negation, the cyclonic state B. The anticyclonic state A turns out to have lower energy.

In the free energy F, we know the internal energy U is based on the expected value of the Lagrangian $\langle L \rangle$. The information-theoretic entropy S is dependent, in particular, on the locations of vortex spots, regardless of the cyclonic or anticyclonic nature of the spots. Therefore if all other factors are equal — that is if the height and horizontal divergence distributions are equal in A and B, and the relative vorticity distributions are negative of each other, and their entropies are equal in value — then the preferred state in positive temperatures will be A, with an anticyclonic predominance and a Great-Red-Spot-like, spot, as opposed to its cyclonic counterpart B.

11.2.2 *North-south Asymmetry and the Energy Terms in ∇h*

It will turn out crucially for the correct prediction of one of the key Jovian features by the non-quasi-geostrophic, strongly divergent Shallow-Water Model that the part of the total mechanical energy that is uniquely dependent on the gradient of the surface height h, and which is represented, through judicious choice of the gauge-freedom in the arbitrary constant of the stream function, by a term that is a multiple of the potential vorticity, – see chapter 2 — is responsible for the north-south asymmetry that is clearly observed in the form of the largest and highest anticyclonic spot in the Jovian atmosphere being the Red Spot in the south hemisphere, along with other lower southern anticyclonic spots such as the White Ovals [22]. As can be shown directly from the presence of a cosine of co-latitude expression, the terms linear in ∇h in the total kinetic energy (2.77) has the required north-south asymmetry in the form of an energy gap which, for a given anticyclonically dominant end-state, favors its main coherent spots to be located in the southern hemisphere, because the internal energy and hence the free energy of such a configuration is lower and therefore preferred – via Planck's theorem – by the statistical Shallow-Water Model over its antipodal counterpart which instead has its main anticyclonic spots in the northern hemisphere.

11.2.3 *Large Relative Enstrophies and High Rim Velocities*

Jupiter spins rapidly. Therefore its planetary vorticity is quite large. Unless the relative vorticity contained in structures such as the Great Red Spot and the Limaye bands are also large then the coherent spots and any bands will not be observable against the background. Furthermore earlier work in a non-quasi-geostrophic model suggests that large horizontal divergence enstrophy will be necessary to predict features of Jupiter's atmosphere.

This suggests that Monte Carlo trials on the Shallow-Water Model will not produce a Great Red Spot-like spot unless we have large values for the relative vorticity enstrophy and the horizontal divergence enstrophy. And we will examine the role of these enstrophies and the associated kinetic energy of the relative motions for the self-organization of large coherent spots. We are interested in the effect of the large relative enstrophy on the detailed velocity profile of the spot.

As we have large relative enstrophies, the corresponding relative kinetic energy terms in the Lagrangian — KE_ζ and KE_δ — we can expect to be significant compared to other energy terms. These two terms are cubic energy functionals as the height of the fluid layer is not separated out of the energy integral, while the angular momentum AM and the moment of inertia IM terms are quadratic functionals in the height, relative vorticity enstrophy, and horizontal divergence fields.

The dominant values of KE_ζ and KE_δ and the properties of the logarithmic kernel in these functionals combine with the fluid-surface height to provide a theoretical result which is not proved here:

Conjecture 11.1. *Given that there is a high Great Red Spot-like spot — whether anticyclonic or cyclonic is irrelevant here — in the equilibrium state, the relative vorticity and horizontal fields of this statistical equilibrium consist of nearly concentric rings of opposing signs and decreasing amplitudes, centered at the unique, highest point of the Great Red Spot-like spot. The radial distribution of these fields are similar to the Bessel function, although their detailed form is yet to be worked out.*

Suppose we have a Great Red Spot-like structure which is anticyclonic in the south. The centermost relative vorticity will be very positive; in the coloring scheme we use, deep red. The first ring from the center of the spot will have a very negative relative vorticity, represented as deep blue. The boundary of the deep red region coincides with the rim of the anticyclonic spot, and, significantly, there is a large counter-clockwise rim velocity far exceeding the velocity field in the interior of the spot. And furthermore as the result on the eigenfunctions of the kinetic energy operator states that the nearly concentric rings of opposite-signed vorticity will be centered on the unique focal point of the center of the Great Red Spot, then the minor coherent spots will not share a similar high rim velocity.

We will see this numerically in the Monte Carlo results of section 11.3. And the unique high rim velocity has been observed in the Great Red Spot by Voyager 1 and 2.

11.2.4 *Angular Momentum, Moment of Inertia, Entropy, and the Location of the High Spot*

In the previous chapter we saw that the relative angular momentum AM and moment of inertia IM affected the latitude at which a cyclonic vortex appeared in negative temperatures. We expect similar effects for the anticyclonic vortex in positive temperatures.

It is the angular momentum term which provides us with the anticyclonic predominance of the spots in the end-state. It also affects the latitude of the highest spot, since the cosine term in AM will be most negative when the anticyclonic spot is nearest the south pole, where the colatitude is π. The lower free energy and lower internal energy is preferred in the positive statistical mechanics temperatures and therefore we see the highest anticyclonic spot driven to the south pole.

Given a southern highest anticyclonic spot the sine-squared term of IM will have its lowest positive value when the highest spot is nearer the south pole. Therefore, considering the internal energy, we expect both the angular momentum and the moment of inertia terms to make more probable anticyclonic highest spots near the south pole.

A relatively large entropy S has a contrary effect on the statistically preferable location for the highest spot: the equatorial region has a higher degeneracy. With positive temperatures the free energy could be minimized by maximizing entropy and therefore making more probable such spots nearer the equator.

Therefore between the AM and IM terms and the entropy S we may expect the highest spot to be optimally located in some southern latitude, with the specific location dependent on the temperature or mean energy of the total mechanical energy reservoir which we derive from the small scales of the flow and the massive rotating planet.

We will seek therefore a positive temperature not too small in value, allowing entropy to be large enough to place a Great Red Spot at 20 degrees south latitude. Lower temperatures may be expected to put their spots nearer the south pole, and higher temperatures will eventually drive the Shallow-Water Model to a disorganized end state through what appears to be a first-order phase transition.

11.3 Monte Carlo Simulations and Results

As in the last chapter we set up a Metropolis-Hastings Monte Carlo experiment, canonical in the mechanical energy while microcanonical in the circulations, entrophies, and total height. This is computationally costly although months of continuous runs using ordinary personal computers or workstations are adequate to do a million sweeps or so, enough to find equilibrated states. Since we anticipate finding Great Red Spot-like structures we again use Jupiter parameters for the physical constants: the radius $R = 7.15 \times 10^7 m$, the spin rate $\Omega = 1.76 \times 10^{-4} s^{-1}$, the surface gravity $g = 22.9 \frac{m}{s^2}$, and the average height of the active atmospheric later $H = 2.0 \times 10^4 m$.

What we will describe here are numerical aspects of the robust end-state, the equilibrium found, in a narrow window of inverse temperature β, or the total mechanical energy space. In particular the first feature we will find are anticyclonic, high-pressure, high-rim velocity properties in the Great Red Spot-like highest spot in Figures 11.2, 11.3, and 11.4. The second feature will be numerical results which suggest the self-organization of coherent spots at low energy-to-enstrophy ratios in the Jovian atmosphere will occur at a first-order phase transition with latent heat, shown in Figure 11.1. Third, the banded vorticity profile, with alternating zones or belts in a Limaye-like structure, Figure 11.6, and multiple smaller and lower predominantly-anticyclonic spots which appear in Figures 11.3 and 11.4. It cannot be emphasized enough that except for the data used to show a first-order transition, all the color plots in this chapter, including those projected onto the zonal harmonics to produce evidence for the Limaye bands, are from a single robust end-state of a single long Monte Carlo run.

These Metropolis-Hastings routines are done on the spin-lattice model with a mesh near-uniformly distributed across the sphere. Like before, a particle Monte Carlo method generated the mesh. Initial randomized distributions of relative vorticity, height and, satisfying the stated constraints, are used to start the lattice Monte Carlo simulations. To ease the additional costs of computing the $grad(h)$ terms, the initial part of the Monte Carlo simulations are executed without the energy terms that are linear in $grad(h)$, and with randomized initial states which may have zero total potential vorticity. After a fairly long run, an intermediate state that have nonvanishing value of total potential vorticity and also north-south asymmetric with respect to the full L is continued in the last part of the Monte Carlo algorithm where the part of L that depends on $grad(h)$ are now included in the enthalpy simulated, albeit, at much lower frequency than the part of L with antipodal symmetry, again to lower computational costs.

There is a special note regarding the visual representation of these results. To better depict the detailed structure of the relative vorticity and horizontal fields centered at the peak of the Great Red Spot, these figures have a mild cutoff filters. The amplitudes at the eleven lattice sites clustered within the Great Red Spot anticyclonic spot are truncated before plotting Monte Carlo data sets for the same end-state as those in Figures 11.3 and 11.4.

11.3.1 *Key Features of the Great Red Spot-like Structure*

In Figure 11.3 we see an equilibrium state with a family of nearly concentric rings, alternating in direction, with decreasing amplitudes, centered at the highest spot in the relative vorticity field. It is presented similarly although not identically in the field. This matches the theoretical prediction described in section 11.2.3.

At the center of the highest spot the relative vorticity is its largest positive value. The first ring surrounding the spot has a large negative value. This lets us understand what is happening at the border of this Great Red Spot-like storm. The boundary of the red, anticyclonic, spot, experiences a maximal additive or reinforcing effect in the velocity fields as the opposite-signed vorticity regions swirl past one another.

The rim of our simulated Great Red Spot has a large counter-clockwise velocity, which agrees partially with the actual measurements made by Voyagers 1 and 2 [6], and also in agreement with some members of the family of uniform-q potential vorticies described in [70]. Specifically the agrement is with uniform-q potential vortices in which the vortex semidiameter is only two to three times the Rossby radius and therefore indicates some solid-body rotation in the interior of the vortex with highest velocity at the rim. There are similar vorticity profiles reported by intermediate-geostrophic models in [100].

Uniform-q potential vortices with a larger radius, where the semidiameters were five to ten times the Rossby radius, would in contrast have nearly zero vorticity in the interior, with an exponential rise to the peak on the inside of the circumferential band, dropping to a negative peak value on the outside edge of the band.

11.3.2 *First-Order Phase Transition with Latent Heat*

One of the features we hope to capture in proposing a statistical mechanics model for Shallow-Water Flows at positive temperatures are the robust and long-lived giant vortical storms found in gas giants as self-organized structures which arise in phase transitions. We do not know a priori that there are phase transitions relevant to Great Red Spot-like phenomena in this model, but we can look in numerical data for evidence of them, and if we do find such evidence we can try to understand numerically what type of transition it may be.

In non-divergent barotropic fluids we found evidence for second-order phase transitions [20]. In the Shallow-Water Model in negative temperatures we found evidence suggesting a first-order phase transition. And in examining the total energy, the kinetic energy, and the potential energy as functions of temperature we gather evidence that the formation of anticyclonic spots in the Shallow-Water Model in positive temperatures is related to a first-order phase transition. There is a large amount of energy exchange occurring at a constant temperature, presenting us with an energy gap we can interpret as latent heat.

In Figure 11.1 we see the total energy, kinetic energy, and potential energy plotted as functions of the statistical mechanics temperature. All these energies see a jump at a critical temperature T_c where $k_B T_C$ is approximately 2400 in the corresponding units for the atmosphere of Jupiter. The highest coherent spots appear only when the temperature is below T_c. The locations of these spots is near the south pole for temperatures very much lower than the critical temperature, which is in accord with the theoretical predictions of section 11.2.4. With a low entropy the minimum free energy is achieved more by minimizing the kinetic energy plus potential energy,

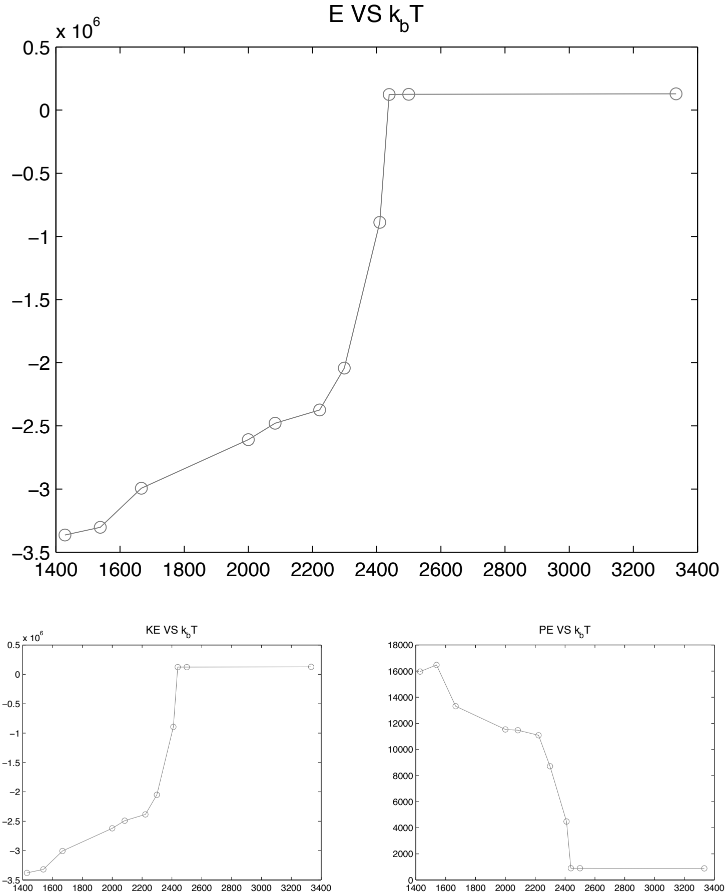

Fig. 11.1 Phase transition: energy versus temperature.

and those are minimized for a spot near the south pole.

An interesting side note is that as the inverse temperature β becomes larger — that is, as the temperature $k_B T$ becomes smaller — the kinetic energy decreases while the potential energy increases. The total energy decreases because the increase in kinetic energy is less than the decrease in potential energy.

11.3.3 *Multiple High Spots in the Same Macrostate*

One of the interesting results of the Monte Carlo simulations regards the presence and the types of multiple smaller and lower coherent spots for the same preferred end-state. These are obscured in the unfiltered data used to produce Figure 11.2 due to the visualization software's assignment of a color range for height data. That we hoped to see these alternate, smaller spots encouraged the imposing of a cutoff filter for the greatest peak.

In Figures 11.3a and 11.4a the Great Red Spot-like structure appears as a significant spot in the southern hemisphere, and a handful of other high spots are also in the nearer hemisphere. In Figures 11.3b and 11.4b are multiple smaller and lower spots on the hemisphere opposite the Great Red Spot location. The types of these spots — cyclonic or anticyclonic — can be read off of the height data.

There are several cyclonic spots on the opposite hemisphere from the Great Red Spot and in the north. There are also several cyclonic spots on the hemisphere near the Great Red Spot and in the south. Generally the anticyclonic spots we see on the Great Red Spot's hemisphere but in the north, or opposite the Great Red Spot's hemisphere and in the south. This rough distribution of cyclonic and anticyclonic spots matches the observed predominance in the southern Jupiter atmosphere of these storms.

By comparing the plots of vorticity and locating the anticyclonic small spots — red spots, in Figure 11.3 — to the plots of atmospheric heights and locating the high spots of atmospheric pressure — again red spots, in Figure 11.4 — we find that the small anticyclonic spots are associated with high-pressure regions, while the small cyclonic spot are associated with low-pressure regions.

11.3.4 *Belts and Zones*

The most dominant feature of Jupiter's visible atmosphere, after the Great Red Spot, is its alternating banded structures. By convention astronomers refer to the lighter stripes as zones and the darker stripes as belts and have a range of names for each long-lasting band along the range of latitudes [46] [83].

In Figure 11.5 an image of Jupiter's bands as taken by the Cassini spacecraft are shown, along with an idealized representation of these belts and zones.

Can we identify zones and bands in the Monte Carlo -produced spin-lattice equilibrium data, even though mesh sites were placed with no regard for regular latitude placements? In fact, we can, if we start from the Great Red Spot-like end-state with the peak values of relative vorticity, height, and at the eleven mesh sites making up the Great Red Spot truncated. With this truncated set of data we can form the spectral projection of this set onto the orthogonal set of zonal spherical harmonics $\Phi_{l,0}$. This gives us an approximation to the zone and band structure underlying the vorticity, height, and data.

In Figure 11.6 we see this (partial) spectral projection in each of the variables. Qualitatively, they are a strong match to the zones and belts of the actual Jupiter in Figure 11.5, and the number of zones and belts in the simulation agrees with the total numbers of zones and belts in the actual model. This model suggests interesting detail in the Limaye-like belts produced by the Monte Carlo simulation which has yet to be studied in full.

11.4 Conclusion

We formulated a Shallow-Water Model on the rotating sphere with the intention of constructing and simulating phenomena of Jupiter's atmosphere. In the last chapter and this we have used extensive Monte Carlo simulations to understand the typical statistical equilibrium configurations of this model when using a canonical Lagrangian/total mechanical energy model for the underlying Shallow-Water Equations and a microcanonical model for total height, for vorticity and divergence circulations, and for quadratic enstrophies of relative vorticity and horizontal divergence.

In both negative and positive temperatures we have seen that the angular momentum term in the Lagrangian is one of the physical quantities leading to interesting features of the Jovian atmosphere. It appears to be the physical effect determining whether anticyclonic or cyclonic vorticities are more likely to appear in the atmosphere of a rapidly spinning planet. In positive statistical mechanics temperatures we see it play an important role in the anticyclonic nature of the Great Red Spot and predominance of the anticyclonic spots in the atmosphere of Jupiter, which agree with the measurements by Voyagers 1 and 2 of actual Jupiter, corroborated by the information derived from studying the impact of comet Shoemaker-Levy 9 into Jupiter [15]. The angular momentum term is the one opening an energy gap between cyclonic and anticyclonic dominated flow states.

By applying a cutoff filter to the relative vorticity and the fluid-surface height distributions of a particular equilibrated end-state of the Monte Carlo simulation we find a predominance of small anticyclonic spots in the southern atmosphere which matches observations of Jupiter. With the cutoff data as well we can use spherical harmonics to identify evidence for a zone-belt banded structure that resembles the zones and belts we expect to see as well. That we have this zonal structure suggests that this model is deserving of more study as a model of Jupiter.

That the statistical equilibrium of this non-quasi-geostrophic Shallow-Water Model gives predictions which agree with the key features of Jupiter as observed by Voyager and Cassini is indicated first by the simulation's formation of a unique large anticyclonic spot with a high rim velocity like the Great Red Spot. Second, we see zonal jets organized in an alternating zones-and-belts pattern which resembles the Limaye banded structure. And finally we see multiple, lower coherent spots which reflect the anticyclonic predominance observed in the southern atmosphere of Jupiter, with a significant majority of these southern anticyclonic spots placed on the far side of the planet from the Great Red Spot.

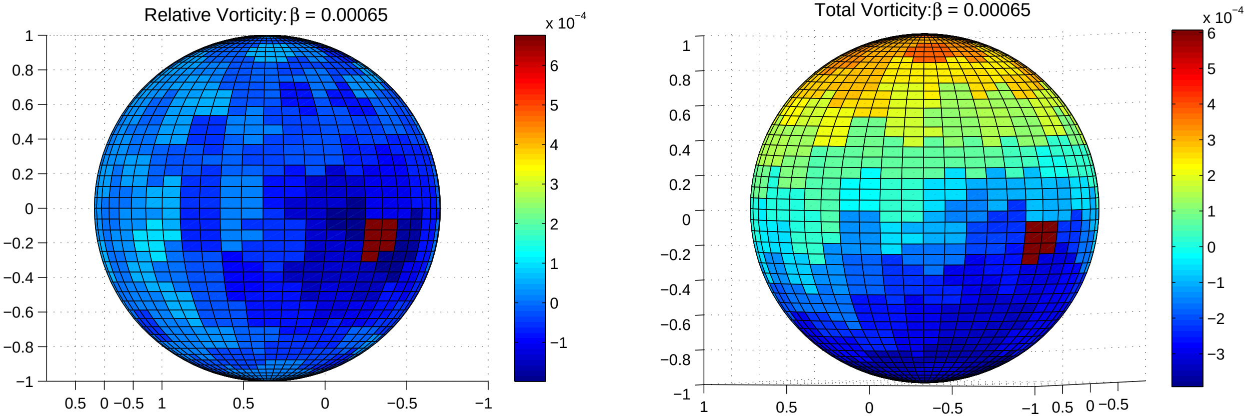

Fig. 11.2 Great Red Spot - like spot from Monte Carlo data with Jupiter's parameters and $\beta = 0.00062$, $Q_{\delta^2} = 7 \times 10^8$, $Q_{\zeta^2} = 3 \times 10^8$. Relative vorticity field (left) and total vorticity field (right).

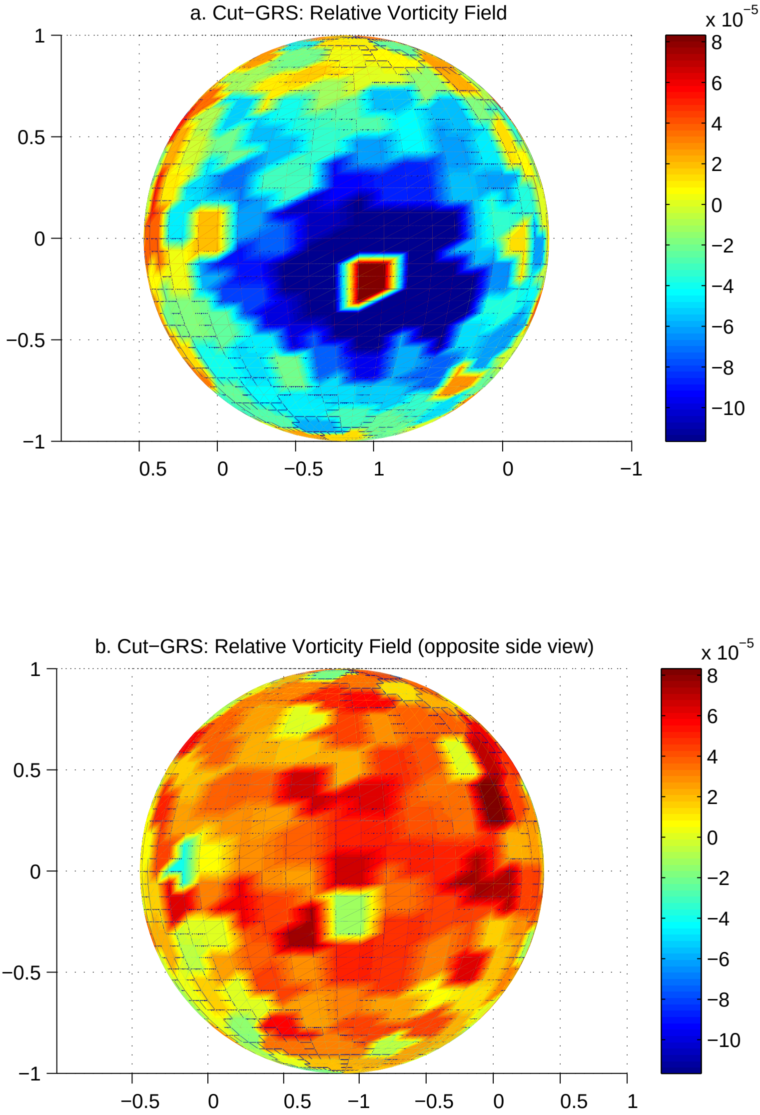

Fig. 11.3 High rim-velocity of Great Red Spot and Smaller Spots of the relative vorticity field: after imposing a filter to cut-off the highest values of the relative vorticity field. Figure a is from the side with a Great Red Spot; Figure b is from the opposite side.

a. Cut−GRS: Height Field

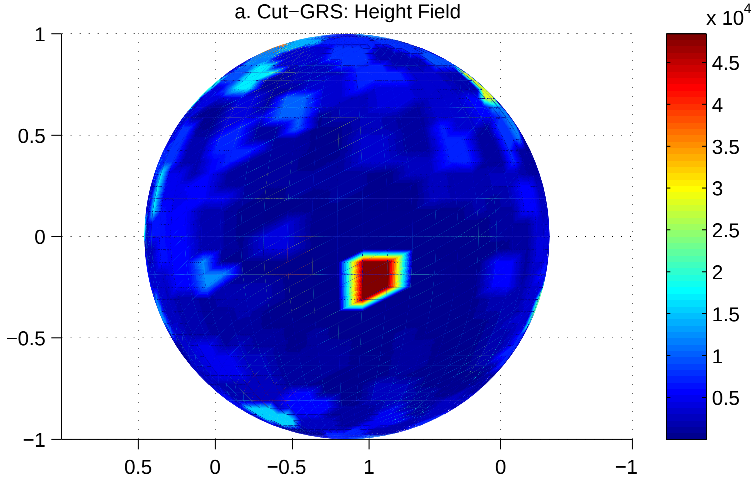

b. Cut−GRS: Height Field (opposite side view)

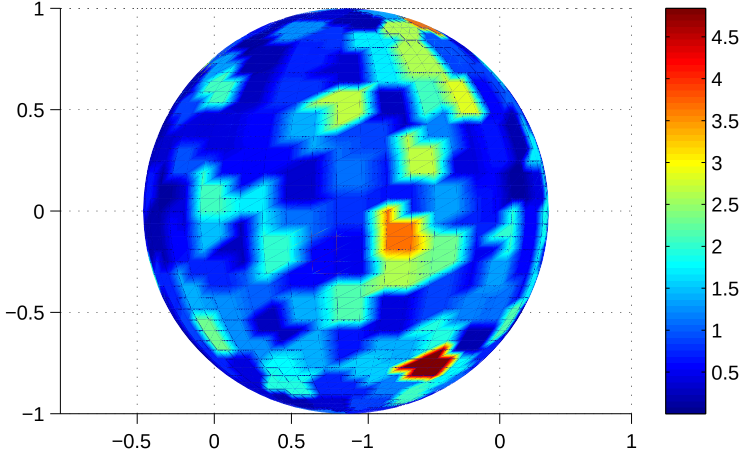

Fig. 11.4 Small Spots of the fluid height field: after imposing a filter to cut-off the highest values of the height field. Figure a is from the side with a Great Red Spot, Figure b is from the opposite side.

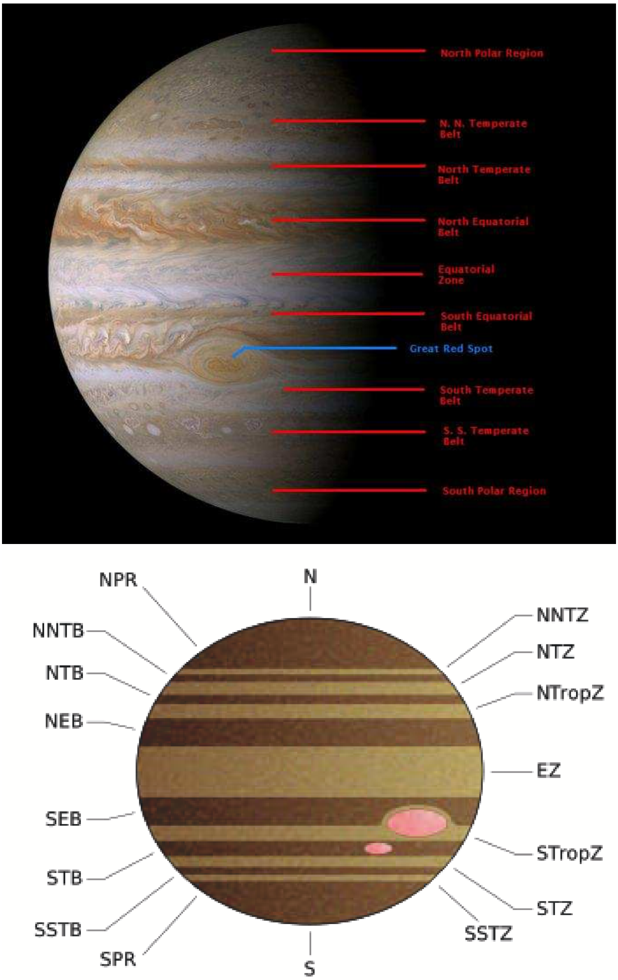

Fig. 11.5 Bands structure on Jupiter: the first picture is taken by Cassini spacecraft and the other is an idealized illustration of Jupiter's belts and zones.

a. Bands Structure: Relative Vorticity Field

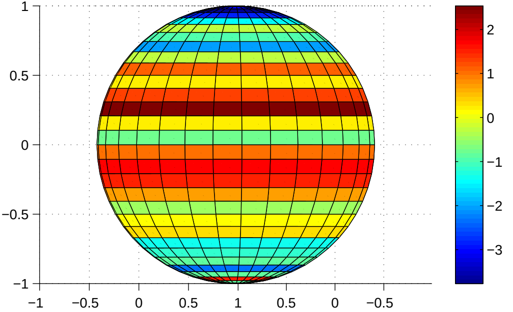

b. Bands Structure: Height Field

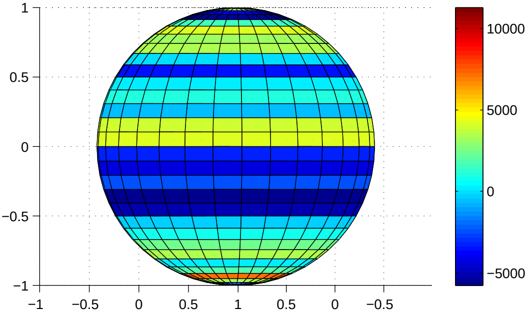

c. Bands Structure: Divergence Field

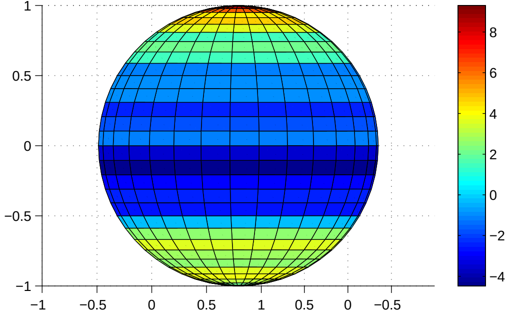

Fig. 11.6 Bands structure after projection onto zonal modes: Figure a is the relative vorticity field; Figure b is the modified fluid height field (with new 0 level due to Great Red Spot-cutoff filter), and c is the field.

Bibliography

[1] S V Antipov, M V Nezlin, E N Snezhkin, A S Trubinikov, Nature **323** (1986) 238 - 240.

[2] S V Antipov, M V Nezlin, E N Snezhkin, A S Trubinikov, P Marcus, J Sommeria, H Swinney, Nature **343** (1990) 517 - 518.

[3] V I Arnold, *Am Math Soc Transl* **79**, 267 (1965).

[4] S M Assad, C C Lim, *Statistical equilibrium of the Coulomb / Vortex gas on the unbounded two-dimensional place*, Discrete and Continuous Dynamical Systems B **5** (2005) 1 - 14.

[5] Richard Baum, William Sheehan, *In Search of Planet Vulcan.*

[6] R F Beebe, G S Orton, and R A West, *In Time-Variable Phenomena in the Jovian System*, NASA, 1989, SP-494, 327 - 335.

[7] B A Berg, *Multicanonical Recursions*, J Stat Phys **82** (1996) 323.

[8] T H Berlin, M Kac, *The Spherical Model of a Ferromagnet*, Phys Rev **86** (1952) 821 - 835.

[9] Denis Blackmore, Jyoti Champanerkar, Chengwen Wang. *A generalized Poincaré-Birkhoff theorem with applications to coaxial vortex ring motion*, Discrete and Continuous Dynamical Systems B **5** (2005) 15 - 48.

[10] D Blackmore, O Knio, *Hamiltonian structure for vortex filament flows*, ZAMM **81S** (2001) 45 - 48.

[11] E Caglioti, P L Lions, C Marchioro, M Pulvirenti, *A Special Class of Stationary Flows for Two-Dimensional Euler Equations: A Statistical Mechanics Description*, Commun Math Phys **143** (1992) 501 - 525.

[12] G Carnevale and J Frederiksen, *Nonlinear stability and statistical mechanics of flow over topography*, J Fluid Mech **175** (1987) 157 - 181.

[13] J Cho, L Polvani, *The Emergence of Jets and Vortices in Freely Evolving, Shallow-Water Turbulence on a Sphere*, Phys Fluids **8** (1995) 1531 - 1552.

[14] A Chorin, *Vorticity and Turbulence*, Springer-Verlag, 1995.

[15] Michael D Collins, B Edward McDonald, W A Kuperman, William L Siegmann, *Jovian Acoustics and Comet Shoemaker-Levy 9*, Journal of the Acoustical Society of America **97 (4)** (1995) 2147 - 2158.

[16] P Constantin, Weinan E, E Titi, *Onsager's Conjectore on the Energy Conservation for Solutions of Euler's Equation*, Commun Math Phys **165**

(1994) 207 - 209.

[17] Athena Coustenis, Fred Taylor, *Titan: The Earth-like Moon*, World Scientific, 1999.

[18] P J Dellar, R Salmon, *Shallow Water Equations with a Complete Coriolis Force and Topography*, Phys Fluids **17** (2005) 106601

[19] X Ding, C C Lim, *Equilibrium phases in an energy-relative enstrophy statistical mechanics model of barotropic flows on a rotating sphere — non-conservation of angular momentum*, American Meteorological Society Proceedings, 2006.

[20] X Ding, C C Lim, *Phase transitions to super-rotation in a coupled barotropic fluid — rotating sphere system*, Physica A **374** (2007) 152 - 164.

[21] X Ding, C C Lim, *First-Order Phase Transition and High energy Cyclonic Spots in a Shallow Water Model on a Rapidly Rotating Sphere*, preprint, 2008.

[22] X Ding, C C Lim, *Statistical Predictions of anticyclonic predominance, the Great Red Spot's high rim velocity, and Limaye's zones-belts — a Shallow-Water Model*, preprint, 2008.

[23] P D Ditlevsen, *Turbulence and Climate Dynamics*, Niels Bohr Institute, Copenhagen, Denmark, 2004.

[24] T E Dowling, A P Ingersoll, *Jupiter's Great Red Spot as a Shallow-Water System*, J Atmos Sci **46** (1989) 3256 - 3278.

[25] T E Dowling, *Dynamics of Jovian Atmospheres*, Annu. Rev. Fluid Mech., 1995, 27, 293 - 334

[26] James A Dunne, Eric Burgess, *The Voyage of Mariner 10: Mission to Venus and Mercury*, NASA SP-424, Scientific and Technical Information Office, Washington DC, 1978.

[27] S F Edwards, J B Taylor, *Negative Temperature States of Two-Dimensional Plasmas and Vortex Flows*, Proc R Soc Lond A **336** (1974) 257 - 271.

[28] I Ekeland, R Temam, *Convex Analysis and Variational Problems*, North-Holland, Amsterdam, 1976.

[29] R Fjortoft, *Application of integral theorems in deriving criteria of stability for laminar flows and for the baroclinic circular vortex*, Geophys Publ **17** (1950) 1 -

[30] R Fjortoft, Tellus **5** (1953) 225 -

[31] C Foias, R Saut, Indiana Univ Math J **33** (1984) 457 -

[32] Francois Forgot, *Alien Weather at the Poles of Mars*. Science 19 November 2004 1298 - 1299.

[33] D G Fox, S A Orszag, *Inviscid Dynamics of Two-Dimensional Turbulence*, Phys Fluids **16** (1973) 169 - 171.

[34] J S Frederiksen, *Eastward and Westward flows over Topography in Nonlinear and Linear Barotropic Models*, J Atmos Sci **39** (1982) 247 - 2489.

[35] J S Frederiksen, B L Sawford,*Statistical Dynamics of Two-Dimensional Inviscid Flows on a Sphere*, J Atmos Sci **31** (1980) 717 - 732.

[36] A Del Genio, W Zhuo, T Eichler, *Equatorial Superrotation in a slowly rotating GCM: Implications for Titan and Venus*, Icarus **101** (1993) 1 - 17.

[37] G Golitsyn, *Some Problems of Venus' Atmospheric Dynamics*, Icarus 60

(1984), 289 - 306.
[38] A Gill, *Atmospheric and Oceanic Dynamics* Cambridge University Press.
[39] J M Hammersley, D C Handscomb, *Monte Carlo Methods*, Methuen & Co, London; Wiley, New York City, 1964.
[40] A D Hatzes, D D Wenkert, A P Ingersoll, G E Danileson, *Oscillations and velocity structure of a long-lived cyclonic spot*, J Geophys Res **86** (1981) 8745 - 8749.
[41] G van Heijst, H Clercs, D Molenaar, *The Effects of Solid Boundaries on Confined Two-Dimensional Turbulence*, J Fluid Mech **554** (2006) 411 - 431.
[42] D Holm, J Marsden, T Ratiu, A Weinstein, Phys Rep **123** 1 (1985).
[43] James Holton, *An Introduction to Dynamic Meteorology*, Academic Press, 1992.
[44] Kerson Huang, *Statistical Mechanics, Second Edition.* John Wiley & Sons, 1988.
[45] R Iacono, *On the existence of Arnold-stable barotropic flows on a rotating sphere*, Phys Fluids **15** (2003) 3879 - 3882.
[46] A P Ingersoll, T E Dowling, P J Gierasch, G S Orton, P L Read, A Sanchez-Lavega, A P Showman, A A Simon-Miller, and A R Vasavada, *Dynamics of Jupiter's atmosphere. In Jupiter: The Planet, Satellites, and Magnetosphere*, Cambridge University Press 2004.
[47] S Jung, P Morrison, H Swinney, *Statistical Mechanics of Two-Dimensional Turbulence*, J Fluid Mech **554** (2006) 433 - 456.
[48] Y Kitamura, Y Matsuda, *Numerical experiments of two-level decaying turbulence on a rotating sphere*, Fluid Dynamics Research **34** (2004) 33 - 57.
[49] Heinz-Siegfried Kitzerow, Christian Bahr, *Chirality in Liquid Crystals.*
[50] R H Kraichnan, *Statistical Dynamics of Two-Dimensional Flows*, J Fluid Mech **67** (1975) 155 - 175.
[51] P D Lax, *Functional Analysis* Wiley-Interscience, New York, 2002.
[52] C Leith, *Diffusion Approximation for Two-Dimensional Turbulence*, Phys Fluids **11** (1968) 671.
[53] C Leith, *Minimum Enstrophy Vortices*, Phys Fluids **27** (1984) 1388 - 1395.
[54] C C Lim, *Energy Maximizers and Robust Symmetry Breaking in Vortex Dynamics on a Non-Rotating Sphere*, SIAM J Applied Math **65** (2005) 2093 - 2106.
[55] C C Lim, *Energy extremals and nonlinear stability in an energy-relative enstrophy theory of a coupled barotropic flow — rotating sphere system*, J. Math Phys. 48(1), 1 - 21, 2007.
[56] C C Lim, *Extremal Free Energy in a Simple Mean Field Theory for a Coupled Barotropic Fluid — Rotating Sphere System*, Discrete & Cont. Dyn. Sys. A, 19(2), 361 - 386, 2007.
[57] C C Lim, *Phase Transitions and Coherent Structures inan Energy-Enstrophy Theory for Axisymmetric Flows*, Phys Fluids **15** (2003) 478 - 487.
[58] C C Lim, *Phase Transitions to Super-Rotation in a Coupled Barotropic Fluid — Rotating Sphere System*, Plenary Talk, Proc IUTAM Symp, Steklov Institute, Moscow, August 25 - 30, 2006, in IUTAM Symp.

On Hamiltonian Dyn., Vortex structures, Turbulence, eds. A. Borisov, V. Kozlov, I. Mamaev, M. Sokolovskiy, p 151-161,Springer-Verlag, 2007. http://www.rpi.edu/∼limc/IUTAM06.pdf.

[59] C C Lim, *Energy-enstrophy theory for coupled fluid rotating sphere system — exact solutions for super-rotations*, in Proceedings of the International Workshop "Collective phenomena in macroscopic systems, Villa Olmo, Como, Italy 4 - 6 December 2006", G. Bertin, R. Pozzoli, M. Rome' & K.R. Sreenivasan Eds., page 96 - 106, World Scientific, 2007.

[60] C C Lim, S M Assad, *Self-containment radius for rotating planar flows*, Regular and Chaotic Dyn **10** (2005) 239 - 255.

[61] C C Lim, R S Mavi, *Phase Transitions of Barotropic Flows coupled to a Massive Rotating Sphere — Derivation of a Fixed Point Equation by the Bragg Method*, Physica A, **380** (2007) 43 - 60.

[62] C C Lim, J Montaldi, M Roberts, *Relative Equilibria of Point Vortices on a Sphere*, Physica D **148** (2001) 97 - 135.

[63] C C Lim, J Nebus, *The spherical model of logarithmic potentials as examined by Monte Carlo analysis*, Physics of Fluids **16** (2004) 4020 - 4027.

[64] C C Lim, J Nebus, *Vorticity, Statistical Mechanics, and Monte Carlo Simulations*, Springer-Verlag, New York City, 2006.

[65] C C Lim, J Shi, *The Role of Higher Vorticity Moments in a Variational Theory for Coupled Barotropic Flows on a Rotating Sphere*, Discrete and Cont. Dyn. Sys. B, 2008.

[66] C C Lim, N Induruwege, *A simple Lagrangian for the rotating shallow water equations*, preprint 2009.

[67] C C Lim, D Zhu, *Variational Analysis of Energy-Enstrophy Theory on the Sphere, Discrete and Continuous Dynamical Systems*, Supplemental Volume (2005) 611 - 620.

[68] T S Lundgren, Y B Pointin, *Statistical Mechanics of Two-Dimensional Vortices*, J Stat Phys **17** (1977) 323 -

[69] S R Maassen, H Clercx, G van Heijst, *Self-Organization of Decaying Quasi-Two-Dimensional Turbulence in Stratified Field in Rectangular Containers*, J Fluid Mech **495** (2003) 19 - 33.

[70] P Marcus, *Jupiter's Great Red Spot and Other Vortices*, Ann Rev Astron and Astrophys **31** (1993) 527 - 573.

[71] P Marcus, Nature **331** (1988), 693 - 696.

[72] R S Mavi, C C Lim, *Phase Transitions of Barotropic Flows on a Rotating Sphere — Non-conservation of Angular Momentum*, American Meteorological Society Proceedings, Atlanta, 2006.

[73] G Morandi, F Napoli, E Ercoless, *Statistical Mechanics: An Intermediate Course*, World Scientific, Singapore, 2001.

[74] J Miller, *Statistical Mechanics of Euler Equations in Two Dimensions*, Phys Rev Lett **65** (1990) 2137 - 2140.

[75] D Montgomery, G Joyce, *Statistical mechanics of "negative temperature" states*, Phys Fluids **19** (1974) 1139 - 1145.

[76] G Morandi, F Napoli, E Ercoless, *Statistical Mechanics: An Intermediate Course*, World Scientific, Singapore 2001.

[77] Mu Mu, T G Shepherd, *On Arnol'd's Second Nonlinear Stability Theorem for Two-Dimensional Quasi-Geostrophic Flow*, Geophys Astrophys Fluid Dyn **75** (1994) 21 - 37

[78] P Newton, *The N-Vortex Problem: Analytical Techniques*, Springer-Verlag 2001.

[79] P Newton, H Shokraneh, Proc R Soc London A **462** (2006) 149 -

[80] L Onsager, *Statistical Hydrodynamics*, Nuovo Cimento Suppl **6** (1949) 279 - 289.

[81] Michael Plischke, Birger Bergensen. *Equilibrium Statistical Mechanics.* 2nd Edition. World Scientic, Singapore, 1994.

[82] A M Polyakov, *Gauge Fields and Strings*, Harwood Academic Publishers, 1987.

[83] C C Porco, R A West, A McEwen, A D Del Genio, A P Ingersoll, P Thomas, S Squyres, L Dones, C D Murray, T V Johnson, J A Burns, A Brahic, G Neukum, J Veverka, J M Barbara, T Denk, M Evans, J J Ferrier, P Geissler, P Helfenstein, T Roatsch, H Throop, M Tiscareno, A R Vasavada, *Cassini Imaging of Jupiter's Atmosphere, Satellites, and Rings*, Science, 2003, 299, 1541 - 1547.

[84] R Robert, J Sommeria, *Statistical Equilibrium States for Two-Dimensional Flows*, J Fluid Mech **229** (1991) 291 - 319.

[85] John H Rogers, *The Giant Planet Jupiter*, Cambridge University Press, 1995.

[86] R Salmon, G Holloway, M C Hendershott, *The equilibrium statistical mechanics of simple quasigeostrophic methods*, J Fluid Mech **75** (1976) 691 - 703.

[87] G Schubert, S W Bougher, C C Covey, A D Del Genio, A S Grossman, J. L. Hollingworth, S S Limaye, R E Young, *Venus Atmosphere Dynamics: A Continuing Enigma*, in *Exploring Venus as a Terrestrial Planet* eds. L Esposito, E Stofan, and T Cravens, p 101 - 120, AGU 2007.

[88] T G Shepherd, *Applications of Hamiltonian Theory to GFD*, 1993 GFD Summer School Lecture Notes, Woods Hole Oceanographic Institution Technical Report WHOI-94-12 (1994) 113 - 152

[89] T G Shepherd, *Non-Ergodicity of Inviscid Two-Dimensional Flow on a Beta-Plane and on the Surface of a Rotation Sphere*, J Fluid Mech, **184** (1987) 289 - 302.

[90] T G Shepherd, *Symmetries, Conservation Laws, and Hamiltonian structure in Geophysical Fluid Dynamics*, Adv Geophys **32** 287 - 338.

[91] D Smith, *Variational Methods in Optimization* (Dover, New York City).

[92] J Sommeria, *Experimental Study of the Two-Dimensional Inverse Energy Cascade in a Square Box*, J Fluid Mech **170** (1986) 139 - 168.

[93] J Sommeria, S D Meyers and H Swinney, Nature **331** (1988) 689 - 693.

[94] H E Stanley, *Introduction to Phase Transitions and Critical Phenomena*, Oxford University Press, New York City, 1971.

[95] J B Taylor, *Negative Temperature States of Two-Dimensional Plasmas and Vortex Fluids*, Proc Roy Soc A **336** (1974) 257

[96] M J Thill, *On The Free Energy Monte Carlo Algorithm*, cond-mat/9703234

(1997)

[97] Lu Ting, Denis Blackmore, *Bifurcation of Motions of three vortices and applications*, Proceedings 2004 ICTAM Conference Warsaw (2004).

[98] K K Tung, J Atmos Sci **38** (1981) 308.

[99] Dieter Vollhardt, Peter Wölfle, *The Superfluid Phases of Helium 3.*

[100] G P Williams, T Yamagata, *Geostrophic Regimes, Intermediate Solitary Vortices and Jovian Eddies*, J. Atmos. Sci., 1984, 41, 453 - 478.

[101] G. Wolansky, *The Barotropic Vorticity Eqn under Forcing and Dissipation: Bifurcation of Non-symmetric responses and Multiplicity of Solutions*, SIAM J Appl Math, 49 (**6**), 1585 - 1607.

[102] S Yoden, M Yamada, *A Numerical Experiment on Two-Dimensional Decaying Turbulence on a Rotation Sphere*, J Atmos Sci **50** (1993) 631.

[103] W R Young, *Selective Decay of Enstrophy and the Excitation of Barotropic Waves in a Channel*, J Atmos Sci Vol 44 No 19 (1987).

Index